The Dissertation Committee for John Elliott Ortmann, Jr. Certifies that this is the approved version of the following Dissertation:

Optical and Electro-Optical Phenomena in Transition Metal Oxide Thin Film Heterostructures

Committee:

Alexander A. Demkov, Supervisor

Alejandro L. De Lozanne

John G. Ekerdt

Keji Lai

Maxim Tsoi

Optical and Electro-Optical Phenomena in Transition Metal Oxide Thin Film Heterostructures

by

John Elliott Ortmann, Jr.

Dissertation

Presented to the Faculty of the Graduate School of

The University of Texas at Austin

in Partial Fulfillment

of the Requirements

for the Degree of

Doctor of Philosophy

The University of Texas at Austin

May 2019

Dedication

To my Pawpaw, Jesse Wesley Ortmann.

January 1, 1936 – October 13, 2018

Acknowledgements

There are many people who deserve acknowledgement for offering me their support and assistance as I have pursued a PhD. With me from the beginning has been my wonderful wife, Lauren, who has seen the highs and lows firsthand and has always been there to celebrate or suffer with me accordingly. Without her, this journey would have been all the more difficult and I am forever grateful for her unwavering support and love in the face of any and all obstacles. I am beyond excited for the next chapter(s) in our life together.

My parents, John and Kathy Ortmann, have also been unbelievably supportive, not only throughout my postgraduate studies, but indeed throughout my entire life. They have consistently encouraged me to pursue my passions, whatever they may be, and have actively facilitated any amount of success I have had to this point. I consider myself exceptionally fortunate to have come from such great people.

On the academic side, I am forever grateful for the support and guidance of my advisor, Professor Alexander Demkov. Alex's sincere enthusiasm for the subjects at hand, coupled with his willingness to allow and encourage me to pursue my own interests, has helped me to grow immensely as a scientist and as a man during my time in graduate school.

From the Demkov group, Dr. Agham Posadas has been an invaluable resource. The depth of his knowledge is truly astounding, and I appreciate the amount of his own time he has given up helping me in my pursuits. Furthermore, I would like to thank the other members of the group for their help during my PhD studies. Both those members who came and left before me (Drs. Lin, Fredrickson, O'Hara, Kormondy, Ponath, and Gao as well as Jacqueline Geler Kremer and Matthew Butcher) and those who will outlast me (Donghan

Shin, Ali Hamze, Tobias Hadamek, Wei Guo, Marc Reynaud, Wente Li, Fatima Al-Quaiti, Ilya Beskin, Therese Paoletta, and Margaret Duncan) have contributed to where I am today.

I am also grateful for the generous support I have received from the members of the Neuromorphic Devices & Systems Group at IBM Research – Zurich, both during my stays there and since my return to Texas. In particular, Drs. Jean Fompeyrine and Stefan Abel, as well as soon-to-be-Dr. Felix Eltes, made me feel welcome from the beginning and have continued to support me in our shared pursuits over the past several years. I am especially indebted to Dr. Stefan Abel for the generous allocation of his time in assisting and mentoring me. I have learned a lot from him since my initial arrival in Zürich in 2016 and I hope to work with him again in the future.

Additionally, I would like to acknowledge and thank the many collaborators I have worked with throughout this journey. You have all contributed significantly both to my own knowledge and to the knowledge of the scientific community. I like to think we have made some progress together.

Lastly, I would like to thank my PhD committee, Professors de Lozanne, Ekerdt, Lai, and Tsoi, for taking the time to listen to me talk about what I have accomplished over the past six years.

Abstract

Optical and Electro-Optical Phenomena in Transition Metal Oxide Thin Film Heterostructures

John Elliott Ortmann, Jr., PhD

The University of Texas at Austin, 2019

Supervisor: Alexander A. Demkov

Beginning in the mid-20th-Century and continuing to the present day, integrated circuit technology has advanced at a remarkable pace. Dedicated materials research has been at the heart of this advancement, with materials development preceding technological advancement at nearly every stage. As humanity barrels onward into the 21st-Century and our data and computational demands grow ever larger, new computing hardware designed to handle increasingly difficult computational challenges is quickly becoming necessary in order to continue the historical breakneck pace of advancement. Just as in the early days of the integrated circuit, materials advancement will likely be the key to developing the next generation of computing hardware.

In this thesis, I investigate two materials systems well-suited for implementation in next-generation optical computing technologies: transition metal oxide quantum wells and Pockels-active $BaTiO_3$ thin film heterostructures. Both materials systems are promising for use in a wide variety of optical and electro-optical devices central to integrated photonic technologies, including quantum cascade lasers, photodetectors, electro-optic modulators and switches.

For the case of transition metal oxide quantum wells, I focus on the famous $SrTiO_3/LaAlO_3$ materials system. I first investigate the structural and optical properties of arbitrarily thick, high-quality $SrTiO_3/LaAlO_3$ heterostructures grown on oxide substrates. Then, I demonstrate the monolithic integration of these heterostructures on silicon, bringing them one step closer to technological relevance. Finally, I present detailed simulations of the optical and electro-optical performance of integrated photonic devices based on $SrTiO_3/LaAlO_3$ heterostructures.

In bulk form, the transition metal oxide $BaTiO_3$ has some of the largest known Pockels coefficients. However, early work suggests the coefficients are reduced by roughly a factor of ten when fabricated as a thin film. Here, I demonstrate the first $BaTiO_3$-based integrated devices showing bulk-like Pockels coefficients. Then, I iterate on the initial design of the devices in order to optimize them for ultra-low-power refractive index tuning. The resulting devices achieve refractive index tuning with power consumption many orders of magnitude less than previous reports. Taken together, the investigations in this thesis will hopefully open the door for the development of new kinds of optical and electro-optical devices for use in integrated photonics technologies.

Table of Contents

List of Tables

List of Figures

Chapter 1: Introduction

1.1 Materials Development in Computing Technologies

Beginning roughly with the advent of the integrated electronic circuit in the mid-20th Century, computing has played an ever-increasing role in our daily lives. No longer is computational power a luxury afforded to few. Rather, it has become a necessity in nearly every aspect of modern society. From banking to shopping, entertainment to navigation, our infrastructure has come to rely on computation in a way that would have been nearly unfathomable just half a century ago.

The journey of personal computers from luxury product to central societal feature would not have been possible without concentrated efforts in materials development. Semiconductors, most notably silicon (Si) and its native oxide SiO_2, form the basis of conventional integrated electronics. Through the development of advanced materials growth and processing techniques, nearly defect-free Si/SiO_2 interfaces can be formed [1], allowing for the rapid miniaturization of Si-based metal-oxide-semiconductor field-effect transistors (MOSFETs; Figure 1.1a). It is this miniaturization that has driven the rapid increase in computing power, speed and efficiency for decades (Figure 1.1b).

However, as MOSFETs continued to shrink, SiO_2 soon became problematic as a gate dielectric material due to unacceptable levels of leakage current through the extremely thin layers required for device scaling [2]. To solve this problem, further materials development was necessary. An ideal gate dielectric material is one that can simultaneously provide a relatively large value of capacitance and excellent electrical isolation through the minimization of leakage current. Because both capacitance and leakage scale inversely with the thickness of the gate, these two requirements would at first appear to conflict with one another. However, the gate capacitance C is controlled by both the dielectric layer

thickness t and the material's dielectric constant κ according to $C \propto \frac{\kappa}{t}$. Therefore, gate dielectric layers can be kept relatively thick (thus reducing leakage current) and high capacitance can be simultaneously maintained through the development of so-called "high-κ" materials, or, those with large dielectric constants.

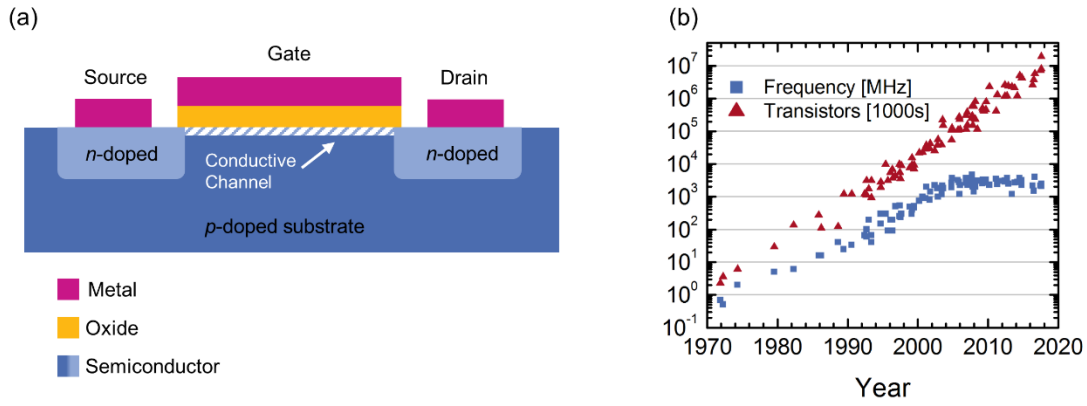

Figure 1.1: (a) Schematic of a MOSFET device showing the source, drain, and gate electrodes (pink), gate dielectric layer (yellow) and semiconductor substrate (blue). A conductive channel can be electrically formed between the source and drain regions and allows the device to be switched between "off" and "on" states. Here, I have shown the substrate as *p*-type doped and the source and drain regions as *n*-type doped, but the opposite configuration is also possible. (b) Plot of the operating frequency (blue) and number of transistors (red) per microprocessor as a function of year.

As a result of the shortcomings of SiO_2 as a gate dielectric material, intense materials research and development efforts were launched focusing on the discovery and development of new high-κ dielectrics [3], [4]. Of particular interest were those materials which could be integrated with Si substrates for use in industrial complementary metal-oxide-semiconductor (CMOS) processes [5], [6]. These materials research efforts came to fruition when Intel launched a new 45 nm technology node in 2007 in which a new material, hafnium dioxide (HfO_2), was used as a gate dielectric [7], [8]. Ultimately, HfO_2-based devices outperformed traditional SiO_2-based devices [9], [10], once again

demonstrating the fundamental importance of materials development in the advancement of computing technologies.

Today, further scaling of integrated circuits is becoming increasingly challenging using conventional methodologies [11], [12]. As a result, many alternative paths toward faster and more efficient computing technologies are being explored, including optical [13], [14], quantum [15], [16], and neuromorphic [17] computing. Not surprisingly, nearly all alternative computing technologies currently being explored first require dedicated materials research efforts before they can hope to become commercially viable.

Although many paths have been explored and many breakthroughs have occurred throughout the relatively short history of the microelectronics industry, all development has had one thing in common: materials development precedes technological development. Therefore, as we enter a time of uncertainty, with the end of Moore's Law in sight [18], [19] and copper interconnects reaching their fundamental limits [20], materials development is more important than ever to continue driving computing technologies forward. In this thesis, I explore the development of a specific type of promising materials: transition metal oxide (TMO) thin films. These explorations follow not only a path of intellectual curiosity, but also seek to relate the novel phenomena observed in TMO thin films and heterostructures to their practical potential for use in next-generation computing hardware. At the end, I provide a roadmap for bridging the gap between materials development and technological development and offer specific examples in which TMO thin films and thin film heterostructures may find use in novel technologies.

1.2 Transition Metal Oxides and their Thin Film Heterostructures

Transition metals are a class of metallic elements corresponding approximately to those found in Groups 3 through 12 of the periodic table (Figure 1.2). These elements are

characterized by a partially filled *d* shell and, in contrast to most other elements in the periodic table, can often display several stable valence states. In practice, the lanthanide and actinide metals are also typically considered transition metals, although these elements have a fully occupied *d* shell and a partially filled *f* shell.

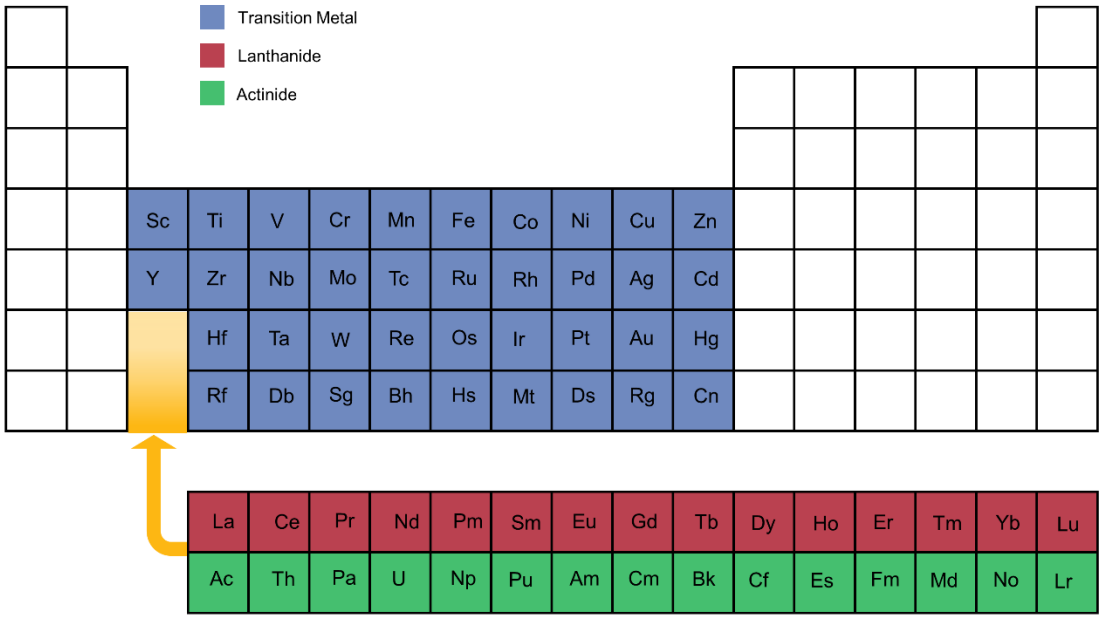

Figure 1.2: Periodic table of the elements, showing the *d*-shell transition metals (blue), lanthanides (red) and actinides (green). Oxides of these elements will be the primary focus of this thesis.

Transition metal oxides (TMOs) are formed through the bonding of one or more transition metals with oxygen. The phenomenon of variable valence in transition metals allows for the formation of a huge array of different TMOs with a wide variety of different electronic configurations. In the bonding process, the *s* electrons of the transition metal or metals are transferred to oxygen, leaving the partially occupied outer *d* shell (or, in the case of the lanthanides and actinides, *f* shell) of the transition metals as the highest occupied electronic states. It is these highly correlated outer electrons that determine the properties

of the TMO. In this context, "highly correlated" means the behavior of a given electron depends sensitively on its interactions with other electrons within the system.

The nontrivial correlation effects between the outer electrons of TMOs result in a plethora of interesting electronic, magnetic, structural, and optical phenomena in these materials [21]. Behaviors such as metal-insulator transitions [22], superconductivity [23]–[25], multiferroicity [26], [27], ultra-fast structural phase transitions [28], and large optical nonlinearities [29], to name a few, have all been observed in TMOs.

When fabricated in the form of thin films, TMOs display an even wider array of electronic, magnetic, structural and optical properties, many of which have no bulk analogues [30], [31]. This is because thin films offer extra degrees of freedom in tuning materials properties due to their reduced dimensionality and the potential to form thin film heterostructures by stacking several distinct materials. The fabrication of thin film heterostructures can often artificially alter or break crystalline symmetry [32]–[35], leading to the observation of emergent phenomena not present in bulk materials. TMO thin films heterostructures have shown phenomena as diverse and unexpected as interfacial superconductivity between two insulators [36]–[39], interfacial magnetism between materials that are non-magnetic in bulk form [38]–[43], and strong polarization enhancement through the layering of nominally non-ferroelectric materials with traditional ferroelectrics [44]. It is this wealth of diverse phenomena that make TMO thin film heterostructures fascinating both from the point of view of fundamental physics and for the development of novel technology.

1.3 The Work in this Thesis

In this thesis, I investigate a particular class of TMO materials with a characteristic chemical formula, ABO_3, where A and B are both metallic elements with at least one

coming from the transition metals. Such TMOs are part of a materials family known as the perovskites. In addition to a common chemical formula, many ABO_3-type perovskites share a common crystal structure (Fig. 1.3a). This common crystal structure allows for epitaxial integration between different TMO perovskites with typically small mismatches in lattice parameters (Fig. 1.3b) and facilitates the fabrication of a multitude of possible TMO perovskite thin film heterostructures.

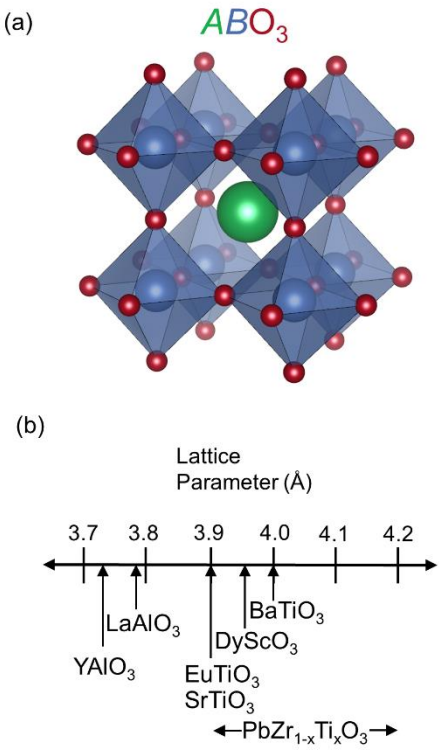

Figure 1.3: (a) Cubic crystal structure of ABO_3 perovskites. Green spheres represent *A*-site cations, blue spheres represent *B*-site cations and red spheres represent oxygen. Schematic made using VESTA software [45] (b) Lattice parameters of several common ABO_3 perovskite materials. Lattice constants referenced from [46] and [47].

Most of the work in this thesis focuses on two distinct perovskite device structures: TMO quantum wells (QWs) and TMO heterostructures displaying the Pockels effect, a nonlinear optical effect resulting in the change of a material's refractive index under the application of an electric field. Both QWs and Pockels-active materials have a wide range of potential technological applications, including electro-optic modulators and switches [48]–[51], lasers [52] and other light sources [53], photodetectors [54], [55], optical memories [56], and neuromorphic computing [57].

The rest of this thesis is organized as follows. Chapter 2 provides an overview of the primary experimental techniques used to carry out this research. Here, I focus on the fundamental techniques found at every stage of this research and leave the explanations of more specialized methods to the relevant chapters in which they first appear. Chapter 3 details systematic structural investigations of TMO QW heterostructures grown epitaxially on oxide substrates. Chapter 4 discusses the optical properties of the TMO QW heterostructures structurally characterized in Chapter 3. In Chapter 5, I describe the monolithic integration of the TMO QW heterostructures from Chapters 3 and 4 on Si. The integration of these structures on Si is an important milestone toward their use in practical technologies. Chapter 6 presents simulation efforts pertaining to the incorporation of TMO QWs into integrated photonics technologies and discusses the potential electro-optic operation of such devices. Chapter 7 details the experimental testing of integrated photonic devices based on the Pockels effect in $BaTiO_3$ (BTO). Finally, Chapter 8 summarizes the work in this thesis, provides an outlook for TMO-based integrated devices and hardware, and presents a roadmap for bridging the gap between materials development and technological development.

1.4 REFERENCES

[1] T. Hattori, "Chemical Structures of the SiO_2 Si Interface," *Crit. Rev. Solid State Mater. Sci.*, vol. 20, no. 4, pp. 339–382, Jan. 1995.

[2] H. Iwai, "Roadmap for 22nm and beyond (Invited Paper)," *Microelectron. Eng.*, vol. 86, no. 7–9, pp. 1520–1528, Jul. 2009.

[3] G. D. Wilk, R. M. Wallace, and J. M. Anthony, "High-κ gate dielectrics: Current status and materials properties considerations," *J. Appl. Phys.*, vol. 89, no. 10, pp. 5243–5275, May 2001.

[4] G. Ribes, J. Mitard, M. Denais, S. Bruyere, F. Monsieur, C. Parthasarathy, E. Vincent, and G. Ghibaudo, "Review on high-*k* dielectrics reliability issues," *IEEE Trans. Device Mater. Reliab.*, vol. 5, no. 1, pp. 5–19, Mar. 2005.

[5] E. P. Gusev, D. A. Buchanan, E. Cartier, A. Kumar, D. DiMaria, S. Guha, A. Callegari, S. Zafar, P. C. Jamison, D. A. Neumayer, M. Copel, M. A. Gribelyuk, H. Okorn-Schmidt, C. D'Emic, P. Kozlowski, K. Chan, N. Bojarczuk, L.-A. Ragnarsson, P. Ronsheim, K. Rim, R. J. Fleming, A. Mocuta, and A. Ajmera, "Ultrathin high-K gate stacks for advanced CMOS devices," in *International Electron Devices Meeting. Technical Digest (Cat. No.01CH37224)*, 2001, p. 20.1.1-20.1.4.

[6] J. Robertson and R. M. Wallace, "High-K materials and metal gates for CMOS applications," *Mater. Sci. Eng. R Reports*, vol. 88, pp. 1–41, Feb. 2015.

[7] K. Mistry, C. Allen, C. Auth, B. Beattie, D. Bergstrom, M. Bost, M. Brazier, M. Buehler, A. Cappellani, R. Chau, C.-H. Choi, G. Ding, K. Fischer, T. Ghani, R. Grover, W. Han, D. Hanken, M. Hattendorf, J. He, J. Hicks, R. Huessner, D. Ingerly, P. Jain, R. James, L. Jong, S. Joshi, C. Kenyon, K. Kuhn, K. Lee, H. Liu, J. Maiz, B. McIntyre, P. Moon, J. Neirynck, S. Pae, C. Parker, D. Parsons, C. Prasad, L. Pipes, M. Prince, P. Ranade, T. Reynolds, J. Sandford, L. Shifren, J. Sebastian, J. Seiple, D. Simon, S. Sivakumar, P. Smith, C. Thomas, T. Troeger, P. Vandervoorn, S. Williams, and K. Zawadzki, "A 45nm Logic Technology with High-k+Metal Gate Transistors, Strained Silicon, 9 Cu Interconnect Layers, 193nm Dry Patterning, and 100% Pb-free Packaging," in *2007 IEEE International Electron Devices Meeting*, 2007, no. May 2014, pp. 247–250.

[8] M. Bohr, R. Chau, T. Ghani, and K. Mistry, "The High-*k* Solution," *IEEE Spectr.*, vol. 44, no. 10, pp. 29–35, Oct. 2007.

[9] Y.-S. Lin, R. Puthenkovilakam, and J. P. Chang, "Dielectric property and thermal stability of HfO_2 on silicon," *Appl. Phys. Lett.*, vol. 81, no. 11, pp. 2041–2043, Sep. 2002.

[10] E. P. Gusev, C. Cabral, M. Copel, C. D'Emic, and M. Gribelyuk, "Ultrathin HfO_2 films grown on silicon by atomic layer deposition for advanced gate dielectrics applications," *Microelectron. Eng.*, vol. 69, no. 2–4, pp. 145–151, Sep. 2003.

[11] R. Courtland, "Transistors could stop shrinking in 2021," *IEEE Spectr.*, vol. 53, no. 9, pp. 9–11, Sep. 2016.

[12] A. P. Jacob, R. Xie, M. G. Sung, L. Liebmann, R. T. P. Lee, and B. Taylor, "Scaling Challenges for Advanced CMOS Devices," *Int. J. High Speed Electron. Syst.*, vol. 26, no. 01n02, p. 1740001, Mar. 2017.

[13] S. Wakelin and A. C. Walker, "Digital optical computing," *Phys. Educ.*, vol. 29, no. 3, pp. 155–159, May 1994.

[14] H. Yang, V. Khayrudinov, V. Dhaka, H. Jiang, A. Autere, H. Lipsanen, Z. Sun, and H. Jussila, "Nanowire network–based multifunctional all-optical logic gates," *Sci. Adv.*, vol. 4, no. 7, p. eaar7954, Jul. 2018.

[15] A. Steane, "Quantum computing," *Reports Prog. Phys.*, vol. 61, no. 2, pp. 117–173, Feb. 1998.

[16] J. Preskill, "Quantum Computing in the NISQ era and beyond," *Quantum*, vol. 2, no. July, p. 79, Aug. 2018.

[17] C. Sung, H. Hwang, and I. K. Yoo, "Perspective: A review on memristive hardware for neuromorphic computation," *J. Appl. Phys.*, vol. 124, no. 15, p. 151903, Oct. 2018.

[18] G. E. Moore, "Cramming more components onto integrated circuits," *Electronics*, vol. 38, no. 8, 1975.

[19] M. M. Waldrop, "The chips are down for Moore's law," *Nature*, vol. 530, no. 7589, pp. 144–147, Feb. 2016.

[20] K. Yamada, Y. Urino, T. Nakamura, and Y. Arakawa, "Integrated Silicon-based Optical Interconnect for Fast, Compact, Energy-efficient Electronic Circuit Systems," *NTT Tech. Rev.*, vol. 11, no. 2, 2010.

[21] C. N. R. Rao, "Transition Metal Oxides," *Annu. Rev. Phys. Chem.*, vol. 40, no. 1, pp. 291–326, Oct. 1989.

[22] M. Imada, A. Fujimori, and Y. Tokura, "Metal-insulator transitions," *Rev. Mod. Phys.*, vol. 70, no. 4, pp. 1039–1263, Oct. 1998.

[23] T. Sakudo, "Oxide superconductors," *Ferroelectrics*, vol. 95, no. 1, pp. 37–41, Jul. 1989.

[24] K. Takada, H. Sakurai, E. Takayama-Muromachi, F. Izumi, R. A. Dilanian, and T. Sasaki, "Superconductivity in two-dimensional CoO_2 layers," *Nature*, vol. 422, no. 6927, pp. 53–55, Mar. 2003.

[25] Y. Kamihara, H. Hiramatsu, M. Hirano, R. Kawamura, H. Yanagi, T. Kamiya, and H. Hosono, "Iron-Based Layered Superconductor: LaOFeP," *J. Am. Chem. Soc.*, vol. 128, no. 31, pp. 10012–10013, Aug. 2006.

[26] S.-W. Cheong and M. Mostovoy, "Multiferroics: a magnetic twist for ferroelectricity," *Nat. Mater.*, vol. 6, no. 1, pp. 13–20, Jan. 2007.

[27] M. Mostovoy, "Multiferroics go high-T_C," *Nat. Mater.*, vol. 7, no. 4, pp. 269–270, Apr. 2008.

[28] A. Cavalleri, C. Tóth, C. W. Siders, J. A. Squier, F. Ráksi, P. Forget, and J. C. Kieffer, "Femtosecond Structural Dynamics in VO_2 during an Ultrafast Solid-Solid Phase Transition," *Phys. Rev. Lett.*, vol. 87, no. 23, p. 237401, Nov. 2001.

[29] M. Ando, K. Kadono, M. Haruta, T. Sakaguchi, and M. Miya, "Large third-order optical nonlinearities in transition-metal oxides," *Nature*, vol. 374, no. 6523, pp. 625–627, Apr. 1995.

[30] H. Y. Hwang, Y. Iwasa, M. Kawasaki, B. Keimer, N. Nagaosa, and Y. Tokura, "Emergent phenomena at oxide interfaces," *Nat. Mater.*, vol. 11, no. 2, pp. 103–113, Feb. 2012.

[31] J. Chakhalian, J. W. Freeland, A. J. Millis, C. Panagopoulos, and J. M. Rondinelli, "Colloquium: Emergent properties in plane view: Strong correlations at oxide interfaces," *Rev. Mod. Phys.*, vol. 86, no. 4, pp. 1189–1202, Oct. 2014.

[32] N. Sai, B. Meyer, and D. Vanderbilt, "Compositional Inversion Symmetry Breaking in Ferroelectric Perovskites," *Phys. Rev. Lett.*, vol. 84, no. 24, pp. 5636–5639, Jun. 2000.

[33] H. Yamada, M. Kawasaki, Y. Ogawa, and Y. Tokura, "Perovskite oxide tricolor superlattices with artificially broken inversion symmetry by interface effects," *Appl. Phys. Lett.*, vol. 81, no. 25, pp. 4793–4795, Dec. 2002.

[34] M. P. Warusawithana, E. V. Colla, J. N. Eckstein, and M. B. Weissman, "Artificial Dielectric Superlattices with Broken Inversion Symmetry," *Phys. Rev. Lett.*, vol. 90, no. 3, p. 036802, Jan. 2003.

[35] Y. Ogawa, H. Yamada, T. Ogasawara, T. Arima, H. Okamoto, M. Kawasaki, and Y. Tokura, "Nonlinear Magneto-Optical Kerr Rotation of an Oxide Superlattice with Artificially Broken Symmetry," *Phys. Rev. Lett.*, vol. 90, no. 21, p. 217403, May 2003.

[36] N. Reyren, S. Thiel, A. D. Caviglia, L. F. Kourkoutis, G. Hammerl, C. Richter, C. W. Schneider, T. Kopp, A.-S. Rüetschi, D. Jaccard, M. Gabay, D. A. Muller, J.-M. Triscone, and J. Mannhart, "Superconducting Interfaces Between Insulating Oxides," *Science (80-.).*, vol. 317, no. 5842, 2007.

[37] J. Biscaras, N. Bergeal, A. Kushwaha, T. Wolf, A. Rastogi, R. C. Budhani, and J. Lesueur, "Two-dimensional superconductivity at a Mott insulator/band insulator interface $LaTiO_3/SrTiO_3$," *Nat. Commun.*, vol. 1, no. 7, pp. 1–5, Oct. 2010.

[38] L. Li, C. Richter, J. Mannhart, and R. C. Ashoori, "Coexistence of magnetic order and two-dimensional superconductivity at $LaAlO_3/SrTiO_3$ interfaces," *Nat. Phys.*, vol. 7, no. 10, pp. 762–766, Sep. 2011.

[39] J. A. Bert, B. Kalisky, C. Bell, M. Kim, Y. Hikita, H. Y. Hwang, and K. A. Moler, "Direct imaging of the coexistence of ferromagnetism and superconductivity at the $LaAlO_3/SrTiO_3$ interface," *Nat. Phys.*, vol. 7, no. 10, pp. 767–771, Sep. 2011.

[40] A. Brinkman, M. Huijben, M. van Zalk, J. Huijben, U. Zeitler, J. C. Maan, W. G. van der Wiel, G. Rijnders, D. H. A. Blank, and H. Hilgenkamp, "Magnetic effects at the interface between non-magnetic oxides," *Nat. Mater.*, vol. 6, no. 7, pp. 493–496, Jul. 2007.

[41] B. Kalisky, J. A. Bert, B. B. Klopfer, C. Bell, H. K. Sato, M. Hosoda, Y. Hikita, H. Y. Hwang, and K. A. Moler, "Critical thickness for ferromagnetism in $LaAlO_3/SrTiO_3$ heterostructures," *Nat. Commun.*, vol. 3, p. 922, Jun. 2012.

[42] J.-S. Lee, Y. W. Xie, H. K. Sato, C. Bell, Y. Hikita, H. Y. Hwang, and C.-C. Kao, "Titanium d_{xy} ferromagnetism at the $LaAlO_3/SrTiO_3$ interface," *Nat. Mater.*, vol. 12, no. 8, pp. 703–706, Jun. 2013.

[43] F. Bi, M. Huang, S. Ryu, H. Lee, C.-W. Bark, C.-B. Eom, P. Irvin, and J. Levy, "Room-temperature electronically-controlled ferromagnetism at the $LaAlO_3/SrTiO_3$ interface," *Nat. Commun.*, vol. 5, p. 5019, Sep. 2014.

[44] H. N. Lee, H. M. Christen, M. F. Chisholm, C. M. Rouleau, and D. H. Lowndes, "Strong polarization enhancement in asymmetric three-component ferroelectric superlattices," *Nature*, vol. 433, no. 7024, pp. 395–399, Jan. 2005.

[45] K. Momma and F. Izumi, "VESTA 3 for three-dimensional visualization of crystal, volumetric and morphology data," *J. Appl. Crystallogr.*, vol. 44, no. 6, pp. 1272–1276, Dec. 2011.

[46] D. G. Schlom, L.-Q. Chen, X. Pan, A. Schmehl, and M. A. Zurbuchen, "A Thin Film Approach to Engineering Functionality into Oxides," *J. Am. Ceram. Soc.*, vol. 91, no. 8, pp. 2429–2454, Aug. 2008.

[47] R. Uecker, R. Bertram, M. Brützam, Z. Galazka, T. M. Gesing, C. Guguschev, D. Klimm, M. Klupsch, A. Kwasniewski, and D. G. Schlom, "Large-lattice-parameter perovskite single-crystal substrates," *J. Cryst. Growth*, vol. 457, pp. 137–142, Jan. 2017.

[48] D. A. Holm and H. F. Taylor, "Infrared phase modulators with multiple quantum wells," *IEEE J. Quantum Electron.*, vol. 25, no. 11, pp. 2266–2271, 1989.

[49] E. B. Dupont, D. Delacourt, and M. Papuchon, "Mid-infrared phase modulation via Stark effect on intersubband transitions in GaAs/GaAlAs quantum wells," *IEEE J. Quantum Electron.*, vol. 29, no. 8, pp. 2313–2318, 1993.

[50] B. Chmielak, M. Waldow, C. Matheisen, C. Ripperda, J. Bolten, T. Wahlbrink, M. Nagel, F. Merget, and H. Kurz, "Pockels effect based fully integrated, strained silicon electro-optic modulator," *Opt. Express*, vol. 19, no. 18, p. 17212, Aug. 2011.

[51] F. Eltes, M. Kroh, D. Caimi, C. Mai, Y. Popoff, G. Winzer, D. Petousi, S. Lischke, J. E. Ortmann, L. Czornomaz, L. Zimmermann, J. Fompeyrine, and S. Abel, "A novel 25 Gbps electro-optic Pockels modulator integrated on an advanced Si photonic platform," in *2017 IEEE International Electron Devices Meeting (IEDM)*, 2017, p. 24.5.1-24.5.4.

[52] J. Faist, F. Capasso, D. L. Sivco, C. Sirtori, A. L. Hutchinson, and A. Y. Cho, "Quantum Cascade Laser," *Science (80-.).*, vol. 264, no. 5158, pp. 553–556, Apr. 1994.

[53] T. Müller, J. Skiba-Szymanska, A. B. Krysa, J. Huwer, M. Felle, M. Anderson, R. M. Stevenson, J. Heffernan, D. A. Ritchie, and A. J. Shields, "A quantum light-emitting diode for the standard telecom window around 1,550 nm," *Nat. Commun.*, vol. 9, no. 1, p. 862, Dec. 2018.

[54] B. F. Levine, "Quantum-well infrared photodetectors," *J. Appl. Phys.*, vol. 74, no. 8, p. R1, Oct. 1993.

[55] Q. Wu, T. D. Hewitt, and X. -C. Zhang, "Two-dimensional electro-optic imaging of THz beams," *Appl. Phys. Lett.*, vol. 69, no. 8, pp. 1026–1028, Aug. 1996.

[56] S. Abel, D. J. Stark, F. Eltes, J. E. Ortmann, D. Caimi, and J. Fompeyrine, "Multi-Level Optical Weights in Integrated Circuits," in *2017 IEEE International Conference on Rebooting Computing (ICRC)*, 2017, vol. 2017–Janua, pp. 1–3.

[57] S. Abel, F. Eltes, J. E. Ortmann, A. Messner, P. Castera, T. Wagner, D. Urbonas, A. Rosa, A. M. Gutierrez, D. Tulli, P. Ma, B. Baeuerle, A. Josten, W. Heni, D. Caimi, L. Czornomaz, A. A. Demkov, J. Leuthold, P. Sanchis, and J. Fompeyrine, "Large Pockels effect in micro- and nanostructured barium titanate integrated on silicon," *Nat. Mater.*, vol. 18, no. 1, pp. 42–47, Jan. 2019.

Chapter 2: Experimental Methods

In this chapter, I discuss the primary experimental techniques used for the fabrication and characterization of TMO thin film heterostructures throughout this thesis. This is not an exhaustive list of the methodologies employed in the undertaking of this research. However, these techniques are used at virtually every stage of this research and therefore form the foundation of the experimental work. Where more specialized methods are used, they will be noted and discussed in the relevant chapter.

2.1 Molecular Beam Epitaxy

Molecular beam epitaxy (MBE) has been described as the "gold standard" experimental technique for the fabrication of thin films and thin film heterostructures [1]. Originally developed for the precise deposition of crystalline semiconductors [2], traditional MBE is conducted by evaporating or sublimating metallic or semiconducting elements or compounds under ultra-high vacuum (UHV) conditions. Because the mean-free path of the evaporated materials is much longer in UHV than the source-to-sample distance within an MBE chamber, the evaporated materials form an atomic or molecular "beam" that impinges on the surface of a (typically crystalline) substrate (Figure 2.1), ideally resulting in epitaxial growth of the deposited material. The substrate is often kept at an elevated temperature in order to facilitate solid-state reactions between the evaporated material and the substrate. The slow growth rates and high-purity environment of an MBE chamber allow for layer-by-layer growth of thin films and offer precise control over stoichiometric and geometric features of the films or heterostructures, including the potential to realize atomically-sharp interfaces.

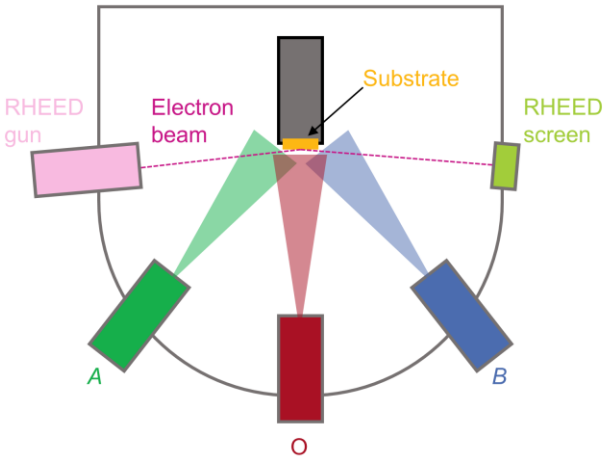

Figure 2.1: Generalized schematic of an oxide MBE chamber for the growth of ABO_3-type perovskites. Metallic sources for *A* and *B* species are shown in green and blue, respectively, and an oxygen source is shown in red. The RHEED gun (light pink) and phosphor RHEED screen (light green) are also shown with the electron beam (pink) incident on the substrate (yellow).

For the growth of oxide thin films, traditional MBE can be modified through the addition of an oxidant source to form oxide MBE [1], [3], [4]. The oxidant source is often chosen to be molecular oxygen [5]–[12], although purified ozone [13]–[16] and oxygen plasma [17]–[21] sources have also been developed to aid in the oxidation of difficult-to-oxidize materials such as bismuth, lead, and copper. The principle of oxide MBE is nearly identical to traditional semiconductor MBE, with a few important caveats. First, the pressure induced in the MBE chamber by the oxidizing species must be kept reasonably low such as to ensure the maintenance of a long mean-free path within the MBE chamber. The scattering of the oxidizing species from the substrate will result in an elevation of background pressure within the MBE. This background pressure should ideally be kept below 1×10^{-5} Torr, although the exact threshold pressure will depend somewhat on MBE geometry [1]. As a second and related consideration, supplemental vacuum pumping is typically required in oxide MBE systems as compared to traditional MBE systems in order to handle the additional gas flow from the oxidant. Finally, care must be maintained when operating the reflection high-energy electron diffraction (RHEED) gun in the presence of

an oxidizing species as the filament can burn out in environments other than UHV. RHEED will be described in more detail in the following section.

In the Materials Physics Laboratory at the University of Texas, our oxide MBE system (Figure 2.2) features ten metal sources, molecular oxygen and oxygen plasma oxidation sources, and both molecular nitrogen and nitrogen plasma sources for the growth of nitrides. Of the ten metal sources, six are evaporated using effusion cells while the other four are evaporated via an electron beam evaporator. Effusion cells (Figure 2.3) operate using resistive heating elements wrapped around a crucible containing the source metal. The heating of the source crucible results in evaporation of the source metal with the evaporation rate controlled via the temperature to which the crucible is heated. For metals with high melting points, effusion cell evaporation is often not feasible and electron beam evaporation is used instead in which a beam of accelerated electrons is focused into a crucible containing a source metal. The electrons deposit their energy into the source metal and subsequently heat it, resulting in its evaporation. Examples of metal commonly used in the electron beam evaporator in our lab include cobalt, niobium and platinum.

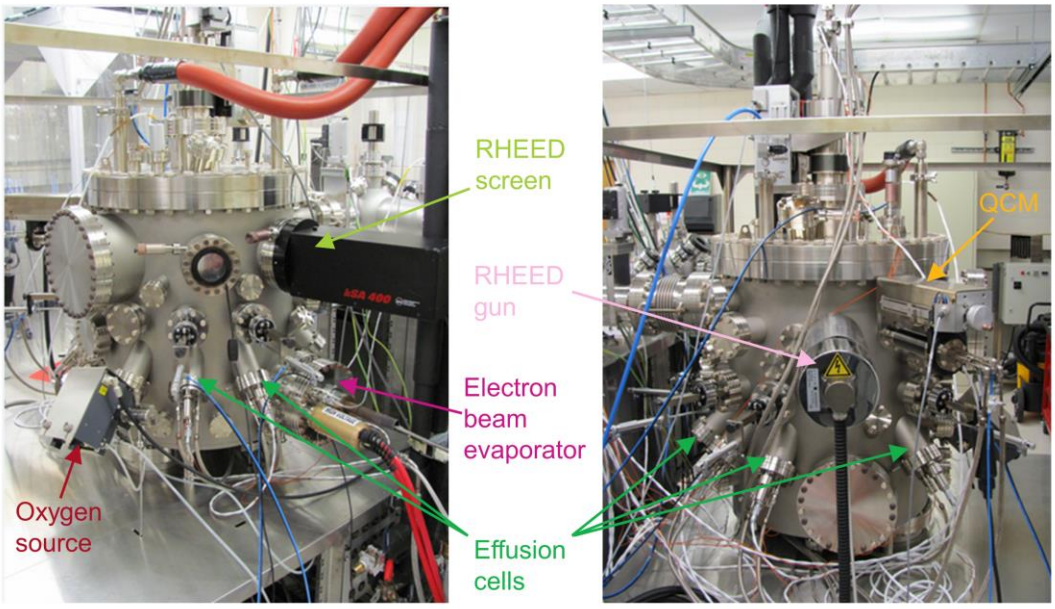

Figure 2.2: Photographs of the MBE in the Materials Physics Laboratory at the University of Texas at Austin on which much of the materials synthesis work in this thesis was performed. The locations of the constituent components of the MBE system have been noted in the images.

Tight control of sample stoichiometry is necessary for the fabrication of high-quality TMO thin films and thin film heterostructures. For the case of ABO_3 perovskites, the greatest stoichiometric consideration is given to the *A*:*B* cation ratio [22], [23], which should ideally be 1:1. This ratio is controlled by the relative evaporation rates of the *A* and *B* metallic sources, necessitating a method for measuring these evaporation rates. In our system, measurement of atomic fluxes is accomplished via a quartz crystal monitor (QCM). The QCM uses a quartz resonator operated at high frequency to measure the thickness of a deposited material. By averaging the QCM's thickness measurements over time, one can derive the deposition rate of a given metal and thereby exercise control over the

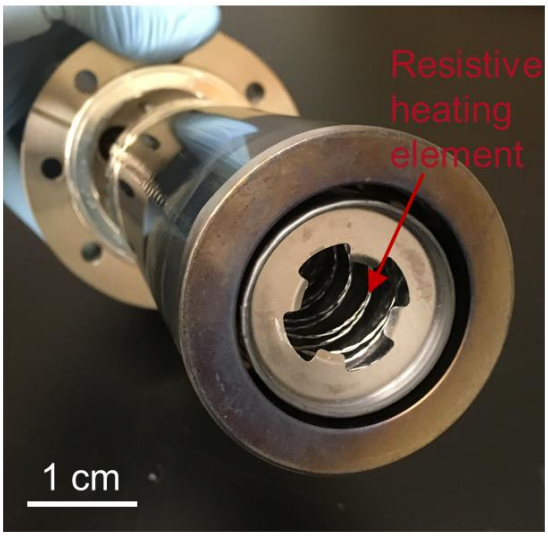

stoichiometry of a target growth compound. The deposition rates in our oxide MBE are typically calibrated to coincide with approximately one monolayer (ML) per minute.

Figure 2.3: Photograph of an effusion cell used for metal source evaporation in MBE. The coiled resistive heating element can be seen inside the effusion cell opening. Note the crucible is absent in this photograph.

For epitaxial deposition, the thickness corresponding to one ML of a given metal depends on the two-dimensional atomic density of the substrate material. Specifically, the typical one-to-one correspondence between deposited atoms and the surface atoms of the substrate necessitate the deposited material and the substrate to have the same two-dimensional atomic density. Because the two-dimensional atomic density n_{2D} is given by

$$n_{2D} = \frac{\rho N_A t}{M}, \tag{2.1}$$

where ρ is the density of the deposited metal, N_A is Avogadro's number, t is the ML thickness and M is the deposited metal's atomic weight, n_{2D} depends on the metallic species being evaporated. By using the two-dimensional density of the substrate material as an input, the ML thickness of a given deposited metal can be calculated using Equation (2.1). For the growth of ABO_3 perovskites, ensuring evaporation rates are tuned such that one ML of both A and B species are deposited over equal times will result in the formation of a stoichiometric film (assuming equal sticking coefficients between A and B metallic species).

2.2 Reflection High-Energy Electron Diffraction

While QCM measurements provide a convenient means for calibrating metallic evaporation rates before thin film growth begins, in practice, it is helpful to also have a method for monitoring the progress of film growth in real time. Although many methods have been developed for the real-time monitoring of thin film growth [24]–[27], perhaps none are as widely used as RHEED [28]. RHEED is a surface-sensitive electron diffraction technique that can be used to monitor the morphology and crystalline symmetry of the thin film surface during growth. High-energy electrons (typically between 10 and 30 keV) are accelerated toward the sample surface at a glancing angle. After diffracting from the sample surface, the electrons impinge on a phosphor screen and the resulting pattern can be imaged using a camera (Figure 2.1). The surface sensitivity of RHEED stems in large part from the glancing angle of incidence of the electron beam.

To a good approximation, the surface diffraction of electrons can be described using the kinematic theory of diffraction [28]. That is, the transfer of energy from the imaging electron beam to the sample surface is assumed to be negligible, allowing us to invoke the conservation of momentum and energy between the incoming electron beam and the outgoing electron beam that is incident on the phosphor screen. Although in reality there is some inelastic scattering of electrons from the sample surface, these electrons can be filtered out from the final RHEED pattern in principle [29] and can be generally ignored in the analysis of the resulting RHEED pattern. Only electrons satisfying the diffraction condition

$$\overrightarrow{k'} - \overrightarrow{k_0} = \vec{G} \tag{2.2}$$

interfere constructively with one another after interacting with the sample surface, where $\overrightarrow{k'}$, $\overrightarrow{k_0}$, and $\vec{G}$ are the incoming electron wave vector, outgoing electron wave vector and sample reciprocal lattice vector, respectively. Therefore, for a fixed incoming electron

wave vector, we see that only specific, high-symmetry directions of the sample surface (corresponding to reciprocal lattice vectors) result in constructive interference and a corresponding high-intensity RHEED pattern. These high-symmetry directions correspond to intersections of the sample's reciprocal lattice vectors with the Ewald sphere, as described in detail in [28] and [30].

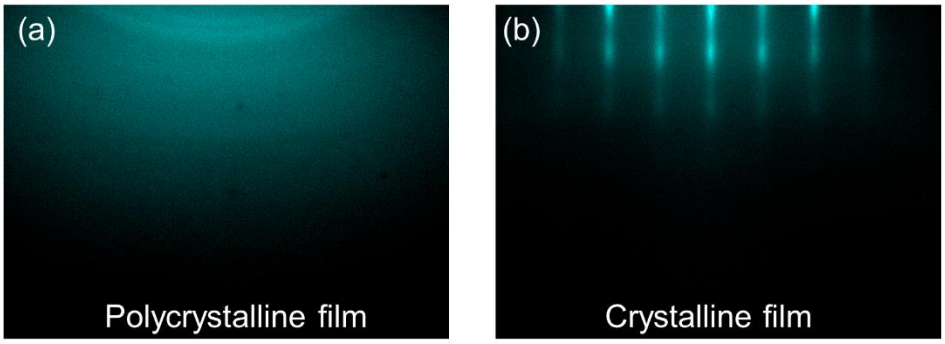

Figure 2.4: The RHEED patterns characteristic of a polycrystalline film (a), showing circular patterns of electron intensity, and a crystalline film (b), showing clear diffraction streaks. For an amorphous film, the RHEED image is without pattern and shows simply a strong background intensity.

By studying the RHEED pattern from a film, one can learn many things, both quantitative and qualitative, about the film's surface. For one thing, one can determine whether the surface is crystalline, polycrystalline or amorphous (Figure 2.4), as each of these morphologies results in specific RHEED characteristics. Furthermore, one can measure the in-plane lattice parameters of a crystalline film's surface by measuring the distance between streaks in the RHEED pattern. This method has been used to measure the structural relaxation of TMO thin films in real time during film growth [31]. Although a formula for the RHEED streak spacing can be derived as a function of crystalline lattice parameters, unknown geometric quantities (e.g., angle of incidence) in a real RHEED system can make such calculations impractical. However, by comparing the streak spacing

of a sample with a known lattice constant to the streak spacing in a film, one can extract the lattice constant of the film without reference to the RHEED system's uncertain geometric quantities [12].

2.3 X-RAY DIFFRACTION

X-Ray diffraction (XRD) is a ubiquitous and powerful technique for the characterization of solids. In particular, XRD can provide information on a plethora of properties of *crystalline* solids, including crystalline thin films, such as in- and out-of-plane lattice constants, crystalline quality, film thickness, and preferred crystalline orientations [32], [33]. It is an important complementary technique to RHEED, as it provides information on the volume of the system under study rather than only on the system's surface.

As its name implies, a specific diffraction condition is at the heart of XRD. That condition, named "Bragg's Law" after the surname of the father-son duo who discovered it in the early 20th Century [34], simply and elegantly relates the wavelength λ and incidence angle θ of incoming X-rays to the distance between atomic planes in a periodic crystal d according to

$$2d \sin\theta = n\lambda, \tag{2.3}$$

where n is an integer called the diffraction order. The lattice plane distance d is commonly referred to as the lattice parameter.

While it is convenient to describe RHEED in terms of the thin film's reciprocal lattice, the description of Bragg's Law can easily be given in real space. The key realization from Bragg and Bragg is that the difference in the path lengths between X-rays that reflect from different depths within a crystal must equal an integer number of wavelengths in order for constructive interference to occur. Geometrically, one can see (Figure 2.5) that the

difference in the path lengths between parallel beams is given by the left-hand side of the diffraction condition in Equation (2.3). The right-hand side, meanwhile, enforces the condition of this path length difference being equal to an integer number of wavelengths.

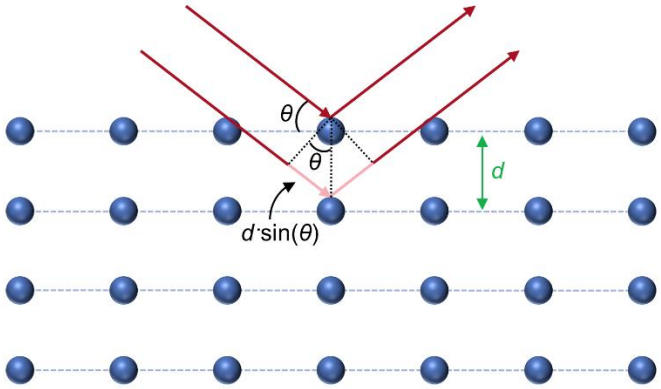

Figure 2.5: Atomic-scale schematic showing the path length difference between X-rays reflected from successive atomic planes of a crystalline lattice. The total path length difference, represented by the light red lines, can be seen to equal $2d \sin\theta$, in agreement with Equation (2.3).

The formulation of Bragg's Law in terms of incidence angle implies the use of a certain experimental geometry in which the X-ray source is rotated. Such an experimental apparatus is called an X-ray diffractometer. In practice, both the X-ray source and detector are often rotated simultaneously in order to map out a series of incidence angles. This is the procedure for a so-called θ-2θ scan. A characteristic spectrum resulting from a θ-2θ scan features several distinct, sharp peaks corresponding to reflections from different lattice planes (Figure 2.6). From the incidence angles at which these peaks occur, Equation (2.3) can be used to calculate the corresponding lattice parameters.

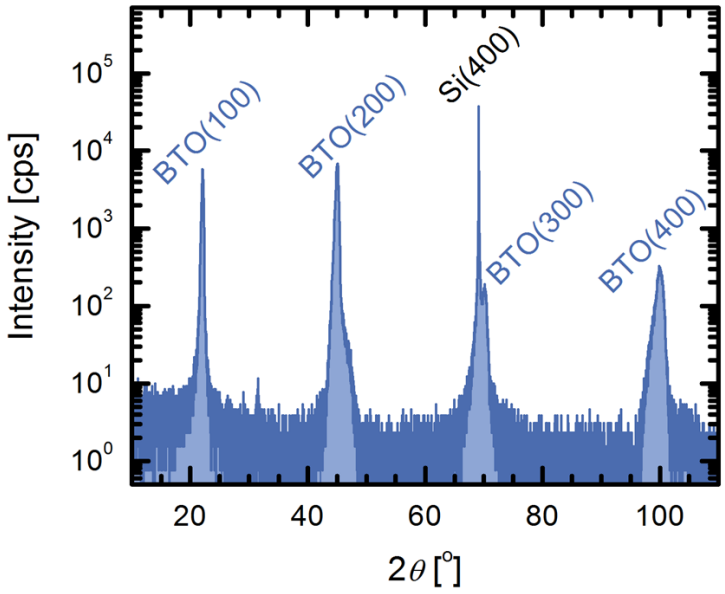

Figure 2.6: Out-of-plane XRD spectrum of an 80 nm $BaTiO_3$ (BTO) film on a Si substrate. Four BTO peaks and one peak from the Si substrate can be seen.

In addition to θ-2θ scans, several other experimental geometries are also possible. These include so-called ϕ-$2\theta_\chi$ scans, in which the detector and X-ray source are rotated in the plane of the thin film [33]. In analogy with θ-2θ scans, such a measurement provides information on the in-plane lattice parameters. Especially in the case of thin films, the in-plane lattice parameters may be notably different from the out-of-plane parameters and may furthermore be a function of substrate choice, film thickness, and stoichiometry. Additionally, so-called ω scans are commonly employed (also known as "rocking curves"). These scans are performed by fixing the positions of the X-ray source and detector and rocking the angle of the sample slightly. A rocking curve measurement provides information on the uniformity and crystalline quality of the sample, as slight misorientations between crystalline domains will broaden the rocking curve. While this is not an exhaustive list of possible XRD measurements, the measurements listed here

provide the basis for the bulk of the XRD measurements presented in this thesis. For a nice overview of XRD techniques for thin film characterization, see [33].

2.4 Transmission Electron Microscopy

Transmission electron microscopy (TEM) is an experimental technique for locally imaging the atomic structure of a material. Just as XRD offers a nice complement to RHEED measurements, TEM offers a nice complement to XRD measurements. That is because TEM is a *local* technique, offering a detailed view of a small portion of the sample under study, while XRD is a *global* technique that averages over a large portion of the sample (roughly, the X-ray spot size on the sample times the sample thickness). Especially in the study of crystalline thin films, local measurements such as TEM can provide extremely valuable information on the local, nm-scale properties of matter.

A transmission electron microscope (I will also abbreviate the microscope itself as "TEM"; the context in which the acronym is used should provide clarity) uses high-energy electrons (typically 100 to 400 keV) to image the local atomic structure of a sample under study [35]. At such high energies, electrons have a de Broglie wavelength of approximately 4 pm, significantly smaller than an atom's diameter [35]. This small wavelength allows for excellent spatial resolution of TEM as compared to optical microscopy. In reality, the theoretical wavelength-limited resolution of TEM is not reached due to deficiencies in electron lenses. Nevertheless, the resolution of TEM still significantly outperforms many other imaging techniques and TEM has therefore become an indispensable part of thin film research.

TEM works by transmitting a beam of high-energy electrons through a thin sample and collecting the scattered electrons using a (typically circular) detector (Figure 2.7). The detector collects scattered electrons over some finite solid angle $d\Omega$ corresponding to an

electron scattering cross-section $^{d\sigma}/_{d\Omega}$. As the beam of focused, high-energy electrons is scanned across the sample, the intensity of the scattered electron beam changes, corresponding to local changes of the sample's atomic structure. From this change of scattered intensity, an atomic-scale image of the sample can be reconstructed.

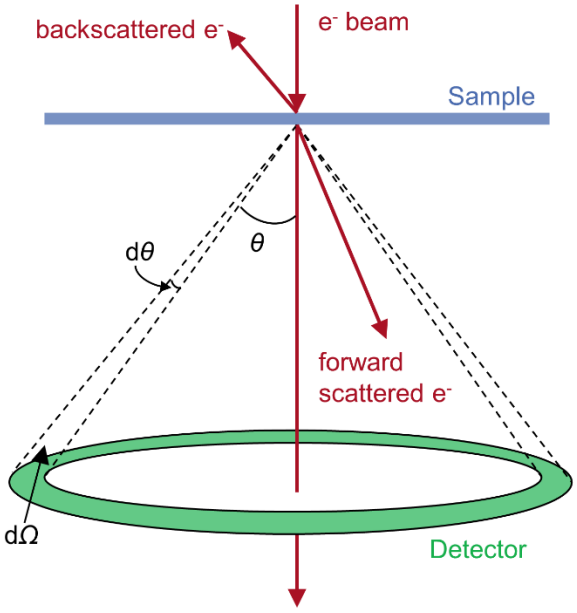

Figure 2.7: Schematic of the experimental geometry of TEM. An incident electron beam (red) is accelerated toward a thin sample (blue). Some of the beam travels directly through the sample while some of the beam is scattered (forwards and backwards). Some of the forward scattered electrons are collected by a circular detector (green) encompassing a solid angle dΩ.

Assuming an elastic Coulomb interaction between the imaging electron beam and the sample, the differential elastic cross section can be computed as

$$\frac{d\sigma_{el}}{d\Omega} \propto \frac{Z^2}{\left(\sin^2 {}^{\theta}/_{2} + \alpha\right)^2}, \tag{2.4}$$

where Z is the atomic number of the interacting atom in the sample, θ is the scattering angle of the electron beam and α is a screening factor that takes into account the outer electrons of the interacting atom in the sample [36]. The proportionality constants in Equation (2.4) are related to the electron beam energy and the fundamental constants of the electron. An important consequence of Equation (2.4) is that the intensity of the elastically scattered electron beam is proportional to the square of the atomic number of the scatterer Z. As a

result, TEM can distinguish between lighter and heavier atoms present in a sample (Figure 2.8). This makes TEM an especially powerful technique for the study of TMO thin film heterostructures where multiple materials with different constituent atoms are layered in a (hopefully) well-defined sequence.

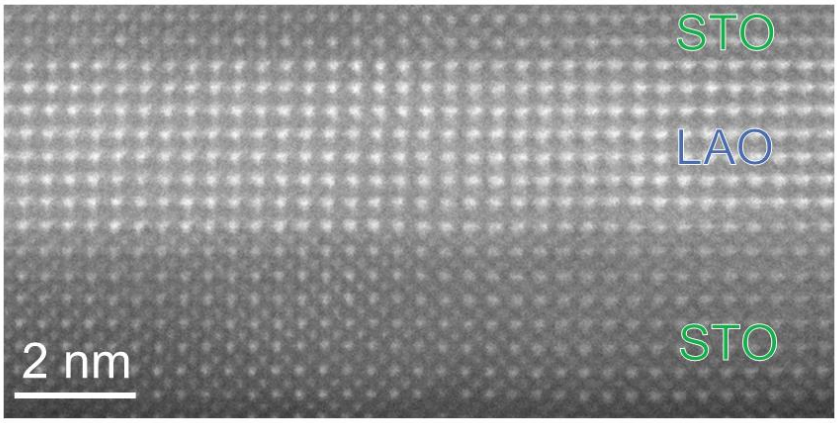

Figure 2.8: TEM image of a $SrTiO_3$/$LaAlO_3$ (STO/LAO) heterostructure. The LAO region is brighter due to the higher atomic number of La as compared to Sr (Z_{La} = 57, Z_{Sr} = 38).

2.5 REFERENCES

[1] D. G. Schlom, "Perspective: Oxide molecular-beam epitaxy rocks!," *APL Mater.*, vol. 3, no. 6, p. 062403, Jun. 2015.

[2] A. Y. Cho and J. R. Arthur, "Molecular beam epitaxy," *Prog. Solid State Chem.*, vol. 10, pp. 157–191, Jan. 1975.

[3] W. A. Doolittle, A. G. Carver, and W. Henderson, "Molecular beam epitaxy of complex metal-oxides: Where have we come, where are we going, and how are we going to get there?," *J. Vac. Sci. Technol. B Microelectron. Nanom. Struct.*, vol. 23, no. 3, p. 1272, 2005.

[4] D. G. Schlom, L.-Q. Chen, X. Pan, A. Schmehl, and M. A. Zurbuchen, "A Thin Film Approach to Engineering Functionality into Oxides," *J. Am. Ceram. Soc.*, vol. 91, no. 8, pp. 2429–2454, Aug. 2008.

[5] R. A. Betts and C. W. Pitt, "Growth of thin-film lithium niobate by molecular beam epitaxy," *Electron. Lett.*, vol. 21, no. 21, p. 960, 1985.

[6] R. A. McKee, F. J. Walker, J. R. Conner, E. D. Specht, and D. E. Zelmon, "Molecular beam epitaxy growth of epitaxial barium silicide, barium oxide, and barium titanate on silicon," *Appl. Phys. Lett.*, vol. 59, no. 7, pp. 782–784, Aug. 1991.

[7] R. A. McKee, F. J. Walker, E. D. Specht, G. E. Jellison, L. A. Boatner, and J. H. Harding, "Interface stability and the growth of optical quality perovskites on MgO," *Phys. Rev. Lett.*, vol. 72, no. 17, pp. 2741–2744, Apr. 1994.

[8] R. A. McKee, F. J. Walker, and M. F. Chisholm, "Crystalline Oxides on Silicon: The First Five Monolayers," *Phys. Rev. Lett.*, vol. 81, no. 14, pp. 3014–3017, Oct. 1998.

[9] N. Iwata, G. Pindoria, T. Morishita, and K. Kohn, "Preparation and Magnetic Properties of EuO Thin Films Epitaxially Grown on MgO and $SrTiO_3$ Substrates," *J. Phys. Soc. Japan*, vol. 69, no. 1, pp. 230–236, Jan. 2000.

[10] W. Tian, J. C. Jiang, X. Q. Pan, J. H. Haeni, Y. L. Li, L. Q. Chen, D. G. Schlom, J. B. Neaton, K. M. Rabe, and Q. X. Jia, "Structural evidence for enhanced polarization in a commensurate short-period $BaTiO_3/SrTiO_3$ superlattice," *Appl. Phys. Lett.*, vol. 89, no. 9, p. 092905, Aug. 2006.

[11] J. E. Ortmann, N. Nookala, Q. He, L. Gao, C. Lin, A. B. Posadas, A. Y. Borisevich, M. A. Belkin, and A. A. Demkov, "Quantum Confinement in Oxide Heterostructures: Room-Temperature Intersubband Absorption in $SrTiO_3/LaAlO_3$ Multiple Quantum Wells," *ACS Nano*, vol. 12, no. 8, pp. 7682–7689, Aug. 2018.

[12] J. E. Ortmann, A. B. Posadas, and A. A. Demkov, "The MBE growth of arbitrarily thick $SrTiO_3/LaAlO_3$ quantum well heterostructures for use in next-generation optoelectronic devices," *J. Appl. Phys.*, vol. 124, no. 1, p. 015301, Jul. 2018.

[13] B. R. Johnson, K. M. Beauchamp, T. Wang, J. Liu, K. A. McGreer, J. Wan, M. Tuominen, Y. Zhang, M. L. Mecartney, and A. M. Goldman, "*In situ* growth of $DyBa_2Cu_3O_{7-x}$ thin films by molecular beam epitaxy," *Appl. Phys. Lett.*, vol. 56, no. 19, pp. 1911–1913, May 1990.

[14] B. R. Johnson, N. Anand, Y. Zhang, J. Maps, K. Mauersberger, D. D. Berkley, M. Tuominen, L. E. Conroy, K. M. Beauchamp, J. Morton, A. M. Goldman, and M. L. Mecartney, "*In situ* formation of superconducting $YBa_2Cu_3O_{7-x}$ thin films using pure ozone vapor oxidation," *Appl. Phys. Lett.*, vol. 53, no. 20, pp. 1973–1975, 2002.

[15] A. Bhattacharya, X. Zhai, M. Warusawithana, J. N. Eckstein, and S. D. Bader, "Signatures of enhanced ordering temperatures in digital superlattices of $(LaMnO_3)_m/(SrMnO_3)_{2m}$," *Appl. Phys. Lett.*, vol. 90, no. 22, p. 222503, May 2007.

[16] E. J. Monkman, C. Adamo, J. A. Mundy, D. E. Shai, J. W. Harter, D. Shen, B. Burganov, D. A. Muller, D. G. Schlom, and K. M. Shen, "Quantum many-body

interactions in digital oxide superlattices," *Nat. Mater.*, vol. 11, no. 10, pp. 855–859, Oct. 2012.

[17] R. J. Spah, H. F. Hess, H. L. Stormer, A. E. White, and K. T. Short, "Parameters for *in situ* growth of high T_c superconducting thin films using an oxygen plasma source," *Appl. Phys. Lett.*, vol. 53, no. 5, pp. 441–443, Aug. 1988.

[18] D. G. Schlom, J. N. Eckstein, E. S. Hellman, S. K. Streiffer, J. S. Harris, M. R. Beasley, J. C. Bravman, T. H. Geballe, C. Webb, K. E. von Dessonneck, and F. Turner, "Molecular beam epitaxy of layered Dy-Ba-Cu-O compounds," *Appl. Phys. Lett.*, vol. 53, no. 17, pp. 1660–1662, Oct. 1988.

[19] J. Kwo, M. Hong, D. J. Trevor, R. M. Fleming, A. E. White, R. C. Farrow, A. R. Kortan, and K. T. Short, "*In situ* epitaxial growth of $Y_1Ba_2Cu_3O_{7-x}$ films by molecular beam epitaxy with an activated oxygen source," *Appl. Phys. Lett.*, vol. 53, no. 26, pp. 2683–2685, Dec. 1988.

[20] S. A. Chambers, "Epitaxial growth and properties of thin film oxides," *Surf. Sci. Rep.*, vol. 39, no. 5–6, pp. 105–180, Aug. 2000.

[21] J. Kabelac, S. Ghosh, P. Dobal, and R. Katiyar, "rf oxygen plasma assisted molecular beam epitaxy growth of $BiFeO_3$ thin films on $SrTiO_3$ (001)," *J. Vac. Sci. Technol. B Microelectron. Nanom. Struct.*, vol. 25, no. 3, p. 1049, 2007.

[22] C. M. Brooks, L. F. Kourkoutis, T. Heeg, J. Schubert, D. A. Muller, and D. G. Schlom, "Growth of homoepitaxial $SrTiO_3$ thin films by molecular-beam epitaxy," *Appl. Phys. Lett.*, vol. 94, no. 16, p. 162905, 2009.

[23] L. Qiao, T. C. Droubay, T. Varga, M. E. Bowden, V. Shutthanandan, Z. Zhu, T. C. Kaspar, and S. A. Chambers, "Epitaxial growth, structure, and intermixing at the $LaAlO_3/SrTiO_3$ interface as the film stoichiometry is varied," *Phys. Rev. B*, vol. 83, no. 8, p. 085408, Feb. 2011.

[24] B. Johs, D. Doerr, S. Pittal, I. B. Bhat, and S. Dakshinamurthy, "Real-time monitoring and control during MOVPE growth of CdTe using multiwavelength ellipsometry," *Thin Solid Films*, vol. 233, no. 1–2, pp. 293–296, Oct. 1993.

[25] M. Kildemo and B. Drévillon, "Real time monitoring of the growth of transparent thin films by spectroscopic ellipsometry," *Rev. Sci. Instrum.*, vol. 67, no. 5, pp. 1956–1960, May 1996.

[26] S. Kowarik, A. Gerlach, W. Leitenberger, J. Hu, G. Witte, C. Wöll, U. Pietsch, and F. Schreiber, "Energy-dispersive X-ray reflectivity and GID for real-time growth studies of pentacene thin films," *Thin Solid Films*, vol. 515, no. 14, pp. 5606–5610, May 2007.

[27] S. Kowarik, A. Gerlach, M. W. A. Skoda, S. Sellner, and F. Schreiber, "Real-time studies of thin film growth: Measurement and analysis of X-ray growth oscillations

beyond the anti-Bragg point," *Eur. Phys. J. Spec. Top.*, vol. 167, no. 1, pp. 11–18, Feb. 2009.

[28] A. Ichimiya and P. I. Cohen, *Reflection High-Energy Electron Diffraction*, no. December 2004. Cambridge: Cambridge University Press, 2004.

[29] Y. Horio, Y. Hashimoto, and A. Ichimiya, "A new type of RHEED apparatus equipped with an energy filter," *Appl. Surf. Sci.*, vol. 100–101, no. 1, pp. 292–296, Jul. 1996.

[30] J. E. Mahan, K. M. Geib, G. Y. Robinson, and R. G. Long, "A review of the geometrical fundamentals of reflection high-energy electron diffraction with application to silicon surfaces," *J. Vac. Sci. Technol. A Vacuum, Surfaces, Film.*, vol. 8, no. 5, pp. 3692–3700, Sep. 1990.

[31] L. S.-J. Peng, X. X. Xi, B. H. Moeckly, and S. P. Alpay, "Strain relaxation during in situ growth of $SrTiO_3$ thin films," *Appl. Phys. Lett.*, vol. 83, no. 22, p. 4592, Dec. 2003.

[32] C. Suryanarayana and M. G. Norton, *X-Ray Diffraction*. Boston, MA: Springer US, 1998.

[33] K. Inaba, "X-Ray Thin Film Measurement Techniques," *Rigaku J.*, vol. 24, no. 1, pp. 10–15, 2008.

[34] W. H. Bragg and W. L. Bragg, "The Reflection of X-rays by Crystals," *Proc. R. Soc. A Math. Phys. Eng. Sci.*, vol. 88, no. 605, pp. 428–438, Jul. 1913.

[35] D. B. Williams and C. B. Carter, *Transmission Electron Microscopy*. Boston, MA: Springer US, 2009.

[36] N. Jiang, "Electron beam damage in oxides: a review," *Reports Prog. Phys.*, vol. 79, no. 1, p. 016501, Jan. 2016.

Chapter 3: Structural Properties of Ultra-Thick $SrTiO_3/LaAlO_3$ Quantum Well Heterostructures

3.1 Introduction to the $SrTiO_3/LaAlO_3$ Materials System[1]

In Section 1.2 of this thesis, I briefly discussed the wide range of emergent states that have been observed in TMO thin film heterostructures. Perhaps nowhere is the phenomenon of emergence in TMO thin film heterostructures more neatly embodied than in the $SrTiO_3/LaAlO_3$ (STO/LAO) system. STO and LAO are both band insulating materials with band gaps of approximately 3.3 eV and 5.6 eV, respectively [1], [2]. However, in 2004, Ohtomo and Hwang reported the surprising observation of a high-mobility two-dimensional electron gas at the interface of these two insulating materials [3]. Since that landmark discovery, hundreds, if not thousands, of reports have been published in an attempt to elucidate the underlying mechanisms responsible for this surprising phenomenon (a few examples are given by [4]–[12]).

Besides an interest in fundamental physics, much of the literature on the STO/LAO system has focused on its use in next-generation electronic devices [13]–[16]. The high charge densities and extremely thin materials stacks that will be required for next-generation transistors are challenges that oxides appear uniquely suited to solve. In particular, the STO/LAO interface has been reported to sustain a planar charge density an order of magnitude greater than that which is typically found in traditional Si-based transistors [3], [16].

But while the STO/LAO system shows great promise for electronics, the scientific community had overlooked another technologically useful feature of this famous materials system until quite recently. In 2015, Choi *et al*. measured a huge conduction band offset of

[1] Material in this chapter based on J. E. Ortmann, A. B. Posadas, and A. A. Demkov, *J. Appl. Phys.*, vol. 124, no. 1, p. 015301, Jul. 2018 and J. E. Ortmann, N. Nookala, Q. He, L. Gao, C. Lin, A. B. Posadas, A. Y. Borisevich, M. A. Belkin, and A. A. Demkov, *ACS Nano*, vol. 12, no. 8, pp. 7682–7689, Aug. 2018.

2.34 eV between STO and LAO [17]. In other words, besides hosting a high-density, high-mobility two-dimensional gas at the interface, the STO/LAO system can also be described as an exceptionally deep quantum well (Figure 3.1). Quantum wells (QWs) offer immense potential to engineer a plethora of electrical, optical, and electro-optical devices [18]–[25]. The study of novel, and possibly greatly improved, next-generation QW devices is therefore a subject of significant research interest. Such devices typically rely on the optical and/or electrical modulation of charge carriers between confined states for operation. Generally speaking, the operating energy range of a QW device (e.g., the output wavelength of a quantum cascade laser) is related to the band offset in the materials system, with a larger band offset implying a larger operating energy range.

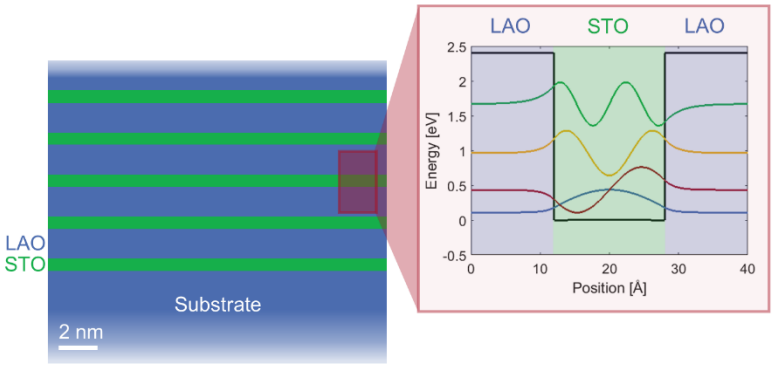

Figure 3.1: Generalized sample schematic (left) and corresponding band structure (right). Four electronic wave functions calculated with a Poisson-Schrödinger solver are plotted in the band profile.

For many years, GaAs/AlGaAs has been the materials system of choice for QW devices due to the high quality with which these materials can be fabricated by MBE [26]. However, the maximum conduction band offset in this system is significantly less than 1 eV [27], seriously limiting the operating energy range of devices constructed from the GaAs/AlGaAs materials system. With the advent of and recent progress in oxide MBE, the STO/LAO system seems to be a prime contender for use in next-generation QW devices with an extended operating energy range relative to traditional GaAs-based QW devices.

However, before such devices can hope to compete with traditional QW devices, it is first critical to perfect the growth of high-quality STO/LAO QW heterostructures.

Many fundamental issues render the growth of STO/LAO QW heterostructures particularly challenging. Significant structural distortions have consistently been reported at the STO/LAO interfaces, complicating the growth of thick heterostructures [28]. Because many QW devices require relatively thick heterostructures for their construction [21], [23], the problem of growth must be overcome before the STO/LAO system can become useful in QW devices. In this chapter, I detail my structural characterizations of arbitrarily thick STO/LAO QW heterostructures and present evidence for thickness-independent material quality of STO/LAO heterostructures fabricated with MBE, in contrast to previous reports of the STO/LAO system.

3.2 Surface Characterization

The maintenance of a consistent, high-quality crystalline surface is critical for the successful epitaxial fabrication of TMO heterostructures. When employing a layer-by-layer growth method such as MBE, what is currently the "surface" at any given point during sample growth quickly becomes the "substrate" as additional material is deposited. When depositing TMOs on a rough or disordered surface, the resulting film would also be expected to be rough or disordered. Such disorder can become compounded over time, leading to the thickness-dependent degradation of crystalline quality [28].

As described in Section 2.2, RHEED offers a convenient method for monitoring surface quality *in situ*. During the deposition of STO/LAO QW heterostructures (described in detail in [29]), RHEED was employed to observe the surface at various stages throughout growth (Figure 3.2) [29]. Qualitatively, a relatively smooth, crystalline surface was

observed regardless of heterostructure thickness. No thickness-dependent degradation of crystalline quality was apparent by observing the RHEED signal.

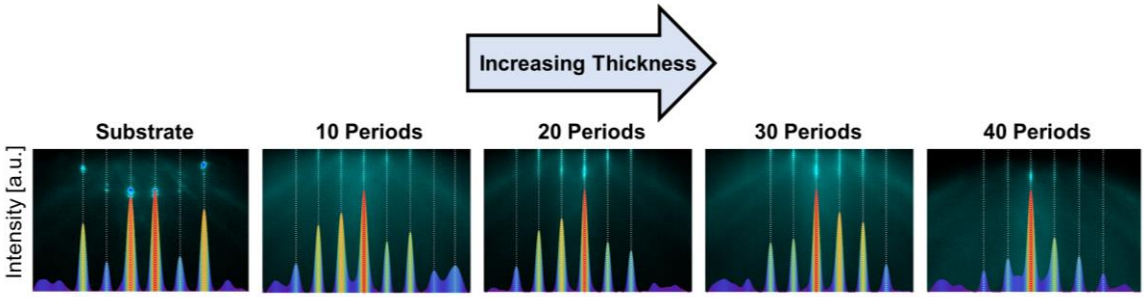

Figure 3.2: Thickness-dependent RHEED images of the surface of an STO/LAO QW heterostructure taken along the LAO ⟨100⟩ azimuth. The total number of well/barrier periods is indicated above each panel. The RHEED images are overlaid with integrated intensity maps that enable the calculation of the in-plane lattice constant by comparing the peak-to-peak spacing with that measured for the LAO substrate. The substrate in-plane lattice constant is taken to be 3.8 Å.

In addition to qualitative observations of the crystalline surface, the in-plane lattice constant was also measured by RHEED at various stages of heterostructure growth. RHEED images were analyzed by integrating the observed electron intensities along the vertical direction and counting the pixels between integrated intensity peaks. By measuring the peak-to-peak spacing at various stages of growth and comparing to the peak-to-peak spacing from a substrate of a known lattice constant, the average in-plane lattice constant can be computed. In this way, I extracted an in-plane lattice constant of 3.8 ± 0.1 Å independent of sample thickness, in nice agreement with the bulk LAO lattice constant [30].

Because the heterostructures are grown on LAO substrates, unrelaxed heterostructures would be expected to be strained to the in-plane LAO lattice constant. The observation of a thickness-independent in-plane lattice constant indicates the crystalline lattice of the heterostructure does not substantially relax as thickness is increased. This

phenomenon is likely due in part to the heterostructure design in which strained STO wells are interspersed with nominally unstrained LAO barriers. It is possible the unstrained LAO barriers structurally reinforce the STO wells and keep them from relaxing. The rapid relaxation of strained STO, especially at high growth temperatures, has been previously measured by RHEED [31].

The apparent lack of a fundamental mechanism limiting the total thickness to which STO/LAO QW heterostructures can be grown has important implications for device fabrication. Materials systems that cannot be easily grown in thick, complex layered structures present challenges for device fabrication. One example of such a system can be found in InGaN/GaN QWs [32]. Despite a widely tunable band discontinuity, the 12% lattice mismatch between InN and GaN severely complicates the growth of thick, high-quality QW heterostructures from this materials system [33]. While creative fabrication techniques have been developed to circumvent this problem to a degree [33], [34], the relative ease with which thick STO/LAO QW heterostructures can be fabricated should be seen as an advantage favoring the TMO system.

3.3 X-RAY CHARACTERIZATION

Out-of-plane θ-2θ XRD scans provide additional information on the crystalline structure of the STO/LAO QW heterostructures. Clear superlattice peaks can be observed throughout the entire spectra of the measured samples (Figure 3.3). The observation of clear superlattice peaks in out-of-plane XRD spectra is in agreement with previous studies of short-period oxide heterostructures [35]–[38] and is an indicator of the high crystalline quality of the heterostructures.

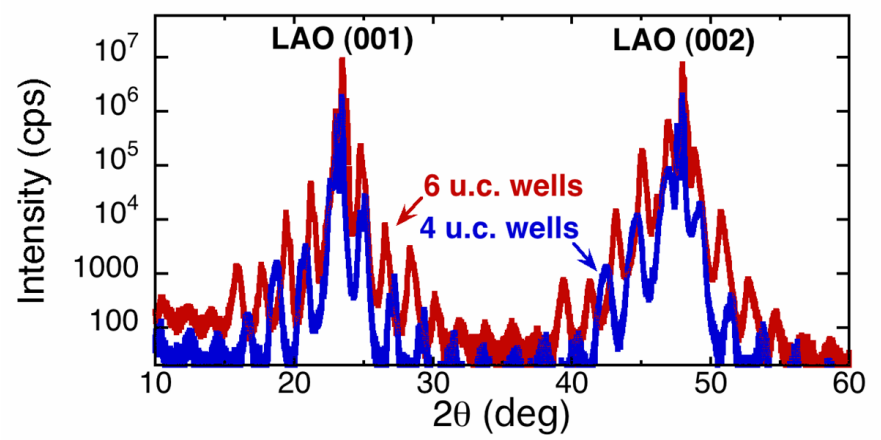

Figure 3.3: Out-of-plane θ-2θ XRD scan of a four and six unit cell (u.c.)-well STO/LAO QW heterostructure. Superlattice peaks can be clearly observed throughout the spectra.

Superlattice peaks result from the additional, long-range periodicity arising from the layering of distinct materials (here, STO and LAO). The spacing between adjacent superlattice peaks is governed by Bragg's Law and is indicative of the period length L of the heterostructure, defined as the thickness of one LAO barrier plus the thickness of one STO well. From the spectra, the period length can be calculated according to

$$L = \frac{\Delta n \cdot \lambda}{2|\Delta \sin\theta|}, \tag{3.1}$$

where Δn is the change in order number between two superlattice peaks and $\Delta\sin(\theta)$ is the corresponding change in the sine of the Bragg angle between the same two superlattice peaks.

Applying Equation (3.1) between adjacent superlattice peaks, the average period length can be tracked as a function of total heterostructure thickness (Figure 3.4). Although the measured period lengths of both the four and six unit cell-well samples deviate somewhat from the nominal period lengths, the calculated period lengths are constant as a function of sample thickness. The observation of thickness-independent period lengths agrees with the conclusion drawn from RHEED measurements of a lack of substantial lattice relaxation in the heterostructures. Additionally, the results of Figure 3.4 suggest the STO/LAO QW heterostructures are relatively robust to thermal cycling, as the samples

were repeatedly heated to 800 °C for growth and subsequently cooled to room temperature for *ex situ* XRD measurements.

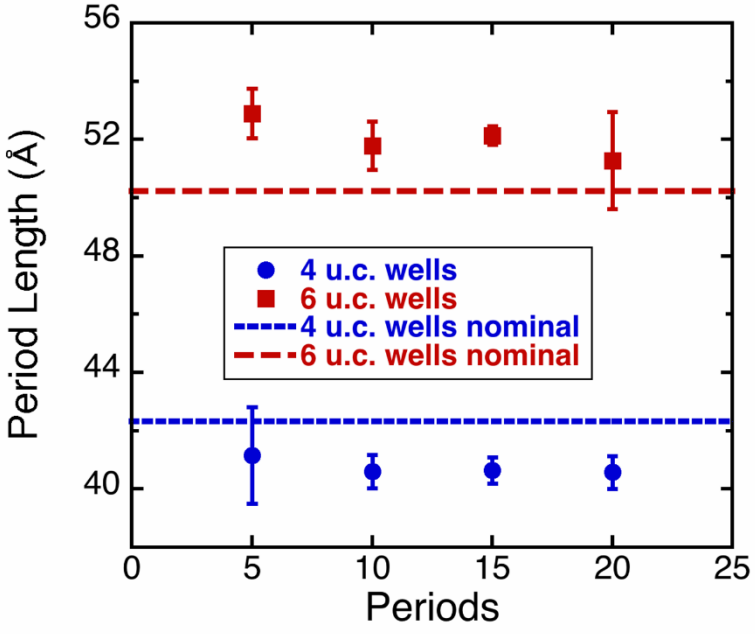

Figure 3.4: Average period length calculated from θ-2θ XRD scans as a function of total number of periods. The nominal period lengths of the two samples are plotted as dashed and dotted lines for comparison. Error bars are standard deviations of period length calculated from averaging over many adjacent superlattice peaks.

Reciprocal space mapping (RSM) carried out on both four and six unit cell-well samples (Figure 3.5) helps elucidate the in-plane lattice structure of the STO/LAO QW heterostructures. RSM is an XRD technique in which both the in- and out-of-plane source-to-sample and sample-to-detector angles are varied simultaneously, typically in a grid-like pattern [39]. As the name implies, this method allows one to map out a region of reciprocal space and, in the process, gather information on both the in- and out-of-plane characteristics of the crystalline lattice.

The superlattice peaks visible in the θ-2θ scan of Figure 3.3 can also be seen in the RSMs. As expected, the peaks occur at different points in the out-of-plane direction of reciprocal space, corresponding to additional periodicity in the out-of-plane direction of the sample. Notably, the in-plane reciprocal lattice vectors of the two samples are slightly different, as indicated by the blue and red dotted lines in Figure 3.5. An average in-plane

lattice constant of 3.83 Å was calculated for the four unit cell-well sample while an average in-plane lattice constant of 3.85 Å was calculated for the six unit cell-well sample. Both of these in-plane lattice constants are somewhat relaxed relative to the in-plane lattice constant of the LAO substrate (approximately 3.79 Å). Not surprisingly, the six unit cell-well sample shows slightly more relaxation relative to the four unit cell-well sample, owing to the propensity of strained STO to relax quite rapidly [31]. The observation of slight lattice relaxation in our STO/LAO QW heterostructures shows that, while high crystalline quality can be maintained even in very thick samples, relaxation of the STO wells is likely to become an issue if the STO wells are grown thick.

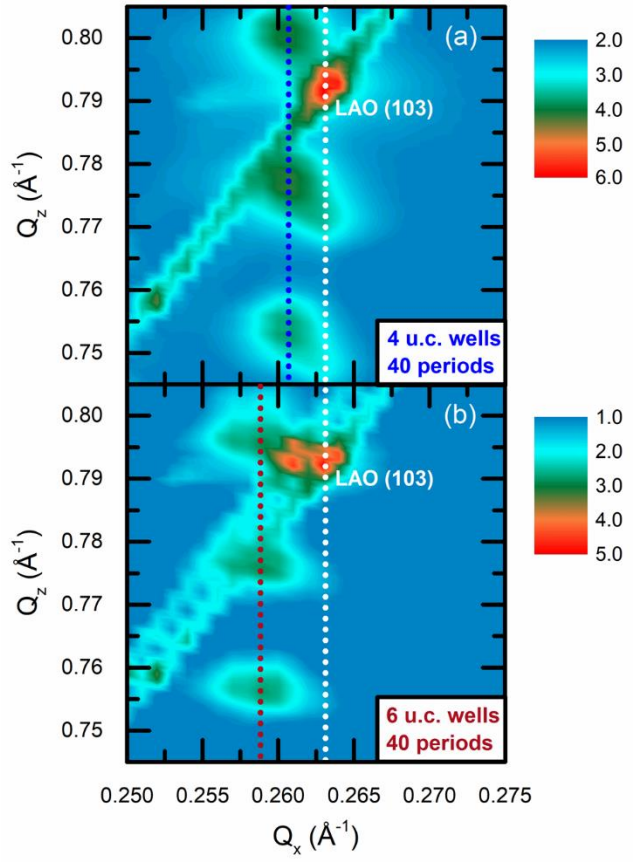

Figure 3.5: RSM of a 40-period four and six unit cell-well STO/LAO QW heterostructure. Color mapping is given by $\log_{10}$ of X-ray intensity. The dotted lines indicate the average in-plane lattice constant of the two samples.

Rocking curves were also collected using the same QW heterostructures characterized by RSM and discussed above. The full-width at half maximum (FWHM, $\Delta\omega$) of the four unit cell-well sample's rocking curve was determined to be 0.084° by fitting the data to a Lorentzian curve (Figure 3.6a). As mentioned briefly in Section 2.3, the FWHM of the rocking curve is an indicator of crystalline quality, with narrower rocking curves indicating a greater

uniformity of the underlying crystalline lattice [40]. Notably, the rocking curve of the four unit cell-well sample is even narrower than some bare STO films [41], [42], further confirming the exceptional crystalline quality of the sample.

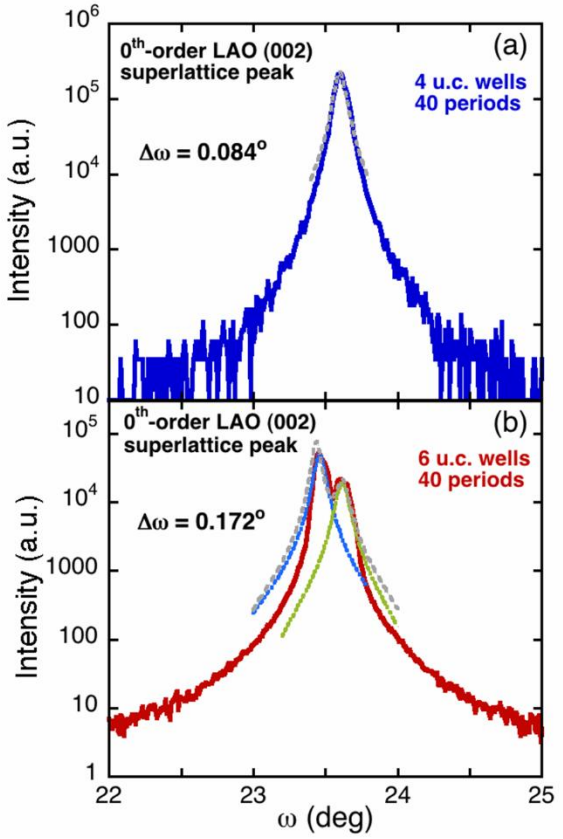

Figure 3.6: Rocking curves centered around the 0th-order LAO (002) superlattice peak of (a) four unit cell-well and (b) six unit cell-well STO/LAO QW heterostructures. The dashed lines represent Lorentzian fits to the data.

The rocking curve of the six unit cell-well sample is noticeably different from that of the four unit cell-well sample in that it features a double peak (Figure 3.6b). The double peak, or "twinning" of the sample, is due to the existence of twin domains in the LAO substrate. Twin domains are commonly observed in bulk LAO [43]–[45]. The twinning of the QW heterostructure results from the epitaxial relationship between the sample and the substrate and indicates the strict maintenance of such a relationship throughout sample growth. Due to the twinning, the rocking curve of the six unit cell-well sample was fit with a double Lorentzian, yielding a total FWHM of 0.172°. Each of the twin domains in the six unit cell-well sample contributes roughly 0.086° to the rocking curve, suggesting a consistent crystalline quality between the four and six unit cell-well samples.

Thickness-dependent X-ray reflectivity (XRR) measurements were also performed on both four and six unit cell-well QW heterostructures (Figure 3.7). XRR is a powerful X-ray measurement technique uniquely suited for extracting thin film parameters. XRR spectra are collected by guiding X-rays to the sample surface at a grazing angle of incidence. Just like the out-of-plane XRD scans described above and in Section 2.3, XRR spectra are collected using the θ-2θ diffractometer geometry. For small incidence angles θ, the X-rays are reflected from the sample surface and do not penetrate substantially into the film [46]. As θ is increased, X-rays begin to penetrate into the sample where they refract from any interfaces, such as the film/substrate interface or the interface between adjacent films in a heterostructure. These refracted X-rays interfere with X-rays reflected from the sample surface leading to the appearance of an interference pattern in XRR spectra known as Kiessig fringes [47]. The spacing of the Kiessig fringes yields information on the sample thickness. In addition, XRR allows for the extraction of the film density and surface and interfacial roughness. These quantities are typically extracted by fitting the collected XRR spectra to a model, a point I return to in more detail below.

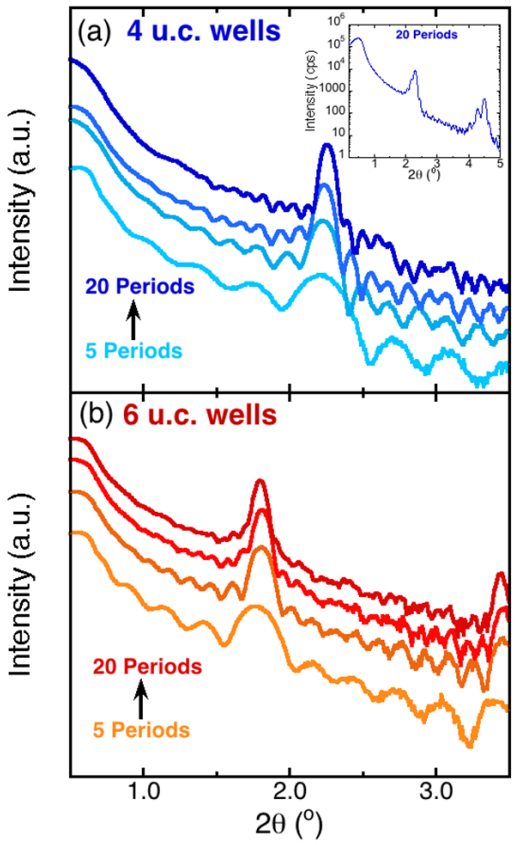

Figure 3.7: Thickness-dependent XRR spectra of (a) four unit cell-well and (b) six unit cell-well STO/LAO QW heterostructures. The spectra have been offset vertically for clarity. Inset: XRR spectrum of 20-period, four unit cell-well STO/LAO QW heterostructure taken out to $2\theta = 5.0°$.

The thickness-dependent XRR spectra of Figure 3.7 are plotted together for comparison and have been offset for clarity. As expected, the frequency of the Kiessig oscillations roughly doubles with a doubling of the number of QW periods. In addition to clear Kiessig fringes, the XRR spectra also show large Bragg peaks. The occurrence of these peaks in the XRR spectra is a result of the periodic modulation of the electron density along the direction normal to the sample surface, in agreement with the nominal sample design and the previous X-ray characterization.

The XRR spectra of Figure 3.7 have all been fit using *GenX* software [48] in order to extract the materials properties of the heterostructures. By employing the relations between materials properties and XRR spectra laid out in [46], [49] and [50], the layer thicknesses and interfacial roughness were extracted using the sample geometry (layer ordering, materials compositions, etc.) as input in *GenX*. An example fit is shown in Figure 3.8.

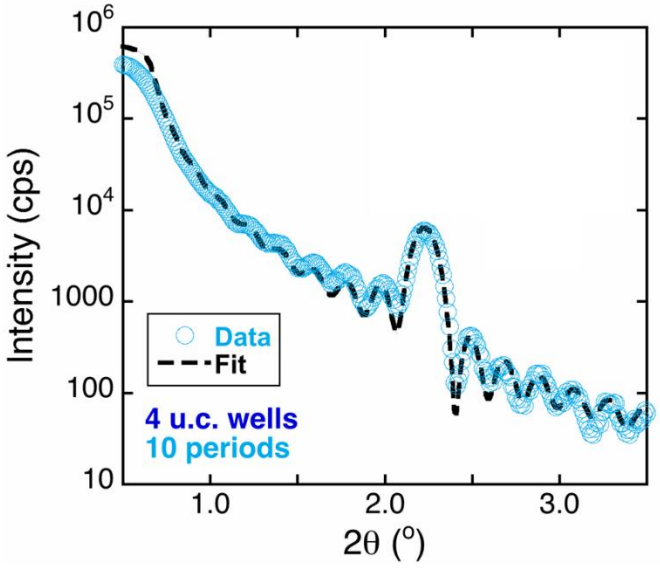

Figure 3.8: XRR spectrum of 10-period, four unit cell-well STO/LAO QW heterostructure with fit.

From the fitting, I extracted the thickness-dependent period length (Figure 3.9a) and interfacial roughness (Figure 3.9b). In agreement with the XRD results (Figure 3.4), the period length appears to be independent of thickness. Furthermore, the interfacial roughness does not appear to increase with increasing sample thickness within the errors of the extracted values. Plotted with the extracted interfacial roughness values are two reference values: one from previously-reported STO/LAO heterostructures grown by pulsed laser deposition (PLD) [28] and one from TEM measurements of an MBE-grown sample fabricated at UT and discussed in greater detail in Section 3.4 and [51]. By either method, the extracted interfacial roughness of the measured STO/LAO QW heterostructures is significantly reduced relative to the PLD-grown sample.

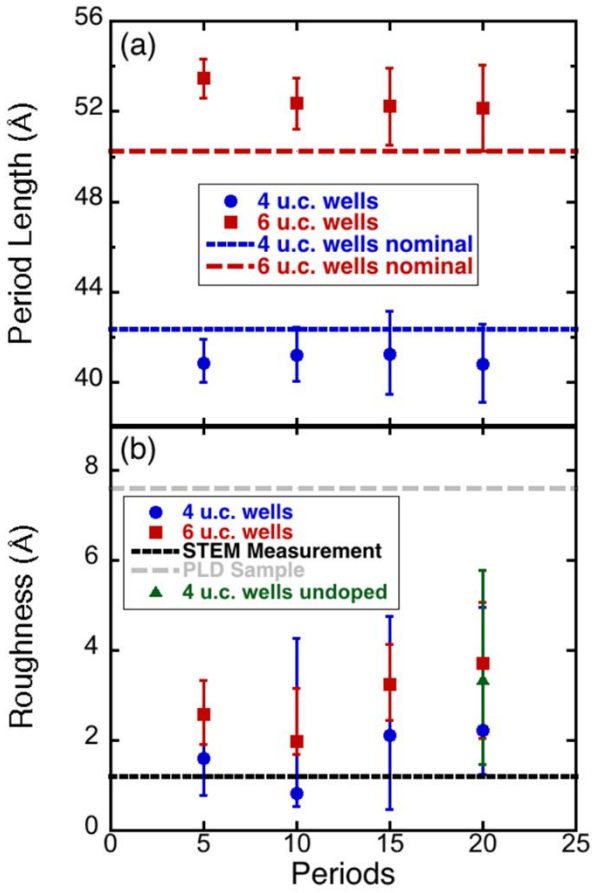

Figure 3.9: (a) Period length and (b) interfacial roughness of STO/LAO QW heterostructures extracted from fitting of XRR spectra. In (a), the nominal period lengths are plotted as dashed and dotted lines for comparison. In (b), the interfacial roughness of STO/LAO QW heterostructures as extracted from STEM measurements of my sample (black, dotted) and a previously-reported PLD-grown sample (gray, dashed, [28]) are plotted for comparison.

The reason for the improvement in the MBE-grown samples is not immediately clear. One possibility is that the *n*-type lanthanum doping of the STO wells provides extra charge at the STO/LAO interfaces, thereby avoiding the polar catastrophe [3], [6]. Density functional theory (DFT) calculations have indicated that doping via cation intermixing reduces the interfacial dipole energy [52], suggesting that intentional lanthanum doping of the STO wells may also reduce the interfacial dipole energy without the need for cation intermixing. However, the XRR measurement of a four unit cell-well STO/LAO QW heterostructure with undoped STO wells indicates the undoped sample has a similar interfacial roughness to the doped samples (green triangle, Fig 3.9b). The measurement of the undoped sample therefore makes the interpretation of doping-induced interface smoothing unlikely. Another possibility is that the MBE method itself is responsible for the improved interfacial quality. Some studies

have indicated MBE-grown films are less sensitive to deviations in growth conditions than their PLD-grown counterparts [53]–[56]. Detailed, systematic studies of interface quality in STO/LAO QW heterostructures under different growth conditions and with different compositions will need to be undertaken before the observed improvement can be fully understood.

3.4 Local Structural and Interfacial Characterization with TEM

While X-ray measurements provide a powerful, non-destructive method for evaluating the average crystalline properties of solids, TEM measurements allow for the collection of detailed information on local atomic structure. The wide-field, *Z*-contrast scanning TEM (STEM) measurement of a four unit cell-well STO/LAO QW heterostructure (Figure 3.10) allows one to directly observe the successive layering of STO and LAO in the heterostructure. Because of the *Z*-contrast property of the imaging method (described in Section 2.4), the LAO barrier layers appear bright in the image while the STO well layers appear darker. The excellent, uniform periodicity of the heterostructure can be clearly seen throughout the sample.

In addition to the STEM imaging, electron energy loss spectroscopy (EELS) mapping of the titanium (Ti) and lanthanum (La) cations are presented in Figure 3.10. EELS is a local spectroscopic technique that measures the change in the kinetic energy of an electron beam after it has interacted with a sample [57]. The measured energy losses are characteristic to different ions and allow for the differentiation of the chemical makeup of a solid with the spatial resolution of TEM. The EELS mapping of the STO/LAO QW heterostructure indicates a clear chemical separation between STO wells and LAO barriers in the heterostructure, in agreement with the X-ray characterization results of the previous

section. Clear chemical and physical separation between well and barrier layers is crucial for achieving our goal of confining electrons within the STO wells.

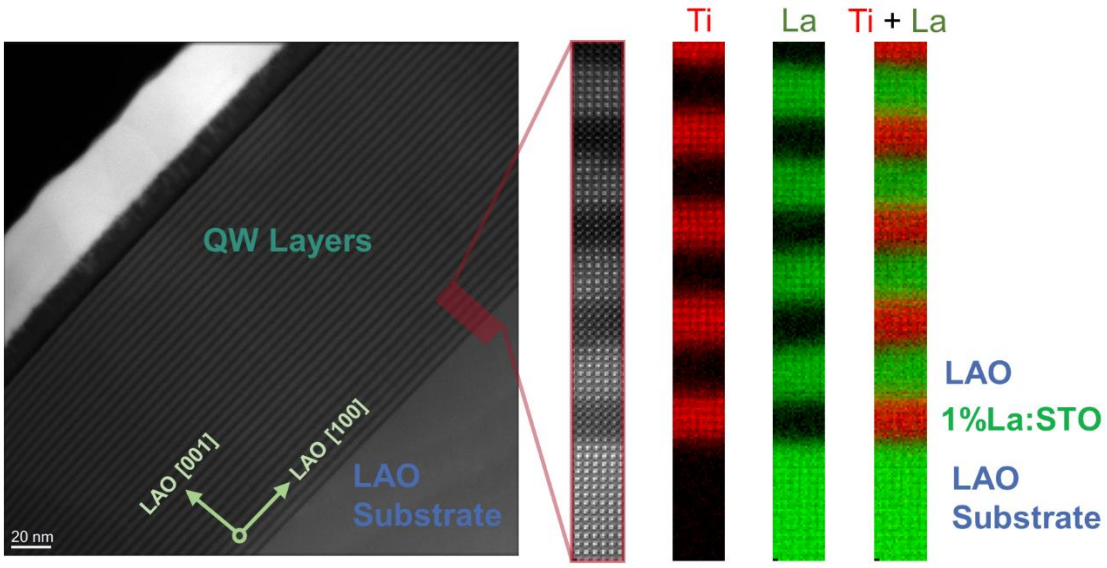

Figure 3.10: STEM image of a 40-period, four unit cell-well STO/LAO QW heterostructure (left). On the right, a zoomed-in STEM image of the heterostructure is presented, along with Ti (red) and La (green) EELS mapping.

In order to study the interfacial quality of the QWs in detail, statistical analysis of interfacial roughness was carried out using STEM intensity mapping of a 40-period, nominally four unit cell-QW heterostructure. The analysis proceeds by first collecting a STEM image of the sample (Figure 3.11a). In this case, an approximately 50×50 nm^2 region of the sample (corresponding to roughly 11 well/barrier periods) was imaged. Notably, no misfit dislocations are apparent over this relatively large region of the sample. From the STEM image in Figure 3.11a, a map of integrated *A*-site intensities was produced for each La and Sr column in the image (Figure 3.11b). By appropriately thresholding the intensities (Figure 3.11c), a binary map of the sample can be created where black pixels correspond to unit cells of STO while white pixels correspond to unit cells of LAO (Figure

3.11d). The binary map lends itself easily to statistical analysis and allows for the extraction of average structural parameters of the sample. An average well width of 4.32 ± 0.63 unit cells was extracted from the binary image, in good agreement with the design value of 4 unit cells.

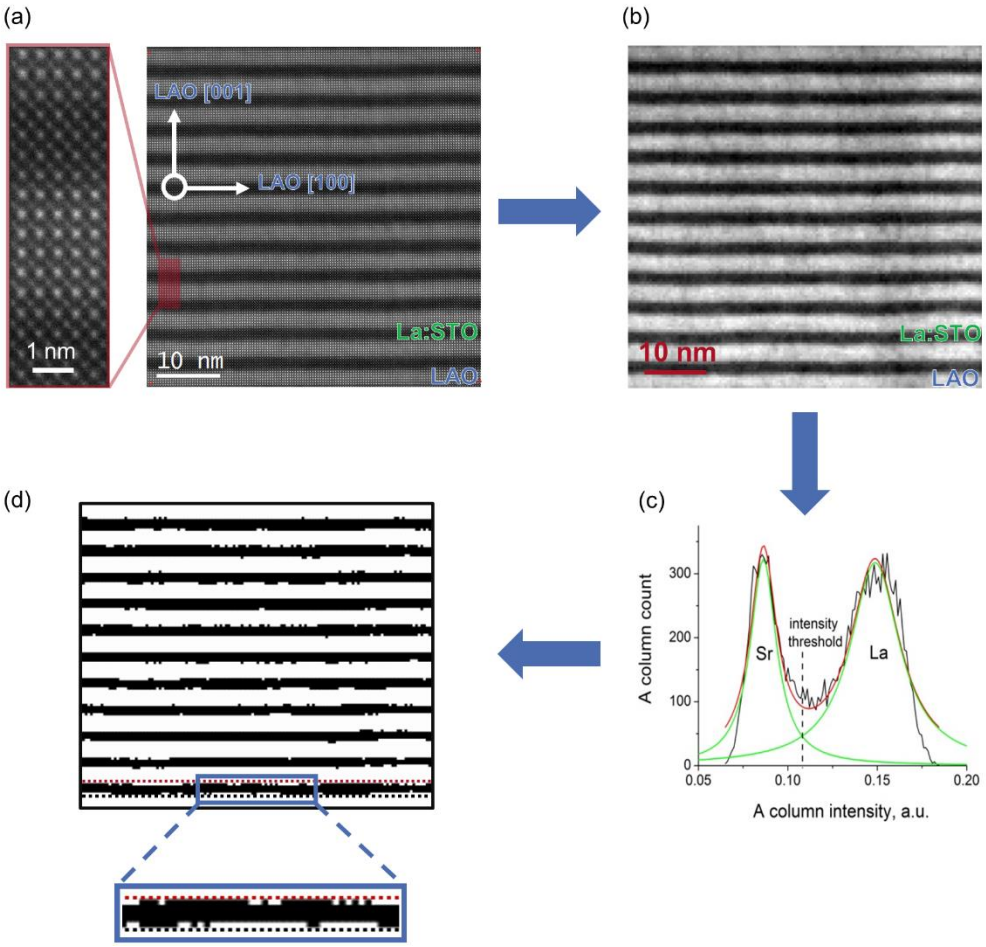

Figure 3.11: (a) STEM image of four unit cell-well STO/LAO QW heterostructure. (b) *A*-site intensity map generated from the STEM image in (a). (c) Integrated intensity showing the threshold between the intensity generated from interaction of the TEM electron beam with a Sr ion and a La ion. (d) Binary map showing STO unit cells in black and LAO unit cells in white.

Interfacial roughness was also quantified from statistical analysis of the binary map in Figure 3.11d. Due to the polar nature of LAO, arising from the alternating layers of

charged $(LaO)^+$ and $(AlO_2)^-$, the STO/LAO system can host two distinct types of interfaces, each with their own characteristic structural distortions. The so-called *n*-type interface, consisting of $TiO_2/(LaO)^+/(AlO_2)^-$ layer ordering, has been shown to roughen by approximately two to three unit cells due to cation intermixing [5], [28], [52], [58]. The *p*-type interface, consisting of $SrO/(AlO_2)^-/(LaO)^+$ layer ordering, is often found to be smoother than the *n*-type interface but has been shown to host oxygen vacancies and corresponding octahedral distortions [7], [9].

The average interfacial roughness of the *n*-type interface was found to be $\sigma_n = 0.24 \pm 0.25$ unit cells while that of the *p*-type interface $\sigma_p = 0.34 \pm 0.26$ unit cells. The interfacial roughness values calculated from STEM image analysis are in nice agreement with those extracted via XRR. Surprisingly, the STO/LAO QW heterostructure studied here does not show asymmetric interfacial roughness, in disagreement with many previous studies [9], [17], [28]. Furthermore, the calculated interfacial roughness is significantly less than previous reports for both interfaces [28]. The symmetric roughness is a peculiarity compared to previous reports and will require systematic study in order to develop a full, physical understanding of the phenomenon. Regardless, the structural characterization reported in this chapter indicates the STO/LAO QW heterostructures on LAO substrates are grown with excellent crystalline quality. In the next chapter, I move on to the optical experiments and the demonstrations of intersubband absorption in the STO/LAO QW heterostructures.

3.5 REFERENCES

[1] J. Robertson, "Band offsets of wide-band-gap oxides and implications for future electronic devices," *J. Vac. Sci. Technol. B Microelectron. Nanom. Struct.*, vol. 18, no. 3, pp. 1785–1791, 2000.

[2] S.-G. Lim, S. Kriventsov, T. N. Jackson, J. H. Haeni, D. G. Schlom, A. M. Balbashov, R. Uecker, P. Reiche, J. L. Freeouf, and G. Lucovsky, "Dielectric

functions and optical bandgaps of high-*K* dielectrics for metal-oxide-semiconductor field-effect transistors by far ultraviolet spectroscopic ellipsometry," *J. Appl. Phys.*, vol. 91, no. 7, pp. 4500–4505, Apr. 2002.

[3] A. Ohtomo and H. Y. Hwang, "A high-mobility electron gas at the $LaAlO_3/SrTiO_3$ heterointerface," *Nature*, vol. 427, no. 6973, pp. 423–426, Jan. 2004.

[4] M. Huijben, G. Rijnders, D. H. A. Blank, S. Bals, S. Van Aert, J. Verbeeck, G. Van Tendeloo, A. Brinkman, and H. Hilgenkamp, "Electronically coupled complementary interfaces between perovskite band insulators," *Nat. Mater.*, vol. 5, no. 7, pp. 556–560, Jul. 2006.

[5] P. R. Willmott, S. A. Pauli, R. Herger, C. M. Schlepütz, D. Martoccia, B. D. Patterson, B. Delley, R. Clarke, D. Kumah, C. Cionca, and Y. Yacoby, "Structural Basis for the Conducting Interface between $LaAlO_3$ and $SrTiO_3$," *Phys. Rev. Lett.*, vol. 99, no. 15, p. 155502, Oct. 2007.

[6] J. Lee and A. A. Demkov, "Charge origin and localization at the *n*-type $SrTiO_3/LaAlO_3$ interface," *Phys. Rev. B*, vol. 78, no. 19, p. 193104, Nov. 2008.

[7] Z. Zhong, P. X. Xu, and P. J. Kelly, "Polarity-induced oxygen vacancies at $LaAlO_3/SrTiO_3$ interfaces," *Phys. Rev. B*, vol. 82, no. 16, p. 165127, Oct. 2010.

[8] M. Huijben, A. Brinkman, G. Koster, G. Rijnders, H. Hilgenkamp, and D. H. A. Blank, "Structure-Property Relation of $SrTiO_3/LaAlO_3$ Interfaces," *Adv. Mater.*, vol. 21, no. 17, pp. 1665–1677, May 2009.

[9] R. Yamamoto, C. Bell, Y. Hikita, H. Y. Hwang, H. Nakamura, T. Kimura, and Y. Wakabayashi, "Structural comparison of *n*-type and *p*-type $LaAlO_3/SrTiO_3$ interfaces," *Phys. Rev. Lett.*, vol. 107, no. 3, p. 036104, Jul. 2011.

[10] H. Y. Hwang, Y. Iwasa, M. Kawasaki, B. Keimer, N. Nagaosa, and Y. Tokura, "Emergent phenomena at oxide interfaces," *Nat. Mater.*, vol. 11, no. 2, pp. 103–113, Feb. 2012.

[11] A. McCollam, S. Wenderich, M. K. Kruize, V. K. Guduru, H. J. A. Molegraaf, M. Huijben, G. Koster, D. H. A. Blank, G. Rijnders, A. Brinkman, H. Hilgenkamp, U. Zeitler, and J. C. Maan, "Quantum oscillations and subband properties of the two-dimensional electron gas at the $LaAlO_3/SrTiO_3$ interface," *APL Mater.*, vol. 2, no. 2, p. 022102, Feb. 2014.

[12] J. Chakhalian, J. W. Freeland, A. J. Millis, C. Panagopoulos, and J. M. Rondinelli, "Colloquium: Emergent properties in plane view: Strong correlations at oxide interfaces," *Rev. Mod. Phys.*, vol. 86, no. 4, pp. 1189–1202, Oct. 2014.

[13] R. Ramesh and D. G. Schlom, "Whither Oxide Electronics?," *MRS Bull.*, vol. 33, no. 11, pp. 1006–1014, Nov. 2008.

[14] J. Mannhart, D. H. A. Blank, H. Y. Hwang, A. J. Millis, and J.-M. Triscone, "Two-Dimensional Electron Gases at Oxide Interfaces," *MRS Bull.*, vol. 33, no. 11, pp. 1027–1034, Nov. 2008.

[15] D. F. Bogorin, P. Irvin, C. Cen, and J. Levy, "$LaAlO_3/SrTiO_3$-based device concepts," in *Multifunctional Oxide Heterostructures*, Oxford University Press, 2010, pp. 364–388.

[16] L. Bjaalie, B. Himmetoglu, L. Weston, A. Janotti, and C. G. Van de Walle, "Oxide interfaces for novel electronic applications," *New J. Phys.*, vol. 16, no. 2, p. 025005, Feb. 2014.

[17] M. Choi, C. Lin, M. Butcher, C. Rodriguez, Q. He, A. B. Posadas, A. Y. Borisevich, S. Zollner, and A. A. Demkov, "Quantum confinement in transition metal oxide quantum wells," *Appl. Phys. Lett.*, vol. 106, no. 19, p. 192902, May 2015.

[18] L. L. Chang, L. Esaki, and R. Tsu, "Resonant tunneling in semiconductor double barriers," *Appl. Phys. Lett.*, vol. 24, no. 12, pp. 593–595, Jun. 1974.

[19] T. C. L. G. Sollner, W. D. Goodhue, P. E. Tannenwald, C. D. Parker, and D. D. Peck, "Resonant tunneling through quantum wells at frequencies up to 2.5 THz," *Appl. Phys. Lett.*, vol. 43, no. 6, pp. 588–590, Sep. 1983.

[20] K. Wakita, Y. Kawamura, Y. Yoshikuni, and H. Asahi, "Long-wavelength waveguide multiple-quantum-well (MQW) optical modulator with 30:1 on/off ratio," *Electron. Lett.*, vol. 22, no. 17, p. 907, 1986.

[21] B. F. Levine, "Quantum-well infrared photodetectors," *J. Appl. Phys.*, vol. 74, no. 8, p. R1, Oct. 1993.

[22] E. B. Dupont, D. Delacourt, and M. Papuchon, "Mid-infrared phase modulation via Stark effect on intersubband transitions in GaAs/GaAlAs quantum wells," *IEEE J. Quantum Electron.*, vol. 29, no. 8, pp. 2313–2318, 1993.

[23] J. Faist, F. Capasso, D. L. Sivco, C. Sirtori, A. L. Hutchinson, and A. Y. Cho, "Quantum Cascade Laser," *Science (80-.).*, vol. 264, no. 5158, pp. 553–556, Apr. 1994.

[24] J. R. Meyer, C. A. Hoffman, F. J. Bartoli, and L. R. Ram-Mohan, "Infrared electro-optical modulators based on field-induced Γ- L intervalley transfer," *Appl. Phys. Lett.*, vol. 67, no. 19, pp. 2756–2758, Nov. 1995.

[25] W. S. Choi, S. A. Lee, J. H. You, S. Lee, and H. N. Lee, "Resonant tunnelling in a quantum oxide superlattice," *Nat. Commun.*, vol. 6, p. 7424, Jun. 2015.

[26] N. Chand, "MBE growth of high-quality GaAs," *J. Cryst. Growth*, vol. 97, no. 2, pp. 415–429, Sep. 1989.

[27] T.-H. Shieh and S.-C. Lee, “Transport mechanism of X band electrons in AlAs electrode through GaAs/AlAs/GaAs structure by varying GaAs well thickness,” *Appl. Phys. Lett.*, vol. 63, no. 24, p. 3350, 1993.

[28] N. Nakagawa, H. Y. Hwang, and D. A. Muller, “Why some interfaces cannot be sharp,” *Nat. Mater.*, vol. 5, no. 3, pp. 204–209, Mar. 2006.

[29] J. E. Ortmann, A. B. Posadas, and A. A. Demkov, “The MBE growth of arbitrarily thick $SrTiO_3/LaAlO_3$ quantum well heterostructures for use in next-generation optoelectronic devices,” *J. Appl. Phys.*, vol. 124, no. 1, p. 015301, Jul. 2018.

[30] S. Geller and V. B. Bala, “Crystallographic studies of perovskite-like compounds. II. Rare earth alluminates,” *Acta Crystallogr.*, vol. 9, no. 12, pp. 1019–1025, Dec. 1956.

[31] L. S.-J. Peng, X. X. Xi, B. H. Moeckly, and S. P. Alpay, “Strain relaxation during in situ growth of $SrTiO_3$ thin films,” *Appl. Phys. Lett.*, vol. 83, no. 22, p. 4592, Dec. 2003.

[32] M. R. Krames, O. B. Shchekin, R. Mueller-Mach, G. O. Mueller, L. Zhou, G. Harbers, and M. G. Craford, “Status and Future of High-Power Light-Emitting Diodes for Solid-State Lighting,” *J. Disp. Technol.*, vol. 3, no. 2, pp. 160–175, Jun. 2007.

[33] D. M. Van Den Broeck, D. Bharrat, A. M. Hosalli, N. A. El-Masry, and S. M. Bedair, “Strain-balanced InGaN/GaN multiple quantum wells,” *Appl. Phys. Lett.*, vol. 105, no. 3, p. 031107, Jul. 2014.

[34] J. R. Riley, S. Padalkar, Q. Li, P. Lu, D. D. Koleske, J. J. Wierer, G. T. Wang, and L. J. Lauhon, “Three-Dimensional Mapping of Quantum Wells in a GaN/InGaN Core–Shell Nanowire Light-Emitting Diode Array,” *Nano Lett.*, vol. 13, no. 9, pp. 4317–4325, Sep. 2013.

[35] D. G. Schlom, L.-Q. Chen, X. Pan, A. Schmehl, and M. A. Zurbuchen, “A Thin Film Approach to Engineering Functionality into Oxides,” *J. Am. Ceram. Soc.*, vol. 91, no. 8, pp. 2429–2454, Aug. 2008.

[36] P. Zubko, N. Jecklin, A. Torres-Pardo, P. Aguado-Puente, A. Gloter, C. Lichtensteiger, J. Junquera, O. Stéphan, and J.-M. Triscone, “Electrostatic Coupling and Local Structural Distortions at Interfaces in Ferroelectric/Paraelectric Superlattices,” *Nano Lett.*, vol. 12, no. 6, pp. 2846–2851, Jun. 2012.

[37] K. Zhao, G. Chen, B.-S. Li, and A. Shen, “Mid-infrared intersubband absorptions in ZnO/ZnMgO multiple quantum wells,” *Appl. Phys. Lett.*, vol. 104, no. 21, p. 212104, May 2014.

[38] J. A. Mundy, C. M. Brooks, M. E. Holtz, J. A. Moyer, H. Das, A. F. Rébola, J. T. Heron, J. D. Clarkson, S. M. Disseler, Z. Liu, A. Farhan, R. Held, R. Hovden, E. Padgett, Q. Mao, H. Paik, R. Misra, L. F. Kourkoutis, E. Arenholz, A. Scholl, J. A.

Borchers, W. D. Ratcliff, R. Ramesh, C. J. Fennie, P. Schiffer, D. A. Muller, and D. G. Schlom, "Atomically engineered ferroic layers yield a room-temperature magnetoelectric multiferroic," *Nature*, vol. 537, no. 7621, pp. 523–527, Sep. 2016.

[39] P. F. Fewster, "Reciprocal space mapping," *Crit. Rev. Solid State Mater. Sci.*, vol. 22, no. 2, pp. 69–110, Jun. 1997.

[40] K. Inaba, "X-Ray Thin Film Measurement Techniques," *Rigaku J.*, vol. 24, no. 1, pp. 10–15, 2008.

[41] J. Ravichandran, W. Siemons, H. Heijmerikx, M. Huijben, A. Majumdar, and R. Ramesh, "An Epitaxial Transparent Conducting Perovskite Oxide: Double-Doped $SrTiO_3$," *Chem. Mater.*, vol. 22, no. 13, pp. 3983–3987, Jul. 2010.

[42] S.-H. Baek and C.-B. Eom, "Epitaxial integration of perovskite-based multifunctional oxides on silicon," *Acta Mater.*, vol. 61, no. 8, pp. 2734–2750, May 2013.

[43] Y. Lin, Y. B. Chen, T. Garret, S. W. Liu, C. L. Chen, L. Chen, R. P. Bontchev, A. Jacobson, J. C. Jiang, E. I. Meletis, J. Horwitz, and H.-D. Wu, "Epitaxial growth of dielectric $CaCu_3Ti_4O_{12}$ thin films on (001) $LaAlO_3$ by pulsed laser deposition," *Appl. Phys. Lett.*, vol. 81, no. 4, pp. 631–633, Jul. 2002.

[44] A. P. Zhuravel, A. V. Ustinov, K. S. Harshavardhan, and S. M. Anlage, "Influence of $LaAlO_3$ surface topography on rf current distribution in superconducting microwave devices," *Appl. Phys. Lett.*, vol. 81, no. 26, pp. 4979–4981, Dec. 2002.

[45] J. Q. Chen, X. Wang, Y. H. Lu, A. Roy Barman, G. J. You, G. C. Xing, T. C. Sum, S. Dhar, Y. P. Feng, Ariando, Q.-H. Xu, and T. Venkatesan, "Defect dynamics and spectral observation of twinning in single crystalline $LaAlO_3$ under subbandgap excitation," *Appl. Phys. Lett.*, vol. 98, no. 4, p. 041904, Jan. 2011.

[46] M. Yasaka, "X-ray thin-film measurement techniques V. X-ray reflectivity measurement," *Rigaku J.*, vol. 26, pp. 1–9, Jan. 2010.

[47] H. Kiessig, "Untersuchungen zur Totalreflexion von Röntgenstrahlen," *Ann. Phys.*, vol. 402, no. 6, pp. 715–768, 1931.

[48] M. Björck and G. Andersson, "GenX: an extensible X-ray reflectivity refinement program utilizing differential evolution," *J. Appl. Cryst*, vol. 40, pp. 1174–1178, 2007.

[49] L. G. Parratt, "Surface Studies of Solids by Total Reflection of X-Rays," *Phys. Rev.*, vol. 95, no. 2, pp. 359–369, Jul. 1954.

[50] S. K. Sinha, E. B. Sirota, S. Garoff, and H. B. Stanley, "X-ray and neutron scattering from rough surfaces," *Phys. Rev. B*, vol. 38, no. 4, pp. 2297–2311, Aug. 1988.

[51] J. E. Ortmann, N. Nookala, Q. He, L. Gao, C. Lin, A. B. Posadas, A. Y. Borisevich, M. A. Belkin, and A. A. Demkov, "Quantum Confinement in Oxide Heterostructures: Room-Temperature Intersubband Absorption in $SrTiO_3/LaAlO_3$ Multiple Quantum Wells," *ACS Nano*, vol. 12, no. 8, pp. 7682–7689, Aug. 2018.

[52] L. Qiao, T. C. Droubay, V. Shutthanandan, Z. Zhu, P. V Sushko, and S. A. Chambers, "Thermodynamic instability at the stoichiometric $LaAlO_3/SrTiO_3$ (001) interface," *J. Phys. Condens. Matter*, vol. 22, no. 31, p. 312201, Aug. 2010.

[53] E. J. Tarsa, E. A. Hachfeld, F. T. Quinlan, J. S. Speck, and M. Eddy, "Growth-related stress and surface morphology in homoepitaxial $SrTiO_3$ films," *Appl. Phys. Lett.*, vol. 68, no. 4, p. 490, Aug. 1996.

[54] T. Ohnishi, M. Lippmaa, T. Yamamoto, S. Meguro, and H. Koinuma, "Improved stoichiometry and misfit control in perovskite thin film formation at a critical fluence by pulsed laser deposition," *Appl. Phys. Lett.*, vol. 87, no. 24, p. 241919, 2005.

[55] T. Ohnishi, K. Shibuya, T. Yamamoto, and M. Lippmaa, "Defects and transport in complex oxide thin films," *J. Appl. Phys.*, vol. 103, no. 10, p. 103703, 2008.

[56] C. M. Brooks, L. F. Kourkoutis, T. Heeg, J. Schubert, D. A. Muller, and D. G. Schlom, "Growth of homoepitaxial $SrTiO_3$ thin films by molecular-beam epitaxy," *Appl. Phys. Lett.*, vol. 94, no. 16, p. 162905, 2009.

[57] R. F. Egerton, "Electron energy-loss spectroscopy in the TEM," *Reports Prog. Phys.*, vol. 72, no. 1, p. 016502, Jan. 2009.

[58] L. Qiao, T. C. Droubay, T. Varga, M. E. Bowden, V. Shutthanandan, Z. Zhu, T. C. Kaspar, and S. A. Chambers, "Epitaxial growth, structure, and intermixing at the $LaAlO_3/SrTiO_3$ interface as the film stoichiometry is varied," *Phys. Rev. B*, vol. 83, no. 8, p. 085408, Feb. 2011.

Chapter 4: Room-Temperature Intersubband Absorption in $SrTiO_3/LaAlO_3$ Multiple Quantum Wells

4.1 Theory of Intersubband Transitions[2]

Having successfully fabricated STO/LAO QWs of a high crystalline quality, I now shift focus to the optical modulation of confined charge carriers between quantized energy levels within the STO wells. The event of a charge carrier transitioning between confined states in QWs is called an intersubband transition. Such transitions underlie the operation of many QW devices, including quantum cascade lasers [1], QW infrared photodetectors [2], [3], and some electro-optic modulators [4]. The specific case of optical absorption resulting from photon-stimulated intersubband transitions is known as intersubband absorption.

Intersubband transitions (so-named because the particles transition between quantized subbands that reside within the same band) are distinct from interband transitions that traditionally drive semiconductor light sources [5], [6]. The confinement of the electronic wave functions along the direction normal to the plane of the well and the fact that the transitions occur within the same electronic band, rather than between bands, impose special restraints and symmetries on the accessible transitions. These symmetries inform experimental design and must be considered before intersubband absorption can be observed.

Deriving the absorption coefficient from Fermi's golden rule can elucidate many of the symmetries of intersubband absorptions. Utilizing Bloch's Theorem, the total wave function in real-space can be written

$$\psi_i(\vec{r}) = f_i(\vec{r})u_v(\vec{r}), \tag{4.1}$$

[2] Material in this chapter based on J. E. Ortmann, N. Nookala, Q. He, L. Gao, C. Lin, A. B. Posadas, A. Y. Borisevich, M. A. Belkin, and A. A. Demkov, *ACS Nano*, vol. 12, no. 8, pp. 7682–7689, Aug. 2018.

where $f_i(\vec{r})$ is an envelope function that varies slowly over the distance of one lattice constant with quantum numbers represented by *i* and $u_v(\vec{r})$ is the lattice-periodic Bloch function of band *v* at an extremum of the Brillouin zone [7]. While the Bloch function can be assumed to be the same throughout all materials of the heterostructure, the envelope function will depend sensitively on the shape of the QW potential. Because the QW potential only confines the electrons along one direction (I will call this the *z* direction), the envelope function can be written as a product of free-electron plane waves in the *x* and *y* directions with wave vector $\overrightarrow{k_\perp} = \hat{\imath}k_x + \hat{\jmath}k_y$ and a confined electronic wave function $\phi_n(z)$ according to

$$f_{n\overrightarrow{k_\perp}}(\vec{r}) = \frac{1}{\sqrt{A}} e^{i\overrightarrow{k_\perp}\cdot\vec{r}} \phi_n(z). \tag{4.2}$$

Here, the normalization constant *A* is the area of the sample. The confined states can then be calculated by solving the one-dimensional Schrödinger equation in $\phi_n(z)$ with the appropriate potential $V(z)$ [7]. For most cases of practical relevance, the Schrödinger equation in $\phi_n(z)$ must be solved numerically, with the transfer-matrix approach being commonly employed [8].

From the real-space wave function of Equation (4.1), the transition rate W_{if} from an initial state *i* to a final state *f* induced by interaction with an electromagnetic field can be calculated with Fermi's golden rule:

$$W_{if} = \frac{2\pi}{\hbar} \left|\langle \psi_i | H' | \psi_f \rangle\right|^2 \delta\left(E_f - E_i - \hbar\omega\right), \tag{4.3}$$

where $\hbar\omega$ is the energy of the incoming photon. H' is the interaction Hamiltonian $H' = \left({}^{e}/_{2m^*}\right)\left(\vec{A}\cdot\vec{p} + \vec{p}\cdot\vec{A}\right)$, where -*e* is the electron charge, m^* is the electron effective mass, $\vec{A}$ is the vector potential of the incoming electromagnetic wave and $\vec{p}$ is the electron momentum [7]. Employing the dipole approximation, valid in the limit where the photon wavelength is much longer than the QW width, Equation (4.3) can be rewritten as

$$W_{if} \propto \left|\langle\psi_i|\vec{e}\cdot\vec{p}|\psi_f\rangle\right|^2 \delta(E_f - E_i - \hbar\omega), \tag{4.4}$$

where $\vec{e}$ is the polarization vector of the incoming electromagnetic wave and the proportionality constants are given by fundamental constants and the electromagnetic field strength and frequency [7].

The photon-induced transitions are therefore governed by the matrix element $\langle\psi_i|\vec{e}\cdot\vec{p}|\psi_f\rangle$ from Equation (4.4). This matrix element can be broken down into component elements according to [9]

$$\langle\psi_i|\vec{e}\cdot\vec{p}|\psi_f\rangle = \vec{e}\cdot\langle u_\nu|\vec{p}|u_{\nu'}\rangle\langle f_n|f_{n'}\rangle + \vec{e}\cdot\langle u_\nu|u_{\nu'}\rangle\langle f_n|\vec{p}|f_{n'}\rangle, \tag{4.5}$$

where ν and ν' are the indices of the initial and final band states while n and n' are the indices of the initial and final subband states. Clearly, for the case of intersubband transitions, $\nu = \nu'$ and the first term of Equation (4.5) vanishes [7]. Thus, only the second term of Equation (4.5) contributes to intersubband transitions of confined charge carriers. Because $\nu = \nu'$, $\langle u_\nu|u_{\nu'}\rangle = 1$, leaving the transition rate in Equation (4.4) proportional to

$$W_{if} \propto \left|\left\langle f_{n\overrightarrow{k_\perp}}\middle|\vec{e}\cdot\vec{p}\middle|f_{n'\overrightarrow{k'_\perp}}\right\rangle\right|^2 \delta(E_f - E_i - \hbar\omega). \tag{4.6}$$

The $e_x p_x$ and $e_y p_y$ terms of Equation (4.6) do not contribute to the optical absorption at finite frequency [7], leaving only the z component of the electromagnetic field to induce intersubband transitions. The matrix element of Equation (4.4) can therefore finally be written as

$$\langle f_n|p_z|f_{n'}\rangle = \int dz\phi_n^*(z)p_z\phi_{n'}(z). \tag{4.7}$$

The expression of Equation (4.7) represents the polarization selection rule of intersubband transitions [2], [7], [10]. This rule states that only electromagnetic fields with some component of the polarization vector normal to the plane of the wells can induce intersubband transitions in QWs. The polarization selection rule imposes constraints on the manner in which experimental demonstrations of intersubband transitions can proceed

(Figure 4.1). In particular, experiments utilizing normal incidence of electromagnetic radiation cannot hope to stimulate intersubband transitions in QWs because the optical electric field will always be wholly contained in the plane of the wells (no *z* component or polarization).

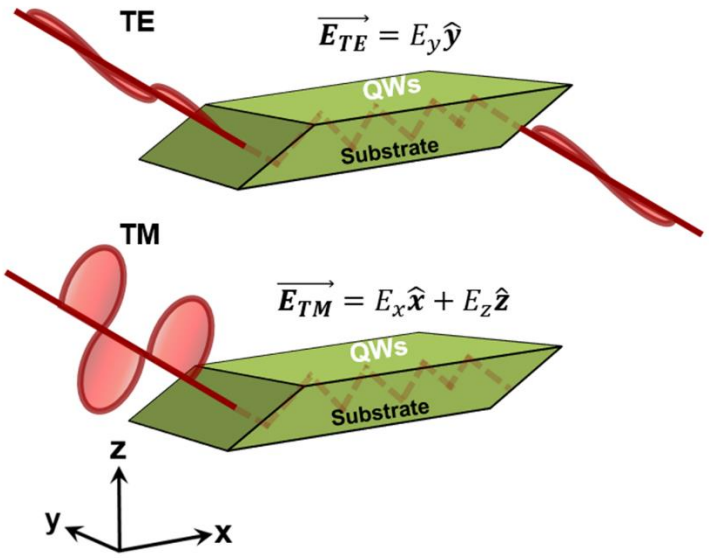

Figure 4.1: Schematic of the geometry used for the experiments in this chapter. As the incoming electromagnetic wave bounces off the QWs, transverse-electric (TE)-polarized light will not stimulate intersubband absorption because the optical electric field is totally in the plane of the wells. Transverse-magnetic (TM)-polarized light, on the other hand, will stimulate intersubband absorption because a component of the optical electric field is normal to the plane of the wells.

Depending on the symmetry of the confining potential, not all intersubband transitions are allowed. The allowable transitions can be examined by considering the oscillator strength between states *n* and *n'* [7]

$$s_{nn'} = \frac{2}{m^*\hbar\omega_{nn'}}|\langle f_n|p_z|f_{n'}\rangle|^2. \tag{4.8}$$

For the instructive case of an infinite, symmetric well, the electronic wave functions take the form

$$\phi_n(z) = \sqrt{\frac{2}{L}} \sin\left(\frac{n\pi z}{L}\right), \tag{4.9}$$

where L is the width of the QW. Utilizing Equation (4.9) in the oscillator strength (4.8), one finds that only parity-changing transitions are allowed (n = even/odd and n' = odd/even) due to the symmetry of the wave functions (Figure 4.2). When the symmetry of the wave functions is broken, the parity-changing selection rule is relaxed. The wave function symmetry can be broken in many ways, for example by doping, application of an external electric field, or coupling between neighboring wells.

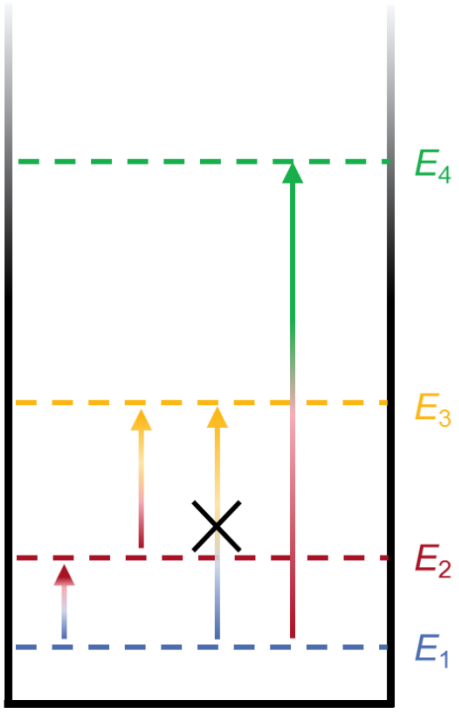

Figure 4.2: Schematic demonstrating allowable transitions within an infinite, symmetric QW. Only parity-changing transitions are allowed (even-to-odd or odd-to-even). Thus, the 1-to-3 transition is not allowed, for example.

4.2 Intersubband Absorption Experimental Results

With the experimental constraints discussed in Section 4.1 in mind, the absorption characteristics of the STO/LAO QW heterostructures described in detail in Chapter 3 were measured. The measurements were carried out with Fourier transform infrared (FTIR) spectroscopy. FTIR is an optical spectroscopy method in which a broadband light source is guided to a sample and the wavelength-dependent absorption spectrum is extracted via a Michelson interferometer after interaction with the sample [11]. The absorption measurements were carried out at room temperature.

To prepare them for optical characterization, the STO/LAO QW heterostructures were first coated with titanium/gold with thicknesses of approximately 2 nm and 100 nm, respectively. Two parallel edges of the square, $10 \times 10\ mm^2$ samples were then shaved down at 45° angles to make entrance and exit facets for the FTIR light source (Figure 4.3). The titanium/gold coating served as a reflective coating and allowed for the incident light to undergo multiple interactions with the multiple QWs (MQWs) as it passed through the sample. The experimental setup (Figure 4.4) featured a mid-IR/near-IR light source, ZnSe linear polarizer for enforcement of the polarization selection rule of Equation (4.7), and liquid nitrogen-cooled mercury-cadmium-telluride IR detector. Two BaF_2 lenses, one immediately after the light source and the other immediately before the detector, were also used to focus the beam into the entrance facet of the sample and into the detector aperture, respectively.

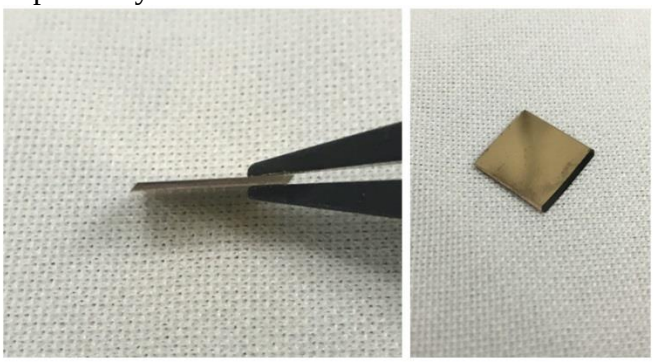

Figure 4.3: A photograph of an STO/LAO QW heterostructure prepared for optical characterization. The sample has been coated with Ti/Au and 45° entrance and exit facets have been fabricated.

The FTIR absorption spectra of a five, four, and three unit-cell MQW heterostructure were measured with FTIR (Figure 4.5a). Spectra were collected once with the light source polarized in the plane of the wells (transverse electric, or, TE polarization) and again with the light source polarized normal to the plane of the wells (transverse magnetic, or, TM polarization). The absorption spectra collected with TE polarization were subtracted from those collected with TM polarization according to the procedure outlined in the Supporting Information of [12], allowing for the

discrimination of intersubband absorption from other potential absorption mechanisms present in the samples.

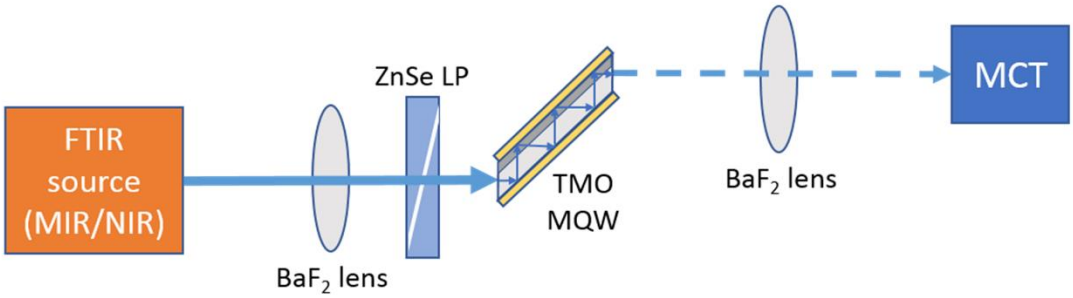

Figure 4.4: Schematic of experimental setup used for intersubband absorption measurements. The FTIR light source is focused into the entrance facet of the multiple QW (MQW) sample by a BaF_2 lens and polarized via a ZnSe linear polarizer (LP). A second BaF_2 lens focuses the outcoming light into the mercury-cadmium-telluride (MCT) detector.

The experimental absorption spectra match nicely with what would be expected for quantum-confined transitions. In particular, the absorption energies scale inversely with QW width. Furthermore, the absorption amplitudes scale directly with QW width, reflecting the reduction in ground-state electron population as the well width is decreased. Besides the polarization dependence, the experimentally observed absorption energies are also significantly higher than reported phonon energies in either LAO [13] or STO [14], giving greater support to the interpretation that the observed absorptions arise from intersubband transitions.

Below the experimental results of Figure 4.5a, the theoretical absorption spectra of five, four, and three-unit cell QW heterostructures computed with tight binding are plotted for comparison (Figure 4.5b). The tight binding method has been previously employed for the computation of absorption spectra in similar TMO QWs [15]. In Figure 4.5b, the absorption spectra are represented by the imaginary part of the dielectric function of

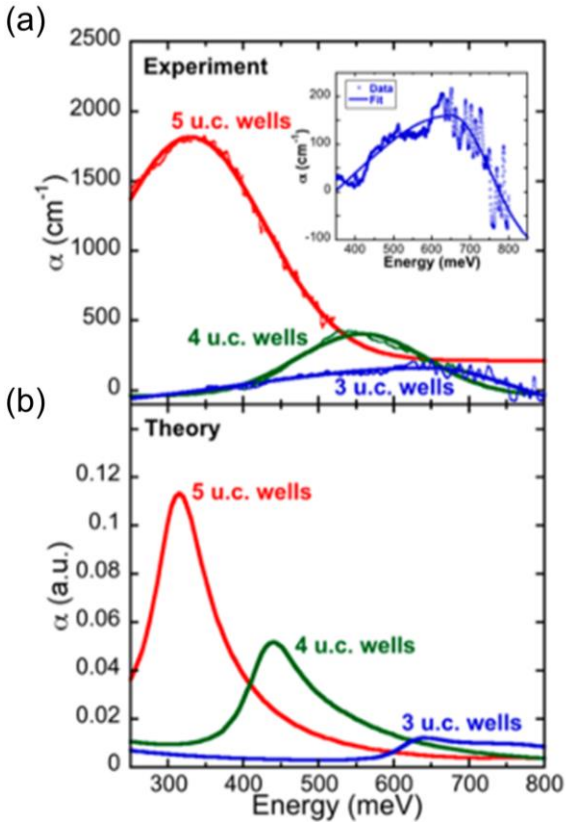

STO/LAO QWs. It can be seen that the experimental and tight binding results agree nicely, both in terms of transition energy and qualitatively in terms of the scaling of absorption strength with QW width.

Figure 4.5: (a) Experimental measurements of intersubband absorption in five, four, and three unit cell-well STO/LAO MQWs. The circles are measured data while the solid lines are Gaussian fits to the data. Inset: Zoom-in of three unit cell-well data and corresponding bi-Gaussian fit [12]. (b) Tight-binding calculations of intersubband absorption spectra of five, four, and three unit cell-well STO/LAO MQWs.

The successful *n*-type doping of the STO QWs was verified with room-temperature Hall measurements. The Hall effect [16] is the formation of an electric potential in the direction perpendicular to current flow when a material is placed in an external magnetic field oriented normal to the sample surface. The so-called Hall voltage forms as a result of the Lorentz force experienced by the free electrons, causing them to congregate on one side of the sample. The ratio of the Hall voltage to the Hall current defines the Hall resistance. The carrier concentration *n* can be extracted from the slope of the Hall resistance vs magnetic field curve (Figure 4.6a) according to

$$n = \frac{1}{e \cdot \text{slope} \cdot t}, \tag{4.10}$$

where t is the sample thickness. From these measurements, $n = 3.5 \times 10^{20}$ cm^{-3} was extracted, corresponding to approximately 2.2% doping. The measured doping is notably higher than the design value of 1% doping. The origin of the excess doping can most likely

be traced to the presence of oxygen vacancies in the heterostructures, which are also an *n*-type dopant in STO. Oxygen vacancies have frequently been reported in STO films [17]–[19] and the measured carrier concentration of STO thin films has been found to reduce with oxygen or air annealing [20]–[23]. However, for the case of intersubband absorptions, it is only necessary to ensure sufficient charge has been doped into the STO wells in order to support the interpretation of the observed absorptions as arising from intersubband transitions. Hence, the measurement of doping beyond the design value does not impact the conclusions of the absorption measurements and in fact supports them by indicating there is clearly enough charge within the STO wells for the observation of intersubband absorption.

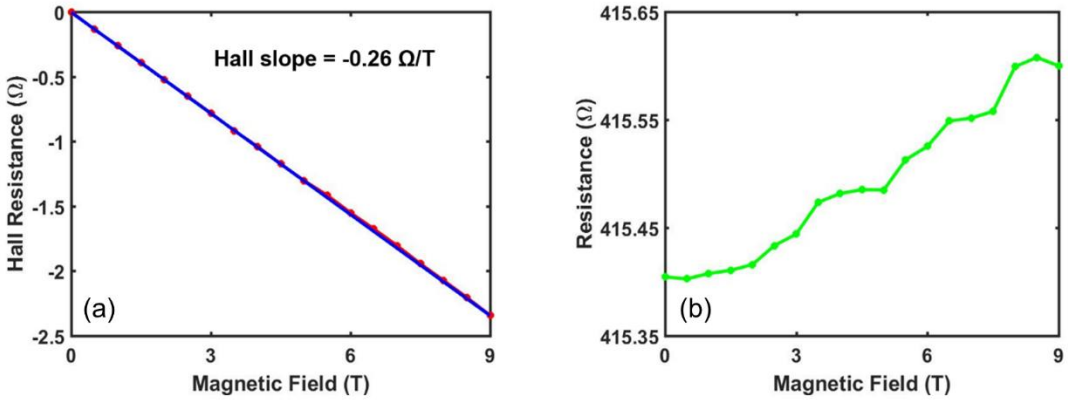

Figure 4.6: (a) Hall resistance versus magnetic field *B* of a four unit cell-well STO/LAO QW heterostructure taken at room temperature. (b) Room-temperature magnetoresistance of the same sample.

Finally, the room-temperature electron mobility μ of the STO/LAO QW heterostructures was also measured by magnetoresistance (Figure 4.6b). Using the expression

$$\mu = \frac{1}{e \cdot n \cdot t \cdot R(B = 0)}, \tag{4.11}$$

where $R(B = 0)$ is the zero-field sample resistance, a mobility of 6.3 $cm^2 \cdot V^{-1} \cdot s^{-1}$ was extracted. This value is in line with previous reports of room-temperature mobility in STO [23]–[26]. Because the electron mobility is closely related to sample quality, these measurements further support the claims of high sample quality from the previous chapter.

4.3 Density Functional Theory Calculations

First-principles calculations of the density of states (DOS) and charge density in STO/LAO QW heterostructures were conducted with DFT. DFT calculations were performed using the local-density approximation [27] for the projector-augmented-wave pseudopotentials [28] as implemented in the Vienna Ab-Initio Simulation Package [29]. Symmetric QW supercells with compositions ranging from $(LAO)_{7.5}/(STO)_{3.5}$ to $(LAO)_{7.5}/(STO)_{5.5}$ in steps of one unit cell of STO were used for the calculations. Symmetric supercells were chosen in order to avoid the artificial formation of an electric field across the STO wells due to the oppositely polarized STO/LAO interfaces [30], [31]. In the real samples, the free charge in the STO wells should screen an electric field arising from the asymmetric STO/LAO interfaces.

The STO conduction band is formed primarily from the Ti t_{2g} states. In bulk STO, these three orbitals (d_{xy}, d_{xz}, and d_{yz}) are triply degenerate [32]. However, symmetry breaking at the interface between thin films can remove this degeneracy and lead to electronic reconstructions [33]. For the case of STO QWs, taking the confinement direction to be along *z*, the Ti d_{xy} band will be largely unaffected by the QW potential while the energies of the Ti d_{xz} and d_{yz} bands will become quantized. Therefore, the Ti d_{xy} contributions to the DOS are ignored in the DFT calculations, as electrons in this band will not contribute to intersubband absorption.

The calculated DOS for a three, four, and five-unit cell well STO/LAO QW heterostructure (Figure 4.7a) show sharp peaks throughout the conduction band. These peaks have been shown to correspond to QW states through tight binding calculations [15]. Therefore, the energy spacing between sharp peaks in the STO conduction band should represent the energies of intersubband transitions. From the calculated DOS, the ground state-to-first excited state energies are 510, 420, and 350 meV for three, four, and five unit cells QWs, respectively. The DFT results for the five-unit cell QW agree closely with experiments while the calculated energies for the four- and three-unit cell well samples differ from measured values by approximately 0.1 eV. The discrepancy can be easily explained by slight variations in nominal and actual QW widths in the measured samples.

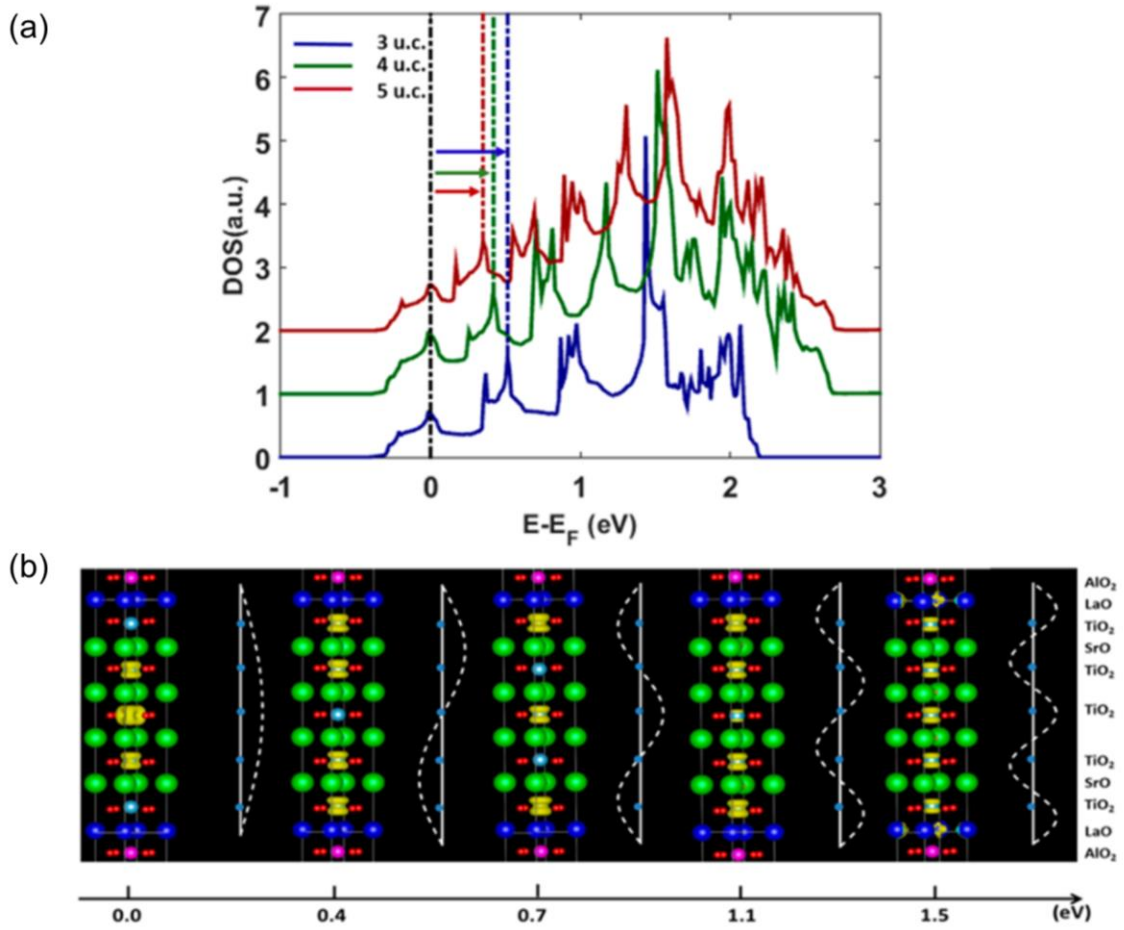

Figure 4.7: (a) Ti d_{xz}/d_{yz} DOS of a three, four, and five unit cell-well STO/LAO QW calculated with DFT. The sharp peaks in the DOS correspond to confined QW states. The intersubband transition energies are indicated by arrows. (b) Real-space charge density of the five sharp peaks in the five unit cell-well DOS. The sinusoidal variation of charge density is indicated to the right of each panel and confirms the sharp states observed in the DOS correspond to QW states.

The real-space charge density of the sharp states in the STO conduction band of the five-unit cell QW have also been plotted (Figure 4.7b). A sinusoidal variation in charge density across the STO well can be observed for all states. Examining Equation (4.9), one can see that such sinusoidal variation should be expected for QW states. The spatial

dependence of the real-space charge density therefore supports the interpretation of the sharp states in the STO conduction band DOS as QW states.

4.4 REFERENCES

[1] J. Faist, F. Capasso, D. L. Sivco, C. Sirtori, A. L. Hutchinson, and A. Y. Cho, "Quantum Cascade Laser," *Science (80-.).*, vol. 264, no. 5158, pp. 553–556, Apr. 1994.

[2] D. D. Coon and R. P. G. Karunasiri, "New mode of IR detection using quantum wells," *Appl. Phys. Lett.*, vol. 45, no. 6, pp. 649–651, Sep. 1984.

[3] B. F. Levine, "Quantum-well infrared photodetectors," *J. Appl. Phys.*, vol. 74, no. 8, p. R1, Oct. 1993.

[4] E. B. Dupont, D. Delacourt, and M. Papuchon, "Mid-infrared phase modulation via Stark effect on intersubband transitions in GaAs/GaAlAs quantum wells," *IEEE J. Quantum Electron.*, vol. 29, no. 8, pp. 2313–2318, 1993.

[5] E. F. Schubert, "Light-Emitting Diodes," in *Wiley Encyclopedia of Electrical and Electronics Engineering*, Hoboken, NJ, USA: John Wiley & Sons, Inc., 2014, pp. 1–10.

[6] W. L. Ng, M. A. Lourenço, R. M. Gwilliam, S. Ledain, G. Shao, and K. P. Homewood, "An efficient room-temperature silicon-based light-emitting diode," *Nature*, vol. 410, no. 6825, pp. 192–194, Mar. 2001.

[7] M. Helm, "Chapter 1 The Basic Physics of Intersubband Transitions," in *Semiconductors and Semimetals*, vol. 62, 1999, pp. 1–99.

[8] E. O. Kane, "Basic Concepts of Tunneling," in *Tunneling Phenomena in Solids*, Boston, MA: Springer US, 1969, pp. 1–11.

[9] G. Bastard, *Wave mechanics applied to semiconductor heterostructures*. United States: John Wiley and Sons Inc, 1990.

[10] H. C. Liu, M. Buchanan, and Z. R. Wasilewski, "How good is the polarization selection rule for intersubband transitions?," *Appl. Phys. Lett.*, vol. 72, no. 14, pp. 1682–1684, Apr. 1998.

[11] C. Berthomieu and R. Hienerwadel, "Fourier transform infrared (FTIR) spectroscopy," *Photosynth. Res.*, vol. 101, no. 2–3, pp. 157–170, Sep. 2009.

[12] J. E. Ortmann, N. Nookala, Q. He, L. Gao, C. Lin, A. B. Posadas, A. Y. Borisevich, M. A. Belkin, and A. A. Demkov, "Quantum Confinement in Oxide Heterostructures: Room-Temperature Intersubband Absorption in $SrTiO_3/LaAlO_3$ Multiple Quantum Wells," *ACS Nano*, vol. 12, no. 8, pp. 7682–7689, Aug. 2018.

[13] T. Willett-Gies, E. DeLong, and S. Zollner, "Vibrational properties of bulk $LaAlO_3$ from Fourier-transform infrared ellipsometry," *Thin Solid Films*, vol. 571, pp. 620–624, Nov. 2014.

[14] A. A. Sirenko, C. Bernhard, A. Golnik, A. M. Clark, J. Hao, W. Si, and X. X. Xi, "Soft-mode hardening in $SrTiO_3$ thin films," *Nature*, vol. 404, no. 6776, pp. 373–376, Mar. 2000.

[15] C. Lin, A. Posadas, M. Choi, and A. A. Demkov, "Optical properties of transition metal oxide quantum wells," *J. Appl. Phys.*, vol. 117, no. 3, p. 034304, Jan. 2015.

[16] E. H. Hall, "On a New Action of the Magnet on Electric Currents," *Am. J. Math.*, vol. 2, no. 3, p. 287, Sep. 1879.

[17] N. Nakagawa, H. Y. Hwang, and D. A. Muller, "Why some interfaces cannot be sharp," *Nat. Mater.*, vol. 5, no. 3, pp. 204–209, Mar. 2006.

[18] G. Herranz, M. Basletić, M. Bibes, C. Carrétéro, E. Tafra, E. Jacquet, K. Bouzehouane, C. Deranlot, A. Hamzić, J.-M. Broto, A. Barthélémy, and A. Fert, "High Mobility in $LaAlO_3/SrTiO_3$ Heterostructures: Origin, Dimensionality, and Perspectives," *Phys. Rev. Lett.*, vol. 98, no. 21, p. 216803, May 2007.

[19] Z. Zhong, P. X. Xu, and P. J. Kelly, "Polarity-induced oxygen vacancies at $LaAlO_3/SrTiO_3$ interfaces," *Phys. Rev. B*, vol. 82, no. 16, p. 165127, Oct. 2010.

[20] S. Thiel, "Tunable Quasi-Two-Dimensional Electron Gases in Oxide Heterostructures," *Science (80-.).*, vol. 313, no. 5795, pp. 1942–1945, Sep. 2006.

[21] A. Brinkman, M. Huijben, M. van Zalk, J. Huijben, U. Zeitler, J. C. Maan, W. G. van der Wiel, G. Rijnders, D. H. A. Blank, and H. Hilgenkamp, "Magnetic effects at the interface between non-magnetic oxides," *Nat. Mater.*, vol. 6, no. 7, pp. 493–496, Jul. 2007.

[22] W. Siemons, G. Koster, H. Yamamoto, W. A. Harrison, G. Lucovsky, T. H. Geballe, D. H. A. Blank, and M. R. Beasley, "Origin of Charge Density at $LaAlO_3$ on $SrTiO_3$ Heterointerfaces: Possibility of Intrinsic Doping," *Phys. Rev. Lett.*, vol. 98, no. 19, p. 196802, May 2007.

[23] M. Choi, A. B. Posadas, C. A. Rodriguez, A. O'Hara, H. Seinige, A. J. Kellock, M. M. Frank, M. Tsoi, S. Zollner, V. Narayanan, and A. A. Demkov, "Structural, optical, and electrical properties of strained La-doped $SrTiO_3$ films," *J. Appl. Phys.*, vol. 116, no. 4, p. 043705, Jul. 2014.

[24] H. P. R. Frederikse and W. R. Hosler, "Hall mobility in $SrTiO_3$," *Phys. Rev.*, vol. 161, no. 3, pp. 822–827, 1967.

[25] J. Ravichandran, W. Siemons, H. Heijmerikx, M. Huijben, A. Majumdar, and R. Ramesh, "An Epitaxial Transparent Conducting Perovskite Oxide: Double-Doped $SrTiO_3$," *Chem. Mater.*, vol. 22, no. 13, pp. 3983–3987, Jul. 2010.

[26] J. Ravichandran, W. Siemons, M. L. Scullin, S. Mukerjee, M. Huijben, J. E. Moore, A. Majumdar, and R. Ramesh, "Tuning the electronic effective mass in double-doped $SrTiO_3$," *Phys. Rev. B*, vol. 83, no. 3, p. 035101, Jan. 2011.

[27] J. P. Perdew and A. Zunger, "Self-interaction correction to density-functional approximations for many-electron systems," *Phys. Rev. B*, vol. 23, no. 10, pp. 5048–5079, May 1981.

[28] P. E. Blöchl, "Projector augmented-wave method," *Phys. Rev. B*, vol. 50, no. 24, pp. 17953–17979, Dec. 1994.

[29] G. Kresse and J. Furthmüller, "Efficient iterative schemes for *ab initio* total-energy calculations using a plane-wave basis set," *Phys. Rev. B*, vol. 54, no. 16, pp. 11169–11186, Oct. 1996.

[30] M. S. Park, S. H. Rhim, and A. J. Freeman, "Charge compensation and mixed valency in $LaAlO_3$/$SrTiO_3$ heterointerfaces studied by the FLAPW method," *Phys. Rev. B*, vol. 74, no. 20, p. 205416, Nov. 2006.

[31] N. C. Bristowe, E. Artacho, and P. B. Littlewood, "Oxide superlattices with alternating *p* and *n* interfaces," *Phys. Rev. B*, vol. 80, no. 4, p. 045425, Jul. 2009.

[32] Y. Tokura, "Orbital Physics in Transition-Metal Oxides," *Science (80-.).*, vol. 288, no. 5465, pp. 462–468, Apr. 2000.

[33] D. Doennig and R. Pentcheva, "Control of orbital reconstruction in $(LaAlO_3)_M/(SrTiO_3)_N$ (001) quantum wells by strain and confinement," *Sci. Rep.*, vol. 5, no. 1, p. 7909, Jul. 2015.

Chapter 5: Monolithic Integration of $SrTiO_3/LaAlO_3$ Quantum Wells on Silicon (001)

5.1 Epitaxial Integration of Oxides on Silicon[3]

Since its invention in the middle part of the 20th Century, integrated circuit technology has driven the rapid development of computation and the microelectronics industry [1]. The unprecedented pace of development has been due in large part to the industry-wide adoption of standard CMOS processes. CMOS allows for the low-cost, high-volume manufacture of integrated circuits. The extraordinary success of CMOS technology and the widespread existing CMOS infrastructure within the microelectronics industry means that any competitive next-generation computing technologies should be manufacturable based on CMOS processes. It is the requirement of CMOS-compatibility that has, for example, driven the quickly expanding interest in silicon photonics [2].

Large (typically 300 mm in diameter), high-quality silicon wafers form the basis of standard CMOS processes. These wafers comprise the building blocks of modern integrated circuits and most CMOS processes have been optimized around the use of such silicon substrates. Thus, any new practical technologies must at a minimum be integrable with silicon for introduction into CMOS. While the STO/LAO QW heterostructures described in the previous chapters would appear to hold much promise for use in optical and electro-optical devices, in their previously-discussed form (i.e., grown on bulk LAO substrates), they offer limited potential for use in realistic technologies due to their incompatibility with standard CMOS processes.

Before STO/LAO QWs can hope to become technologically relevant for use in integrated circuitry and photonics, a process must be developed for their integration with

[3] Material in this chapter based on J. E. Ortmann, S. Kwon, A. B. Posadas, M. J. Kim, and A. A. Demkov, *J. Appl. Phys.*, vol. 125, no. 15, p. 155302, Apr. 2019.

silicon substrates. One option would be the development of a wafer-bonding process whereby STO/LAO QW heterostructures are first epitaxially grown on bulk LAO substrates (as in the previous two chapters) and then bonded to silicon wafers. Such a wafer bonding process has been successfully employed for the integration of the complex oxide barium titanate with standard CMOS processes [3]–[6]. However, the complexity of such wafer-bonding processes is often considerable, as is the cost. A more desirable alternative would be the development of a process allowing for the direct, epitaxial integration of STO/LAO QW heterostructures on silicon substrates.

On the surface, it would appear the direct epitaxial deposition of oxides, such as STO and LAO, on crystalline silicon would be unlikely to succeed due to two seemingly conflicting requirements. First, for the epitaxial deposition of any material, a clear atomic registry must be maintained between the substrate's crystalline lattice and that of the deposited material. This necessitates a clear crystalline order in both the substrate and the film. Second, the growth of TMO materials obviously requires the introduction of oxygen into the growth chamber. However, in the presence of even low oxygen pressures, silicon spontaneously forms the native oxide SiO_2 on its surface [7]. Unlike crystalline silicon, SiO_2 is amorphous, rendering the epitaxial deposition of any material on SiO_2 impossible due to the random atomic orientation of atoms within the SiO_2 layer. Therefore, one may suspect that the direct deposition of crystalline oxides on silicon is destined to fail due to the rapid amorphization of the silicon surface upon introduction of the requisite oxidant into the growth chamber.

However, these seemingly contradictory requirements have in fact been reconciled for the epitaxial deposition of some crystalline oxides on silicon. In 1991, McKee *et al*. [8] reported the epitaxial integration of barium silicide ($BaSi_2$) barium oxide (BaO) and barium titanate ($BaTiO_3$, BTO) with silicon (001) substrates. In order to avoid amorphization of

the silicon substrate upon introduction of the oxidant into the growth chamber, a $BaSi_2$ template layer was first formed on the silicon surface by submonolayer deposition of Ba [8]. Apparently, the stabilization of a $BaSi_2$ interlayer protects the surface silicon atoms from amorphization by allowing them to bond with Ba and significantly limiting their propensity to oxidize. The silicon-Ba bonds protect the underlying silicon from oxidation even in the presence of an oxidizing species. After the formation of the $BaSi_2$ interlayer, the silicon surface is resilient enough to the presence of oxygen to allow for the subsequent deposition of BaO and, ultimately, BTO while maintaining epitaxial registry between the film and the substrate.

Later, the epitaxial deposition of TMO films on silicon was extended to STO via the formation of a $SrSi_2$ interfacial template [9]. The mechanism of oxidation protection of the silicon surface via submonolayer Sr deposition was subsequently studied by DFT [10]. As postulated by McKee *et al*., DFT studies confirm that the presence of Sr on the silicon surface delays oxidation and prevents the vertical growth of amorphous SiO_2. Since the original demonstration of epitaxial STO integration on the silicon (001) surface, very high-quality epitaxial STO thin films have been reported on silicon [11], [12], allowing for the integration of a wide variety of other oxides with silicon substrates via an STO buffer layer [13]–[18]. It is through such an STO buffer layer that the epitaxial integration of STO/LAO QW heterostructures on silicon can be achieved.

5.2 Sample Design, Growth, and Surface Characterization

The sample design used for the study of silicon-integrated STO/LAO QWs is shown in Figure 5.1. The QW heterostructure itself is identical to that which is studied in the previous two chapters, with alternating layers of LAO barriers and La-doped STO wells. However, as the QWs are here being integrated on silicon, the sample must begin

with the deposition of an epitaxial STO buffer layer on the silicon (001) surface. It is upon this buffer layer that the deposition of the QW heterostructure will proceed.

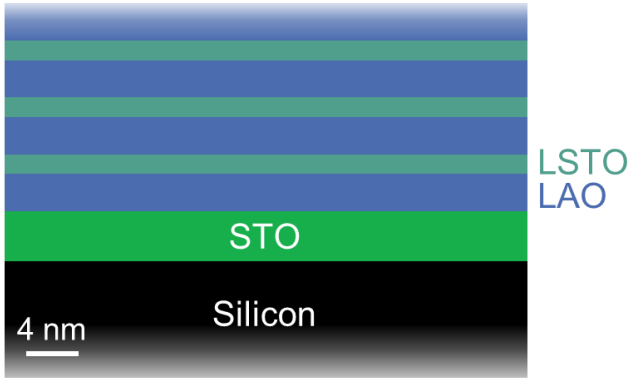

Figure 5.1: Generalized sample schematic of silicon-integrated STO/LAO QW heterostructures (LSTO = La-doped STO). The QWs are integrated on silicon via a crystalline STO buffer layer.

The deposition procedure for the STO buffer layer is described in detail in [19]. In short, deposition begins with the Sr deoxidation of the silicon surface in UHV [20]. After removal of the native oxide, a $SrSi_2$ Zintl template [21] is formed via deposition of ½ ML of Sr on the silicon (001) surface in UHV at a substrate temperature of 650 °C. The substrate temperature is reduced to 200 °C after formation of the Zintl template. Once the temperature is stable at 200 °C, molecular oxygen is slowly added to the MBE until the chamber pressure reaches approximately 7×10^{-8} Torr. Then, Sr and Ti are co-deposited on the silicon surface in the presence of oxygen at a rate of roughly 1 ML per minute. After the deposition of approximately 1.5 – 2 ML of STO, the oxygen pressure is gradually raised to a final pressure of approximately 5×10^{-7} Torr over a period of two to three minutes. After the desired thickness of STO has been reached (typically five to ten unit cells), the deposition ceases and the oxygen valve is closed, allowing the chamber to return to UHV conditions.

When deposited in this fashion, the STO buffer layer will be amorphous. However, if proper cation and oxygen stoichiometry have been achieved during deposition, the film can be crystallized by ramping the substrate temperature to approximately 550 – 600 °C in

UHV. Crystallization can be monitored via *in situ* RHEED. The formation of a streaky RHEED pattern indicates the successful crystallization of the STO template (Figure 2.4b). After crystallization, the STO template is typically annealed for five to ten minutes in UHV and/or O_2 at a pressure of approximately 5×10^{-7} Torr to allow for full crystallization of the film. If annealing in O_2, an SiO_2 interlayer will form at the interface of the STO film and the silicon substrate [22]. However, because this amorphous interlayer forms *after* epitaxial deposition of STO, the epitaxial registry between the STO film and the underlying silicon substrate will be maintained, although the STO lattice constants will be altered by the formation of the SiO_2 interlayer and the mismatched thermal expansion coefficients of the heterostructure [23].

After deposition of the STO buffer layer, the STO/LAO QW heterostructure is deposited using a similar growth procedure to that described in Chapter 3 and References [19], [24]. Deposition is typically undertaken at a substrate temperature of approximately 750 °C under an oxygen partial pressure of $1 – 5 \times 10^{-6}$ Torr. Again, STO wells are *n*-type doped with 1% La and both STO wells and LAO barriers are deposited using a layer-by-layer, shuttered growth method. STO unit cells are nominally terminated by a TiO_2 layer, while LAO unit cells are nominally terminated by an AlO_2 layer.

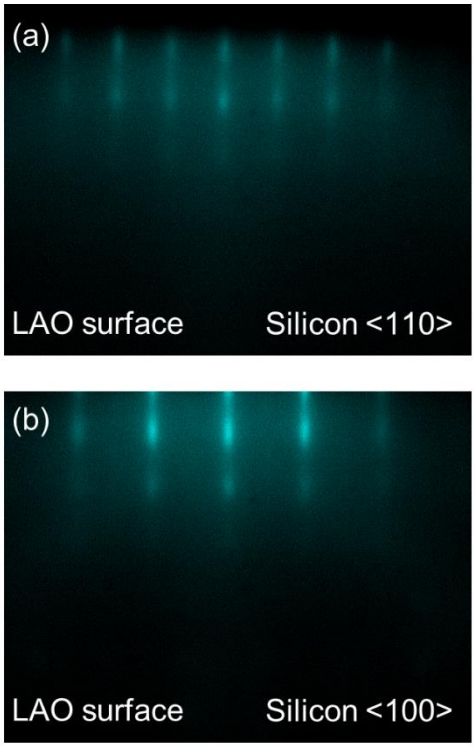

Figure 5.2: RHEED images of the top LAO surface of a ten-period, four unit cell-well STO/LAO QW heterostructure on silicon. Images were captured along the (a) silicon ⟨110⟩ and (b) silicon ⟨100⟩ azimuths. Because of the 45° rotation of the TMO unit cell relative to the silicon unit cell, these correspond to the LAO ⟨100⟩ and LAO ⟨110⟩ azimuths, respectively.

As before, the surface characteristics of the heterostructure are monitored with *in situ* RHEED (Figure 5.2). The heterostructure surface was found to remain crystalline and of a consistent quality up to the greatest thicknesses studied (~ 460 Å). No thickness-dependent degradation of surface quality was observed with RHEED, in agreement with studies of STO/LAO QW heterostructures grown on LAO [24]. Some intensity modulations can be seen in the RHEED patterns of Figure 5.2, indicating the presence of small, three-dimensional structures on the surface. However, the surface remains sufficiently flat for the continued deposition of crystalline oxide layers at all stages of heterostructure growth. This observation indicates thicker heterostructures can be achieved than that which is reported here with no clear thickness-limiting mechanism identified by RHEED.

5.3 X-RAY CHARACTERIZATION

The out-of-plane θ-2θ XRD scan (Figure 5.3a) indicates that the silicon-integrated STO/LAO QW heterostructure is indeed single crystalline, as suggested from RHEED imaging of the surface. Only one orientation of TMO films is visible in the data, with clear Bragg peaks arising due to reflections from the TMO (001) and (002) lattice planes.

Similarly to the QW heterostructures from Chapters 3 and 4 grown on LAO substrates, superlattice peaks are also clearly visible around the TMO (001) and (002) Bragg peaks stemming from the additional long-range periodicity of the QW structure. This is consistent with previous reports of short-period oxide superlattices [25]–[28]. The average out-of-plane lattice constant of one well/barrier period is calculated as 3.82 Å from the XRD data, in good agreement with the nominal value of 3.84 Å calculated by assuming fully strained films.

A high-resolution θ-2θ XRD scan around the TMO (002) Bragg peak (Figure 5.3b) more clearly shows the superlattice peaks. Superlattice peaks can be clearly observed out to second order. From the relative spacing of the superlattice peaks, the average period length can be calculated from Equation (3.1) as 41.8 Å. This value matches closely with the design value of 42.2 Å one calculates by assuming an out-of-plane lattice constant of 3.93 Å for La-doped STO as previously measured [29].

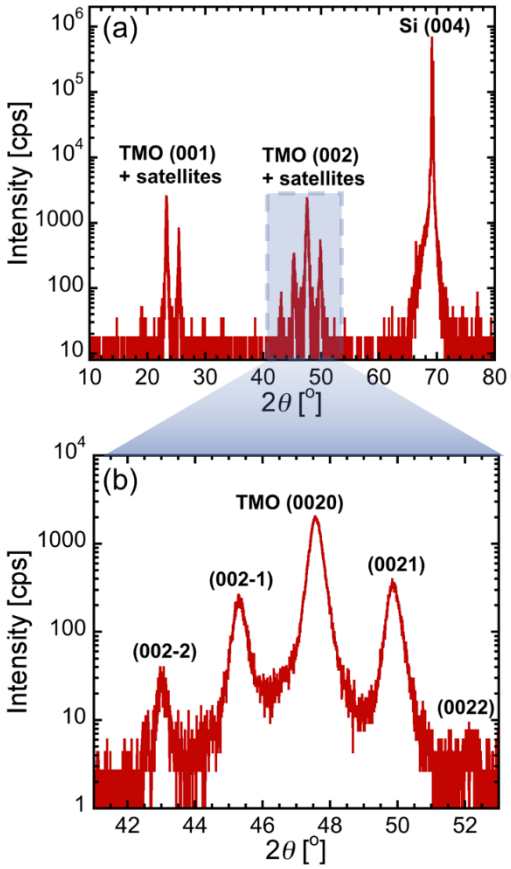

Figure 5.3: (a) Out-of-plane θ-2θ XRD scan of a ten-period, four unit cell-well STO/LAO QW heterostructure on silicon. Clear superlattice peaks are seen around the TMO (001) and (002) peaks. The strong silicon substrate peak is also observed at approximately $2\theta = 69°$. (b) High-resolution θ-2θ XRD scan around the TMO (002) peak showing clear superlattice peaks. The fourth plane index represents the order of the superlattice peak (e.g., (0022) is the 2nd-order superlattice peak around the TMO (002) Bragg peak).

The rocking curve around the TMO (002) Bragg peak (labeled as (0020) in Figure 5.3b) was also measured (Figure 5.4). The rocking curve data can be nicely fit with a Gaussian function from which a FWHM ($\Delta\omega$) of approximately 0.8° is extracted. The FWHM of the measured silicon-integrated QW heterostructure is within the range of previously-reported thin epitaxial STO films on silicon [17], [18] but is notably larger than some reports of thick STO films on silicon [11], [12]. It is also significantly larger than that of the STO/LAO QWs grown on LAO substrates from Chapters 3 and 4 and References [24], [30].

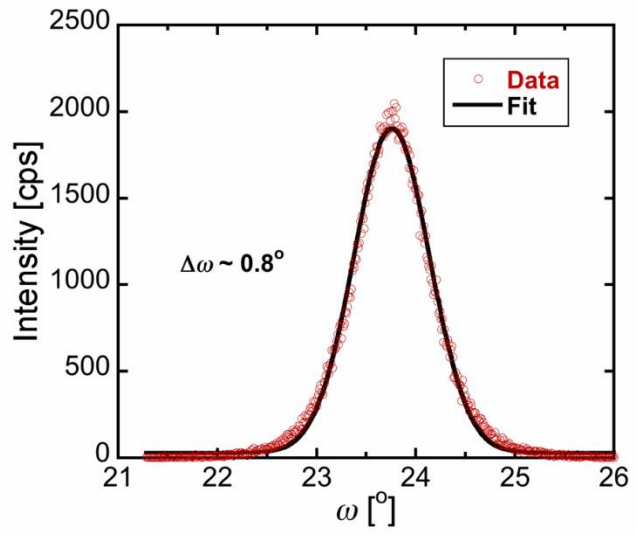

Figure 5.4: Rocking curve around the TMO (002) Bragg peak of a ten-period, four unit cell-well STO/LAO QW heterostructure on silicon. The data are represented by red, open circles while the Gaussian fit to the data is shown as a solid, black line.

As described in Section 2.3, the FWHM of the rocking curve is an indicator of a sample's crystalline quality. In particular, broad rocking curves may indicate a significant amount of misalignment between crystalline domains, also known as mosaicity. The larger mosaicity of the STO/LAO QW heterostructures deposited on silicon as compared to those deposited on LAO substrates may be the result of defects stemming from strain relaxation or stoichiometric imperfections in the TMO films. The mosaicity of thick epitaxial STO films on silicon has been shown to decrease with high-temperature oxygen annealing, likely due to the healing of such defects [11], [12]. Dedicated processing studies will likely allow for improved crystalline quality of silicon-integrated STO/LAO QW heterostructures as compared to the sample reported here.

5.4 STEM Characterization

STEM was used to map the local atomic structure of the ten-period, four unit cell-well STO/LAO QW heterostructure from Figures 5.2 – 5.4. *Z*-contrast high-angle annular dark field (HAADF) imaging (Figure 5.5) shows clear separation between the LAO barriers and STO wells throughout the heterostructure. As discussed in Section 3.4, abrupt physical and chemical separation between barrier and well layers is critical for the formation of a

confining potential in the STO wells and is thus necessary for the fabrication of TMO-based QW devices. The observation of a well-ordered STO/LAO QW heterostructure integrated on silicon is therefore encouraging from the point of view of device fabrication. From the STEM imaging, an STO well thickness of approximately 14 Å and LAO barrier thickness of approximately 28 Å is extracted. These values are in good agreement with the design values of 15.7 Å and 26.5 Å, respectively. Furthermore, the STEM-calculated period length of 42 Å agrees well with the period length of 41.8 Å calculated from XRD measurements (Figure 5.3).

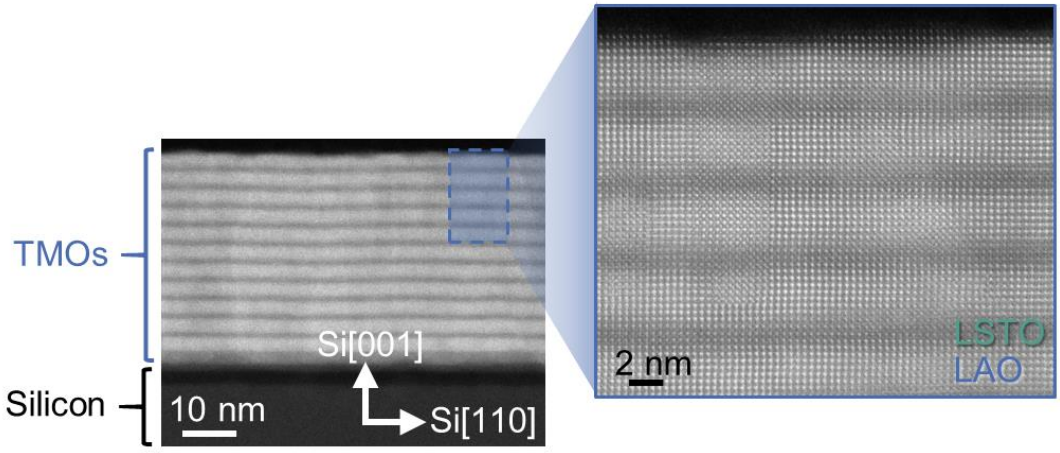

Figure 5.5: STEM imaging of a ten-period, four unit cell-well STO/LAO QW heterostructure on silicon. LAO barriers appear bright while STO wells appear darker. Some mosaicity can be clearly seen in the high-magnification image (right).

Although clear well/barrier separation is observable, some mosaicity can be clearly seen in the high-magnification image in Figure 5.5. Thus, STEM imaging has confirmed the presence of crystalline domain formation and misalignment that was inferred from the rocking curve (Figure 5.4). Notably, such mosaicity is not observed in STEM-HAADF imaging of the STO/LAO QW heterostructures grown on LAO substrates from Chapter 3 and Reference [30].

The defects apparent in the silicon-integrated STO/LAO MQW of Figure 5.5 can stem from several mechanisms, including imperfect cation stoichiometry and/or oxygen vacancies. STO, in particular, is known to easily give up oxygen [31], resulting in oxygen-deficient and perhaps defective STO films [32], [33]. Strontium vacancy clustering has also been observed in titanium-rich STO thin films [34], while evidence for oxygen vacancy clustering in oxygen-deficient STO thin films has been presented both experimentally [35] and theoretically [36]. Any of the above mechanisms could contribute to the defects observed in the silicon-integrated STO/LAO QW heterostructure. However, the prevalence of such defects can likely be significantly reduced through the systematic development of optimized growth and processing techniques for STO/LAO QWs on silicon.

In Section 5.1, I discussed the difficulties associated with epitaxially depositing oxides on the silicon surface stemming from rapid amorphization of the silicon surface in the presence of oxygen. If amorphization of the silicon surface occurs *before* film deposition, epitaxial growth is not possible. However, the high-magnification STEM image of the silicon/TMO interface in Figure 5.6 shows the interfacial structure that results when silicon amorphization occurs *after* film deposition. In the image, a thin layer (approximately 5 nm) of amorphous SiO_2 can be clearly seen between the silicon substrate and the STO buffer layer. Crystalline silicon from the substrate can be seen at the bottom of the image and the crystalline STO buffer layer and beginnings of the QW heterostructure can be seen at the top.

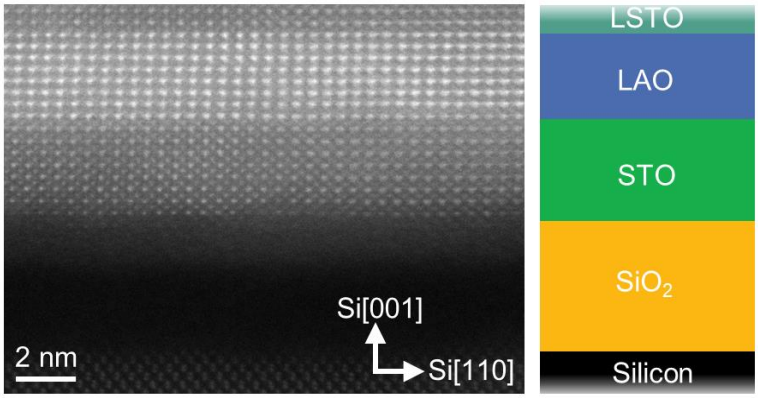

Figure 5.6: High-resolution STEM image of the interface of a ten-period, four unit cell-well STO/LAO QW heterostructure on silicon. The crystalline silicon substrate can be seen at the bottom, followed by a thin amorphous SiO_2 interlayer and the first crystalline TMO layers of the heterostructure.

The formation of the SiO_2 interlayer seen in Figure 5.6 likely begins during O_2 annealing of the STO buffer layer (Section 5.2). Silicon oxidation may also occur during the initial deposition of the first LAO barrier, as a relatively high oxygen pressure of approximately $1 - 5 \times 10^{-6}$ Torr is used for LAO growth. STO films have a fairly high oxygen diffusivity [22], [37], permitting oxygen from the growth chamber to react with the silicon surface and form SiO_2 even after deposition of an STO buffer layer. If necessary, the SiO_2 interlayer thickness can be minimized and even eliminated by modifying the growth procedure of both the STO buffer layer [22], [23] and the subsequent LAO barrier layer [14].

Depending on the intended device application, the SiO_2 interlayer may or may not be a significant factor in device performance. For the case of silicon-integrated TMOs as high-κ gate dielectrics (Section 1.1), it is critical to form abrupt silicon/TMO interfaces without an SiO_2 interlayer [38]. However, for many optical devices, including in integrated photonics applications, the SiO_2 interlayer will likely have a negligible impact on device performance [16]. In fact, the SiO_2 interlayer may even prove beneficial in some geometries. It has been noted [6] that TMO thin films for use in integrated photonic and electro-optic applications exhibit improved electrical and optical isolation when integrated

with SiO_2 rather than directly on silicon. This suggests the intriguing possibility of purposely growing a thick SiO_2 interlayer beneath epitaxial, silicon-integrated TMO thin films as a method of improving the performance of integrated photonic and electro-optic devices. Work is ongoing at UT in exploration of this possibility.

5.5 Mechanism of Integration and Extension to Other TMO Systems

As first discussed in Chapter 3, the growth of high-quality, arbitrarily thick STO/LAO heterostructures has presented a consistent challenge to oxide researchers. The STO/LAO system's characteristic interfacial defects, arising in large part from the polar nature of LAO, have been shown to compound during long growth cycles and lead to the eventual instability of the heterostructures [39]. The work presented in Chapter 3 showed a solution to this problem of growth and demonstrated the successful growth of arbitrarily thick STO/LAO QW heterostructures on LAO substrates with excellent crystalline quality. While the exact mechanisms responsible for the improved crystalline quality and reduced interfacial roughness relative to previous reports have not been completely understood, the success can be attributed in part to the careful control of stoichiometry through a multi-step growth process in which atomic fluxes are regularly recalibrated [24]. As the results in this chapter show no evidence of thickness-dependent degradation of crystalline quality up to a heterostructure thickness of approximately 460 Å, one would expect a similar multi-step growth process to help enable the production of thick, high-quality STO/LAO QW heterostructures on silicon.

Another important consideration for the growth and design of silicon-integrated STO/LAO QW heterostructures is epitaxial strain. The thick STO/LAO MQWs from Chapters 3 and 4 utilized LAO for both the substrate and the barrier layers [24], [30]. As a result, only the STO wells were strained. For the growth of STO/LAO heterostructures on

silicon, however, the situation is different as both the wells and the barriers are strained to the silicon substrate. The LAO barrier layers experience a nominal tensile strain of approximately 1.3%, while the STO well layers are nominally compressively strained by 1.7%. While these are relatively modest strains, previous studies have demonstrated rapid lattice relaxation of strained STO thin films, especially at elevated growth temperatures [40]. Indeed, strain relaxation may already play some role in the formation of defects observed in STEM imaging (Figure 5.5). On the other hand, the close agreement between the nominal lattice constants and those determined from XRD and STEM results indicates strain relaxation is not substantial in the silicon-integrated heterostructure presented in this chapter. Perhaps the alternating layers of tensiley (LAO) and compressively (STO) strained materials, as well as the relatively thin (< 3 nm) well and barrier layers, work to keep the constituent layers of the heterostructure strained throughout the heterostructure. However, strain relaxation may become a substantial issue for the fabrication of TMO heterostructures with thicker constituent layers and/or larger lattice mismatches than those of STO/LAO and should therefore not be ignored as a design consideration.

The thermal budget of the heterostructure must also be considered when analyzing the epitaxial integration of TMO thin films on silicon. Because the integration of TMO films on silicon proceeds via an epitaxial STO buffer layer, the possibility of reactions at the STO/silicon interface is of particular concern. Significant reactions at the STO/silicon interface have been reported for growth temperatures greater than approximately 800 °C [41]–[43]. Such interfacial reactions can be observed through the appearance of additional peaks in XRD spectra as well as seen directly in STEM imaging. As the silicon-integrated heterostructure of this chapter is grown at a nominal temperature of 750 °C, quite close to the observed threshold of 800 °C, it is not clear *a priori* whether interfacial reactions between the silicon substrate and STO buffer layer will play a significant role in

heterostructure fabrication. However, there are no observable signatures of STO/silicon reactions in any of the characterization methods, including XRD (Figure 5.3) and STEM (Figures 5.5 and 5.6). The absence of interfacial reactions is likely an important explanatory factor for the successful integration of high-quality STO/LAO MQWs on silicon.

Finally, I discuss general design features that should be considered for the successful epitaxial integration of other complex TMO systems on silicon substrates. As discussed above, strain balancing is clearly an important factor. While there is no clear evidence of significant strain relaxation in the silicon-integrated STO/LAO MQWs of this chapter, large lattice mismatches between constituent oxide thin films and the silicon crystalline lattice can complicate the growth of thick, high-quality TMO heterostructures on silicon. The presence of one tensiley strained material (LAO) and one compressively strained material (STO) in the MQWs presented here is also likely beneficial for growth. The formation of an MQW structure on silicon in which both the well and barrier materials are compressively or tensiley strained would likely result in significant strain relaxation during sample growth and may lead to considerable degradation of crystalline quality as sample thickness is increased. However, it may be possible to control strain throughout the sample and circumvent the above-mentioned issues by engineering appropriately lattice-matched buffer layers atop the STO template.

Thermal considerations are also important for the monolithic integration of complex TMO heterostructures on silicon. High-temperature interfacial reactions between the silicon substrate and STO buffer layer can degrade the crystalline quality of the subsequently-deposited heterostructure. Importantly, there is no evidence for interfacial reactions in the silicon-integrated STO/LAO QW heterostructure grown at a temperature of 750 °C, outside of the SiO_2 interlayer shown in Figure 5.6. The results of this chapter

therefore indicate that TMO heterostructures requiring a growth temperature of 750 °C or less can be integrated on silicon without exceeding the thermal budget that can be tolerated by the STO/silicon interface. This observation significantly expands the universe of possible TMO materials that can be monolithically integrated on silicon for the formation of complex TMO-based devices.

5.6 REFERENCES

[1] G. E. Moore, "Cramming more components onto integrated circuits," *Electronics*, vol. 38, no. 8, 1975.

[2] D. Thomson, A. Zilkie, J. E. Bowers, T. Komljenovic, G. T. Reed, L. Vivien, D. Marris-Morini, E. Cassan, L. Virot, J.-M. Fédéli, J.-M. Hartmann, J. H. Schmid, D.-X. Xu, F. Boeuf, P. O'Brien, G. Z. Mashanovich, and M. Nedeljkovic, "Roadmap on silicon photonics," *J. Opt.*, vol. 18, no. 7, p. 073003, Jul. 2016.

[3] F. Eltes, M. Kroh, D. Caimi, C. Mai, Y. Popoff, G. Winzer, D. Petousi, S. Lischke, J. E. Ortmann, L. Czornomaz, L. Zimmermann, J. Fompeyrine, and S. Abel, "A novel 25 Gbps electro-optic Pockels modulator integrated on an advanced Si photonic platform," in *2017 IEEE International Electron Devices Meeting (IEDM)*, 2017, p. 24.5.1-24.5.4.

[4] J. E. Ortmann, F. Eltes, D. Caimi, and S. Abel, "Electric Field Tuning of $BaTiO_3$-on-Silicon Multi-Ring Resonators via the Pockels Effect," in *2018 IEEE 15th International Conference on Group IV Photonics (GFP)*, 2018, no. c, pp. 1–2.

[5] A. Messner, F. Eltes, P. Ma, S. Abel, B. Baeuerle, A. Josten, W. Heni, D. Caimi, J. Fompeyrine, and J. Leuthold, "Integrated Ferroelectric $BaTiO_3$/Si Plasmonic Modulator for 100 Gbit/s and Beyond," in *Optical Fiber Communication Conference*, 2018, vol. Part F84-O, no. c, p. M2I.6.

[6] S. Abel, F. Eltes, J. E. Ortmann, A. Messner, P. Castera, T. Wagner, D. Urbonas, A. Rosa, A. M. Gutierrez, D. Tulli, P. Ma, B. Baeuerle, A. Josten, W. Heni, D. Caimi, L. Czornomaz, A. A. Demkov, J. Leuthold, P. Sanchis, and J. Fompeyrine, "Large Pockels effect in micro- and nanostructured barium titanate integrated on silicon," *Nat. Mater.*, vol. 18, no. 1, pp. 42–47, Jan. 2019.

[7] B. E. Deal and A. S. Grove, "General Relationship for the Thermal Oxidation of Silicon," *J. Appl. Phys.*, vol. 36, no. 12, pp. 3770–3778, Dec. 1965.

[8] R. A. McKee, F. J. Walker, J. R. Conner, E. D. Specht, and D. E. Zelmon, "Molecular beam epitaxy growth of epitaxial barium silicide, barium oxide, and barium titanate on silicon," *Appl. Phys. Lett.*, vol. 59, no. 7, pp. 782–784, Aug. 1991.

[9] R. A. McKee, F. J. Walker, and M. F. Chisholm, "Crystalline Oxides on Silicon: The First Five Monolayers," *Phys. Rev. Lett.*, vol. 81, no. 14, pp. 3014–3017, Oct. 1998.

[10] K. D. Fredrickson, H. Seo, and A. A. Demkov, "Mechanism of oxidation protection of the Si(001) surface by sub-monolayer Sr template," *J. Appl. Phys.*, vol. 120, no. 6, p. 065301, Aug. 2016.

[11] J. W. Park, S. H. Baek, C. W. Bark, M. D. Biegalski, and C. B. Eom, "Quasi-single-crystal (001) $SrTiO_3$ templates on Si," *Appl. Phys. Lett.*, vol. 95, no. 6, p. 061902, Aug. 2009.

[12] S.-H. Baek and C.-B. Eom, "Epitaxial integration of perovskite-based multifunctional oxides on silicon," *Acta Mater.*, vol. 61, no. 8, pp. 2734–2750, May 2013.

[13] W. A. Doolittle, A. G. Carver, and W. Henderson, "Molecular beam epitaxy of complex metal-oxides: Where have we come, where are we going, and how are we going to get there?," *J. Vac. Sci. Technol. B Microelectron. Nanom. Struct.*, vol. 23, no. 3, p. 1272, 2005.

[14] J. W. Reiner, A. Posadas, M. Wang, M. Sidorov, Z. Krivokapic, F. J. Walker, T. P. Ma, and C. H. Ahn, "Electrical properties and interfacial structure of epitaxial $LaAlO_3$ on Si (001)," *J. Appl. Phys.*, vol. 105, no. 12, p. 124501, Jun. 2009.

[15] S. Abel, T. Stöferle, C. Marchiori, C. Rossel, M. D. Rossell, R. Erni, D. Caimi, M. Sousa, A. Chelnokov, B. J. Offrein, and J. Fompeyrine, "A strong electro-optically active lead-free ferroelectric integrated on silicon," *Nat. Commun.*, vol. 4, no. 1, p. 1671, Dec. 2013.

[16] C. Xiong, W. H. P. Pernice, J. H. Ngai, J. W. Reiner, D. Kumah, F. J. Walker, C. H. Ahn, and H. X. Tang, "Active Silicon Integrated Nanophotonics: Ferroelectric $BaTiO_3$ Devices," *Nano Lett.*, vol. 14, no. 3, pp. 1419–1425, Mar. 2014.

[17] R. Guo, Z. Wang, S. Zeng, K. Han, L. Huang, D. G. Schlom, T. Venkatesan, Ariando, and J. Chen, "Functional ferroelectric tunnel junctions on silicon," *Sci. Rep.*, vol. 5, no. 1, p. 12576, Dec. 2015.

[18] J. M. Vila-Fungueiriño, J. Gázquez, C. Magén, G. Saint-Girons, R. Bachelet, and A. Carretero-Genevrier, "Epitaxial $La_{0.7}Sr_{0.3}MnO_3$ thin films on silicon with excellent magnetic and electric properties by combining physical and chemical methods," *Sci. Technol. Adv. Mater.*, vol. 19, no. 1, pp. 702–710, Dec. 2018.

[19] J. E. Ortmann, S. Kwon, A. B. Posadas, M. J. Kim, and A. A. Demkov, "Monolithic integration of transition metal oxide multiple quantum wells on silicon (001)," *J. Appl. Phys.*, vol. 125, no. 15, p. 155302, Apr. 2019.

[20] Y. Wei, X. Hu, Y. Liang, D. C. Jordan, B. Craigo, R. Droopad, Z. Yu, A. Demkov, J. L. Edwards, and W. J. Ooms, "Mechanism of cleaning Si(100) surface using Sr

or SrO for the growth of crystalline $SrTiO_3$ films," *J. Vac. Sci. Technol. B Microelectron. Nanom. Struct.*, vol. 20, no. 4, p. 1402, 2002.

[21] A. A. Demkov, H. Seo, X. Zhang, and J. Ramdani, "Using Zintl-Klemm intermetallics in oxide-semiconductor heteroepitaxy," *Appl. Phys. Lett.*, vol. 100, no. 7, p. 071602, Feb. 2012.

[22] W. Guo, A. B. Posadas, and A. A. Demkov, "Deal-Grove-Like Thermal Oxidation of Si (001) Under an Ultrathin Layer of $SrTiO_3$," vol. Unpublished, 2019.

[23] M. Choi, A. Posadas, R. Dargis, C.-K. Shih, A. A. Demkov, D. H. Triyoso, N. David Theodore, C. Dubourdieu, J. Bruley, and J. Jordan-Sweet, "Strain relaxation in single crystal $SrTiO_3$ grown on Si (001) by molecular beam epitaxy," *J. Appl. Phys.*, vol. 111, no. 6, p. 064112, Mar. 2012.

[24] J. E. Ortmann, A. B. Posadas, and A. A. Demkov, "The MBE growth of arbitrarily thick $SrTiO_3/LaAlO_3$ quantum well heterostructures for use in next-generation optoelectronic devices," *J. Appl. Phys.*, vol. 124, no. 1, p. 015301, Jul. 2018.

[25] J. A. Mundy, C. M. Brooks, M. E. Holtz, J. A. Moyer, H. Das, A. F. Rébola, J. T. Heron, J. D. Clarkson, S. M. Disseler, Z. Liu, A. Farhan, R. Held, R. Hovden, E. Padgett, Q. Mao, H. Paik, R. Misra, L. F. Kourkoutis, E. Arenholz, A. Scholl, J. A. Borchers, W. D. Ratcliff, R. Ramesh, C. J. Fennie, P. Schiffer, D. A. Muller, and D. G. Schlom, "Atomically engineered ferroic layers yield a room-temperature magnetoelectric multiferroic," *Nature*, vol. 537, no. 7621, pp. 523–527, Sep. 2016.

[26] D. G. Schlom, L.-Q. Chen, X. Pan, A. Schmehl, and M. A. Zurbuchen, "A Thin Film Approach to Engineering Functionality into Oxides," *J. Am. Ceram. Soc.*, vol. 91, no. 8, pp. 2429–2454, Aug. 2008.

[27] P. Zubko, N. Jecklin, A. Torres-Pardo, P. Aguado-Puente, A. Gloter, C. Lichtensteiger, J. Junquera, O. Stéphan, and J.-M. Triscone, "Electrostatic Coupling and Local Structural Distortions at Interfaces in Ferroelectric/Paraelectric Superlattices," *Nano Lett.*, vol. 12, no. 6, pp. 2846–2851, Jun. 2012.

[28] K. Zhao, G. Chen, B.-S. Li, and A. Shen, "Mid-infrared intersubband absorptions in ZnO/ZnMgO multiple quantum wells," *Appl. Phys. Lett.*, vol. 104, no. 21, p. 212104, May 2014.

[29] M. Choi, A. B. Posadas, C. A. Rodriguez, A. O'Hara, H. Seinige, A. J. Kellock, M. M. Frank, M. Tsoi, S. Zollner, V. Narayanan, and A. A. Demkov, "Structural, optical, and electrical properties of strained La-doped $SrTiO_3$ films," *J. Appl. Phys.*, vol. 116, no. 4, p. 043705, Jul. 2014.

[30] J. E. Ortmann, N. Nookala, Q. He, L. Gao, C. Lin, A. B. Posadas, A. Y. Borisevich, M. A. Belkin, and A. A. Demkov, "Quantum Confinement in Oxide Heterostructures: Room-Temperature Intersubband Absorption in $SrTiO_3/LaAlO_3$ Multiple Quantum Wells," *ACS Nano*, vol. 12, no. 8, pp. 7682–7689, Aug. 2018.

[31] A. B. Posadas, K. J. Kormondy, W. Guo, P. Ponath, J. Geler-Kremer, T. Hadamek, and A. A. Demkov, "Scavenging of oxygen from $SrTiO_3$ during oxide thin film deposition and the formation of interfacial 2DEGs," *J. Appl. Phys.*, vol. 121, no. 10, p. 105302, Mar. 2017.

[32] K. J. Kormondy, L. Gao, X. Li, S. Lu, A. B. Posadas, S. Shen, M. Tsoi, M. R. McCartney, D. J. Smith, J. Zhou, L. L. Lev, M.-A. Husanu, V. N. Strocov, and A. A. Demkov, "Large positive linear magnetoresistance in the two-dimensional t_{2g} electron gas at the EuO/$SrTiO_3$ interface," *Sci. Rep.*, vol. 8, no. 1, p. 7721, Dec. 2018.

[33] W. Guo, A. B. Posadas, S. Lu, D. J. Smith, and A. A. Demkov, "EuO epitaxy by oxygen scavenging on $SrTiO_3$ (001): Effect of $SrTiO_3$ thickness and temperature," *J. Appl. Phys.*, vol. 124, no. 23, p. 235301, Dec. 2018.

[34] Y. Tokuda, S. Kobayashi, T. Ohnishi, T. Mizoguchi, N. Shibata, Y. Ikuhara, and T. Yamamoto, "Strontium vacancy clustering in Ti-excess $SrTiO_3$ thin film," *Appl. Phys. Lett.*, vol. 99, no. 3, p. 033110, Jul. 2011.

[35] D. A. Muller, N. Nakagawa, A. Ohtomo, J. L. Grazul, and H. Y. Hwang, "Atomic-scale imaging of nanoengineered oxygen vacancy profiles in $SrTiO_3$," *Nature*, vol. 430, no. 7000, pp. 657–661, Aug. 2004.

[36] D. D. Cuong, B. Lee, K. M. Choi, H.-S. Ahn, S. Han, and J. Lee, "Oxygen Vacancy Clustering and Electron Localization in Oxygen-Deficient $SrTiO_3$: LDA + *U* Study," *Phys. Rev. Lett.*, vol. 98, no. 11, p. 115503, Mar. 2007.

[37] R. A. De Souza, "Oxygen Diffusion in $SrTiO_3$ and Related Perovskite Oxides," *Adv. Funct. Mater.*, vol. 25, no. 40, pp. 6326–6342, Oct. 2015.

[38] J. Robertson, "High dielectric constant gate oxides for metal oxide Si transistors," *Reports Prog. Phys.*, vol. 69, no. 2, pp. 327–396, Feb. 2006.

[39] N. Nakagawa, H. Y. Hwang, and D. A. Muller, "Why some interfaces cannot be sharp," *Nat. Mater.*, vol. 5, no. 3, pp. 204–209, Mar. 2006.

[40] L. S.-J. Peng, X. X. Xi, B. H. Moeckly, and S. P. Alpay, "Strain relaxation during in situ growth of $SrTiO_3$ thin films," *Appl. Phys. Lett.*, vol. 83, no. 22, p. 4592, Dec. 2003.

[41] L. V. Goncharova, D. G. Starodub, E. Garfunkel, T. Gustafsson, V. Vaithyanathan, J. Lettieri, and D. G. Schlom, "Interface structure and thermal stability of epitaxial $SrTiO_3$ thin films on Si (001)," *J. Appl. Phys.*, vol. 100, no. 1, p. 014912, Jul. 2006.

[42] G. J. Yong, R. M. Kolagani, S. Adhikari, W. Vanderlinde, Y. Liang, K. Muramatsu, and S. Friedrich, "Thermal stability of $SrTiO_3$/SiO_2/Si Interfaces at Intermediate Oxygen Pressures," *J. Appl. Phys.*, vol. 108, no. 3, p. 033502, Aug. 2010.

[43] F. Hanzig, J. Hanzig, E. Mehner, C. Richter, J. Veselý, H. Stöcker, B. Abendroth, M. Motylenko, V. Klemm, D. Novikov, and D. C. Meyer, "Crystallization

dynamics and interface stability of strontium titanate thin films on silicon," *J. Appl. Crystallogr.*, vol. 48, no. 2, pp. 393–400, Apr. 2015.

Chapter 6: Designing Integrated Electro-Optic Devices from $SrTiO_3/LaAlO_3$ Quantum Wells

6.1 Introduction to Integrated Optical and Electro-Optical Devices

Photonic integrated circuits (PICs) are the optical analogue of traditional electronic integrated circuits. Just as integrated circuits revolutionized the microelectronics industry during the 20^{th}-Century, integrated photonics promises to revolutionize many technological fields in the coming years, including data transfer, high-throughput computing and sensing [1]–[3]. The advantages of integrated photonic technologies are numerous, including drastic weight reduction relative to traditional microelectronics and the potential for high-speed and ultra-low power operation. Amongst integrated photonics technologies, silicon photonics is of particular interest due to its inherent CMOS compatibility, leading to drastically reduced manufacturing costs relative to non-CMOS photonic technologies.

Fully extending the analogy of PICs to integrated electronics, one can infer the devices necessary for the development of wholly functional PICs. At the most basic level, a self-contained photonic circuit would require an integrated light source, waveguides to shuttle the optical signal around the chip, and an integrated photo-detector. Additional elements will also be necessary depending on the intended applications of the PIC. For the case of computing or data transfer, for example, some method of generating bits will be required (in analogy with a MOSFET). This is typically handled through the construction of an electro-optic modulator or switch.

An electro-optic device is one in which there is some coupling between optical and electrical signals. With the exception of waveguides, all the devices mentioned above for PIC development require such a coupling. However, the necessity of incorporating electro-optic devices into PICs presents a challenge for silicon photonics. While silicon is well-

developed as a waveguiding material, it has relatively weak optical nonlinearities compared to many other materials [4]–[9]. While useful optical nonlinearities can be engineered in silicon, they often require high operating voltages, large power consumption, or lattice strain [10]–[16]. Therefore, it is desirable to integrate other materials with strong electro-optic responses into silicon photonics platforms.

QWs offer an excellent geometry for the construction of a wide variety of electro-optic devices. For example, quantum cascade lasers [17] and quantum well photodetectors [18] are potential candidates for integrated light sources and photodetectors, respectively, in a PIC. Furthermore, electro-optic modulators and switches can be fabricated from QWs by utilizing the quantum-confined Stark effect for electro-optic coupling [19]–[21].

While the above-mentioned QW devices have all been demonstrated previously, they typically operate in the mid-infrared region due to the limited potential well depth in traditional semiconductor heterostructures. The relatively low operating energy of QW devices fabricated from traditional semiconductors presents a problem for the incorporation of such materials into PICs, as most photonic applications must operate in the near-infrared. Specifically, wavelengths of 1300 nm and 1550 nm are standard wavelengths in photonic technologies due to the absorption-free characteristics of optical fibers at these wavelengths. The deep potential wells of the STO/LAO system offer the possibility of pushing the operating energy range of QW electro-optic devices into the near-infrared. When combined with their silicon integrability, STO/LAO QWs would appear to be an excellent candidate for use in next-generation integrated electro-optic devices in PIC technologies.

In this chapter, I explore the possibility of fabricating integrated optical and electro-optical devices from the STO/LAO materials system. As I have already demonstrated the potential to integrate STO/LAO QWs with silicon, the optical and electro-optical

characteristics of such devices are of particular interest in order to move forward with this technology. The ability to electrically influence the optical characteristics of STO/LAO QWs via the quantum-confined Stark effect is studied numerically in Section 6.3, after a brief introduction to the physics of the quantum-confined Stark effect in Section 6.2. Then, I consider the necessary parameters for waveguide design and calculate relevant figures of merit in Sections 6.4 and 6.5. Finally, in Section 6.6, I present simulations of the electro-optic performance of an experimentally-realizable STO/LAO electro-optic modulator operating in the near-infrared. The results of this chapter indicate the feasibility of experimentally realizing integrated STO/LAO-based electro-optic devices for use in PIC technologies.

6.2 THE QUANTUM-CONFINED STARK EFFECT

The quantum-confined Stark effect describes the electric field-induced shift in quantized energy levels of particles confined in a potential well [22]. The electric field alters the shape of the potential well, which in turn alters the eigenvalues of the Schrödinger equation (i.e., the quantized energy levels). The Schrödinger equation cannot typically be solved analytically for the case of a QW in an applied electric field, but second-order perturbation theory can be used to estimate the shift of the confined energy levels due to a small electric field [23].

For the case of a small electric field (i.e., $eFL << E_1$, where e is the electron charge, F is the applied electric field strength, L is the QW width, and E_1 is the ground-state energy), only the lowest confined state is shifted in response to the field. This is because the higher-order states are primarily confined by the vertical walls of the potential well, which are not altered by the application of field. In contrast, the ground-state is sensitive

to the slope of the bottom of the potential well, which is altered by the field. The shift of the ground-state energy level ΔE_1 calculated from perturbation theory is [23], [24]

$$\Delta E_1 = -C\frac{m^* e^2 F^2 L^4}{\hbar^2}, \tag{6.1}$$

where C is a constant, m^* is the electron effective mass, and $\hbar$ is the reduced Plank's constant. Thus, the electric field-induced shift in the ground-state energy level is quadratic in field for small applied field strengths.

The negative shift of the ground-state energy results in a blue shift of intersubband transition energy. This is in contrast to the case of interband transitions, in which the quantum-confined Stark shift results in a red shift of the transition energy [23]. As the electric field strength is increased, the initial quadratic dependence of energy shift on applied field becomes linear [24]–[27]. For very high fields, the ground-state-to-first-excited-state transition energy becomes independent of QW width as the two lowest-energy states become effectively confined in a triangular potential due to the large slope of the bottom of the potential well [23]. The quantum-confined Stark effect in intersubband transitions was initially measured by Harwit and Harris in 1987 using GaAs QWs [19].

In addition to shifting the energy levels of the quantized states, the application of an electric field across the QW also breaks the well's inversion symmetry and removes the parity-change selection rules introduced in Section 4.1. The deformation of the potential well decreases the overlap between the ground-state and first-excited-state and therefore reduces the oscillator strength s_{12} calculated from Equation (4.8). Because the oscillator strength obeys the summation rule [23]

$$\sum_{n'} s_{nn'} = 1, \tag{6.2}$$

the reduction of s_{12} oscillator strength must result in the increase of the oscillator strength of other ground-state-to-excited-state intersubband transitions.

6.3 Quantum-Confined Stark Effect in $SrTiO_3/LaALO_3$ Quantum Wells

The wave functions in an STO/LAO QW were calculated using a self-consistent Poisson-Schrödinger solver [28], [29]. The calculated electronic wave functions in an STO/LAO QW with a six unit cell-thick well layer (Figure 6.1a) show that the energy spacing between confined states can significantly exceed 1 eV and enter the near-IR. The effect of an external electric field E_{ext} on the wave functions can also be observed. As expected, the ground state wave function experiences the most significant change in energy $\Delta E_1 \approx 250$ meV as a result of the quantum-confined Stark effect. The shift in energy of the confined states is also clearly seen in the near-infrared absorption spectrum of the QW (Figure 6.1b), calculated according to the method presented in [23]. Notably, the ground-state-to-third-excited state transition ($|1\rangle \rightarrow |4\rangle$) is predicted to occur near the common telecom wavelength of approximately 1550 nm. In the calculation of the absorption spectrum shown in Figure 6.1b, I have considered the case where the QW is doped such as to only populate the ground state.

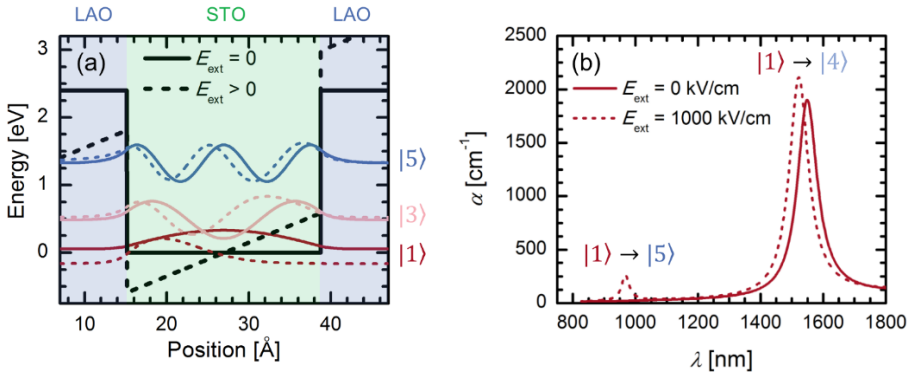

Figure 6.1: (a) Calculated electronic wave functions in a six unit cell-thick STO QW without (solid lines) and with (dashed lines) an applied electric field. The electric field is set to 5×10^8 V/m. For clarity, only the ground-, second-excited, and fourth-excited states are shown. An effective mass of $m^* = 1.02m_e$ is assumed for the calculations. (b) Calculated absorption spectrum of the QW from panel (a) without (solid line) and with (dashed line) applied electric field. Absorption values are calculated for a single QW. The corresponding transitions are noted above the absorption peaks.

While a six unit cell-thick STO QW is predicted to produce intersubband transitions near 1550 nm, transitions near the other critical telecom wavelength of 1300 nm can likely also be realized by utilizing other QW geometries. For example, Poisson-Schrödinger calculations suggest a transition energy of approximately 1300 nm in a two unit cell-thick STO QW (Figure 6.2a). Such a narrow well confines just two electronic states, leaving the $|1\rangle \rightarrow |2\rangle$ transition as the only possibility. However, because the ground state wave function is pushed farther from the conduction band bottom as the well becomes narrower, the magnitude of ΔE_1 is smaller for the two unit cell-well than for the six unit cell-well for a given electric field strength (Figure 6.2b). This observation is consistent with the power-law proportionality of ΔE_1 to QW width L given in Equation (6.1). As a result, the utility of such narrow structures in devices requiring electro-optic switching will be limited as the fields required for switching can become prohibitively large.

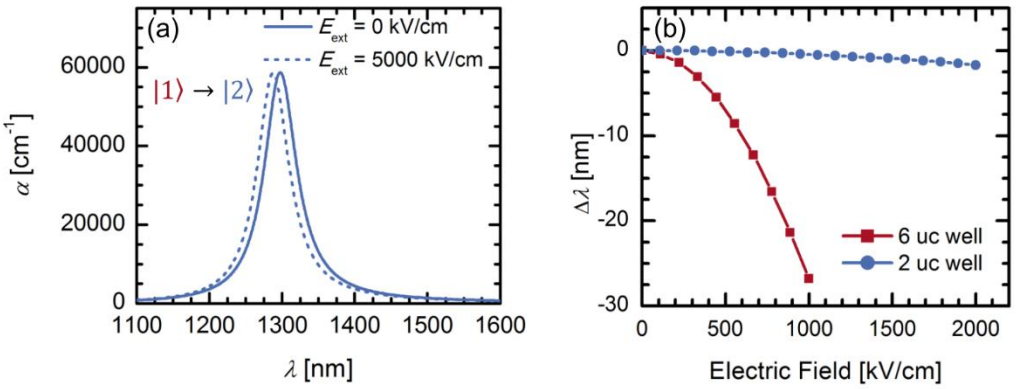

Figure 6.2: (a) Calculated absorption spectrum of a two unit cell-thick STO QW without (solid line) and with (dashed line) applied electric field. Absorption values are calculated for a single QW. An effective mass of $m^* = 1.02m_e$ is assumed for the calculations. (b) Wavelength shift of the $|1\rangle \rightarrow |2\rangle$ transition as a function of applied electric field for a six unit cell-well (red squares) and a two unit cell-well (blue circles) STO QW.

It should be noted that there is some uncertainty in the predicted intersubband transition energies arising from uncertainty in the electron effective mass within the STO QW. The effective mass in STO can vary as a function of doping [30], [31] and strain [32] and is also band-dependent [33]. However, the calculated values reported here represent a good approximation to the expected intersubband transition energies as I have assumed an effective mass value in the calculations ($m^* = 1.02m_e$) that is consistent with the latest theoretical and experimental results for strained, lightly La-doped STO films [31].

6.4 Waveguide Concept and Design Considerations

One of the fundamental components of any PIC is the optical waveguide. Thus, it is necessary to establish a waveguiding geometry incorporating STO/LAO QWs before they can be integrated into PIC technologies. When designing an integrated STO/LAO waveguide or electro-optic device, several design parameters must be taken into account. Firstly, the waveguide must support a transverse magnetic (TM) optical mode. Due to the polarization selection rule (Section 4.1 and [23], [34], [35]), intersubband transitions can only be induced by the component of the optical electric field that is normal to the plane of the wells. Therefore, any devices hoping to make use of intersubband absorptions for operation, such as electro-optic modulators, switches, or photodetectors, must support a TM optical mode. Secondly, an electro-optic device built from QWs must allow for an external electric field to be applied normal to the QW layers. Only components of the external electric field normal to the QW layers will alter the confining potential and lead to Stark shifts of intersubband transition energies.

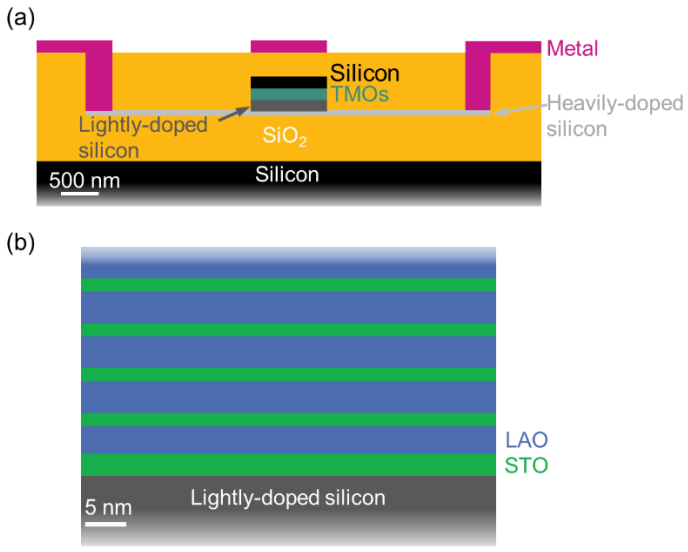

Figure 6.3: (a) Proposed waveguide and device structure for STO/LAO-based electro-optic devices. Fabrication would proceed similarly to that described in [6]. (b) Zoom-in of STO/LAO QW heterostructure integrated on lightly-doped silicon electrode via an epitaxial STO buffer layer.

One proposed device structure (Figure 6.3a) features an STO/LAO QW superlattice epitaxially integrated on lightly-doped silicon (Figure 6.3b) to form a hybrid TMO-silicon waveguide. The lightly-doped silicon layer can then be used as an integrated bottom electrode [6], reducing the distance between the electrodes and thereby reducing the voltage required to realize a given electric field across the QWs. The resulting external electric field is normal to the QWs, allowing for the realization of electric field-deformation of the confining potential and quantum-confined Stark shifts of quantized states. Furthermore, the hybrid TMO-silicon waveguide supports a TM mode (Figure 6.4), allowing for the optical stimulation of intersubband transitions.

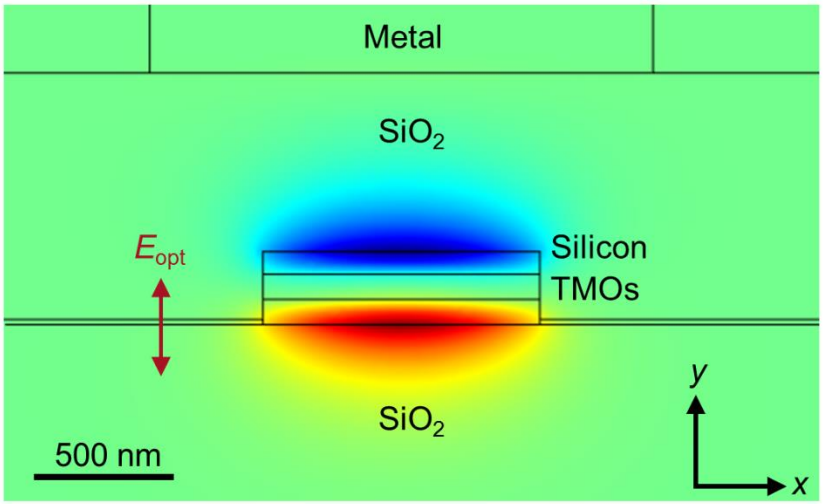

Figure 6.4: Simulated optical mode within the hybrid TMO-silicon waveguide shown schematically in Figure 6.3. The optical electric field E_{opt} is in the *y* direction, corresponding to a TM mode. The waveguide width was taken to be 1 μm, top silicon thickness was taken to be 90 nm and TMO thickness was taken to be 100 nm. The color scale represents the *z* component of the optical electric field where green is zero field, blue is large negative field and red is large positive field.

6.5 Electro-Optic Overlap and Optical Confinement

Two figures of merit are particularly important when evaluating the performance of an electro-optic device such as the one proposed above in Figure 6.3: the electro-optic overlap integral Γ_{EO} and the optical confinement in the electro-optically active TMO layer Γ_{TMO}. The electro-optic overlap Γ_{EO} is a normalized measure of the interaction between the optical mode confined in the waveguide and the external electric field and is defined as [36]

$$\Gamma_{EO} = \frac{S}{V} \frac{\iint E_{opt}^2(x,y) E_{ext}(x,y)\, dx\, dy}{\iint E_{opt}^2(x,y)\, dx\, dy}, \tag{6.3}$$

where *S* is the distance between the top and bottom electrodes, *V* is the applied voltage, E_{ext} is the external electric field and E_{opt} is the electric field of the confined optical mode. The

integrals are both taken over the entire (two-dimensional) cross-section of the device. A larger Γ_{EO} value indicates greater overlap between the applied electric field and the optical mode and therefore more efficient electro-optic operation.

The TMO optical confinement Γ_{TMO} is a normalized measure of the amount of the optical signal present in the electro-optically active TMO layer and is defined as

$$\Gamma_{TMO} = \frac{\iint_{TMO} E_{opt}^2(x,y)\,dx\,dy}{\iint_{All} E_{opt}^2(x,y)\,dx\,dy}, \tag{6.4}$$

where the integral in the numerator is only evaluated over the area of the TMO layer while the integral in the denominator is evaluated over the entire device area. Γ_{TMO} therefore indicates the relative fraction of the optical mode that is available to interact with confined electrons in the QW (e.g., for absorption). In an absorption-based device such as a modulator or a switch, Γ_{TMO} manifests itself in the extinction ratio of the optical absorption as light that is not confined within the TMO layer will not be absorbed and will therefore contribute to the background output optical signal.

Both Γ_{EO} and Γ_{TMO} can be modified by changing the waveguide width w_{WG} and the thickness of the top silicon layer t_{WG} (Figure 6.5). In general, there is a tradeoff between the two figures of merit, with Γ_{EO} increasing and Γ_{TMO} decreasing as the top silicon thickness is increased. This tradeoff can be easily explained by the changing mode shape associated with altering the waveguide dimensions. As the top silicon is made thicker, the optical mode is pulled more into the silicon, decreasing Γ_{TMO}. At the same time, the mode becomes more confined laterally due to the large index contrast between silicon and the surrounding materials, increasing the electro-optic overlap integral Γ_{EO}. The lateral confinement of the mode also increases as the waveguide width decreases, resulting in the observed behavior of increasing Γ_{EO} as w_{WG} decreases for a given t_{WG}. The calculated

values of Γ_{TMO} are competitive with other TMO-based electro-optic devices [9] while the calculated values of Γ_{EO} are somewhat smaller [37]. However, it should be noted that the exact values of Γ_{EO} and Γ_{TMO} are dependent on the specific device design one chooses, which may differ from the one suggested in Figure 6.3.

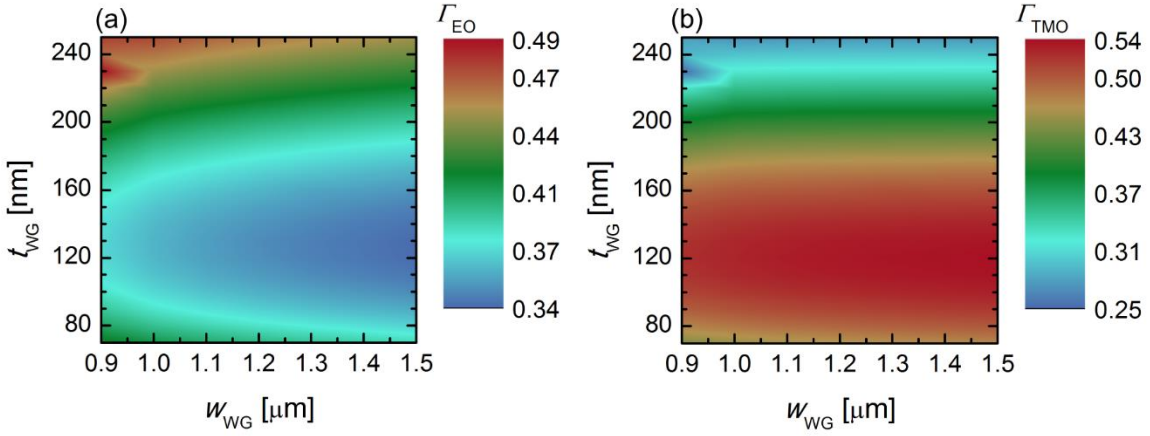

Figure 6.5: (a) Electro-optic overlap Γ_{EO} and (b) TMO optical confinement Γ_{TMO} as a function of waveguide width w_{WG} and top silicon thickness t_{WG}. The TMO heterostructure thickness is taken to be 100 nm.

In addition to the waveguide dimensions, the thickness of the TMO heterostructure t_{TMO} also impacts Γ_{TMO} with thicker heterostructures resulting in increased optical confinement within the TMO layer (Figure 6.6.). In principle, the epitaxial deposition of STO/LAO QW heterostructures of arbitrary thickness should be possible [38], although the exploration of such structures on silicon substrates has only begun rather recently [39]. In any case, by controlling the waveguide dimensions and TMO thickness, one can control the device performance as characterized by the electro-optic overlap Γ_{EO} and the TMO optical confinement Γ_{TMO}.

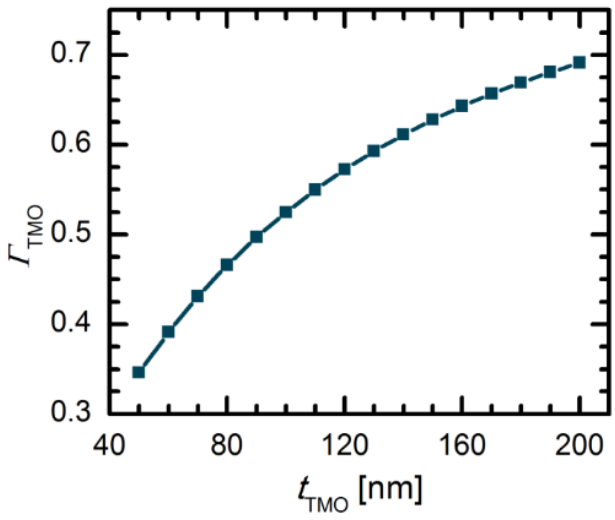

Figure 6.6: Simulated TMO optical confinement Γ_{TMO} in the device structure presented in Figure 6.3 as a function of total STO/LAO QW heterostructure thickness t_{TMO}. Here, w_{WG} = 1 μm and t_{WG} = 90 nm.

6.6 Example Application: Electro-Optic Modulator

As a specific example of an electro-optic device exploiting the quantum-confined Stark effect in the STO/LAO system, I consider an electro-optic modulator utilizing the device geometry presented in Figure 6.3. Such a modulator could operate in the near-IR where the modulated signal is given by the electric field-induced change in optical absorption at a given wavelength, as calculated e.g. in Figure 6.1b or Figure 6.2a. The quantum-confined Stark effect is an excellent mechanism for the construction of an electro-optic modulator due to the high-speed nature of the electric field-induced energy level shifts [40]. High-speed operation should therefore be possible in such a device, a critical feature of next-generation electro-optic modulators [8], [41].

The modulation energy E of an electro-optic modulator in units of J/bit is given by

$$E = \frac{1}{4} C V_D^2, \tag{6.5}$$

where C is the device capacitance and V_D is the drive voltage [42]. From Equation (6.5), one can see that the energy consumption is dependent upon the electrical properties of the device. Therefore, the electrode geometry controls the energy consumption of an electro-optic modulator insofar as the electrode geometry impacts the device capacitance and the needed drive voltage. For the device geometry in Figure 6.3, V_D is tied to the vertical waveguide-to-electrode distance S, while C is related to both S and the lateral waveguide-to-electrode spacing d. By appropriately tuning S and d, the modulation energy can be minimized (Figure 6.7a). However, by bringing the electrodes closer to the waveguide, one may induce additional optical absorption $\Delta\beta_{el}$ due to the interaction between the optical mode and the metallic electrodes (Fig. 7b).

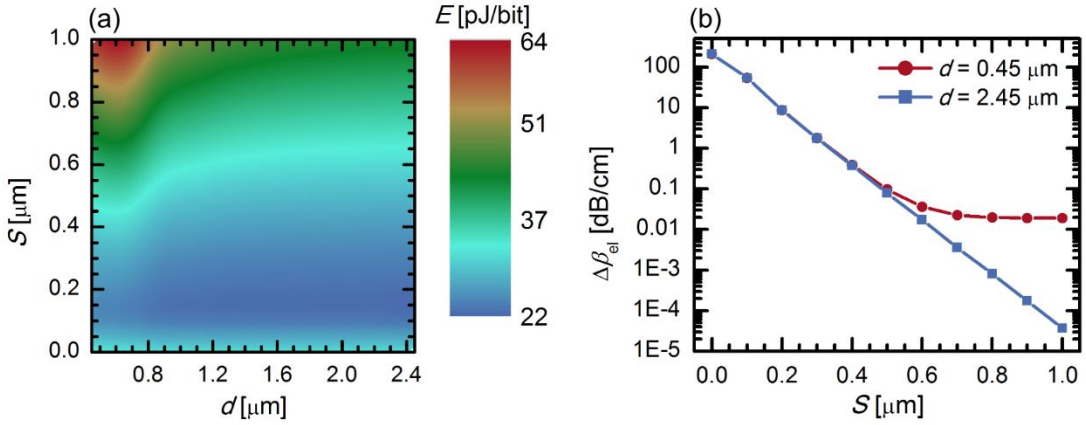

Figure 6.7: (a) Calculated switching energy E of an STO/LAO electro-optic modulator as a function of lateral and vertical waveguide-to-electrode spacing, d and S, respectively. Calculations assume electrode lengths of 100 μm and an electric field of 1000 kV/cm across the STO/LAO layer for switching. (b) Calculated additional optical absorption due to the electrodes $\Delta\beta_{el}$ as a function of S for d = 0.45 μm (red circles) and d = 2.45 μm (blue squares).

The calculations presented in Figure 6.7 suggest that the lateral waveguide-to-electrode distance d should be made large when constructing an electro-optic modulator using the design shown in Figure 6.3. A large value of d minimizes the capacitance between

electrodes in the lateral direction, thereby reducing the switching energy. Furthermore, for $S > 0.4$ μm, a larger value of d corresponds to reduced optical absorption from the electrodes, while the optical absorption is dominated by the top electrode regardless of the lateral electrode spacing for $S \leq 0.4$ μm.

While the exact values of switching energy are dependent on extrinsic factors, such as device length and electrode design, the calculations presented in this chapter suggest switching energies on the order of pJ/bit are possible in the STO/LAO electro-optic modulator studied. This value is competitive with switching energies in some silicon Mach-Zehnder modulators [43], [44], although recent reports of compact silicon ring modulators have reduced the switching energy considerably into the sub-fJ/bit range [15]. The switching energies in STO/LAO modulators are primarily dependent on the rather high electric fields needed to sufficiently modulate the optical absorption energy. By optimizing modulator design such that the voltage needed to reach the switching field can be reduced, the switching energy can be significantly reduced.

The proposed STO/LAO electro-optic modulators also have the advantage that they could likely be fabricated with a relatively small device footprint. Lateral device sizes of approximately 3 μm should be possible, with the lateral electrode spacing and the waveguide width defining the critical feature sizes in the lateral direction. Additionally, only a single, straight waveguide is necessary for the operation such a device. This contrasts with ring resonators or Mach-Zehnder interferometers in which interference of the optical signals between two or more waveguides is required, thereby increasing device footprint. The straight, narrow geometry of the proposed STO/LAO electro-optic modulators should therefore allow for dense device packing.

In this chapter, I have presented calculations supporting the feasibility of producing integrated electro-optic devices operating at terahertz optical frequencies based on the

STO/LAO materials system. Such devices achieve electro-optic operation by utilizing the quantum-confined Stark effect (Sections 6.2 and 6.3) to modulate the energy of intersubband transitions in the STO conduction band and could be constructed using existing thin film growth and semiconductor processing techniques. As a specific example, I present calculations of the switching energy in an STO/LAO electro-optic modulator integrated on silicon. Such modulators have the potential for high-speed operation due to the short time scales needed for electronic energy level modulation by the quantum-confined Stark effect. Additionally, electro-optic devices based on the Stark effect can be engineered for low power operation because the Stark effect is field-driven and does not necessitate current flow for operation. The results of this chapter, when combined with those from the previous chapters, open the door for the fabrication of novel integrated electro-optic devices capable of operating in the near-IR. Furthermore, they suggest the possibility of integrating a wide range of TMO thin films and heterostructures into electro-optic device architectures in order to take advantage of the multitude of emergent phenomena in such materials.

6.7 REFERENCES

[1] K. Yamada, Y. Urino, T. Nakamura, and Y. Arakawa, "Integrated Silicon-based Optical Interconnect for Fast, Compact, Energy-efficient Electronic Circuit Systems," *NTT Tech. Rev.*, vol. 11, no. 2, 2010.

[2] K. Yamada, T. Tsuchizawa, H. Nishi, R. Kou, T. Hiraki, K. Takeda, H. Fukuda, Y. Ishikawa, K. Wada, and T. Yamamoto, "High-performance silicon photonics technology for telecommunications applications," *Sci. Technol. Adv. Mater.*, vol. 15, no. 2, p. 024603, Apr. 2014.

[3] D. Thomson, A. Zilkie, J. E. Bowers, T. Komljenovic, G. T. Reed, L. Vivien, D. Marris-Morini, E. Cassan, L. Virot, J.-M. Fédéli, J.-M. Hartmann, J. H. Schmid, D.-X. Xu, F. Boeuf, P. O'Brien, G. Z. Mashanovich, and M. Nedeljkovic, "Roadmap on silicon photonics," *J. Opt.*, vol. 18, no. 7, p. 073003, Jul. 2016.

[4] R. Soref and B. Bennett, "Electrooptical effects in silicon," *IEEE J. Quantum Electron.*, vol. 23, no. 1, pp. 123–129, Jan. 1987.

[5] J. Leuthold, C. Koos, and W. Freude, “Nonlinear silicon photonics,” *Nat. Photonics*, vol. 4, no. 8, pp. 535–544, Aug. 2010.

[6] L. Chen, M. G. Wood, and R. M. Reano, “12.5 pm/V hybrid silicon and lithium niobate optical microring resonator with integrated electrodes,” *Opt. Express*, vol. 21, no. 22, p. 27003, Nov. 2013.

[7] S. Abel, T. Stöferle, C. Marchiori, C. Rossel, M. D. Rossell, R. Erni, D. Caimi, M. Sousa, A. Chelnokov, B. J. Offrein, and J. Fompeyrine, “A strong electro-optically active lead-free ferroelectric integrated on silicon,” *Nat. Commun.*, vol. 4, no. 1, p. 1671, Dec. 2013.

[8] F. Eltes, M. Kroh, D. Caimi, C. Mai, Y. Popoff, G. Winzer, D. Petousi, S. Lischke, J. E. Ortmann, L. Czornomaz, L. Zimmermann, J. Fompeyrine, and S. Abel, “A novel 25 Gbps electro-optic Pockels modulator integrated on an advanced Si photonic platform,” in *2017 IEEE International Electron Devices Meeting (IEDM)*, 2017, p. 24.5.1-24.5.4.

[9] S. Abel, F. Eltes, J. E. Ortmann, A. Messner, P. Castera, T. Wagner, D. Urbonas, A. Rosa, A. M. Gutierrez, D. Tulli, P. Ma, B. Baeuerle, A. Josten, W. Heni, D. Caimi, L. Czornomaz, A. A. Demkov, J. Leuthold, P. Sanchis, and J. Fompeyrine, “Large Pockels effect in micro- and nanostructured barium titanate integrated on silicon,” *Nat. Mater.*, vol. 18, no. 1, pp. 42–47, Jan. 2019.

[10] G. T. Reed, G. Mashanovich, F. Y. Gardes, and D. J. Thomson, “Silicon optical modulators,” *Nat. Photonics*, vol. 4, no. 8, pp. 518–526, Aug. 2010.

[11] P. Dong, W. Qian, H. Liang, R. Shafiiha, D. Feng, G. Li, J. E. Cunningham, A. V. Krishnamoorthy, and M. Asghari, “Thermally tunable silicon racetrack resonators with ultralow tuning power,” *Opt. Express*, vol. 18, no. 19, p. 20298, Sep. 2010.

[12] B. Chmielak, M. Waldow, C. Matheisen, C. Ripperda, J. Bolten, T. Wahlbrink, M. Nagel, F. Merget, and H. Kurz, “Pockels effect based fully integrated, strained silicon electro-optic modulator,” *Opt. Express*, vol. 19, no. 18, p. 17212, Aug. 2011.

[13] P. Dong, W. Qian, H. Liang, R. Shafiiha, N.-N. Feng, D. Feng, X. Zheng, A. V. Krishnamoorthy, and M. Asghari, “Low power and compact reconfigurable multiplexing devices based on silicon microring resonators,” *Opt. Express*, vol. 18, no. 10, p. 9852, May 2010.

[14] A. H. Atabaki, A. A. Eftekhar, S. Yegnanarayanan, and A. Adibi, “Sub-100-nanosecond thermal reconfiguration of silicon photonic devices,” *Opt. Express*, vol. 21, no. 13, p. 15706, Jul. 2013.

[15] E. Timurdogan, C. M. Sorace-Agaskar, J. Sun, E. Shah Hosseini, A. Biberman, and M. R. Watts, “An ultralow power athermal silicon modulator,” *Nat. Commun.*, vol. 5, no. 1, p. 4008, Dec. 2014.

[16] C. L. Manganelli, P. Pintus, and C. Bonati, "Modeling of strain-induced Pockels effect in Silicon," *Opt. Express*, vol. 23, no. 22, p. 28649, Nov. 2015.

[17] J. Faist, F. Capasso, D. L. Sivco, C. Sirtori, A. L. Hutchinson, and A. Y. Cho, "Quantum Cascade Laser," *Science (80-.).*, vol. 264, no. 5158, pp. 553–556, Apr. 1994.

[18] B. F. Levine, "Quantum-well infrared photodetectors," *J. Appl. Phys.*, vol. 74, no. 8, p. R1, Oct. 1993.

[19] A. Harwit and J. S. Harris, "Observation of Stark shifts in quantum well intersubband transitions," *Appl. Phys. Lett.*, vol. 50, no. 11, pp. 685–687, Mar. 1987.

[20] D. A. Holm and H. F. Taylor, "Infrared phase modulators with multiple quantum wells," *IEEE J. Quantum Electron.*, vol. 25, no. 11, pp. 2266–2271, 1989.

[21] E. B. Dupont, D. Delacourt, and M. Papuchon, "Mid-infrared phase modulation via Stark effect on intersubband transitions in GaAs/GaAlAs quantum wells," *IEEE J. Quantum Electron.*, vol. 29, no. 8, pp. 2313–2318, 1993.

[22] D. A. B. Miller, D. S. Chemla, T. C. Damen, A. C. Gossard, W. Wiegmann, T. H. Wood, and C. A. Burrus, "Band-Edge Electroabsorption in Quantum Well Structures: The Quantum-Confined Stark Effect," *Phys. Rev. Lett.*, vol. 53, no. 22, pp. 2173–2176, Nov. 1984.

[23] M. Helm, "Chapter 1 The Basic Physics of Intersubband Transitions," in *Semiconductors and Semimetals*, vol. 62, 1999, pp. 1–99.

[24] G. Bastard, E. E. Mendez, L. L. Chang, and L. Esaki, "Variational calculations on a quantum well in an electric field," *Phys. Rev. B*, vol. 28, no. 6, pp. 3241–3245, Sep. 1983.

[25] D. Ahn and S. L. Chuang, "Exact calculations of quasibound states of an isolated quantum well with uniform electric field: Quantum-well stark resonance," *Phys. Rev. B*, vol. 34, no. 12, pp. 9034–9037, Dec. 1986.

[26] D. Ahn and S. L. Chuang, "Intersubband optical absorption in a quantum well with an applied electric field," *Phys. Rev. B*, vol. 35, no. 8, pp. 4149–4151, Mar. 1987.

[27] Doyeol Ahn and Shun-lien Chuang, "Calculation of linear and nonlinear intersubband optical absorptions in a quantum well model with an applied electric field," *IEEE J. Quantum Electron.*, vol. 23, no. 12, pp. 2196–2204, Dec. 1987.

[28] I. Tan, G. L. Snider, L. D. Chang, and E. L. Hu, "A self-consistent solution of Schrödinger–Poisson equations using a nonuniform mesh," *J. Appl. Phys.*, vol. 68, no. 8, pp. 4071–4076, Oct. 1990.

[29] M. Choi, C. Lin, M. Butcher, C. Rodriguez, Q. He, A. B. Posadas, A. Y. Borisevich, S. Zollner, and A. A. Demkov, "Quantum confinement in transition metal oxide quantum wells," *Appl. Phys. Lett.*, vol. 106, no. 19, p. 192902, May 2015.

[30] W. Wunderlich, H. Ohta, and K. Koumoto, "Enhanced effective mass in doped $SrTiO_3$ and related perovskites," *Phys. B Condens. Matter*, vol. 404, no. 16, pp. 2202–2212, Aug. 2009.

[31] M. Choi, A. B. Posadas, C. A. Rodriguez, A. O'Hara, H. Seinige, A. J. Kellock, M. M. Frank, M. Tsoi, S. Zollner, V. Narayanan, and A. A. Demkov, "Structural, optical, and electrical properties of strained La-doped $SrTiO_3$ films," *J. Appl. Phys.*, vol. 116, no. 4, p. 043705, Jul. 2014.

[32] A. Janotti, D. Steiauf, and C. G. Van de Walle, "Strain effects on the electronic structure of $SrTiO_3$: Toward high electron mobilities," *Phys. Rev. B*, vol. 84, no. 20, p. 201304, Nov. 2011.

[33] A. F. Santander-Syro, O. Copie, T. Kondo, F. Fortuna, S. Pailhès, R. Weht, X. G. Qiu, F. Bertran, A. Nicolaou, A. Taleb-Ibrahimi, P. Le Fèvre, G. Herranz, M. Bibes, N. Reyren, Y. Apertet, P. Lecoeur, A. Barthélémy, and M. J. Rozenberg, "Two-dimensional electron gas with universal subbands at the surface of $SrTiO_3$," *Nature*, vol. 469, no. 7329, pp. 189–193, 2011.

[34] D. D. Coon and R. P. G. Karunasiri, "New mode of IR detection using quantum wells," *Appl. Phys. Lett.*, vol. 45, no. 6, pp. 649–651, Sep. 1984.

[35] H. C. Liu, M. Buchanan, and Z. R. Wasilewski, "How good is the polarization selection rule for intersubband transitions?," *Appl. Phys. Lett.*, vol. 72, no. 14, pp. 1682–1684, Apr. 1998.

[36] C. M. Kim and R. V. Ramaswamy, "Overlap integral factors in integrated optic modulators and switches," *J. Light. Technol.*, vol. 7, no. 7, pp. 1063–1070, Jul. 1989.

[37] M. Luo and D. Sun, "Ultra-efficient modulation of $BaTiO_3$ crystal thin film waveguide with a two-dimensional optic-electric field matching scheme," *J. Appl. Phys.*, vol. 123, no. 3, p. 034503, Jan. 2018.

[38] J. E. Ortmann, A. B. Posadas, and A. A. Demkov, "The MBE growth of arbitrarily thick $SrTiO_3/LaAlO_3$ quantum well heterostructures for use in next-generation optoelectronic devices," *J. Appl. Phys.*, vol. 124, no. 1, p. 015301, Jul. 2018.

[39] J. E. Ortmann, S. Kwon, A. B. Posadas, M. J. Kim, and A. A. Demkov, "Monolithic integration of transition metal oxide multiple quantum wells on silicon (001)," *J. Appl. Phys.*, vol. 125, no. 15, p. 155302, Apr. 2019.

[40] D. S. Chemla, T. C. Damen, D. A. B. Miller, A. C. Gossard, and W. Wiegmann, "Electroabsorption by Stark effect on room-temperature excitons in GaAs/GaAlAs

multiple quantum well structures," *Appl. Phys. Lett.*, vol. 42, no. 10, pp. 864–866, May 1983.

[41] A. Messner, F. Eltes, P. Ma, S. Abel, B. Baeuerle, A. Josten, W. Heni, D. Caimi, J. Fompeyrine, and J. Leuthold, "Integrated Ferroelectric $BaTiO_3$/Si Plasmonic Modulator for 100 Gbit/s and Beyond," in *Optical Fiber Communication Conference*, 2018, vol. Part F84-O, no. c, p. M2I.6.

[42] D. A. B. Miller, "Energy consumption in optical modulators for interconnects," *Opt. Express*, vol. 20, no. S2, p. A293, Mar. 2012.

[43] L. Liao, D. Samara-Rubio, M. Morse, A. Liu, D. Hodge, D. Rubin, U. D. Keil, and T. Franck, "High speed silicon Mach-Zehnder modulator," *Opt. Express*, vol. 13, no. 8, p. 3129, 2005.

[44] W. M. Green, M. J. Rooks, L. Sekaric, and Y. A. Vlasov, "Ultra-compact, low RF power, 10 Gb/s silicon Mach-Zehnder modulator," *Opt. Express*, vol. 15, no. 25, p. 17106, 2007.

Chapter 7: Integrated Electro-Optic Devices Exploiting the Pockels Effect in $BaTiO_3$

7.1 Introduction to the Pockels Effect[4]

The Pockels effect is an electro-optic effect describing the change of a material's refractive index n in response to an applied electric field. In particular, the Pockels effect is linear in electric field E, in contrast to the more common Kerr effect which is quadratic in the applied field [1]. In equation form, the Pockels effect is commonly and conveniently represented as a linear function of the electric field with proportionality constants given by the zero-field index of refraction n_0 and effective Pockels coefficient r_{eff} according to

$$n(E) = n_0 - \frac{1}{2} n_0^3 r_{eff} E. \tag{7.1}$$

In reality, the Pockels effect is a tensorial property in which the magnitude of the response depends sensitively on the relative angles of the crystalline lattice, optical polarization and applied electric fields. I will return to this point in more detail in Sections 7.2 and 7.3.

The Pockels effect is of great technological interest for use in a wide variety of photonic applications, including communications technologies [2]–[4], neuromorphic computing [5], [6], quantum computing [7] and novel sensing technologies [8]–[10]. The utility of the Pockels effect comes from three primary factors. First, only the real part of the refractive index is modified by the Pockels effect. As a result, large changes in the refractive index of Pockels-active materials should be possible without significantly altering their absorption. This is especially important for applications requiring low optical losses [11], [12] or utilizing long device structures. Second, because the Pockels effect is electric field-driven, rather than current-driven, Pockels devices can in principle be

[4] Some material in this chapter comes from S. Abel, F. Eltes, J. E. Ortmann, A. Messner, P. Castera, T. Wagner, D. Urbonas, A. Rosa, A. M. Gutierrez, D. Tulli, P. Ma, B. Baeuerle, A. Josten, W. Heni, D. Caimi, L. Czornomaz, A. A. Demkov, J. Leuthold, P. Sanchis, and J. Fompeyrine, *Nat. Mater.*, vol. 18, no. 1, pp. 42–47, Jan. 2019.

engineered for low-power operation. Third, the Pockels effect is an ultra-high-speed effect, promising modulation speeds into the tens or hundreds of GHz [13], [14]. As society's computing demands continue to grow, the need for high-throughput computing grows with it, necessitating rapid advancements in optical transceiver and computing technologies [4]. High-speed and low-power operation are important qualities that next-generation electro-optic technologies must display to be considered competitive.

In fact, the Pockels effect is already the workhorse electro-optic effect used for long-haul communications technologies [15], [16], owing in large part to the benefits described above. Unfortunately, the traditional electro-optic material (lithium niobate, $LiNbO_3$) has a relatively small Pockels response and is not directly integrable with silicon. The lack of silicon integrability of lithium niobate has previously stymied efforts to utilize the Pockels effect in integrated photonic technologies by necessitating expensive or inefficient fabrication processes [17], [18]. Overcoming these challenges through the research and development of an improved Pockels material (barium titanate, $BaTiO_3$, BTO) is the subject of this chapter.

7.2 Theory of the Pockels Effect in $BaTiO_3$

An anisotropic medium is one whose macroscopic optical properties depend on direction. One notable example of optical anisotropy is the phenomenon of birefringence. A birefringent material is one whose index of refraction depends on the direction of propagation and the polarization of the probing optical wave. In general, crystalline media, such as the TMO thin films discussed in this thesis, will be optically anisotropic due to the regular, periodic patterns of the underlying atoms and the resulting directional dependence of the local atomic arrangement [1].

The optical and electro-optical properties of an anisotropic medium can be deduced by studying a geometric construction known as the index ellipsoid, given by

$$\sum_{ij} \eta_{ij}\, x_i x_j = 1, \qquad i,j = 1,2,3, \tag{7.2}$$

where η_{ij} are the elements of the (symmetric) impermeability tensor and x_{ij} are orthogonal spatial coordinates [1]. When plotted as a surface in three-space, Equation (7.2) defines an ellipsoid, as shown in Figure 7.1. The impermeability tensor $\overleftrightarrow{\eta}$ is defined with respect to the inverse of the permittivity tensor $\overleftrightarrow{\epsilon}$ according to $\overleftrightarrow{\eta} = \epsilon_o \overleftrightarrow{\epsilon}^{-1}$, where ϵ_o is the vacuum permittivity [1]. Here, the double-arrow notation is used to represent a tensor.

The index ellipsoid construction can be used to determine the refractive indices experienced by an optical mode propagating in an arbitrary direction within an anisotropic medium using the following procedure [1] (Figure 7.1). First, the index ellipsoid is drawn with respect to some coordinate axes. In general, the impermeability tensor of an anisotropic medium will have the following form:

$$\overleftrightarrow{\eta} = \begin{pmatrix} \eta_a & 0 & 0 \\ 0 & \eta_b & 0 \\ 0 & 0 & \eta_c \end{pmatrix}, \tag{7.3}$$

where $\eta_{a,b,c} = 1/n_{a,b,c}^2$ are the inverse squared indices of refraction along some directions *a*, *b*, and *c*. Then, a plane is drawn normal to the direction of wave propagation $\vec{k}$. The intersection of the plane with the index ellipsoid defines an ellipse referred to as the index ellipse. The half-lengths of the minor and major axes of the index ellipse are the refractive indices experienced by an optical mode propagating through the medium. In general, these two refractive indices will not be equal, leading to a polarization dependence of the effective index of refraction. This point is discussed in more detail below in relation to the electro-optical properties of BTO-based photonic devices.

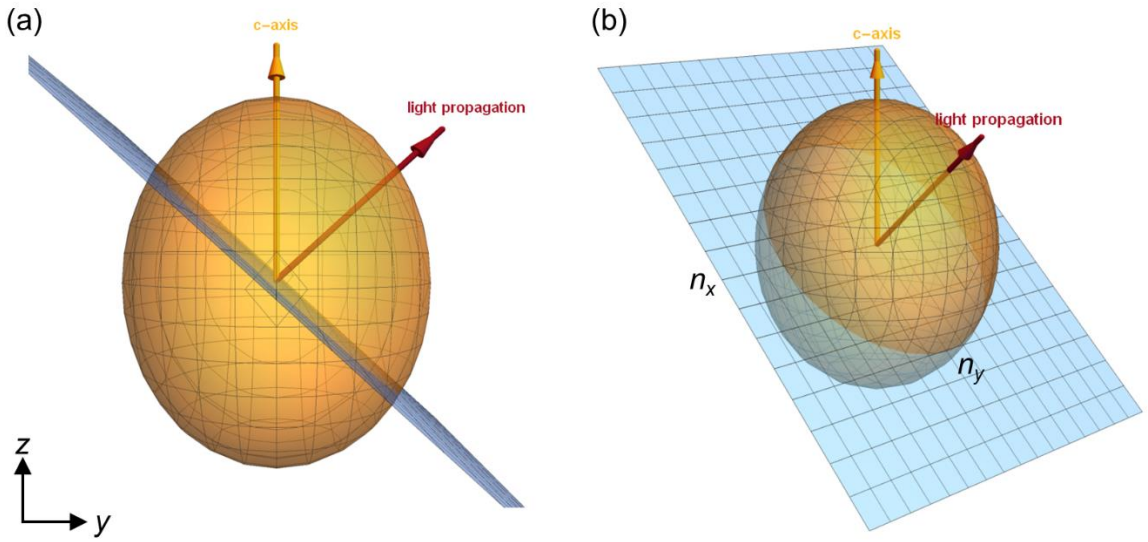

Figure 7.1: Index ellipsoid of an anisotropic medium. Side view shown in (a) and angled view in (b). The direction of light propagation is shown by the red arrow and the crystalline *c*-axis is shown by the yellow arrow. In this representation, the light is traveling at an angle of 45° to the *c*-axis. The indices of refraction n_x and n_y are given by the minor and major axes of the index ellipse, respectively, and are indicated in (b).

The impermeability tensor of Equation (7.3) can be expanded as a function of electric field and used to describe the linear (Pockels) and quadratic (Kerr) electro-optic effects as follows [1]:

$$\eta_{ij}(\vec{E}) = \eta_{ij}(\vec{0}) + \sum_{k} r_{ijk}E_k + \sum_{kl} s_{ijkl}E_kE_l\,, \qquad i,j,k,l = 1,2,3. \tag{7.4}$$

In Equation (7.4) above, r_{ijk} and s_{ijkl} are the elements of the Pockels and Kerr tensors, respectively, and E_{kl} are components of an external electric field. Comparing the above expression with the general form of a Taylor expansion, one can deduce that the Pockels tensor elements $r_{ijk} = \left.\partial\eta_{ij}\right/\partial E_k$ and the Kerr tensor elements $s_{ijkl} = \frac{1}{2}\left.\partial^2\eta_{ij}\right/\partial E_k\partial E_l$, where the derivatives are both to be evaluated at $\vec{E} = \vec{0}$.

In general, the Pockels tensor $\overleftrightarrow{r}$ is a rank-three tensor with 27 unique elements. However, owing to the symmetry of $\overleftrightarrow{\eta}$, $\overleftrightarrow{r}$ is invariant under permutations of the *i* and *j*

indices [1]. As a result, six unique combinations of i and j are realized rather than the nominal nine possible combinations, allowing the third-rank Pockels tensor to be contracted into a 6×3 matrix of independent elements [1], [19]. In practice, the i and j indices are usually contracted into a single index in the manner depicted below in Table 7.1. For example, the Pockels tensor element r_{134} would be contracted into r_{54} by following the procedure in Table 7.1. I will refer to this simplified notation when discussing Pockels tensor elements throughout the remainder of this chapter.

In addition to the symmetry of the impermeability tensor, the symmetry of the crystalline lattice also determines which elements of the Pockels tensor are non-zero. Furthermore, the crystalline space group may impose additional constraints on the Pockels coefficients, such as requiring that some elements of the tensor are equal (degenerate) or have equal magnitudes and opposite signs. For centrosymmetric crystals, $\overleftrightarrow{r} = \overleftrightarrow{0}$ and all elements of the Pockels tensor vanish. For non-centrosymmetric crystals, such as tetragonal BTO, the Pockels tensor has some non-zero elements as well as some degenerate elements. For the remainder of the discussion, I will focus only on the specific case of the Pockels effect in tetragonal BTO.

Table 7.1: Procedure for contracting the i and j indices of the Pockels tensor into a single index

j	i:1	2	3
1	1	6	5
2	6	2	4
3	5	4	3

The non-zero components of the Pockels tensor of BTO are given by only three unique elements (with some degeneracy): r_{13}, r_{33}, and r_{42} [20]. Specifically, the Pockels tensor for tetragonal BTO with the *P4mm* space group can be written as [20]

$$\overleftrightarrow{r}_{BTO} = \begin{pmatrix} 0 & 0 & r_{13} \\ 0 & 0 & r_{13} \\ 0 & 0 & r_{33} \\ 0 & r_{42} & 0 \\ r_{42} & 0 & 0 \\ 0 & 0 & 0 \end{pmatrix}. \tag{7.5}$$

Inserting $\overleftrightarrow{r}_{BTO}$ into Equation (7.4) and ignoring the relatively small Kerr effect in BTO [21], [22], one can derive the impermeability tensor of BTO

$$\overleftrightarrow{\eta}_{BTO}(\vec{E}) = \begin{pmatrix} \eta_o + r_{13}E_z & 0 & r_{42}E_x \\ 0 & \eta_o + r_{13}E_z & r_{42}E_y \\ r_{42}E_x & r_{42}E_y & \eta_e + r_{33}E_z \end{pmatrix}, \tag{7.6}$$

where $\eta_{o,e} = {}^{1}/_{n_{o,e}^2}$ and $n_{o,e}$ are the ordinary and extraordinary refractive indices of BTO, respectively. $E_{x,y,z}$ are orthogonal components of the applied electric field and are typically defined relative to the crystalline *a*, *b*, and *c* axes, respectively. For the case of tetragonal BTO, $a = b \neq c$. As a result, $n_a = n_b = n_o$, while $n_c = n_e \neq n_o$. Thus, tetragonal BTO is a so-called uniaxial material. The tetragonality of BTO also allows for the realization of two different orientations of the BTO within an epitaxial thin film (Figure 7.2): the *a*-axis orientation, in which one of the short (*a*) axes of the BTO unit cell are oriented out-of-plane, and the *c*-axis orientation, in which the BTO long (*c*) axis is oriented out-of-plane. The anisotropic nature of BTO, as well as the intrinsic anisotropy of the Pockels effect, results in different electro-optic responses from the different BTO orientations [23], [24].

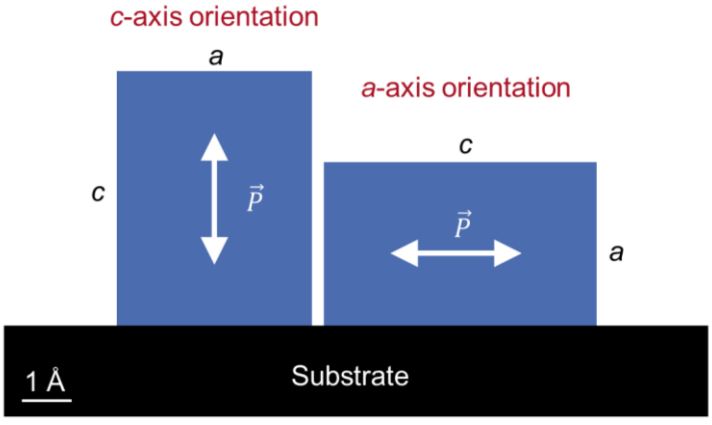

Figure 7.2: Schematic showing the two possible orientations of epitaxial BTO relative to a substrate. The orientations are named according to which axis points out-of-plane. The polarization of BTO is depicted by the white arrows.

Inserting the elements of $\overleftrightarrow{\eta}_{BTO}$ into Equation (7.2), one finds that the index ellipsoid for BTO is electric field-dependent, as expected for a Pockels-active medium. The non-zero off-diagonal elements of $\overleftrightarrow{\eta}_{BTO}$ lead to rotation and deformation of the BTO index ellipsoid under the application of an external electric field. Because the half-lengths of the principle axes of the index ellipsoid define the three indices of refraction $n_{x,y,z}$ [1], the rotation and deformation of the index ellipsoid manifests itself physically as an electric field-induced change in the refractive indices of BTO, as expected for a Pockels-active material.

In addition to the electric field dependence of the refractive indices of BTO, the electro-optical response of BTO also depends on the angles of the applied field and optical polarization with respect to the BTO crystalline lattice. To see this, consider the case of a single-domain, *a*-axis BTO waveguide situated between two electrodes (Figure 7.3). The direction of propagation of the optical mode and the external electric field have a relative angle of 90° that is fixed by the device geometry (this device geometry has been utilized exclusively for the experimental work presented in this chapter). The angle of the applied electric field relative to the BTO *c*-axis θ is allowed to vary. In this geometry, one component of the applied electric field will always be zero, as no field is applied along the crystalline direction pointing out-of-plane. Without loss of generality, I will define this as $E_x = 0$ for the case of *a*-axis BTO. Then, the impermeability tensor of *a*-axis BTO can be re-written as a function of electric field and device angle according to

$$\overleftrightarrow{\eta}_{BTO,a}(E,\theta) = \begin{pmatrix} \eta_o + r_{13}E\cos\theta & 0 & 0 \\ 0 & \eta_o + r_{13}E\cos\theta & -r_{42}E\sin\theta \\ 0 & -r_{42}E\sin\theta & \eta_e + r_{33}E\cos\theta \end{pmatrix}, \qquad (7.7)$$

where E_y has been replaced by $-E\sin\theta$ and E_z has been replaced by $E\cos\theta$ (Figure 7.3). Clearly, the observed electro-optic response in this case depends on the angle of the applied

electric field θ with respect to the BTO long axis as well as on the magnitude of the applied field E.

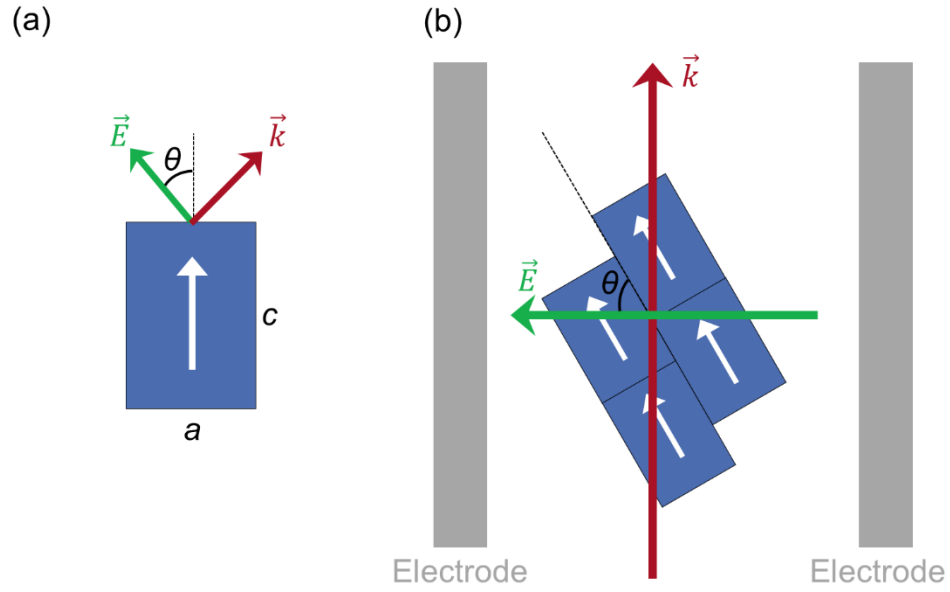

Figure 7.3: Schematics depicting (a) the relative orientations of the applied electric field $\vec{E}$, optical propagation vector $\vec{k}$ and BTO crystalline axes (a and c) in a planar device with single-domain, a-axis BTO and (b) multiple unit cells between two metallic electrodes, as would be the situation for a real device. White arrows represent the ferroelectric polarization of the BTO unit cells.

Castera *et al*. have examined the simplified case of single-domain, a-axis BTO and derived an analytic expression for the index of refraction experienced by a transverse-electric (TE) mode and the corresponding Pockels coefficient [23]:

$$n_{TE}(\theta) = \frac{n_o n_e}{\sqrt{n_e^2 \sin^2\theta + n_o^2 \cos^2\theta}} \tag{7.8}$$

$$r_{TE}(\theta) = r_{33}\cos^3\theta + (r_{13} + 2r_{42})\sin^2\theta \cos\theta. \tag{7.9}$$

These expressions can be inserted into Equation (7.1), with n_{TE} replacing n_0 and r_{TE} replacing r_{eff}, in order to determine the index of refraction experienced by a TE optical mode in single-domain, a-axis BTO for a given electric field strength and angle.

Furthermore, Castera *et al*. have derived the index of refraction experienced by a transverse-magnetic (TM) mode and the corresponding Pockels coefficient [23]:

$$n_{TM}(\theta) = n_o \tag{7.10}$$

$$r_{TM}(\theta) = r_{13}\cos\theta\,. \tag{7.11}$$

In addition to the angular dependence of the electro-optical response, the polarization dependence is also made explicit by Equations (7.8) – (7.11).

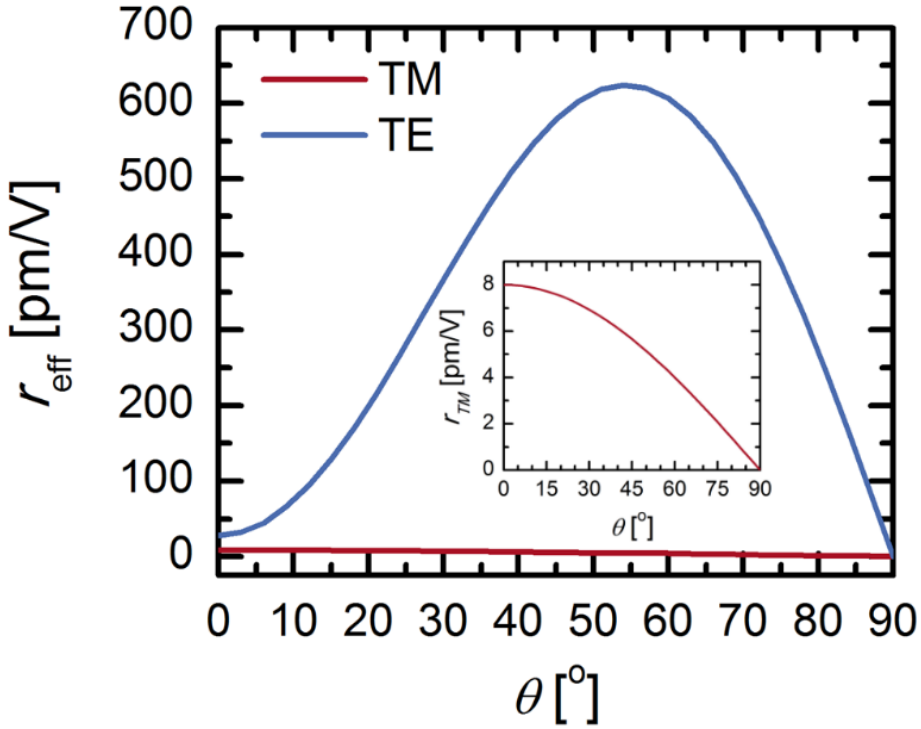

Figure 7.4: Effective Pockels coefficients for single-domain, *a*-axis BTO for TM (red) and TE (blue) polarizations as predicted in [23]. The inset shows a zoom-in of the predicted TM response. Values for r_{13}, r_{33}, and r_{42} have been taken from [25].

The angular-dependent Pockels coefficients from Equations (7.9) and (7.11) are plotted in Figure 7.4. Clearly, the TE mode is predicted to experience a much greater electro-optic response than the TM mode. Interestingly, these equations predict the maximum Pockels response for the TE mode to occur at an electric field angle of

approximately $\theta = 55°$ relative to the BTO *c*-axis. In a later paper [26], Castera *et al*. modified the expressions given by Equations (7.8) and (7.9) to include the effect of the multi-domain structure of BTO. In reality, BTO grown on silicon typically displays a multi-domain crystalline structure with *a*-axis BTO domains oriented at 90° to one another [27], [28] (Figure 7.5). Within each domain, a ferroelectric polarization exists that points along the BTO *c* axis. The magnitude of the electro-optic response from a given domain depends on the relative orientation of the optical electric field and the intrinsic polarization, with oppositely polarized domains typically experiencing equal but opposite Pockels responses [29]. By including the effects of a multi-domain structure, Castera *et al*. predict a maximal Pockels response for the TE mode at an electric field angle of $\theta = 45°$ for the realistic case of a 50:50 domain structure. This prediction matches with recent experimental data, as shown in Section 7.3. In general, both the ferroelectric domain orientation and the crystalline orientation (*a*- vs *c*-axis) contribute to the observed electro-optic response of BTO.

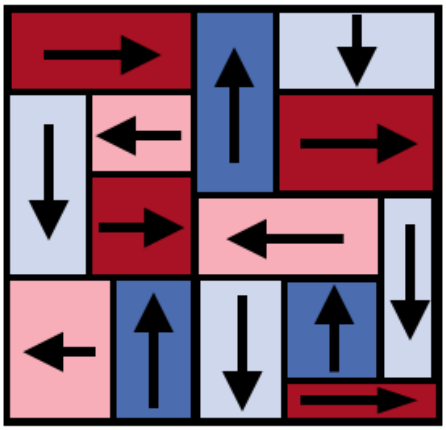

Figure 7.5: Schematic of multi-domain structure of unpoled *a*-axis BTO. For all domains, the ferroelectric polarization (represented by the black arrow) points along the BTO *c*-axis.

7.3 Large Pockels Effect in Micro- and NanoStructured Barium Titanate Integrated on Silicon

7.3.1 Contributions

The following sections are a reproduction of a 2019 paper by Abel, Felix, Ortmann, *et al*. [29] and details work I was involved in at IBM Research – Zurich. Specifically, I conducted much of the electro-optic characterization of the photonic devices, including the experimental measurements and the detailed numerical analysis of the response, with assistance from Dr. Stefan Abel. In addition, I assisted with the high-speed characterization of the photonic devices, as illustrated in Figure 7.9, in collaboration with Pau Castera of Professor Pablo Sanchis's group at Universitat Politècnia de València. Finally, I helped co-write the manuscript with Dr. Stefan Abel, Dr. Jean Fompeyrine and Felix Eltes.

Device design, chip layout, and sample fabrication were performed primarily by Felix Eltes with some assistance from Daniele Caimi. XRD and STEM characterization of the layer stacks were performed by Felix Eltes with some assistance from Dr. Jean Fompeyrine. Detailed vectorial simulations allowing for the extraction of the Pockels coefficients from the measurements were conducted by Darius Urbonas. Plasmonic device characterization was handled collaboratively by Felix Eltes of IBM and Andreas Messner of ETH Zürich.

7.3.2 Introduction

Silicon photonics has become a platform for dense and low-cost integrated photonic circuits for a wide range of applications [5], [6], [8], [30], [31], all of which require fast, energy-efficient electro-optical (EO) switches. State-of-the-art modulators based on silicon [32] rely on the plasma dispersion effect [33] and have two major constraints: First, the change of the real and imaginary parts of the refractive index is linked. A modulation of

only the optical phase is therefore not possible, which renders the use of advanced modulation formats difficult [34], [35]. Second, the operating speed is limited by the charge-carrier lifetimes in forward-biased devices or by the *RC* characteristics in reversed-biased devices [36], leading to a maximal bandwidth of a few tens of GHz. These constraints are not present in discrete modulators that exploit the Pockels effect in lithium niobate ($LiNbO_3$, LNO) single crystals, which have been used for decades in long-haul telecommunication [16]. Because no Pockels effect exists in a centrosymmetric crystal such as silicon, materials with sizeable Pockels coefficients must be integrated onto silicon photonic structures to combine the benefits of bulk Pockels modulators with the low fabrication costs of integrated silicon photonics. Unfortunately, so far, no satisfactory solution exists. The integration of LNO on silicon can only be performed locally [18] or on small wafer scales [17] because no epitaxial deposition process is available. Organic materials with large Pockels coefficients have been integrated on silicon and show high-speed performance [37], [38]. Unfortunately, their limited range of operating temperatures hinders their use in real applications. Lead zirconate titanate (PZT) thin films, a more stable material, have also been used to fabricate active switches on a SiN waveguide platform [39], but no direct integration on compact silicon photonics has been achieved.

Barium titanate ($BaTiO_3$, BTO) has emerged as an excellent candidate to enable Pockels-effect-based devices on silicon for several reasons. First, BTO has one of the largest Pockels coefficients of all materials [40]. Second, it has previously been used in thin-film EO modulators on exotic oxide substrates [41], [42]. Third, BTO can be grown on silicon substrates [22], [43] with large wafer sizes, and with an excellent crystal quality [13]. Previous work reported values of the Pockels coefficients lower than BTO bulk values, but five times larger than bulk LNO [22]. Fourth, BTO is a chemically and thermally stable material. Finally, functional passive photonic structures, such as low-loss

hybrid BTO-Si waveguides, have already been realized [44]. Earlier results were shown on EO switching in BTO-Si waveguides [13], [45], [46] or in BTO plasmonic devices operated at high speed [47], but the influence of undesired effects, such as charge migration or plasma dispersion, could not yet be excluded as the source of the EO response. No proof exists that BTO maintains its superior EO properties when embedded into micro- and nanoscale silicon photonics structures.

In this work, we unambiguously prove the presence of the Pockels effect in BTO integrated into silicon photonic devices by verifying three independent criteria: We show, first, high-speed modulation up to frequencies of 65 GHz, second, the dependence of the EO response on the orientation of the optical and externally applied electrical fields relative to the crystalline orientation of BTO, and third, optical evidence of ferroelectric domain switching. These features are unique signatures of the Pockels effect and exclude other physical switching mechanisms. We extract a Pockels coefficient of $r_{42} \sim 923$ pm/V, which is 30 times larger than in LNO, and the highest value reported in silicon photonic structures.

In the following sections, we first disclose the fabrication of the layer stack containing ferroelectric BTO, in which the Pockels effect is present. Next, we describe the layout and the design of both microscale photonic and nanoscale plasmonic devices used to verify the presence of the Pockels effect. We discuss the need of using two complementary device geometries to fully characterize the EO properties of BTO, as presented in detail in the third section. Finally, we demonstrate the generic applicability of BTO-enhanced photonic structures by performing data modulation at high rates of up to 50 Gbit/s.

7.3.3 Fabrication of BTO Layers

In this section, we show that high-quality, single-crystalline BTO on SiO_2 can be obtained using a combination of epitaxy and direct wafer bonding. With our concept, two prerequisites to enable EO switching in BTO/Si structures are fulfilled: First, the approach yields dense, crystalline, and tetragonal BTO films, which are needed to preserve the Pockels effect [48]. Second, it enables a thick lower cladding below the BTO films, which is required to avoid optical leakage into the substrate. Previous electro-optical BTO/Si devices were based on BTO on silicon-on-insulator (SOI) substrates [45], [46]. However, in such layer stacks, mobile charges in the semiconducting device silicon layer may screen the applied electric field and result in an EO response due to plasma dispersion [40]. To prevent this effect, we fabricated a hybrid amorphous-epitaxial heterostructure without any silicon below the BTO layer using a two-step process.

In the first step, 80- to 225-nm-thick BTO layers are grown by molecular beam epitaxy (MBE) on SOI substrates. To ensure epitaxial growth, the SOI is covered with a 4-nm-thin MBE-grown strontium titanate ($SrTiO_3$, STO) buffer layer [22] (Methods). In the second step, we transfer the BTO layer onto another silicon wafer covered with SiO_2 via direct wafer bonding and substrate back-etching, using Al_2O_3 as bonding interface [49]. The 5- to 10-nm-thick Al_2O_3 layer deposited on both the host and the donor wafer via atomic layer deposition guarantees a high bonding strength [50]. The low surface roughness below 0.4 nm for both wafers (Figure 7.6a) results in a high bonding yield. After thermal treatment, the donor wafer is removed via grinding and multiple etching steps (Methods), resulting in the desired wafer stack of Si/STO/BTO/Al_2O_3/SiO_2/Si (Figure 7.6b). Most of these steps are commonly available in a back-end-of-the-line integration process and enable the addition of functional oxide layers with planarized, oxide-covered wafers fabricated in a standard CMOS process [13].

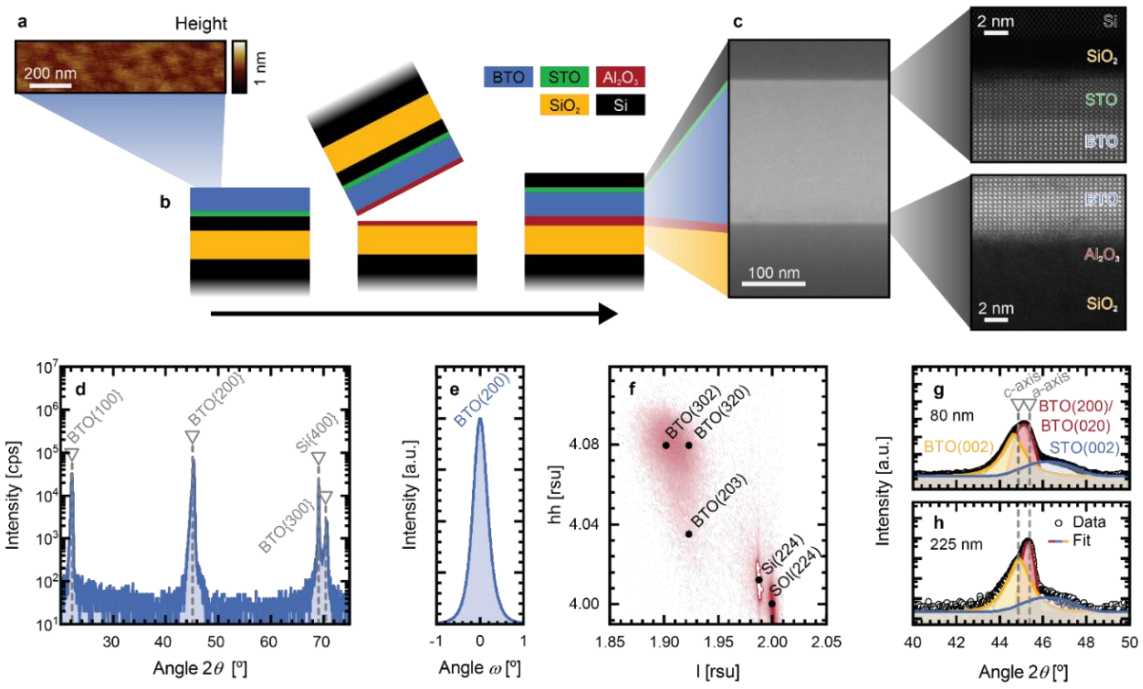

Figure 7.6: (a) Atomic force microscopy image showing the low roughness of BTO prior to the bonding process. (b) Schematic of process (from left to right) to obtain the hybrid stack using direct wafer bonding of an MBE-grown BTO film onto a thermally oxidized acceptor wafer with Al_2O_3 as a bonding interface. (c) The low-resolution cross-sectional image shows a uniform and smooth layer stack, whereas the higher-resolution HRSTEM images (right) reveal the high quality of the crystalline structure of BTO and of the BTO/STO interface formed during the deposition process (top) as well as the sharpness of the bonding interface (bottom). (d) The HRXRD diffractogram confirms the absence of any polycrystalline domains in the final hybrid stack, with only BTO (h00) peaks visible (pseudo-cubic notation), and the epitaxial relationship between silicon and BTO. (e) The high quality of the BTO layer is evidenced by the low mosaicity ($\Delta\omega \approx 0.3°$) extracted from the rocking curve measured on the BTO (200) Bragg peak. (f) Reciprocal space map plotted in reciprocal space units (rsu) around the {224} silicon and {203} BTO Bragg peaks acquired on the hybrid stack. Three possible orientations are revealed, with the long c-axis being parallel to either the [001] (c-axis domains) or to the [110] or [-110] silicon directions (a-axis domains). (g, h) Higher-resolution diffraction around the pseudo-cubic (200) BTO peak, highlighting the relative contributions of the a- and c-axis domains in the BTO layer. The comparison of (g) an 80-nm-thick and (h) a 225-nm-thick BTO layer shows the higher relative fraction of the c-axis domain in thinner films.

The layers show a well-defined crystalline orientation with respect to the wafer as is necessary for obtaining high-performance photonic devices [26]. The crystallinity and interfaces remain of high quality after completion of the process, as is visible at a microscopic level in high-resolution scanning transmission electron microscopy (HRSTEM) images (Figure 7.6c). High-resolution X-ray diffraction (HRXRD) analysis confirms the cube-on-cube epitaxial relationship between the BTO layer and the device silicon layer (Figure 7.6d). The sharp rocking curve (Figure 7.6e) further confirms the high crystalline quality at a macroscopic level.

A more detailed analysis shows that the BTO film has a tetragonal symmetry, consistent with the bulk unit cell of BTO, with two short *a*-axes and one longer *c*-axis (Figure 7.6f). The orientation of these axes is critical for device operation because of the strong dependence of the Pockels effect on the relative orientation of the static electric field, the direction and polarization of the light, and the crystalline orientation [22], [26]. The reciprocal space map around the BTO(203) film peak (Figure 7.6f) shows the presence of two types of *a*-axis-oriented domains which are rotated by 90° in-plane relative to each other, and a smaller fraction of *c*-axis domains (see Figure 7.6 caption). The *c*-axis domains stem from epitaxial strain, and are expected to form at the interface between STO and BTO [22], [28]. Consistently, the relative volume fraction of *c*-axis domains is indeed larger in the 80-nm-thin film (Figure 7.6g) than the 225-nm-thick film (Figure 7.6h).

7.3.4 Device Integration and Characterization

To confirm the Pockels effect in the BTO layer, we test the anisotropy and the frequency behavior of the electro-optic response of various integrated devices. We use racetrack resonators with differently oriented straight sections relative to the BTO crystalline axes (Figure 7.7a). The relatively small footprint of such structures of

~$(100\ \mu m)^2$ allows the fabrication of many separate devices of different orientation, which are needed to probe the angular dependence of the electro-optic response. Resonant devices are well-studied and allow a quantitative analysis of the EO response [51]. Due to the finite photon lifetime, the electro-optic bandwidth of resonant photonic devices is typically limited to few tens of GHz [52], which restricts the usage of such devices for high-speed characterization as needed to validate the Pockels effect. Mach-Zehnder modulators (MZM) can be operated at high-speed without bandwidth limitations due to finite photon lifetimes. However, the larger size of MZMs of several millimeters impacts the electrode bandwidth [36]. Advanced radio frequency (RF) engineering of travelling wave electrodes is required to obtain high-bandwidth BTO/Si based MZM structures. As an alternative, plasmonic phase modulators offer extremely high bandwidth due to the low capacitance resulting from the small device size [53]. In our work, we use such BTO-based plasmonic structures to extend the frequency range of our EO characterization to 65 GHz. Since an accurate quantitative analysis of plasmonic phase modulators is not possible, we used both photonic and plasmonic device types for our analysis of the electro-optic response.

We have therefore fabricated both photonic and plasmonic devices with embedded BTO (Methods). For photonic structures, the device-silicon layer is used to form strip-loaded waveguides cladded with SiO_2. The waveguide is single-mode and supports transverse-electric (TE) (Figure 7.7c) and transverse-magnetic (TM) (Figure 7.7d) polarizations with 39 % (TE) or 55 % (TM) of the optical power confined in the BTO layer. Electrodes separated by 2 μm from the waveguide generate an electric field parallel to the 225-nm-thick BTO layer (Figure 7.7a,b). To analyze the tensorial nature of the EO response, racetrack resonators were fabricated with different angles α relative to the BTO<100> pseudo-cubic crystalline direction (Figure 7.7a). Applying a DC or RF signal to the electrodes (Figure 7.7e), the shift in the resonance wavelength of the resonators is

used to determine the change of the effective mode index Δn_{eff} in the waveguides (Methods).

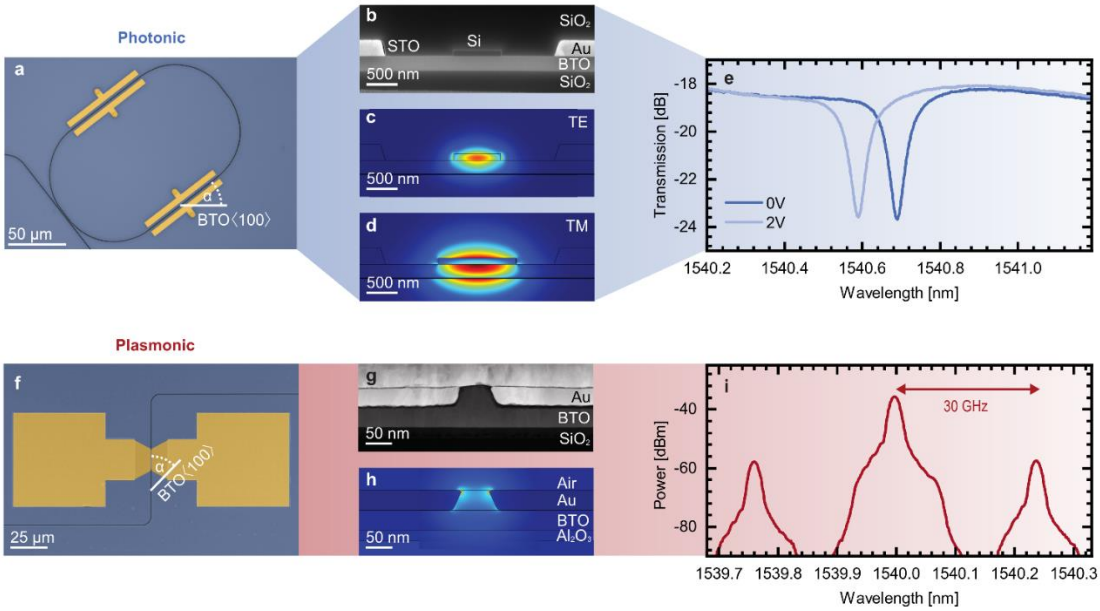

Figure 7.7: (a) False-color optical microscopy image of a photonic ring resonator prior to the fabrication of contact pads. The angle α indicates the orientation of the straight section relative to the BTO<100> axis (pseudo-cubic notation). Waveguides are shown in black, the BTO surface in blue, and the electrodes in yellow. (b) Scanning electron microscopy (SEM) cross-sectional image of the photonic devices between the electrodes. (c, d) Simulated mode profile of the photonic TE and TM mode, respectively (methods). The colors indicate the electric field strength, ranging from blue (low) to red (high). (e) Exemplary transmission spectra of a photonic racetrack resonator for two different bias voltages. The EO response is calculated based on the shift of the resonance wavelength. (f, g, h) Similar figures as (a)-(d) for the plasmonic device, showing the false colored top-view reordered via SEM, the cross section, and the simulated mode profile (same color code as in (c), (d)). (i) Example of a transmission spectrum of a plasmonic phase modulator operated at a wavelength λ = 1540 nm with an RF signal at 30 GHz. The intensity ratio of the peak (λ = 1540.00 nm) to the first sidebands (λ = 1539.75 nm and 1540.24 nm) is used to determine the change of the effective index Δn_{eff} of the plasmonic mode.

The 10-µm-long plasmonic structures are based on an 80-nm-thick BTO layer, from which a 50-nm-wide fin is etched and contacted (Methods). The plasmonic waveguide (Figure 7.7f,g) confining 50% of the optical power in the BTO layer (Figure 7.7h) [54] is coupled to photonic waveguides via tapered structures. We derive Δn_{eff} from the power ratio between spectral bands (Figure 7.7i), which are created by two-wave mixing processes when applying an RF signal to the electrodes (Methods).

7.3.5 Confirmation of Pockels Effect

To confirm the presence of the Pockels effect in BTO, it is crucial to analyze characteristic features of the EO response [55], primarily its frequency dependence to exclude slow EO effects and its anisotropic nature to rule out isotropic EO effects. In addition, the Pockels effect in a ferroelectric should translate into a hysteretic response of the refractive index versus field, consistent with the poling of ferroelectric domains. Here we investigate all these characteristics to confirm the presence of the Pockels effect in our devices.

The modulation of the refractive index at radio frequencies [56] differentiates the Pockels effect from the thermo-optic effect and from ionic diffusion processes, both of which occur at long timescales. We measure a constant EO response up to 30 GHz in photonic devices with Q-factors of $Q = 5 \cdot 10^3$ (Figure 7.8a), which coincides with the cut-off frequency of our experimental equipment (Methods). Due to the finite photon lifetime [52] and peaking effects [57] in resonant structures, the response at higher frequencies cannot be interpreted unambiguously. From the constant EO response up to 30 GHz in photonic devices, we cannot completely exclude a possible contribution of plasma dispersion induced by the strong electric field in the silicon strip above the BTO layer. Non-resonant plasmonic devices, where silicon is absent in the active region, are used to

extend the analysis to higher frequencies. Indeed, the EO response in plasmonic devices is constant in the frequency range from 30 to 65 GHz (Figure 7.8a), and unambiguously supports the presence of the Pockels effect in the BTO-based devices.

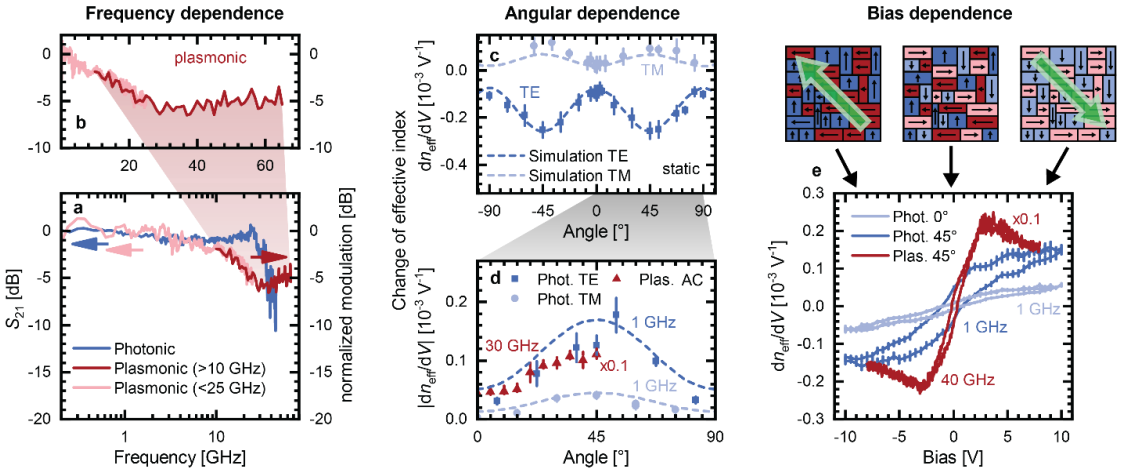

Figure 7.8: (a) Frequency dependence of the EO response of a photonic ring modulator (TE polarization) and a plasmonic phase modulator. (b) Linear zoom into the high-frequency region of the plasmonic modulator up to 65 GHz. (c) Angular dependence of the EO response of photonic devices designed for different optical polarizations for static electric fields and, (d) for photonic and plasmonic devices at alternating electric (AC) fields at 1 GHz and 30 GHz, respectively. The dashed lines in (c) and (d) correspond to the simulated response of the photonic devices using the Pockels tensor extracted from the experiments (Supplementary Note 5). (e) EO hysteresis curve obtained at 1 GHz (photonic devices, TE polarization) and at 30 GHz (plasmonic devices) when sweeping the applied bias in devices oriented at different angles α (see labels). The schematics on top indicate the orientation of the ferroelectric domains for the electric field (green arrow) oriented at α = ±45°.

In contrast to the flat frequency response of the photonic devices, the plasmonic modulators show a reduction of the EO response in the frequency range from ~2 to 30 GHz by ~5 dB (Figure 7.8b). This reduction is attributed to the mechanical boundary conditions in plasmonic devices: At frequencies up to few GHz, horizontal deformation of the BTO fin driven by the piezo-electric effect [58] results in a larger, un-clamped EO response [20]

compared to the high frequency region. Such an effect is not visible in photonic devices, where mechanical motion is suppressed due to clamping from the SiO_2 cladding.

Because of the tensorial nature of the Pockels effect [20], the orientation α of the waveguides (defined in Figure 7.7) should influence the EO response. Indeed, photonic racetrack devices show a clear dependence on α (Figure 7.8c). As the electric-field-induced Δn_{eff} parallel and perpendicular to the BTO layer is anisotropic, the EO response is expected to be sensitive to the polarization of the optical mode. We experimentally confirmed such an anisotropy between the TE and the TM modes in photonic devices (Figure 7.8c,d), and compared it with simulations of the expected EO response. The experimental angular dependence and polarization dependence of the EO response agree quantitatively with the simulations (Figure 7.8c). We determined the two largest non-vanishing coefficients of the Pockels tensor in the BTO layer in the photonic structures to be r_{42} = (923 ± 215) pm/V and r_{33} = (342 ± 93) pm/V. Owing to the small response of the TM devices at □ = 0°, no reliable extraction of the r_{13} coefficient is possible. The similar angular dependences of the EO modulation at static and radio frequencies indicate a common and constant physical effect as the origin of the EO response at all time and length scales probed in our measurements (Figure 7.8d). Here, we limited the analysis to 1 GHz to minimize the influence of finite photon lifetimes on the angular dependence. Our experimental procedure does not allow an accurate quantitative analysis of the Pockels response at RF (Methods). However, the flat frequency response of the S_{21} parameter in the photonic devices (Figure 7.8a) indicates a constant Pockels effect from static (Figure 7.8c) to high frequencies (Figure 7.8d).

Although we can measure an effective, orientation-dependent materials response in plasmonic devices, which qualitatively agrees well with the tensorial nature of the Pockels effect (Figure 7.8d), it is not possible to deconvolute and quantify the Pockels coefficients

as can be done for photonic devices. Nanoscale plasmonic devices are more sensitive to extrinsic effects such as process damages or device geometry as well as intrinsic effects such as dead dielectric layer, or distribution of *c*- and *a*-axis domains in the plasmonic waveguide. Nevertheless, taking these effects into account, the measured effective response of the plasmonic devices can be reproduced using the Pockels coefficients determined on the photonic devices.

In addition to the high-frequency response and the angular dependence, the EO response caused by the BTO layer should lead to a hysteretic behavior when sweeping the bias voltage due to the reorientation of ferroelectric domains. Because the Pockels effect is a linear EO effect, domains with opposing ferroelectric orientations induce an opposite phase shift, resulting in a vanishing EO response for films with equally distributed domains [22]. The EO response will saturate while increasing the bias, once all domains are polarized in the same direction. Indeed, the expected hysteresis is clearly visible in both the microscale photonic and nanoscale plasmonic devices (Figure 7.8e). The coercive field E_c extracted for photonic devices ($E_c = 2 \cdot 10^5$ V/m) is in good agreement with previously reported values for BTO films on silicon of similar thicknesses [22]. In contrast, the coercive field in plasmonic structures is more than one order of magnitude larger ($E_c = 1 \cdot 10^7$ V/m), but remains consistent with a voltage drop over an interfacial non-ferroelectric layer and common observations in thin ferroelectrics, where domain pinning and finite depolarizing fields enhance E_c in devices with reduced dimensions [59].

In the case of photonic devices, the hysteresis loop is not completely pinched at larger voltages due to slow ionic diffusion processes occurring at time scales similar to the sweeping rate used during the hysteresis measurements (Methods). These diffusion effects are related to the surface reactivity of the bonded material stack towards the ambient atmosphere, which take place in the gap between the electrode and the waveguide. As a

consequence, the potential distribution within the device is slightly modified without impacting the angular dependence and the frequency response as discussed above.

7.3.6 Application of the Pockels Effect

Having demonstrated the existence of a strong Pockels effect in our structures, we now demonstrate its potential use for high-speed data communication (Figure 7.9). Recording an eye-diagram is an insightful way to evaluate the performance of an EO modulator. A photonic ring modulator with *Q*-factor $Q = 9 \cdot 10^3$ and a 10-µm-long plasmonic phase modulator with a slot width of 50 nm are used to achieve a high modulation bandwidth (Methods), with data rates of 40 Gbit/s (photonic device) and 50 Gbit/s (plasmonic device). These results show the applicability of the BTO/Si technology for high-speed data transmission. They can also be used to estimate the performance of MZM, which, if well-engineered, are commonly preferred over resonant structures or phase modulators for integrated optical links. The electro-optic response measured in our TE photonic waveguides translates to a $V_\pi \cdot L$ product of 0.45 V·cm, which is competitive with state-of-the-art integrated Si [60] and InP [61] EO phase shifters. Additionally, we estimated the switching energy of an optimized MZM to be 96 fJ/bit, which is in the same range as advanced Si-based Mach-Zehnder modulators [62], [63]. These performance metrics prove the technological relevance of having the Pockels effect available on silicon as an EO switching mechanism.

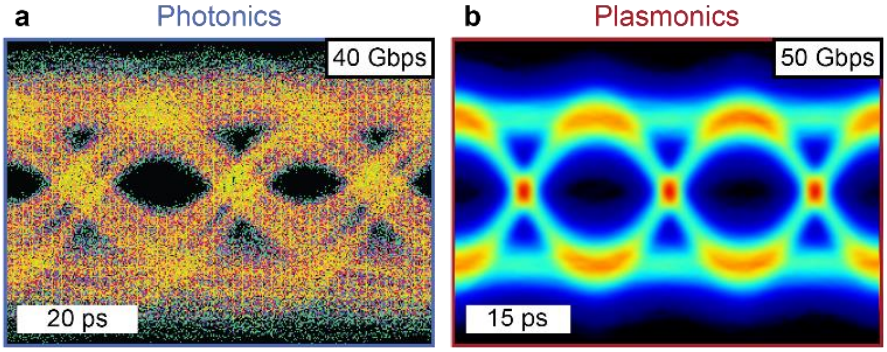

Figure 7.9: (a) Eye-diagram for data rates of 40 Gbit/s (photonic device) and (b) 50 Gbit/s (plasmonic device).

7.3.7 Summary and Conclusions

We have unambiguously demonstrated the presence of the Pockels effect in a hybrid $BaTiO_3$-SiO_2 stack integrated into photonic and plasmonic structures on silicon. While the photonic resonator devices allow for the quantitative determination of the individual Pockels tensor elements of BTO, the plasmonic devices enable bandwidth measurements at frequencies up to 65 GHz. The results from these two complementary device structures demonstrate that BTO maintains its superior electro-optical properties after fabrication of both microscale photonic and nanoscale plasmonic components. Key characteristics, such as the high-speed response, the angular anisotropy, and hysteretic switching, rule out other physical effects as the origin of the EO response. The magnitude of the EO response is bulk-like [20] and many times larger than for any Pockels materials previously integrated on silicon [18], [22], [39]. The chemical and thermal stability of oxides also outperform those of organic nonlinear materials [38], [64].

The use of our structures for data communication at rates of 50 Gbit/s reveals the prospects of this technology for a new class of integrated modulators. Our approach can deliver devices with a competitive $V_\pi \cdot L$, is suited for complex modulation formats, and is compatible with a tight integration within CMOS fabrication lines. Having demonstrated

the presence of the Pockels effect in the materials stack, we foresee that superior electro-optical performance can be obtained by further optimization of the device parameters such as the thickness of the BTO layer, the gap between the electrodes, and the electrode layout optimized for RF operation.

The ability to control the Pockels effect in integrated photonic devices also has profound implications for applications beyond data communication. Sensory [8], [65], [66], mid-infrared [67], and neuromorphic computing applications [5], [6], [68] would also strongly benefit from devices that are operated at reduced operating speeds or exploit non-volatile EO effects. Ultimately, hybrid BTO/Si photonic devices provide an additional degree of freedom for designers to realize not only a new generation of compact, high-speed modulators, but also novel devices such as ultra-low-power tuning elements [46], non-volatile optical memories [69], or microwave-to-optical quantum converters [70].

7.3.8 Methods

MBE deposition was done in a chamber with a base pressure of $< 3 \cdot 10^{-10}$ Torr. Before BTO deposition on 2'' SOI wafers with 100- or 220-nm-thick device silicon layers, a 4-nm STO seed layer was deposited. After HF-cleaning of the substrate, 0.5 mono layers of Sr was deposited at 600-650°C. After cooling to 50°C, the Sr was oxidized in molecular oxygen, followed by the deposition of amorphous STO at an O_2 pressure of $\sim 5 \cdot 10^{-7}$ Torr. The amorphous STO was crystallized by annealing in UHV at 400-500°C, resulting in epitaxial STO. BTO growth was done at 500-600°C under atomic oxygen. A plasma source was used to generate atomic oxygen at a pressure of $\sim 5 \cdot 10^{-6}$ Torr.

Direct wafer bonding was performed using 5- to 10-nm-thick Al_2O_3 layers deposited by atomic layer deposition on both donor and receiver wafers. After surface preparation and bonding, an annealing step was performed at 250°C. The donor wafer was

removed by grinding, followed by wet etching, leaving the device Si of the SOI donor wafer as the top layer.

Fabrication of photonic devices started by epitaxial deposition of 225-nm BTO on a 4-nm STO buffer on an SOI wafer with 100-nm top Si. The BTO and top-Si layers were transferred by direct wafer bonding to a high-resistivity wafer with a 2-µm-thick thermal oxide. Photonic waveguides and grating couplers were fabricated by patterning the top Si layer using inductively coupled plasma (ICP) etching. After waveguide fabrication, the devices were annealed in O_2 at 400°C for 4 h to reduce propagation losses to ~10 dB/cm. Electrodes were deposited in a metallization step. An SiO_2 cladding was deposited by PECVD, in which vias were etched by ICP followed by the final metallization. The width of the waveguides was chosen to be 0.75 and 1.25 µm to ensure single-mode TE and TM operation, respectively. Single mode operation was verified by simulating the 2D mode profiles with PHOENIX and COMSOL. Racetrack resonators with 50 µm (TE) and 75 µm (TM) bend radius, and 75-µm-long straight sections were fabricated along with ring modulators with varying radii.

The photonic components of the plasmonic devices were fabricated in the same way as the photonic devices (using 80-nm BTO deposited on an SOI wafer with 220-nm top Si). After patterning of photonic regions, the plasmonic waveguides were etched into the BTO using ion beam etching. After structuring of the BTO, the electrodes were deposited by a self-aligned metallization process. The propagation losses of the plasmonic structures are ~1.4 dB/µm.

Optical fibers and integrated grating couplers were used to first couple light emitted from a tunable diode laser at a wavelength of $\lambda \sim 1550$ nm into the active devices, and afterwards out of the chip to detect the transmitted power. Applying a voltage to the electrodes creates an electric field in the BTO layer, which results in a modification of the

refractive index because of the Pockels effect. For photonic devices, we tracked these modifications by recording the transmission spectra of the resonators as a function of the bias voltage applied. The change of the refractive index of the BTO layer can be determined from the change of the resonance wavelength λ_0. For hysteresis measurements, we iteratively changed the bias and recorded transmission spectra with a delay of ~10 s. We acquired the frequency dependence of the EO response by modulating the applied voltage from 50 MHz to 40 GHz. We recorded the S_{21} parameter of a TE ring modulator with a radius of 15 µm using a vector network analyzer (VNA) while scanning λ across the resonance and measuring the modulated optical power at a high-speed detector with a 3 dB cut-off frequency of 33 GHz after amplifying, filtering, and attenuating the modulated signal. Note that the values reported for the S_{21} parameters (Figure 7.8b) are extracted off-resonance to minimize effects from the finite photonic lifetime on the EO bandwidth. The nonlinear distortion of the EO response by the erbium-doped fiber amplifier (EDFA) operated close to saturation is considered in the data analysis, but results in inaccuracies which prevent an accurate quantitative analysis of the change of the refractive index from the S_{21} parameters.

To characterize the plasmonic phase shifters, we applied a bias voltage of about 2.5 V and an RF signal of approximately 10 dBm at frequencies f_{RF} between 15 and 65 GHz directly to the electrodes of the phase shifters, and recorded the optical spectrum using an optical spectrum analyzer (OSA). The modulation amplitude was measured as the power ratio between the optical carrier and the modulation sidebands at $f_0 \pm \Delta f_{RF}$. We calibrated the RF power at the input of the RF probe and subtracted the losses of the probe based on the data sheet supplied. To measure the frequency response of plasmonic devices at frequencies lower than 15 GHz, a lightwave component analyzer was used to record the S_{21} parameter of a Mach-Zehnder modulator consisting of two plasmonic phase shifters

between 100 MHz and 25 GHz. The overlap between the S_{21} parameter and the phase shifter modulation in the 15-25 GHz range was used to normalize the phase-shifter modulation to the S_{21} parameter.

To determine the angular dependence, devices with orientations between 0° and 45° were measured with a 30-GHz RF signal. The hysteresis measurement was performed on a single device by varying the bias voltage, while keeping the RF signal constant. Based on the modulation amplitude and the applied RF power, we extracted the modulation index as described in ref. [71]. From the modulation index, we calculated the change of the mode index. For an improved comparison with the photonics measurements, we inverted one wing of the butterfly-shaped hysteresis loop to obtain the hysteresis loop shown in Figure 7.8e.

A TE photonic ring modulator with a radius of 12.5 µm, a coupling gap of 0.35 µm and an electrode gap of 2.75 µm was used to characterize the high-speed data-transmission capability, whereby an NRZ pseudorandom binary sequence (PRBS) of length 2^7-1 delivered by a bit pattern generator (BPG) was applied, connected to an external clock. The modulating signal was applied by high-speed ground-signal-ground (GSG) RF probes to the electrodes. The modulated optical signal was then optically amplified by an EDFA, filtered via an optical filter, and finally photo-detected prior to its visualization at the digital communication analyzer (DCA). In this way, a 40-Gbit/s signal was generated.

A plasmonic phase shifter with a 50-nm-wide and 10-µm-long plasmonic waveguide was used for BPSK data modulation. An electrical 50 Gbit/s signal was generated and amplified before being applied to the modulator. The applied RF voltage peak was 0.8 V at a 50 Ω system, and the DC bias voltage was 2.5 V. A tunable laser, set to 1.55 µm, amplified through an EDFA to 16 dBm was used for the optical input. After the modulator, the optical signal was re-amplified through an EDFA, fed to an optical

coherent receiver and recorded by a digital sampling oscilloscope (DSO, 160 GSa/s, 63 GHz 3-dB bandwidth). The digitized signal was processed offline, including timing recovery, carrier recovery, least mean square (LMS) equalization, symbol decision and error counting.

All simulations are performed with a MEEP Finite Difference Time Domain (FDTD) solver. The calculations were performed using 2D FDTD with the cell size of 8:6 μm (*y*:*z*) using 33-nm grid size and 1-μm-thick perfectly matched layer (PML) boundary conditions. The simulation geometry consisted of a SiO_2 bottom layer, 225-nm BTO, and a 100-nm-thick and 1250/750-nm-wide Si ridge layer cladded with air. The Gaussian-shaped source was positioned in the center of the waveguide, and the size of the source was equal to the dimensions of the waveguide (width = 750/1250 nm, height = 325 nm). The wavelength range was set to 1430 – 1670 nm. The simulated EO response of the photonic devices was compared with the experimental data to extract the elements of the Pockels tensor.

All simulations were performed with COMSOL Multiphysics. Eigenmodes were calculated in 2D Finite Element Method (FEM) simulations with a simulated region of 500:2000 nm^2 (width:height) and five mesh cells per effective wavelength in the simulated materials. The metal surface was meshed with 1.5-nm vertex spacing. First-order scattering boundary conditions were used. The simulation environment consisted of a 1000-nm SiO_2 bottom layer, 20-nm Al_2O_3, 76-nm BTO, 38-nm BTO slab and metal electrodes, and 1000-nm air cladding. The geometry was adapted to the TEM imaging of devices as fabricated and characterized. Simulations were performed at $\lambda = 1550$ nm; material data obtained from ellipsometry was used for BTO and Au.

7.4 Ultra-Low Power Tuning in Hybrid Barium Titanate-Silicon Nitride Electro-Optic Devices on Silicon

7.4.1 Contributions

The following sections are reproduced with permission from *ACS Photonics*, submitted for publication. Unpublished work copyright 2019 American Chemical Society. The manuscript details a series of experiments I conducted at IBM Research – Zurich in the spring of 2018 [72] and is under review with the title "Ultra-Low Power Tuning in Hybrid Barium Titanate-Silicon Nitride Electro-Optic Devices on Silicon."

All electro-optic experiments presented in the manuscript and in the sections below were performed by me with assistance provided by Dr. Stefan Abel and Felix Eltes. Additionally, I designed the devices and the chip layout with significant input from Felix Eltes. XRD materials characterization was performed by Felix Eltes with assistance from Dr. Jean Fompeyrine. Device fabrication was also completed by Felix Eltes with some assistance from Daniele Caimi and Norbert Meier. The manuscript was primarily written by myself and Dr. Stefan Abel, with significant input from Felix Eltes and Dr. Jean Fompeyrine.

7.4.2 Introduction

Decades ago, the development of integrated electronic circuits revolutionized the electronics industry by enabling electronic circuits to be made smaller, faster, and more cheaply. A similar trend has reached optical networks, where the integration of bulk- and fiber-based circuits can nowadays be realized in photonic integrated circuits (PICs) on compact semiconductor substrates. PICs already play a major role in data centers and their use is expected to rapidly expand in the coming years owing to the explosive growth of global network traffic [2], [4], [73]. In addition to well-established transceiver technologies

for data centers, PICs also show promise for use in a wide variety of emerging fields, such as reservoir computing [5], deep learning [6], photonic quantum computing [7], and sensing technologies [8]–[10].

While many materials have been explored for PICs, silicon- and silicon nitride (SiN)-based PIC technologies [30], [74]–[76] have received widespread attention due to their compatibility with existing complementary metal-oxide-semiconductor (CMOS) processes. CMOS compatibility is a critical consideration for technological adoption, as it allows for the reliable and cost-efficient construction of micro- and nanoscale devices and the co-integration of electronic and photonic circuitry on a single chip. Besides CMOS compatibility, both silicon and SiN have their own unique advantages when employed in PICs. For example, silicon offers excellent light confinement and a variety of nonlinear effects that can be useful for the construction of a multitude of photonic devices [74]. On the other hand, SiN can accommodate a broad wavelength range, including visible light, can be stacked to form multi-planar device architectures [77], and can be engineered for very low optical propagation losses [78], [79].

Regardless of one's material platform of choice, a key functionality needed in PICs is the ability to tune the effective refractive index of the guided optical signal. Such refractive index tuning is the building block for electro-optic modulators [31], switches [80], and filters [81]–[84], which are all fundamental components of PICs. Additionally, refractive index tuning can be used to compensate for unavoidable fabrication imperfections [85]–[88] and thermal fluctuations [89], [90] that erode device performance. Such compensation is particularly important for resonant devices, which offer very small footprints but also suffer from a high sensitivity to environmental changes and fabrication tolerances.

Several different mechanisms have been exploited for tuning the effective refractive index in integrated photonic devices. The most prominent are the thermo-optic effect, which is present in both silicon- and SiN-based platforms [90]–[92], and the plasma dispersion effect, which is available in silicon-based devices [31], [33]. Unfortunately, both tuning mechanisms are inherently power consuming. Thermo-optic tuning relies on Joule heating and therefore necessitates significant current flow. Similarly, forward-biased plasma dispersion silicon photonic devices require current flow through a p-n junction. State-of-the-art resonator devices relying on the thermo-optic and plasma dispersion effects for tuning show power consumption on the order of 0.1 – 100 mW/free spectral range (FSR) [89]–[91]. The static tuning power of such devices can be several times larger than their dynamic power consumption [93]–[95], placing severe restrictions on the use of resonant devices in a variety of applications including high throughput data centers and next-generation sensing technology Reverse-biased devices are less power consuming but can induce large optical propagation losses caused by high doping levels and are generally less suited for tuning due to the small accessible refractive index window. By introducing III-V layers and forming hybrid III-V/silicon phase shifters, these loss issues have recently been significantly improved [96]. However, the delicate process of wafer-bonding III-V layers to silicon waveguides complicates fabrication while the unavailability of 200 mm InP wafers limits the scalability of the hybrid III-V/silicon devices. Furthermore, the transparency window of hybrid III-V/silicon devices is limited to wavelengths greater than ~1.3 μm by the III-V layers, in contrast to the large transparent window available in hybrid BTO-SiN devices, which should extend into the visible spectrum.

In contrast to the thermo-optic and plasma dispersion effects, the Pockels effect is a second-order nonlinear optic effect describing the electric field-driven modulation of the refractive index. The Pockels effect is therefore uniquely suited for use in ultra-low power

integrated photonics applications, as no electric current flow or doped regions in the waveguide are required for operation. Additionally, the linear change of refractive index with applied field facilitates the use of Pockels devices in technological applications by reducing the complexity of the control circuitry. As neither silicon nor SiN display a Pockels effect, other materials must be combined with the waveguides. The ferroelectric perovskite $BaTiO_3$ (barium titanate, BTO) is an excellent candidate as it displays a very large Pockels response even in thin-film form [29] and can be readily integrated with silicon *via* an epitaxial $SrTiO_3$ buffer layer [22], [43]. Furthermore, low-loss hybrid BTO-silicon waveguides have already been demonstrated [44], as well as electro-optic operation in hybrid BTO-silicon structures [29], [46], [97] on 200 mm wafer sizes [13], [98].

While hybrid BTO-silicon photonic devices have recently garnered significant attention, the combination of BTO with SiN potentially offers many advantages over a silicon-based platform. For example, the integration of SiN strip waveguides with BTO allows for the combination of ultra-low power refractive index tuning *via* the Pockels effect in BTO with the low optical losses available in SiN [78], [79]. In addition, there are no mobile charge carriers in highly-insulating SiN that can impact electro-optic performance. Finally, due to the different material absorption, the optical wavelength range available in BTO-SiN waveguides is significantly wider than in BTO-Si waveguides, allowing operation in the visible wavelength range, for example. In this work, we fabricate hybrid BTO-SiN racetrack resonators and demonstrate the ability to electrically tune the effective refractive index on the order of 10^{-3}. Our devices feature a remarkably low power consumption of approximately 106 nW/FSR, several orders of magnitude lower than many previous reports [46], [89]–[91], [99]. We demonstrate the technological potential of our hybrid BTO-SiN technology by compensating thermal refractive index variations over a

temperature range of 20 °C as well as by demonstrating tunable multi-resonator optical filters that can be used to compensate for unavoidable fabrication imperfections.

7.4.3 Methods

We epitaxially grow 80 nm single crystalline BTO thin films (Figure 7.10a) by molecular beam epitaxy on silicon-on-insulator substrates and subsequently transfer them to thermally oxidized silicon wafers via wafer-bonding [29]. The device silicon layer of the donor wafer is removed by dry chemical etching. Next, 150 nm SiN is deposited on the BTO layer by plasma-enhanced chemical vapor deposition (PECVD) and patterned to form waveguides using e-beam lithography and reactive ion etching. Finally, a combination of tungsten deposition, SiO_2 deposition, and dry chemical etching processes were used to form side electrodes, vias, cladding, and metal pads for contacting the devices, resulting in a final device structure shown schematically in Figure 7.10b.

Light from a fiber-coupled, tunable continuous-wave laser operating around 1.55 μm was coupled into and out of the devices *via* grating couplers and detected with a power meter. The incoming polarization was set using a polarization controller. A parameter analyzer was used to apply the bias to the devices and to determine the leakage currents. Device temperature was adjusted and monitored *via* an external temperature controller for temperature-dependent measurements. A detailed schematic of the setup used for electro-optic characterization is presented in the Supporting Information section of [72].

Optical mode simulations were performed using COMSOL Multiphysics and the COMSOL RF module. The refractive indices used for the simulations are presented in the Supporting Information of [72]. The perfect electrical conductor boundary condition was applied to all outer boundaries of the 2d simulation cell. The electric field was taken to be perfectly in-plane initially and the wavelength was taken to be 1550 nm.

7.4.4 Ultra-Low Power Refractive Index Tuning

The waveguides of the fabricated devices support a single TE-like mode (Figure 7.10c) with 18% of the optical power confined in the electro-optically active BTO layer. Power confinement in the BTO scales with BTO thickness and can therefore be increased by fabricating devices with thicker BTO layers. The propagation losses are 9.4 dB/cm (Figure 7.11), comparable to previous reports of hybrid BTO-silicon waveguides [13], [29], [44], and can likely be reduced through the development of an optimized fabrication process [44], [79]. Racetrack resonators used for index tuning experiments feature two 75 μm-long straight segments with electrodes separated by 5.1 μm to apply an electric field for electro-optic operation (Figure 7.10d). We designed the electrodes such that the electric field is applied along the BTO⟨011⟩ family of lattice vectors in order to exploit the largest Pockels coefficient, r_{42}, and maximize the electro-optic response [29].

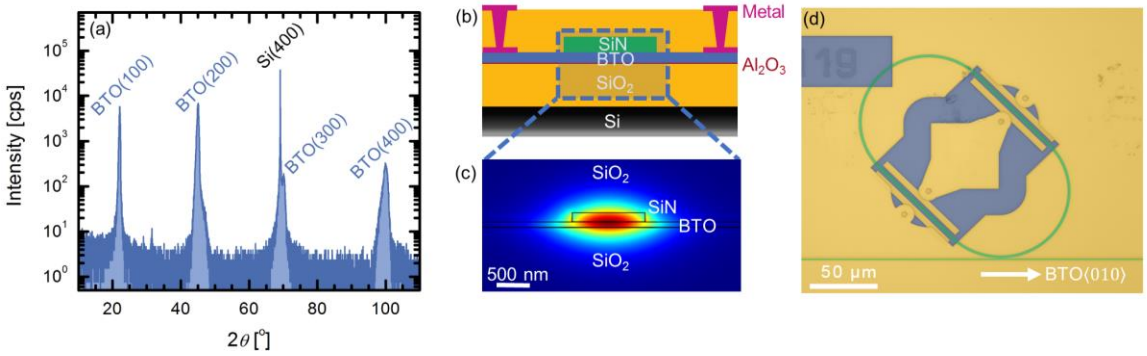

Figure 7.10: (a) Out-of-plane θ-2θ XRD scan showing an epitaxial BTO thin film on silicon. (b) Cross-sectional schematic of hybrid BTO-SiN devices. The BTO layer is 80 nm-thick, while the SiN waveguide is 150 nm-thick and 1.1 μm-wide. (c) Simulated fundamental TE mode in a hybrid BTO-SiN waveguide. The color mapping indicates the norm of the electric field, where red represents regions of high field and blue represents regions of low field. (d) False-color optical micrograph of a hybrid BTO-SiN racetrack resonator used for index tuning experiments, showing the SiN strip waveguides (green), metal electrodes (yellow) and regions of SiO_2 cladding not covered with metal (blue). The white arrow indicates the crystalline orientation of the BTO layer.

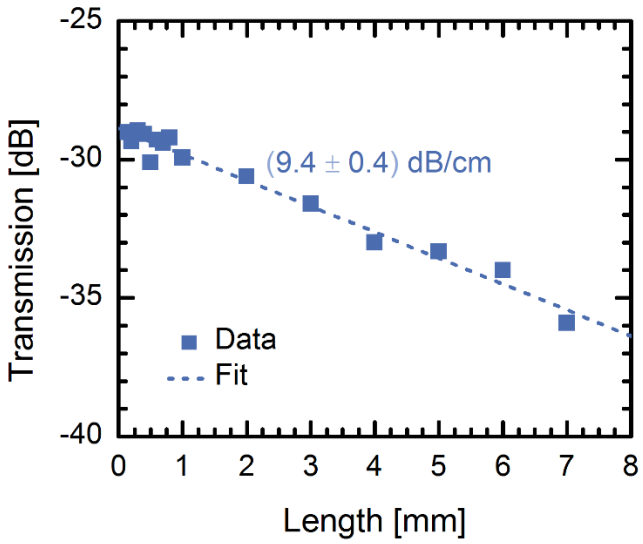

Figure 7.11: Maximum transmission of straight waveguides of different lengths (squares) and linear fit to the data (dashed line).

The transmission spectra of the devices (Figure 7.12a) feature sharp resonances with extinction ratios of approximately 18 dB. Upon applying an electric field across the device, the resonance positions shift, indicating a change in the effective refractive index within the resonator. The electric field E across the waveguide was estimated according to $E = V/d$ where V is the applied bias and d is the separation between electrodes. We track the shift of the effective index as a function of applied field (Figure 7.12b). The refractive index varies linearly with the applied field above fields of approximately 40 kV/cm, as expected for the Pockels effect. At lower fields, the refractive index variation deviates from the linear behavior due to nonlinear contributions from ferroelectric domain switching [13], [22], [29]. Such domain switching results in hysteretic behavior of the refractive index when sweeping the electric field (Figure 7.12b), in line with previous reports [13], [22], [29].

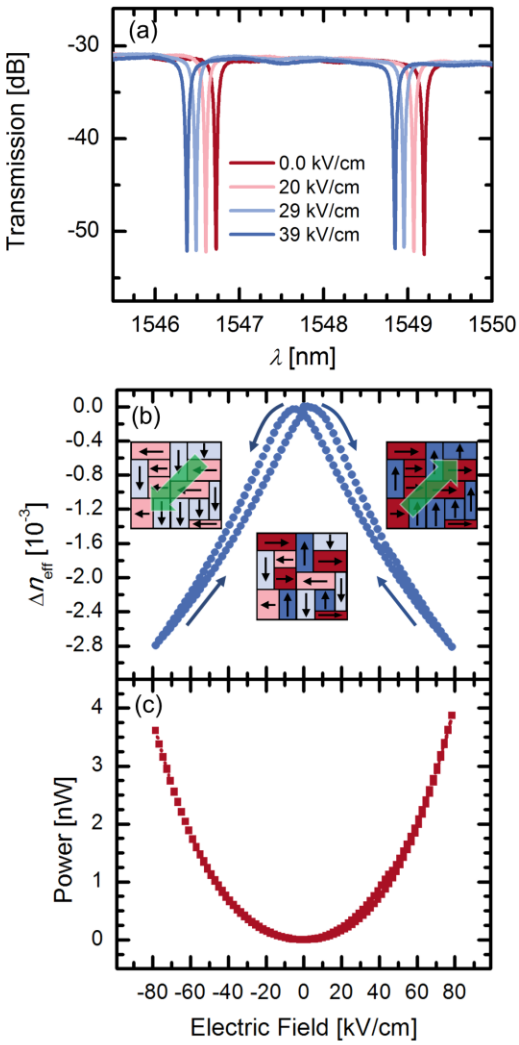

Figure 7.12: (a) Transmission spectra of a racetrack resonator for different electric fields. The position of the resonance is shifted due to the Pockels effect in BTO. (b) The change of the effective refractive index in the active phase shifter section as a function of applied electric field. As expected, the ferroelectric nature of BTO results in a hysteresis in the electro-optic response. Insets are schematics of the top view of the ferroelectric domain structure in the poled (left and right) and unpoled (center) states. The BTO films show four types of ferroelectric domains with the ferroelectric polarization (black arrow) corresponding to the vertical (blue) and horizontal (red) directions [22], [29]. Green arrows represent the applied electric field. (c) Power consumption as a function of the applied field recorded during measurement of the hysteresis loop shown in (b). The power function is defined as the leakage current times the applied voltage.

An effective Pockels coefficient of approximately 343 pm/V is extracted from the index tuning experiments, which agrees with previous reports on BTO thin films [98]. Due to the strong dependence of the effective Pockels coefficient on the crystalline quality, morphology, and symmetry, which in turn strongly depend on deposition conditions [48] and film thicknesses [27], [28], both larger [29] and smaller [22], [48], [97] Pockels coefficients in a similar range as the value determined in this study have been reported in the past.

The application of a bias across the device does not alter the extinction ratios even up to 40 V (78 kV/cm). This behavior is expected, as the Pockels effect does not impact the imaginary part of the refractive index. In contrast, active operation of devices exploiting the plasma dispersion effect typically results in undesired, additional optical absorption [89], [100]. Our devices show ultra-low power consumption (Figure 7.12c) of 106 ± 5 nW/FSR (Figure 7.13), several orders of magnitude less than that in plasma dispersion- and thermo-optic-based electro-optic tuning devices that are compatible with standard PIC integration routes [89]–[91], [99].

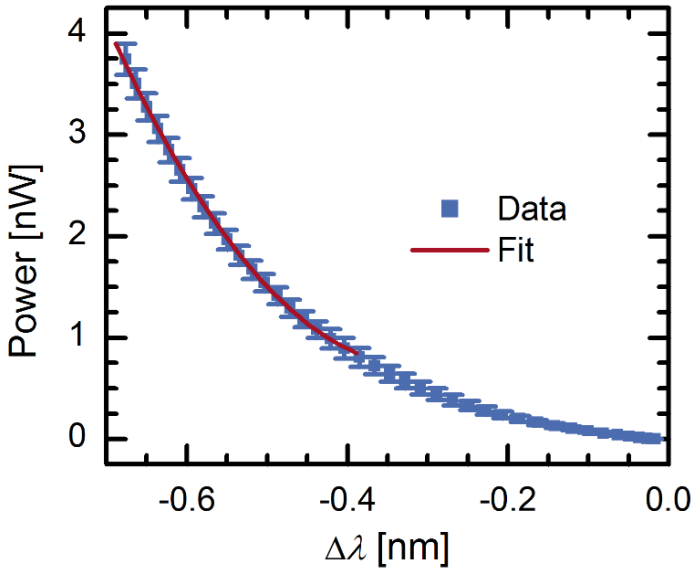

Figure 7.13: Power consumption as a function of $\Delta\lambda$. Closed, blue squares are data points obtained by averaging $P(\Delta\lambda)$ for both positive and negative applied electric fields E and increasing and decreasing magnitude of E (Figure 7.12b). The standard deviation of the measurements is shown as error bars. The solid, red line is a quadratic fit to the data.

It should be noted that a full FSR of tuning is not achieved in the devices reported here. However, the tuning range can be significantly increased for a given electric field and the resonator devices can be optimized for low-bias operation by improving the electrode design and by increasing the BTO thickness and quality in future devices, thereby increasing the optical confinement in BTO as well as the effective Pockels coefficient. We estimate the power consumption of the optimized resonators to be approximately 22 nW/FSR. Furthermore, the BTO-SiN platform can be used to construct linear phase shifters that are well-suited for low-bias operation due to their much greater active length relative to compact resonator devices. Our calculations suggest $V_\pi = 3$ V for a 1 mm-long linear phase shifter constructed from the BTO-SiN platform with a corresponding power consumption $P_\pi \approx 1$ nW. A similar power consumption was recently reported for hybrid III-V/silicon linear phase shifters [96]. However, the small band gap of the III-V materials and challenging fabrication route significantly limits the optically transparent window and integration flexibility relative to the hybrid BTO-SiN platform discussed in this work.

The measured power consumption is the result of a small leakage current across the nominally insulating BTO layer. The leakage current in oxides is typically associated with a Pool-Frenkel type conduction mechanism [101]. The origin of the charge transport are defects in the material such as oxygen vacancies or interfacial traps, which are determined by the material deposition and device fabrication process. Indeed, oxides that can be used for Pockels-active devices can show significant power consumption due to relatively high leakage currents [46], [102]. The realization of exceptionally low leakage current on the order of pA even after device processing and PECVD of SiN is a major achievement and indicates the great promise of the hybrid BTO-SiN platform in realistic, power-sensitive technologies.

7.4.5 Thermal Compensation

Having established ultra-low power refractive index tuning in the hybrid BTO-SiN electro-optic devices, we use the platform to demonstrate two example applications of this technology. First, we use racetrack resonator devices to compensate for thermal refractive index variations. A key challenge facing future integrated photonics technology is the ability to sustain reliable operation in environments subject to temperature fluctuations [103]. Because silicon [104]–[106] and SiN [92] have large thermo-optic coefficients, relatively minor temperature fluctuations can have a significant impact on the effective refractive index of guided modes. In resonators, thermally-induced index fluctuations can therefore alter a device's optical characteristics at a given wavelength unless such index fluctuations are appropriately compensated. Ultra-low power Pockels tuning of the effective refractive index allows for an efficient way to compensate for thermal index drift without dissipating additional heat across the device as would occur in devices exploiting current-driven tuning mechanisms.

To demonstrate thermal refractive index drift compensation *via* Pockels tuning, we analyzed the transmission of the devices in the temperature range from room temperature (25 °C) up to 45 °C (Figure 7.14a). We extracted a thermo-optic resonance shift in our devices of 21.6 pm/°C. At each stable temperature point, we tuned the bias appropriately such as to shift the resonance back to its room-temperature position (Figure 7.14b) and measured the power dissipated across the device at the optimal tuning voltage. Through this procedure, we compensate for thermal refractive index variation over a temperature range of 20 °C while consuming less than 1 nW of static power, four orders of magnitude less than the approximately 50 μW of static power required to compensate for heating of 10 °C in state-of-the-art p-n modulators [89]. Importantly, the minimal power dissipated across our devices during electro-optic operation results in negligible heating, allowing for the compensation of large temperature fluctuations without introducing additional heating from device operation. The negligible heating in our devices also reduces thermal cross-talk as compared to thermo-optic devices [107], allowing for exceedingly local refractive index tuning even for dense device arrays. The relatively high Curie temperature of BTO allows for high-temperature operation in BTO-based electro-optic devices, with the unimpaired operation of BTO-on-silicon plasmonic modulators having been demonstrated up to 130 °C [14].

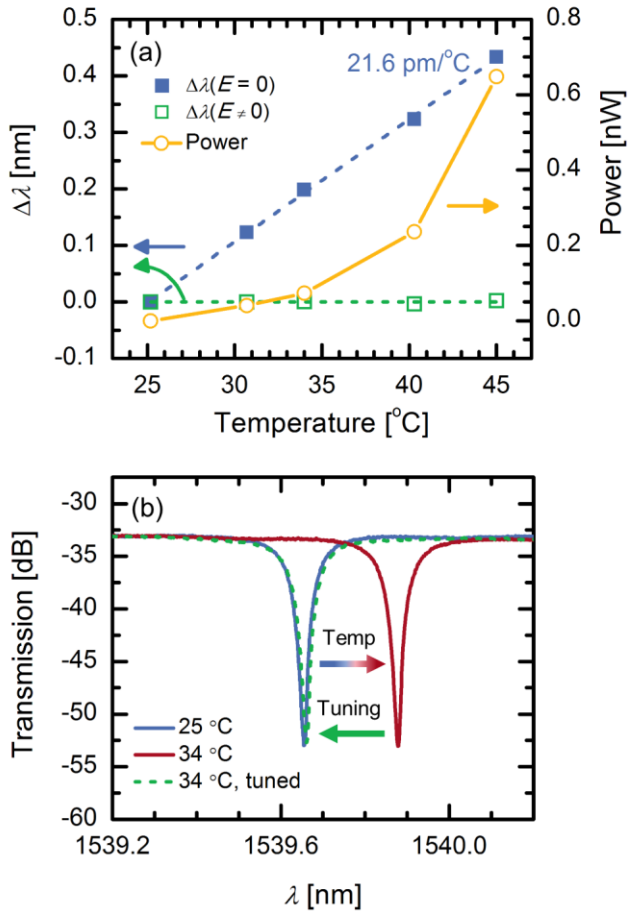

Figure 7.14: (a) Zero-field (blue) and electrically tuned (green) resonance wavelength shift and static tuning power (yellow) as a function of temperature. Dashed lines are linear fits to the data. (b) Racetrack resonator spectra showing the room temperature resonance (blue) and the same resonance at 34 °C, both before (red, solid line) and after (green, dashed line) tuning.

7.4.6 Tunable Multi-Resonator Filters

As a second example application of our hybrid BTO-SiN platform, we fabricated coupled multi-resonator optical filters. Many photonics applications, including quantum information processing [82], wavelength division multiplexing [81], and on-chip reconfigurable networks [84] make use of high-quality optical filters. While many reports have explored the use of coupled resonators as optical filters [108]–[111], resonators suffer

from an extreme sensitivity to fabrication tolerances and even minor imperfections can decouple resonances [85]–[88]. However, by incorporating an optical path length trimming mechanism into the devices to compensate for fabrication imperfections, coupled resonator filters can be made significantly more robust.

We have utilized our BTO-SiN platform to fabricate tunable, multi-racetrack resonator optical filters (Figure 7.15a). The devices feature three racetrack resonators coupled to a straight waveguide, although the design can be extended to a larger number of resonators. Because the purpose of these experiments is to demonstrate the ability to overcome fabrication imperfections in multi-resonator filters *via* low-power electro-optic tuning, we focused on cascaded multi-resonator filters, rather than coupled resonator filters [108], for simplicity. Differences in resonator cavity lengths result in the appearance of three distinct resonances (Figure 7.15b), one for each resonator. By appropriately biasing two of the resonators, the individual resonances can be coalesced into a single resonance whose extinction ratio is equal to the sum of the extinction ratios of the individual resonances (Figure 7.15b). Here, we have purposely designed devices in which the extinction ratios of the individual resonances are only 6 dB to ensure the minimum transmission within the coalesced resonance is still measurable in our experimental setup. However, the multi-resonator tunable filters presented here can in principle be used to fabricate devices with very large extinction ratios. The coalesced resonance can itself also be spectrally-tuned (Figure 7.15c) by appropriately biasing all three resonators. The linear tuning behavior of the refractive index with the electric field (Figure 7.12b) simplifies the determination of the individual resonator bias conditions required for tuning the coalesced resonance.

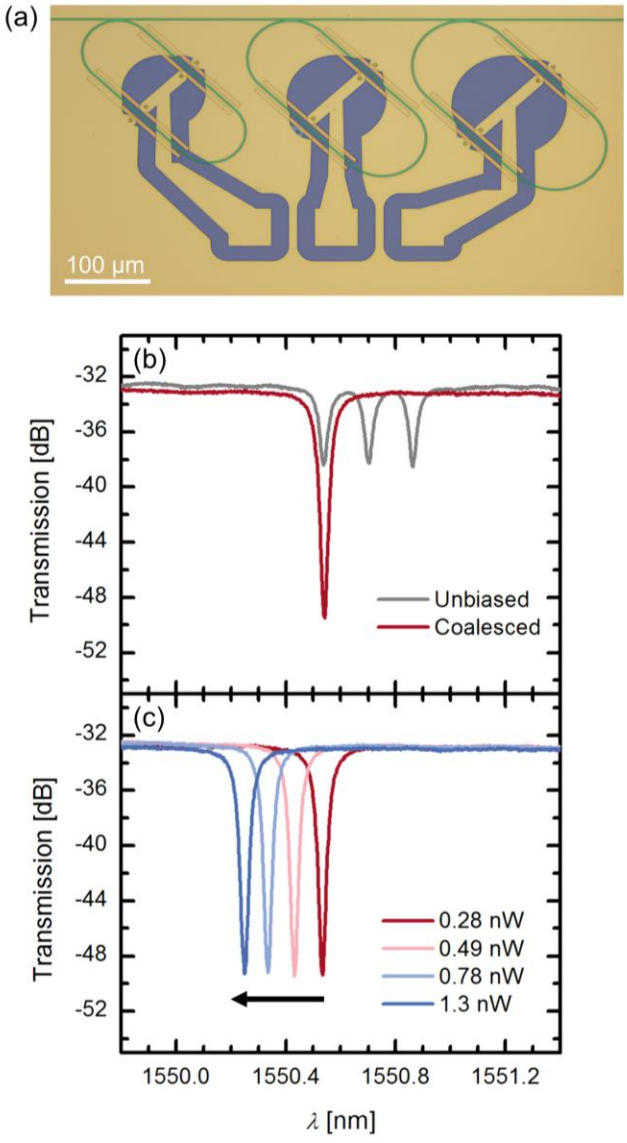

Figure 7.15: (a) False-color optical micrograph of a multi-resonator tunable filter, showing the SiN strip waveguides (green), metal electrodes (yellow) and regions of SiO_2 cladding not covered with metal (blue). (b) Unbiased (gray) and biased (red) spectra of the multi-resonator filter, demonstrating ability to coalesce individual resonances into a single resonance. (c) Coalesced resonance shifted by an external electric field. The arrow indicates the tuning direction and the legend indicates the total tuning power.

7.4.7 Conclusions

In summary, we have demonstrated ultra-low power refractive index tuning in silicon-integrated hybrid BTO-SiN photonic devices. By exploiting the large electric field-driven Pockels effect in BTO, we have realized index tuning with static power consumption of approximately 106 nW/FSR in racetrack resonator devices. We use our devices to compensate for thermal refractive index variations and demonstrate the ability to compensate for heating of 20 °C while consuming less than 1 nW of static power. Additionally, we fabricate multi-resonator optical filters and provide a proof-of-concept demonstration for using the Pockels effect to perform optical path length trimming and overcome decoupling arising from fabrication imperfections.

The devices we present outperform previously reported tuning elements in terms of power consumption by several orders of magnitude. Furthermore, the combination of BTO with SiN enables fully dielectric waveguides with very low propagation losses that extend the optically transparent window into the visible range, allowing the hybrid BTO-SiN platform to find use in a wide variety of next-generation technologies including bio-sensors [112] and LIDAR [113], [114]. Our results show the technological potential of the Pockels-active hybrid BTO-SiN platform for ultra-low power integrated photonic devices. The availability of such devices in integrated photonics shines new light onto the implementation of resonant structures in compact PICs. While such structures offer a variety of attractive properties, such as small footprints and sharp transmission spectra as needed *e.g.* for filters, their applicability has always been limited by the power consumption needed for active tuning. Hybrid BTO-SiN devices can overcome this issue and enable the next generation of photonic applications, including compact communications technologies, optical computing systems, and ultra-sensitive photonic sensors.

7.5 SUMMARY AND FUTURE WORK

The results of this chapter have significantly advanced the state-of-the art of integrated electro-optic devices through the incorporation of the excellent Pockels material BTO. The results from Section 7.3 unambiguously demonstrated the presence of the Pockels effect in hybrid BTO-silicon devices integrated into photonic and plasmonic structures on silicon. While the photonic resonator devices allow for the quantitative determination of the individual Pockels tensor elements of BTO, the plasmonic devices enable bandwidth measurements at frequencies up to 65 GHz. The results from these two complementary device structures demonstrate that BTO maintains its superior electro-optical properties after fabrication of both microscale photonic and nanoscale plasmonic components. Key characteristics, such as the high-speed response, the angular anisotropy, and hysteretic switching, rule out other physical effects as the origin of the electro-optic response. Furthermore, the magnitude of the electro-optic response is bulk-like [20] and many times larger than for any Pockels materials previously integrated on silicon [18], [22], [115]. The chemical and thermal stability of oxides also outperform those of organic nonlinear materials [38], [64].

As a next iteration of the design of BTO-based photonic devices, ultra-low power refractive index tuning was demonstrated in silicon-integrated hybrid BTO-SiN photonic devices. By exploiting the large electric field-driven Pockels effect in BTO, the devices realized index tuning with static power consumption of approximately 106 nW/FSR in racetrack resonator devices. These hybrid BTO-SiN devices were used to compensate for thermal refractive index variations and demonstrated the ability to compensate for heating of 20 °C while consuming less than 1 nW of static power. Additionally, coupled multi-resonator optical filters were fabricated from the BTO-SiN platform and used to provide a

proof-of-concept demonstration for using the Pockels effect to perform optical path length trimming and overcome decoupling arising from fabrication imperfections.

The hybrid BTO-SiN devices presented in Section 7.4 outperform previously reported tuning elements in terms of power consumption by several orders of magnitude. The results show the technological potential of the Pockels-active hybrid BTO-SiN platform for ultra-low power integrated photonic devices. The availability of such devices in integrated photonics shines new light onto the implementation of resonant structures in compact PICs. While such structures offer a variety of attractive properties, such as small footprints and sharp transmission spectra as needed e.g. for filters, their applicability has always been limited by the power consumption needed for active tuning. Hybrid BTO-SiN devices can overcome this issue and enable the next generation of photonic applications, including compact communications technologies, optical computing systems, and ultra-sensitive photonic sensors.

The ability to control the Pockels effect in integrated photonic devices has profound implications for a wide variety of technologies. Sensory [65], [66], mid-infrared [67], and neuromorphic computing applications [5], [68] would all strongly benefit from devices that are operated at reduced operating speeds or exploit non-volatile electro-optic effects. Ultimately, silicon-integrated BTO-based photonic devices provide an additional degree of freedom for designers to realize not only a new generation of compact, high-speed modulators, but also novel devices such as ultra-low-power tuning elements [46], non-volatile optical memories [69], or microwave-to-optical quantum converters [70].

7.6 REFERENCES

[1] B. E. A. Saleh and M. C. Teich, *Fundamentals of Photonics*. New York, USA: John Wiley & Sons, Inc., 1991.

[2] C. Lam, Hong Liu, B. Koley, Xiaoxue Zhao, V. Kamalov, and V. Gill, "Fiber optic communication technologies: What's needed for datacenter network operations," *IEEE Commun. Mag.*, vol. 48, no. 7, pp. 32–39, Jul. 2010.

[3] Z. Zhou, X. Wang, H. Yi, Z. Tu, W. Tan, Q. Long, M. Yin, and Y. Huang, "Silicon photonics for advanced optical communication systems," *Opt. Eng.*, vol. 52, no. 4, p. 045007, Apr. 2013.

[4] D. Thomson, A. Zilkie, J. E. Bowers, T. Komljenovic, G. T. Reed, L. Vivien, D. Marris-Morini, E. Cassan, L. Virot, J.-M. Fédéli, J.-M. Hartmann, J. H. Schmid, D.-X. Xu, F. Boeuf, P. O'Brien, G. Z. Mashanovich, and M. Nedeljkovic, "Roadmap on silicon photonics," *J. Opt.*, vol. 18, no. 7, p. 073003, Jul. 2016.

[5] K. Vandoorne, P. Mechet, T. Van Vaerenbergh, M. Fiers, G. Morthier, D. Verstraeten, B. Schrauwen, J. Dambre, and P. Bienstman, "Experimental demonstration of reservoir computing on a silicon photonics chip," *Nat. Commun.*, vol. 5, p. 3541, Mar. 2014.

[6] Y. Shen, N. C. Harris, S. Skirlo, M. Prabhu, T. Baehr-Jones, M. Hochberg, X. Sun, S. Zhao, H. Larochelle, D. Englund, and M. Soljačić, "Deep learning with coherent nanophotonic circuits," *Nat. Photonics*, vol. 11, no. 7, pp. 441–446, Jun. 2017.

[7] X. Qiang, X. Zhou, J. B. J. Wang, C. M. Wilkes, T. Loke, S. O'Gara, L. Kling, G. D. Marshall, R. Santagati, T. C. Ralph, J. B. J. Wang, J. L. O'Brien, M. G. Thompson, and J. C. F. Matthews, "Large-scale silicon quantum photonics implementing arbitrary two-qubit processing," *Nat. Photonics*, vol. 12, no. 9, pp. 534–539, Sep. 2018.

[8] S. M. Leinders, W. J. Westerveld, J. Pozo, P. L. M. J. van Neer, B. Snyder, P. O'Brien, H. P. Urbach, N. de Jong, and M. D. Verweij, "A sensitive optical micro-machined ultrasound sensor (OMUS) based on a silicon photonic ring resonator on an acoustical membrane," *Sci. Rep.*, vol. 5, no. 1, p. 14328, Nov. 2015.

[9] A. Dutt, C. Joshi, X. Ji, J. Cardenas, Y. Okawachi, K. Luke, A. L. Gaeta, and M. Lipson, "On-chip dual-comb source for spectroscopy," *Sci. Adv.*, vol. 4, no. 3, p. e1701858, Mar. 2018.

[10] D. M. Kita, B. Miranda, D. Favela, D. Bono, J. Michon, H. Lin, T. Gu, and J. Hu, "High-performance and scalable on-chip digital Fourier transform spectroscopy," *Nat. Commun.*, vol. 9, no. 1, p. 4405, Dec. 2018.

[11] A. Politi, J. Matthews, M. G. Thompson, and J. L. O'Brien, "Integrated Quantum Photonics," *IEEE J. Sel. Top. Quantum Electron.*, vol. 15, no. 6, pp. 1673–1684, 2009.

[12] J. L. O'Brien, A. Furusawa, and J. Vučković, "Photonic quantum technologies," *Nat. Photonics*, vol. 3, no. 12, pp. 687–695, 2009.

[13] F. Eltes, M. Kroh, D. Caimi, C. Mai, Y. Popoff, G. Winzer, D. Petousi, S. Lischke, J. E. Ortmann, L. Czornomaz, L. Zimmermann, J. Fompeyrine, and S. Abel, "A novel 25 Gbps electro-optic Pockels modulator integrated on an advanced Si photonic platform," in *2017 IEEE International Electron Devices Meeting (IEDM)*, 2017, p. 24.5.1-24.5.4.

[14] A. Messner, F. Eltes, P. Ma, S. Abel, B. Baeuerle, A. Josten, W. Heni, D. Caimi, J. Fompeyrine, and J. Leuthold, "Integrated Ferroelectric $BaTiO_3$/Si Plasmonic Modulator for 100 Gbit/s and Beyond," in *Optical Fiber Communication Conference*, 2018, vol. Part F84-O, no. c, p. M2I.6.

[15] E. L. Wooten, K. M. Kissa, A. Yi-Yan, E. J. Murphy, D. a. Lafaw, P. F. Hallemeier, D. Maack, D. V. Attanasio, D. J. Fritz, G. J. McBrien, and D. E. Bossi, "A review of lithium niobate modulators for fiber-optic communications systems," *IEEE J. Sel. Top. Quantum Electron.*, vol. 6, no. 1, pp. 69–82, Jan. 2000.

[16] D. Janner, D. Tulli, M. García-Granda, M. Belmonte, and V. Pruneri, "Micro-structured integrated electro-optic $LiNbO_3$ modulators," *Laser Photonics Rev.*, vol. 3, no. 3, pp. 301–313, Apr. 2009.

[17] P. Rabiei, J. Ma, S. Khan, J. Chiles, and S. Fathpour, "Heterogeneous lithium niobate photonics on silicon substrates," *Opt. Express*, vol. 21, no. 21, p. 25573, Oct. 2013.

[18] L. Chen, Q. Xu, M. G. Wood, and R. M. Reano, "Hybrid silicon and lithium niobate electro-optical ring modulator," *Optica*, vol. 1, no. 2, p. 112, Aug. 2014.

[19] A. Yariv and P. Yeh, *Optical Waves in Crystals*. John Wiley & Sons, Inc., 1984.

[20] P. Bernasconi, M. Zgonik, P. Günter, and P. Gunter, "Temperature dependence and dispersion of electro-optic and elasto-optic effect in perovskite crystals," *J. Appl. Phys.*, vol. 78, no. 4, pp. 2651–2658, Aug. 1995.

[21] D. Khatib, B. Jannot, and P. Jullien, "Theory of electro-optic effect in the tetragonal phase of $BaTiO_3$," *Ferroelectr. Lett. Sect.*, vol. 15, no. 1, pp. 1–7, Jan. 1993.

[22] S. Abel, T. Stöferle, C. Marchiori, C. Rossel, M. D. Rossell, R. Erni, D. Caimi, M. Sousa, A. Chelnokov, B. J. Offrein, and J. Fompeyrine, "A strong electro-optically active lead-free ferroelectric integrated on silicon," *Nat. Commun.*, vol. 4, no. 1, p. 1671, Dec. 2013.

[23] P. Castera, D. Tulli, A. M. Gutierrez, and P. Sanchis, "Influence of $BaTiO_3$ ferroelectric orientation for electro-optic modulation on silicon," *Opt. Express*, vol. 23, no. 12, p. 15332, Jun. 2015.

[24] X. Hu, S. Cueff, P. R. Romeo, and R. Orobtchouk, "Modeling the anisotropic electro-optic interaction in hybrid silicon-ferroelectric optical modulator," *Opt. Express*, vol. 23, no. 2, p. 1699, Jan. 2015.

[25] M. Zgonik, P. Bernasconi, M. Duelli, R. Schlesser, P. Günter, M. H. Garrett, D. Rytz, Y. Zhu, and X. Wu, "Dielectric, elastic, piezoelectric, electro-optic, and elasto-optic tensors of $BaTiO_3$ crystals," *Phys. Rev. B*, vol. 50, no. 9, pp. 5941–5949, Sep. 1994.

[26] P. Castera, A. M. Gutierrez, D. Tulli, S. Cueff, R. Orobtchouk, P. Rojo Romeo, G. Saint-Girons, and P. Sanchis, "Electro-Optical Modulation Based on Pockels Effect in $BaTiO_3$ With a Multi-Domain Structure," *IEEE Photonics Technol. Lett.*, vol. 28, no. 9, pp. 990–993, May 2016.

[27] S. Abel, M. Sousa, C. Rossel, D. Caimi, M. D. Rossell, R. Erni, J. Fompeyrine, and C. Marchiori, "Controlling tetragonality and crystalline orientation in $BaTiO_3$ nano-layers grown on Si," *Nanotechnology*, vol. 24, no. 28, p. 285701, Jul. 2013.

[28] C. Dubourdieu, J. Bruley, T. M. Arruda, A. Posadas, J. Jordan-Sweet, M. M. Frank, E. Cartier, D. J. Frank, S. V Kalinin, A. A. Demkov, and V. Narayanan, "Switching of ferroelectric polarization in epitaxial $BaTiO_3$ films on silicon without a conducting bottom electrode," *Nat. Nanotechnol.*, vol. 8, no. 10, pp. 748–754, Oct. 2013.

[29] S. Abel, F. Eltes, J. E. Ortmann, A. Messner, P. Castera, T. Wagner, D. Urbonas, A. Rosa, A. M. Gutierrez, D. Tulli, P. Ma, B. Baeuerle, A. Josten, W. Heni, D. Caimi, L. Czornomaz, A. A. Demkov, J. Leuthold, P. Sanchis, and J. Fompeyrine, "Large Pockels effect in micro- and nanostructured barium titanate integrated on silicon," *Nat. Mater.*, vol. 18, no. 1, pp. 42–47, Jan. 2019.

[30] M. Hochberg and T. Baehr-Jones, "Towards fabless silicon photonics," *Nat. Photonics*, vol. 4, no. 8, pp. 492–494, Aug. 2010.

[31] G. T. Reed, G. Mashanovich, F. Y. Gardes, and D. J. Thomson, "Silicon optical modulators," *Nat. Photonics*, vol. 4, no. 8, pp. 518–526, Aug. 2010.

[32] G. T. Reed, G. Z. Mashanovich, F. Y. Gardes, M. Nedeljkovic, Y. Hu, D. J. Thomson, K. Li, P. R. Wilson, S. W. Chen, and S. S. Hsu, "Recent breakthroughs in carrier depletion based silicon optical modulators," *Nanophotonics*, vol. 3, no. 4–5, pp. 229–245, 2014.

[33] R. Soref and B. Bennett, "Electrooptical effects in silicon," *IEEE J. Quantum Electron.*, vol. 23, no. 1, pp. 123–129, Jan. 1987.

[34] S. Zhalehpour, J. Lin, and L. Rusch, "SiP IQ modulator linearization by memory polynomial pre-distortion model," in *International Photonics Conference of the IEEE*, 2017, p. TuH2.3.

[35] K. Xu, L. G. Yang, J. Y. Sung, Y. M. Chen, Z. Z. Cheng, C. W. Chow, C. H. Yeh, and H. K. Tsang, "Compatibility of silicon Mach-Zehnder modulators for advanced modulation formats," *J. Light. Technol.*, vol. 31, no. 15, pp. 2550–2554, 2013.

[36] D. Petousi, L. Zimmermann, A. Gajda, M. Kroh, K. Voigt, G. Winzer, B. Tillack, and K. Petermann, "Analysis of Optical and Electrical Tradeoffs of Traveling-Wave Depletion-Type Si Mach–Zehnder Modulators for High-Speed Operation," *IEEE J. Sel. Top. Quantum Electron.*, vol. 21, no. 4, pp. 199–206, Jul. 2015.

[37] J. Leuthold, C. Koos, W. Freude, L. Alloatti, R. Palmer, D. Korn, J. Pfeifle, M. Lauermann, R. Dinu, S. Wehrli, M. Jazbinsek, P. Gunter, M. Waldow, T. Wahlbrink, J. Bolten, H. Kurz, M. Fournier, J.-M. Fedeli, H. Yu, and W. Bogaerts, "Silicon-Organic Hybrid Electro-Optical Devices," *IEEE J. Sel. Top. Quantum Electron.*, vol. 19, no. 6, pp. 114–126, Nov. 2013.

[38] W. Heni, Y. Kutuvantavida, C. Haffner, H. Zwickel, C. Kieninger, S. Wolf, M. Lauermann, Y. Fedoryshyn, A. F. Tillack, L. E. Johnson, D. L. Elder, B. H. Robinson, W. Freude, C. Koos, J. Leuthold, and L. R. Dalton, "Silicon–Organic and Plasmonic–Organic Hybrid Photonics," *ACS Photonics*, vol. 4, no. 7, pp. 1576–1590, Jul. 2017.

[39] K. Alexander, J. P. George, J. Verbist, K. Neyts, B. Kuyken, D. Van Thourhout, and J. Beeckman, "Nanophotonic Pockels modulators on a silicon nitride platform," *Nat. Commun.*, vol. 9, no. 1, p. 3444, Dec. 2018.

[40] S. Abel and J. Fompeyrine, "Electro-Optically Active Oxides on Silicon for Photonics," in *Thin Films on Silicon*, vol. 8, V. Narayanan, M. M. Frank, and A. A. Demkov, Eds. World Scientific, 2016, pp. 455–501.

[41] A. Petraru, J. Schubert, M. Schmid, O. Trithaveesak, and C. Buchal, "Integrated optical Mach-Zehnder modulator based on polycrystalline $BaTiO_3$," *Opt. Lett.*, vol. 28, no. 24, pp. 2527–9, 2003.

[42] P. Girouard, P. Chen, Y. K. Jeong, Z. Liu, S.-T. Ho, and B. W. Wessels, "$\chi^{(2)}$ Modulator With 40-GHz Modulation Utilizing $BaTiO_3$ Photonic Crystal Waveguides," *IEEE J. Quantum Electron.*, vol. 53, no. 4, pp. 1–10, Aug. 2017.

[43] A. R. Meier, F. Niu, and B. W. Wessels, "Integration of $BaTiO_3$ on Si (001) using MgO/STO buffer layers by molecular beam epitaxy," *J. Cryst. Growth*, vol. 294, no. 2, pp. 401–406, Sep. 2006.

[44] F. Eltes, D. Caimi, F. Fallegger, M. Sousa, E. O'Connor, M. D. Rossell, B. Offrein, J. Fompeyrine, and S. Abel, "Low-Loss $BaTiO_3$–Si Waveguides for Nonlinear Integrated Photonics," *ACS Photonics*, vol. 3, no. 9, pp. 1698–1703, Sep. 2016.

[45] C. Xiong, W. H. P. Pernice, J. H. Ngai, J. W. Reiner, D. Kumah, F. J. Walker, C. H. Ahn, and H. X. Tang, "Active Silicon Integrated Nanophotonics: Ferroelectric $BaTiO_3$ Devices," *Nano Lett.*, vol. 14, no. 3, pp. 1419–1425, Mar. 2014.

[46] S. Abel, T. Stoferle, C. Marchiori, D. Caimi, L. Czornomaz, M. Stuckelberger, M. Sousa, B. J. Offrein, and J. Fompeyrine, "A Hybrid Barium Titanate–Silicon Photonics Platform for Ultraefficient Electro-Optic Tuning," *J. Light. Technol.*, vol. 34, no. 8, pp. 1688–1693, Apr. 2016.

[47] A. Messner, F. Eltes, P. Ma, S. Abel, B. Baeuerle, A. Josten, W. Heni, D. Caimi, J. Fompeyrine, and J. Leuthold, "Integrated Ferroelectric Plasmonic Optical Modulator," in *Optical Fiber Communication Conference Postdeadline Papers*, 2017, p. Th5C.7.

[48] K. J. Kormondy, Y. Popoff, M. Sousa, F. Eltes, D. Caimi, M. D. Rossell, M. Fiebig, P. Hoffmann, C. Marchiori, M. Reinke, M. Trassin, A. A. Demkov, J. Fompeyrine, and S. Abel, "Microstructure and ferroelectricity of $BaTiO_3$ thin films on Si for integrated photonics," *Nanotechnology*, vol. 28, no. 7, p. 075706, Feb. 2017.

[49] L. Czornomaz, N. Daix, P. Kerber, K. Lister, D. Caimi, C. Rossel, M. Sousa, E. Uccelli, and J. Fompeyrine, "Scalability of ultra-thin-body and BOX InGaAs MOSFETs on silicon," in *Proc. European Solid-State Device Research Conf, (ESSDERC),* 2013, pp. 143–146.

[50] L. Czornomaz, N. Daix, E. Uccelli, V. Djara, D. Caimi, C. Rossel, M. Sousa, H. Siegwart, C. Marchiori, J.-M. Hartmann, and J. Fompeyrine, "Wafer bonding: An integration route for hybrid III-V/SiGe CMOS on 300mm," *ECS Trans.*, vol. 64, no. 5, pp. 199–209, 2014.

[51] W. Bogaerts, P. De Heyn, T. Van Vaerenbergh, K. De Vos, S. Kumar Selvaraja, T. Claes, P. Dumon, P. Bienstman, D. Van Thourhout, and R. Baets, "Silicon microring resonators," *Laser Photon. Rev.*, vol. 6, no. 1, pp. 47–73, Jan. 2012.

[52] G. Li, X. Zheng, J. Yao, H. Thacker, I. Shubin, Y. Luo, K. Raj, J. E. Cunningham, and A. V. Krishnamoorthy, "25 Gb/s 1V-driving CMOS ring modulator with integrated thermal tuning," *Opt. Express*, vol. 19, no. 21, p. 20435, 2011.

[53] C. Hoessbacher, A. Josten, B. Baeuerle, Y. Fedoryshyn, H. Hettrich, Y. Salamin, W. Heni, C. Haffner, C. Kaiser, R. Schmid, D. L. Elder, D. Hillerkuss, M. Möller, L. R. Dalton, and J. Leuthold, "Plasmonic modulator with >170 GHz bandwidth demonstrated at 100 GBd NRZ," *Opt. Express*, vol. 25, no. 3, p. 1762, Feb. 2017.

[54] J. Brosi, C. Koos, L. C. Andreani, J. Leuthold, and W. Freude, "Modulator with a polymer-infiltrated silicon photonic crystal waveguide," *Opt. Express*, vol. 16, no. 6, pp. 180–185, 2008.

[55] M. Borghi, M. Mancinelli, M. Bernard, M. Ghulinyan, G. Pucker, and L. Pavesi, "Homodyne Detection of Free Carrier Induced Electro-Optic Modulation in Strained Silicon Resonators," *J. Light. Technol.*, vol. 34, no. 24, pp. 5657–5668, 2016.

[56] R. B. (Ed) Marcus, *Measurement of High-Speed Signals in Solid State Devices*, vol. 28. Academic Press, Inc, 1990.

[57] J. Müller, F. Merget, S. S. Azadeh, J. Hauck, S. R. García, B. Shen, and J. Witzens, "Optical Peaking Enhancement in High-Speed Ring Modulators," *Sci. Rep.*, vol. 4, p. 6310, 2014.

[58] Q. Zhou, S. Lau, D. Wu, and K. Kirk Shung, "Piezoelectric films for high frequency ultrasonic transducers in biomedical applications," *Prog. Mater. Sci.*, vol. 56, no. 2, pp. 139–174, 2011.

[59] K. M. Rabe, C. H. Ahn, and J.-M. (eds) Triscone, *Physics of Ferroelectrics*, vol. 105, no. 2007. Springer, 2007.

[60] D. Patel, S. Ghosh, M. Chagnon, A. Samani, V. Veerasubramanian, M. Osman, and D. V. Plant, "Design, analysis, and transmission system performance of a 41 GHz silicon photonic modulator," *Opt. Express*, vol. 23, no. 11, p. 14263, 2015.

[61] E. Rouvalis, "Indium Phosphide Based IQ-Modulators for Coherent Pluggable Optical Transceivers," in *2015 IEEE Compound Semiconductor Integrated Circuit Symposium, CSICS 2015*, 2015, pp. 1–4.

[62] T. Baehr-Jones, R. Ding, Y. Liu, A. Ayazi, T. Pinguet, N. C. Harris, M. Streshinsky, P. Lee, Y. Zhang, A. E.-J. Lim, T.-Y. Liow, S. H.-G. Teo, G.-Q. Lo, and M. Hochberg, "Ultralow drive voltage silicon traveling-wave modulator," *Opt. Express*, vol. 20, no. 11, p. 12014, 2012.

[63] J. Ding, H. Chen, L. Yang, L. Zhang, R. Ji, Y. Tian, W. Zhu, Y. Lu, P. Zhou, R. Min, and M. Yu, "Mach-Zehnder silicon optical modulator," vol. 20, no. 7, pp. 59–63, 2012.

[64] C. Haffner, W. Heni, Y. Fedoryshyn, J. Niegemann, A. Melikyan, D. L. Elder, B. Baeuerle, Y. Salamin, A. Josten, U. Koch, C. Hoessbacher, F. Ducry, L. Juchli, A. Emboras, D. Hillerkuss, M. Kohl, L. R. Dalton, C. Hafner, and J. Leuthold, "All-plasmonic Mach–Zehnder modulator enabling optical high-speed communication at the microscale," *Nat. Photonics*, vol. 9, no. 8, pp. 525–528, 2015.

[65] Y. Zhang, R. Han, and T. Xiang, "Application of non-contact optic voltage sensor based on Pockels effect in ±800 kV convertor station," in *2016 IEEE International Conference on High Voltage Engineering and Application (ICHVE)*, 2016.

[66] N. Stan, F. Seng, L. Shumway, R. King, and S. Schultz, "Non-perturbing voltage measurement in a coaxial cable with slab-coupled optical sensors," *Appl. Opt.*, vol. 56, no. 24, pp. 6814–6821, 2017.

[67] T. Jin, L. Li, B. Zhang, H.-Y. G. Lin, H. Wang, and P. T. Lin, "Monolithic Mid-Infrared Integrated Photonics Using Silicon-on-Epitaxial Barium Titanate Thin Films," *ACS Appl. Mater. Interfaces*, vol. 9, no. 26, pp. 21848–21855, Jul. 2017.

[68] S. Abel, D. J. Stark, F. Eltes, J. E. Ortmann, D. Caimi, and J. Fompeyrine, "Multi-Level Optical Weights in Integrated Circuits," in *2017 IEEE International Conference on Rebooting Computing (ICRC)*, 2017, vol. 2017–Janua, pp. 1–3.

[69] C. Ríos, M. Stegmaier, P. Hosseini, D. Wang, T. Scherer, C. D. Wright, H. Bhaskaran, and W. H. P. Pernice, "Integrated all-photonic non-volatile multi-level memory," *Nat. Photonics*, vol. 9, no. September, pp. 725–732, 2015.

[70] C. Javerzac-Galy, K. Plekhanov, N. R. Bernier, L. D. Toth, A. K. Feofanov, and T. J. Kippenberg, "On-chip microwave-to-optical quantum coherent converter based on a superconducting resonator coupled to an electro-optic microresonator," *Phys. Rev. A*, vol. 94, no. 5, p. 053815, 2016.

[71] Y. Shi, L. Yan, and A. E. Willner, "High-speed electrooptic modulator characterization using optical spectrum analysis," *J. Light. Technol.*, vol. 21, no. 10, p. 2358, 2003.

[72] J. E. Ortmann, F. Eltes, D. Caimi, N. Meier, A. A. Demkov, J. Fompeyrine, and S. Abel, "Ultra-Low Power Tuning in Hybrid Barium Titanate-Silicon Nitride Electro-Optic Devices on Silicon," vol. Under Review, 2019.

[73] Z. Zhou, R. Chen, X. Li, and T. Li, "Development trends in silicon photonics for data centers," *Opt. Fiber Technol.*, vol. 44, no. March, pp. 13–23, Aug. 2018.

[74] J. Leuthold, C. Koos, and W. Freude, "Nonlinear silicon photonics," *Nat. Photonics*, vol. 4, no. 8, pp. 535–544, Aug. 2010.

[75] D. J. Moss, R. Morandotti, A. L. Gaeta, and M. Lipson, "New CMOS-compatible platforms based on silicon nitride and Hydex for nonlinear optics," *Nat. Photonics*, vol. 7, no. 8, pp. 597–607, Aug. 2013.

[76] P. Muñoz, G. Micó, L. Bru, D. Pastor, D. Pérez, J. Doménech, J. Fernández, R. Baños, B. Gargallo, R. Alemany, A. Sánchez, J. Cirera, R. Mas, and C. Domínguez, "Silicon Nitride Photonic Integration Platforms for Visible, Near-Infrared and Mid-Infrared Applications," *Sensors*, vol. 17, no. 9, p. 2088, Sep. 2017.

[77] J. Chiles, S. M. Buckley, S. W. Nam, R. P. Mirin, and J. M. Shainline, "Design, fabrication, and metrology of 10 × 100 multi-planar integrated photonic routing manifolds for neural networks," *APL Photonics*, vol. 3, no. 10, p. 106101, Oct. 2018.

[78] W. Stutius and W. Streifer, "Silicon nitride films on silicon for optical waveguides," *Appl. Opt.*, vol. 16, no. 12, p. 3218, Dec. 1977.

[79] T. Domínguez Bucio, A. Z. Khokhar, C. Lacava, S. Stankovic, G. Z. Mashanovich, P. Petropoulos, and F. Y. Gardes, "Material and optical properties of low-temperature NH_3-free PECVD SiN_x layers for photonic applications," *J. Phys. D. Appl. Phys.*, vol. 50, no. 2, p. 025106, Jan. 2017.

[80] D. Nikolova, S. Rumley, D. Calhoun, Q. Li, R. Hendry, P. Samadi, and K. Bergman, "Scaling silicon photonic switch fabrics for data center interconnection networks," *Opt. Express*, vol. 23, no. 2, p. 1159, Jan. 2015.

[81] F. Horst, W. M. Green, S. Assefa, S. M. Shank, Y. A. Vlasov, and B. J. Offrein, "Cascaded Mach-Zehnder wavelength filters in silicon photonics for low loss and flat pass-band WDM (de-)multiplexing," *Opt. Express*, vol. 21, no. 10, p. 11652, May 2013.

[82] N. C. Harris, D. Grassani, A. Simbula, M. Pant, M. Galli, T. Baehr-Jones, M. Hochberg, D. Englund, D. Bajoni, and C. Galland, "Integrated Source of Spectrally Filtered Correlated Photons for Large-Scale Quantum Photonic Systems," *Phys. Rev. X*, vol. 4, no. 4, p. 041047, Dec. 2014.

[83] S. Zheng, N. Zhou, Y. Long, Z. Ruan, J. Du, X. Hu, L. Shen, S. Li, and J. Wang, "Compact tunable photonic comb filter on a silicon platform," *Opt. Lett.*, vol. 42, no. 14, p. 2762, Jul. 2017.

[84] S. Wang, X. Feng, S. Gao, Y. Shi, T. Dai, H. Yu, H.-K. Tsang, and D. Dai, "On-chip reconfigurable optical add-drop multiplexer for hybrid wavelength/mode-division-multiplexing systems," *Opt. Lett.*, vol. 42, no. 14, p. 2802, Jul. 2017.

[85] A. Prinzen, M. Waldow, and H. Kurz, "Fabrication tolerances of SOI based directional couplers and ring resonators," *Opt. Express*, vol. 21, no. 14, p. 17212, Jul. 2013.

[86] S. Pathak, D. Van Thourhout, and W. Bogaerts, "Design trade-offs for silicon-on-insulator-based AWGs for (de)multiplexer applications," *Opt. Lett.*, vol. 38, no. 16, p. 2961, Aug. 2013.

[87] S. Dwivedi, H. D'heer, and W. Bogaerts, "Maximizing Fabrication and Thermal Tolerances of All-Silicon FIR Wavelength Filters," *IEEE Photonics Technol. Lett.*, vol. 27, no. 8, pp. 871–874, Apr. 2015.

[88] W. Bogaerts and L. Chrostowski, "Silicon Photonics Circuit Design: Methods, Tools and Challenges," *Laser Photon. Rev.*, vol. 12, no. 4, p. 1700237, Apr. 2018.

[89] E. Timurdogan, C. M. Sorace-Agaskar, J. Sun, E. Shah Hosseini, A. Biberman, and M. R. Watts, "An ultralow power athermal silicon modulator," *Nat. Commun.*, vol. 5, no. 1, p. 4008, Dec. 2014.

[90] P. Dong, W. Qian, H. Liang, R. Shafiiha, D. Feng, G. Li, J. E. Cunningham, A. V. Krishnamoorthy, and M. Asghari, "Thermally tunable silicon racetrack resonators with ultralow tuning power," *Opt. Express*, vol. 18, no. 19, p. 20298, Sep. 2010.

[91] A. H. Atabaki, A. A. Eftekhar, S. Yegnanarayanan, and A. Adibi, "Sub-100-nanosecond thermal reconfiguration of silicon photonic devices," *Opt. Express*, vol. 21, no. 13, p. 15706, Jul. 2013.

[92] A. Arbabi and L. L. Goddard, "Measurements of the refractive indices and thermo-optic coefficients of S_3N_4 and SiO_x using microring resonances," *Opt. Lett.*, vol. 38, no. 19, p. 3878, Oct. 2013.

[93] M. Georgas, J. Leu, B. Moss, C. Sun, and V. Stojanovic, "Addressing link-level design tradeoffs for integrated photonic interconnects," in *2011 IEEE Custom Integrated Circuits Conference (CICC)*, 2011, pp. 1–8.

[94] R. Ding, Y. Liu, Q. Li, Z. Xuan, Y. Ma, Y. Yang, A. E.-J. Lim, G.-Q. Lo, K. Bergman, T. Baehr-Jones, and M. Hochberg, "A Compact Low-Power 320-Gb/s

WDM Transmitter Based on Silicon Microrings," *IEEE Photonics J.*, vol. 6, no. 3, pp. 1–8, Jun. 2014.

[95] R. Wu, M. A. Seyedi, Y. Wang, J. Hulme, M. Fiorentino, R. G. Beausoleil, and K.-T. Cheng, "Pairing of microring-based silicon photonic transceivers for tuning power optimization," in *2018 23rd Asia and South Pacific Design Automation Conference (ASP-DAC)*, 2018, vol. 2018–Janua, pp. 135–140.

[96] M. Takenaka, J.-H. Han, F. Boeuf, J.-K. Park, Q. Li, C. P. Ho, D. Lyu, S. Ohno, J. Fujikata, S. Takahashi, and S. Takagi, "III–V/Si Hybrid MOS Optical Phase Shifter for Si Photonic Integrated Circuits," *J. Light. Technol.*, vol. 37, no. 5, pp. 1474–1483, Mar. 2019.

[97] W. H. P. Pernice, C. Xiong, F. J. Walker, and H. X. Tang, "Design of a Silicon Integrated Electro-Optic Modulator Using Ferroelectric $BaTiO_3$ Films," *IEEE Photonics Technol. Lett.*, vol. 26, no. 13, pp. 1344–1347, Jul. 2014.

[98] F. Eltes, C. Mai, D. Caimi, M. Kroh, Y. Popoff, G. Winzer, D. Petousi, S. Lischke, J. E. Ortmann, L. Czornomaz, L. Zimmermann, J. Fompeyrine, and S. Abel, "A $BaTiO_3$-Based Electro-Optic Pockels Modulator Monolithically Integrated on an Advanced Silicon Photonics Platform," *J. Light. Technol.*, vol. 37, no. 5, pp. 1456–1462, Mar. 2019.

[99] P. Dong, W. Qian, H. Liang, R. Shafiiha, N.-N. Feng, D. Feng, X. Zheng, A. V. Krishnamoorthy, and M. Asghari, "Low power and compact reconfigurable multiplexing devices based on silicon microring resonators," *Opt. Express*, vol. 18, no. 10, p. 9852, May 2010.

[100] Q. Xu, B. Schmidt, S. Pradhan, and M. Lipson, "Micrometre-scale silicon electro-optic modulator," *Nature*, vol. 435, no. 7040, pp. 325–327, May 2005.

[101] M. Ieda, G. Sawa, and S. Kato, "A Consideration of Poole-Frenkel Effect on Electric Conduction in Insulators," *J. Appl. Phys.*, vol. 42, no. 10, pp. 3737–3740, Sep. 1971.

[102] G. Niu, B. Gautier, S. Yin, G. Saint-Girons, P. Lecoeur, V. Pillard, G. Hollinger, and B. Vilquin, "Molecular beam epitaxy growth of $BaTiO_3$ thin films and crucial impact of oxygen content conditions on the electrical characteristics," *Thin Solid Films*, vol. 520, no. 14, pp. 4595–4599, May 2012.

[103] H. F. Hamann, J. Lacey, A. Weger, and J. Wakil, "Spatially-Resolved Imaging of Microprocessor Power (SIMP): Hotspots in Microprocessors," in *Thermal and Thermomechanical Proceedings 10th Intersociety Conference on Phenomena in Electronics Systems, 2006. ITHERM 2006.*, 2006, vol. 2006, pp. 121–125.

[104] G. Cocorullo, F. G. Della Corte, and I. Rendina, "Temperature dependence of the thermo-optic coefficient in crystalline silicon between room temperature and 550 K at the wavelength of 1523 nm," *Appl. Phys. Lett.*, vol. 74, no. 22, pp. 3338–3340, May 1999.

[105] F. G. Della Corte, M. Esposito Montefusco, L. Moretti, I. Rendina, and G. Cocorullo, "Temperature dependence analysis of the thermo-optic effect in silicon by single and double oscillator models," *J. Appl. Phys.*, vol. 88, no. 12, pp. 7115–7119, Dec. 2000.

[106] J. Komma, C. Schwarz, G. Hofmann, D. Heinert, and R. Nawrodt, "Thermo-optic coefficient of silicon at 1550 nm and cryogenic temperatures," *Appl. Phys. Lett.*, vol. 101, no. 4, p. 041905, Jul. 2012.

[107] C. T. DeRose, N. J. Martinez, R. D. Kekatpure, W. A. Zortman, A. L. Starbuck, A. Pomerene, and A. L. Lentine, "Thermal crosstalk limits for silicon photonic DWDM interconnects," in *2014 Optical Interconnects Conference*, 2014, vol. 5, pp. 125–126.

[108] J. V. Hryniewicz, P. P. Absil, B. E. Little, R. A. Wilson, and P.-T. Ho, "Higher order filter response in coupled microring resonators," *IEEE Photonics Technol. Lett.*, vol. 12, no. 3, pp. 320–322, Mar. 2000.

[109] J. K. Poon, L. Zhu, G. a DeRose, and A. Yariv, "Transmission and group delay of microring coupled-resonator optical waveguides," *Opt. Lett.*, vol. 31, no. 4, p. 456, Feb. 2006.

[110] F. Xia, L. Sekaric, and Y. Vlasov, "Ultracompact optical buffers on a silicon chip," *Nat. Photonics*, vol. 1, no. 1, pp. 65–71, Jan. 2007.

[111] F. Xia, M. Rooks, L. Sekaric, and Y. Vlasov, "Ultra-compact high order ring resonator filters using submicron silicon photonic wires for on-chip optical interconnects," *Opt. Express*, vol. 15, no. 19, p. 11934, 2007.

[112] I. Goykhman, B. Desiatov, and U. Levy, "Ultrathin silicon nitride microring resonator for biophotonic applications at 970 nm wavelength," *Appl. Phys. Lett.*, vol. 97, no. 8, p. 081108, Aug. 2010.

[113] M. J. R. Heck, "Highly integrated optical phased arrays: photonic integrated circuits for optical beam shaping and beam steering," *Nanophotonics*, vol. 6, no. 1, pp. 93–107, Jan. 2017.

[114] C. V. Poulton, A. Yaacobi, D. B. Cole, M. J. Byrd, M. Raval, D. Vermeulen, and M. R. Watts, "Coherent solid-state LIDAR with silicon photonic optical phased arrays," *Opt. Lett.*, vol. 42, no. 20, p. 4091, Oct. 2017.

[115] K. Alexander, J. P. George, B. Kuyken, J. Beeckman, and D. Van Thourhout, "Broadband electro-optic modulation using low-loss PZT- on-silicon nitride integrated waveguides," *CLEO 2017*, p. JTh5C.7, 2017.

Chapter 8: Summary and Outlook

8.1 Summary

In the opening chapter of this thesis, I gave a brief historical overview of the development of computing technologies throughout the 20th-Century and the journey of the integrated circuit from novel concept to ubiquitous technology. In almost all cases, materials development precedes and facilitates technological development. The bulk of this thesis has therefore been devoted to the research and development of materials systems that appear promising for use in next-generation computing technologies, with a particular focus on materials thought to be useful for optical computing and devices. The two primary classes of materials examined are TMO QWs and the Pockels-active material BTO. This work has generated many publications [1]–[9] (with more to come), as well as an estimated five patents, and I hope has pushed the field a bit closer to realizing some of the novel computing technologies that will be necessary to keep up with global data demands and society's exploding computational needs throughout the 21st-Century.

The first major challenge of this research involved overcoming the problem of growth of STO/LAO QW heterostructures. Previous studies encountered difficulties maintaining high crystalline quality throughout the growth of thick STO/LAO heterostructures grown by pulsed-laser deposition [10]. In Chapter 3, I described my efforts at overcoming this challenge using MBE as a growth method. By employing a multi-step growth process in which the deposition rates were frequently re-calibrated, I succeeded in growing STO/LAO QW heterostructures of up to 80 well/barrier periods without evidence of thickness-dependent degradation of crystalline quality. The detailed structural characterization presented in Chapter 3 demonstrates the successful growth of high-quality, arbitrarily thick STO/LAO QW heterostructures on LAO substrates.

After demonstrating successful heterostructure fabrication in Chapter 3, Chapter 4 focused on the optical characterization of the heterostructures, with the goal of demonstrating intersubband transitions between confined states in the STO QWs. The optical characterization in the chapter shows absorption whose energy and amplitude depend on QW width in the manner expected for intersubband absorption. Furthermore, the absorption is polarization-dependent [11], [12], unambiguously confirming intersubband transitions between confined states in the STO QW as the absorption mechanism. The experimental evidence is supported by tight-binding calculations and first-principles theory.

Having demonstrated the capability to induce intersubband transitions in the STO QWs, the goal of Chapter 5 was to demonstrate the integration of high-quality STO/LAO QWs on silicon substrates. The silicon-integration of such QWs is an important prerequisite for their use in practical technologies. The results of Chapter 5 showed that high-quality STO/LAO QW heterostructures can be fabricated on silicon substrates via an epitaxial STO buffer layer. While the crystalline quality appeared to be diminished somewhat relative to the heterostructures deposited on bulk oxide substrates in Chapters 3 and 4, dedicated processing studies can likely improve the crystalline quality of silicon-integrated STO/LAO QW heterostructures.

Chapter 6 concluded the discussion of STO/LAO QW heterostructures by investigating their optical properties when employed in integrated photonic devices that exploit the quantum-confined Stark effect for electro-optic operation. Poisson-Schrödinger calculations suggested the occurrence of intersubband absorption near the critical telecom wavelengths of 1300 nm and 1550 nm in appropriately designed STO/LAO QW heterostructures. The energy of these absorptions can be modified with the application of an external electric field and used for electrical modulation of the optical signal.

Simulations demonstrated how the optical confinement within the active TMO layer and the electro-optic overlap integral can both be modified as a function of waveguide dimensions. Calculations of the switching energy in a proposed electro-optic modulator structure indicated that switching energies on the order of 20 pJ/bit should be possible in these experimentally realizable devices.

In Chapter 7, a different materials system was investigated altogether. Several distinct types of BTO-based photonic devices using the Pockels effect in BTO for electro-optic operation were examined. First, the presence of the Pockels effect in integrated devices was unambiguously demonstrated for the first time using a hybrid BTO-silicon platform. Furthermore, the largest Pockels coefficients ever observed in BTO thin films were extracted from the measurements, with values approaching those of bulk BTO. After confirming the presence of the Pockels effect in integrated BTO devices, the next generation of BTO-based photonic devices was experimentally investigated. In these devices, the semiconducting silicon strip waveguides used in the first devices were replaced with insulating SiN, eliminating the possibility of a parasitic plasma dispersion effect in the strip waveguide impacting the electro-optic performance of the device. The hybrid BTO-SiN devices showed ultra-low power tuning under static electric fields, with tuning powers several orders of magnitude less than previous reports. The Pockels effect in resonant devices was used to compensate for thermally induced index variations over a temperature range of 20 °C and for the fabrication of tunable, multi-resonator optical filters.

Taken together, the investigations in this thesis have hopefully opened the door for the development of new kinds of optical and electro-optical devices for use in integrated photonics platforms. QWs are useful for a wide variety of integrated optical devices, including quantum cascade lasers, photodetectors, and modulators. BTO has already

demonstrated itself as an excellent candidate for high-speed electro-optic modulators and switches. Next, I will provide a brief outlook related to the work in this thesis and discuss the next steps that should be taken for the investigation of these materials platforms.

8.2 OUTLOOK

Below, I have detailed four areas of ongoing investigation related to the work in this thesis. I believe many, or all, of the below-detailed areas are likely to further advance the state-of-the art of integrated oxide-based devices for use in novel computing systems and related hardware.

8.2.1 Resonant Tunneling Devices

Although much of the work in this thesis has focused on materials platforms for integrated optics and optical computing, one common approach to neuromorphic hardware utilizes resistive switching in electrical components, rather than optics, for operation [13]. While some resistive switching devices operate using a two-state system (one high-resistance and one low-resistance state), neural network training is improved through the use of analog switching [14]. Many such systems have been investigated over the years in the hopes of developing and improving neuromorphic hardware [14]–[18]. However, the development of materials platforms that display reliable analog resistive switching has proven challenging.

STO/LAO QWs may prove beneficial for the development of analog resistive switching elements when used in resonant tunneling devices [19]–[24]. In their most basic form, resonant tunneling devices utilize a single QW between two insulating barriers (Figure 8.1a). As the Fermi levels of the top and bottom contacts are shifted by the application of bias, one will eventually become resonant with (i.e., have the same energy

as) a confined state within the QW. When the Fermi level and the confined state are in resonance, the device more easily transmits tunneling current due to the large overlap between electronic levels. As the bias is further increased and the Fermi level moves out of resonance with the confined state, the current quickly drops. At finite temperatures, the corresponding change in resistance as the Fermi level moves in and out of resonance with a confined state is analog (Figure 8.1b) with many stable resistance states realizable. Such resonant tunneling devices would therefore appear to be excellent candidates for use in resistive switching-based neuromorphic hardware.

I have attempted to make such resonant tunneling devices from the STO/LAO system (Figure 8.1a) many times throughout my graduate career and have found the electrical properties of the as-grown structures to be unreliable. This is due in large part to what appears to be an extreme sensitivity of the tunneling current to the crystalline quality of the LAO barriers. Less-than-ideal LAO tends to allow excess leakage current to transmit through the device, burying any traces of resonant tunneling that may be present. To circumvent this problem, I have recently developed a multi-step growth process that appears to significantly reduce the leakage of the devices and will hopefully allow resonant tunneling to be observed and utilized. The multi-step growth process requires removing the sample from UHV and annealing it in air at 800 °C for one hour after the deposition of each LAO barrier. Through this procedure, I have observed a reduction of the leakage current by several orders of magnitude. As a way forward, I would recommend employing a similar multi-step growth process and investigating the tunneling characteristics of such devices in the hopes of eventually incorporating them into neuromorphic systems.

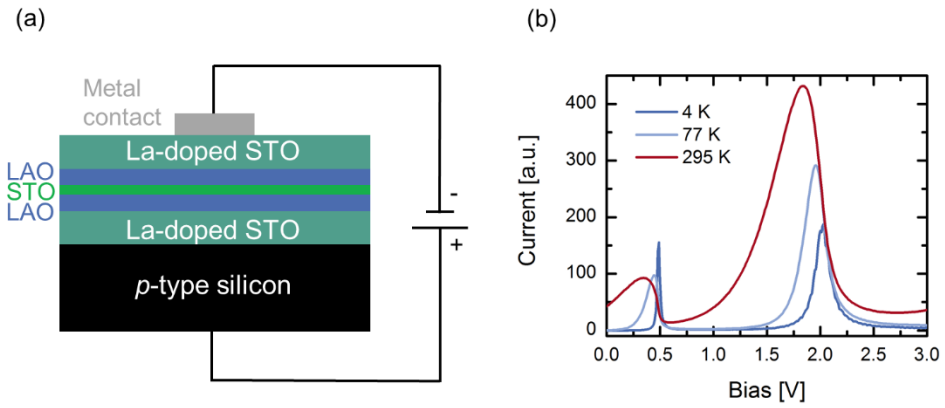

Figure 8.1: (a) Schematic of proposed STO/LAO-based resonant tunneling device. The oxide layer stack is grown on a *p*-type, heavily doped silicon substrate which serves as a bottom contact. (b) Simulated current-voltage curves for STO/LAO double barrier structures at three different temperatures: 4 K (dark blue), 77 K (light blue) and room temperature (dark red). As the bias sweeps through the energy levels of the confined states, there is a large change in resistance that could potentially be used in neuromorphic hardware.

8.2.2 Epitaxial Oxides on Glass

The BTO photonic devices discussed in Chapter 7 featured a layer stack in which crystalline BTO was integrated atop amorphous SiO_2. Such a layer stack is desirable in these devices as it provides superior electrical and optical isolation when compared to BTO-based photonic devices grown directly on silicon. In order to achieve such a layer stack, a complex wafer-bonding approach was employed in which crystalline BTO was first epitaxially grown on silicon and then bonded to a thermally oxidized silicon wafer via an Al_2O_3 bonding layer.

Because of the amorphous nature of SiO_2, and the resulting inability to directly deposit epitaxial oxides on it, such a wafer-bonding approach would appear necessary in order to achieve the desired layer stack. However, wafer-bonding is a difficult process requiring a high level of cleanliness for success and is therefore not feasible in many

university-level laboratories. In response to this issue, I have been involved in the development of a method for realizing epitaxial oxide films on glass (SiO_2) through direct deposition.

The process is detailed in Figure 8.2, along with preliminary TEM images of the resulting structures. In short, STO is first epitaxially grown on a special SOI wafer featuring an extremely thin device silicon layer (approximately 45 Å-thick) atop a thick buried oxide layer. After deposition and subsequent crystallization of the STO film, the device silicon is completely thermally oxidized beneath the STO film by employing the method outlined in [25]. The result is an epitaxial, crystalline STO film atop an arbitrarily thick SiO_2 layer (the SiO_2 thickness depends on the specifications of the initial SOI wafer). Additional perovskite oxide films can then be epitaxially deposited on the STO film. Through such a procedure, the BTO-based photonic devices of Chapter 7, as well as a huge host of other devices, can be directly fabricated on glass without resorting to complex and error-prone wafer-bonding techniques. I foresee this process facilitating a large variety of novel device structures with significantly reduced fabrication requirements relative to the traditional wafer-bonding approach. We are in the process of filing a patent on this concept and also intend to publish our results in the coming months.

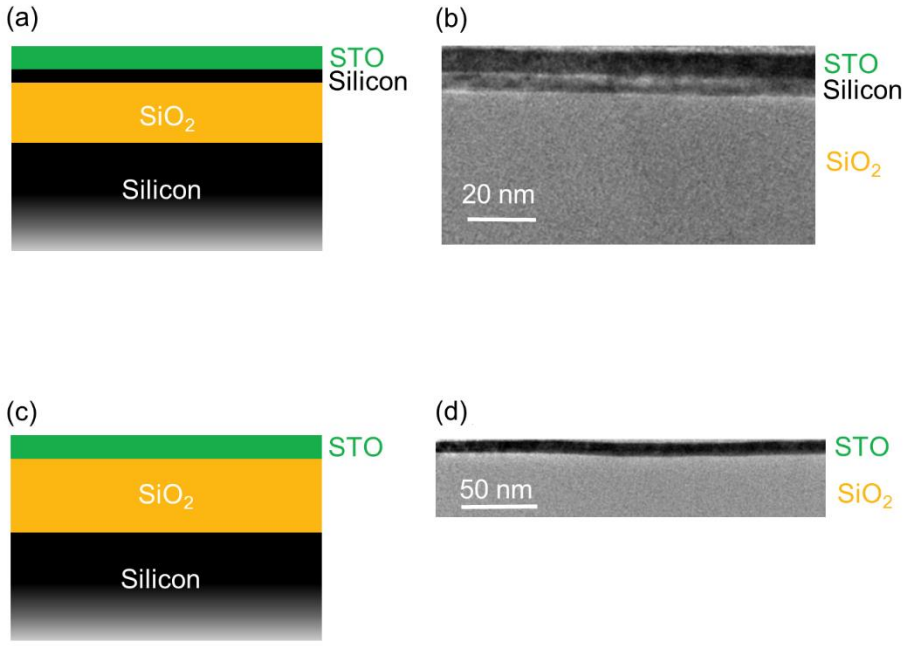

Figure 8.2: (a) Schematic of STO grown epitaxially on special SOI and (b) corresponding TEM image of the as-grown structure. (c) Schematic of STO on SiO_2 after oxidation of the device silicon layer and (d) corresponding TEM image. The STO remains crystalline after oxidation and amorphization of the device silicon.

8.2.3 Silicon-on-Oxide-on-Silicon (SOS)

As the scaling of transistors reaches its fundamental limit, one approach to continue to improve the performance of microelectronic systems is 3D integration [26], [27]. In 3D integration, multiple silicon wafers are bonded together and subsequently electrically interconnected such as to extend the device region out of the plane and more densely pack transistors within a chip.

Just as for the BTO-based photonic devices integrated on SiO_2, the wafer-bonding processes necessary for 3D integration are difficult and costly. A direct deposition route in which subsequent device silicon layers are deposited atop the underlying layer stack is therefore desirable. However, a recent paper by our group and authored by Posadas *et al*.

suggests the direct deposition of silicon on most oxides would be unlikely to succeed due to the propensity of silicon to oxidize and amorphize, including via the scavenging of oxygen from oxide films [28].

Despite these concerns, I have succeeded in directly depositing crystalline silicon films on an oxide layer stack by using a highly-insulating LAO film as an oxygen scavenging barrier (Figure 8.3a). The large band gap of LAO prohibits silicon from stealing oxygen from it and allows for the deposited silicon to remain crystalline rather than amorphize during deposition (Figure 8.3b). Additional device layers could then be fabricated atop the deposited silicon and the procedure repeated many times, thereby facilitating 3D integration. Alternatively, one device silicon layer could be grown atop an insulating oxide layer stack, including one in which functional oxides (such as BTO) are included, thereby producing a novel type of SOI wafer with additional electronic, magnetic, and/or optical functionalities relative to traditional SOI. We are in the process of filing a patent on this concept and also intend to publish our results in the coming months.

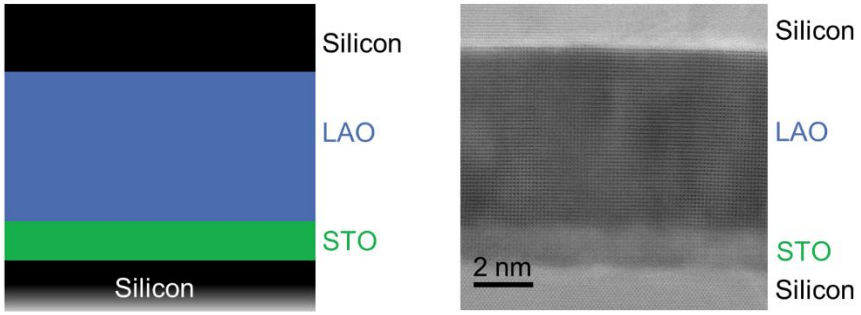

Figure 8.3: (a) Schematic of silicon-on-oxide-on-silicon (SOS) sample geometry and (b) preliminary STEM image of a fabricated SOS sample showing successful fabrication of the intended layer stack, including deposited crystalline silicon (top).

8.2.4 Dynamic Waveguides

In order to confine light in the BTO-based photonic structures of Chapter 7, strip waveguides of silicon and SiN were deposited on top of the BTO film. The use of strip waveguides is typically necessary because BTO cannot be easily patterned into waveguides directly [29]. However, the downside of using such strip waveguides is that the optical confinement in the active BTO layer is somewhat low as much of the light is confined within the strip waveguide itself. It is therefore desirable to fabricate a waveguide entirely from BTO.

Because BTO cannot be patterned directly while maintaining smooth waveguide surfaces, another method for BTO-only waveguide fabrication is needed. One such approach I have investigated is dynamic waveguiding in BTO. In a dynamic waveguide [30], an external signal is utilized to alter the optical properties of a material, thereby making it suitable for the support of an optical mode. For the case of BTO, an external electric field can be used to dynamically generate a low-index core via the Pockels effect within which an optical mode can be confined (Figure 8.4). Such devices result in most of the confined light residing within the electro-optically active BTO layer and can be directly used for high-speed electro-optic modulators and switches. The feasibility of such devices has been tested with simulations and efforts to experimentally fabricate them are ongoing. We are in the process of filing a patent on this concept and also intend to publish our results in the coming months, including in a conference paper by Duncan *et al*. already accepted to the 2019 IEEE MTT-S International Conference on Numerical Electromagnetic and Multiphysics Modeling and Optimization (NEMO).

Figure 8.4: (a) Schematic of the proposed BTO-based dynamic waveguiding device. The doped silicon substrate is used as ground while the field is applied via the top metallic electrodes. (b) Simulated index change in the BTO layer as a result of an applied bias of 5 V. Color scale goes from $\Delta n = 0$ (blue) to $\Delta n = -0.03$ (red). (c) Norm of the electric field of an optical mode confined within the BTO dynamic waveguide under an applied bias of 5 V. The gray rectangles in (b) and (c) indicate the electrodes.

8.3 References

[1] J. E. Ortmann, A. B. Posadas, and A. A. Demkov, "The MBE growth of arbitrarily thick $SrTiO_3/LaAlO_3$ quantum well heterostructures for use in next-generation optoelectronic devices," *J. Appl. Phys.*, vol. 124, no. 1, p. 015301, Jul. 2018.

[2] J. E. Ortmann, N. Nookala, Q. He, L. Gao, C. Lin, A. B. Posadas, A. Y. Borisevich, M. A. Belkin, and A. A. Demkov, "Quantum Confinement in Oxide Heterostructures: Room-Temperature Intersubband Absorption in $SrTiO_3/LaAlO_3$ Multiple Quantum Wells," *ACS Nano*, vol. 12, no. 8, pp. 7682–7689, Aug. 2018.

[3] J. E. Ortmann, F. Eltes, D. Caimi, and S. Abel, "Electric Field Tuning of $BaTiO_3$-on-Silicon Multi-Ring Resonators via the Pockels Effect," in *2018 IEEE 15th International Conference on Group IV Photonics (GFP)*, 2018, no. c, pp. 1–2.

[4] J. E. Ortmann, S. Kwon, A. B. Posadas, M. J. Kim, and A. A. Demkov, "Monolithic integration of transition metal oxide multiple quantum wells on silicon (001)," *J. Appl. Phys.*, vol. 125, no. 15, p. 155302, Apr. 2019.

[5] J. E. Ortmann, F. Eltes, D. Caimi, N. Meier, A. A. Demkov, J. Fompeyrine, and S. Abel, "Ultra-Low Power Tuning in Hybrid Barium Titanate-Silicon Nitride Electro-Optic Devices on Silicon," vol. Under Review, 2019.

[6] F. Eltes, M. Kroh, D. Caimi, C. Mai, Y. Popoff, G. Winzer, D. Petousi, S. Lischke, J. E. Ortmann, L. Czornomaz, L. Zimmermann, J. Fompeyrine, and S. Abel, "A novel 25 Gbps electro-optic Pockels modulator integrated on an advanced Si photonic platform," in *2017 IEEE International Electron Devices Meeting (IEDM)*, 2017, p. 24.5.1-24.5.4.

[7] S. Abel, D. J. Stark, F. Eltes, J. E. Ortmann, D. Caimi, and J. Fompeyrine, “Multi-Level Optical Weights in Integrated Circuits,” in *2017 IEEE International Conference on Rebooting Computing (ICRC)*, 2017, vol. 2017–Janua, pp. 1–3.

[8] S. Abel, F. Eltes, J. E. Ortmann, A. Messner, P. Castera, T. Wagner, D. Urbonas, A. Rosa, A. M. Gutierrez, D. Tulli, P. Ma, B. Baeuerle, A. Josten, W. Heni, D. Caimi, L. Czornomaz, A. A. Demkov, J. Leuthold, P. Sanchis, and J. Fompeyrine, “Large Pockels effect in micro- and nanostructured barium titanate integrated on silicon,” *Nat. Mater.*, vol. 18, no. 1, pp. 42–47, Jan. 2019.

[9] F. Eltes, C. Mai, D. Caimi, M. Kroh, Y. Popoff, G. Winzer, D. Petousi, S. Lischke, J. E. Ortmann, L. Czornomaz, L. Zimmermann, J. Fompeyrine, and S. Abel, “A $BaTiO_3$-Based Electro-Optic Pockels Modulator Monolithically Integrated on an Advanced Silicon Photonics Platform,” *J. Light. Technol.*, vol. 37, no. 5, pp. 1456–1462, Mar. 2019.

[10] N. Nakagawa, H. Y. Hwang, and D. A. Muller, “Why some interfaces cannot be sharp,” *Nat. Mater.*, vol. 5, no. 3, pp. 204–209, Mar. 2006.

[11] H. C. Liu, M. Buchanan, and Z. R. Wasilewski, “How good is the polarization selection rule for intersubband transitions?,” *Appl. Phys. Lett.*, vol. 72, no. 14, pp. 1682–1684, Apr. 1998.

[12] M. Helm, “Chapter 1 The Basic Physics of Intersubband Transitions,” in *Semiconductors and Semimetals*, vol. 62, 1999, pp. 1–99.

[13] T. Gokmen and Y. Vlasov, “Acceleration of Deep Neural Network Training with Resistive Cross-Point Devices: Design Considerations,” *Front. Neurosci.*, vol. 10, no. JUL, pp. 1–13, Jul. 2016.

[14] E. Covi, S. Brivio, A. Serb, T. Prodromakis, M. Fanciulli, and S. Spiga, “Analog Memristive Synapse in Spiking Networks Implementing Unsupervised Learning,” *Front. Neurosci.*, vol. 10, no. OCT, pp. 1–13, Oct. 2016.

[15] M. Kund, G. Beitel, C.-U. Pinnow, T. Rohr, J. Schumann, R. Symanczyk, K. Ufert, and G. Muller, “Conductive bridging RAM (CBRAM): an emerging non-volatile memory technology scalable to sub 20nm,” in *IEEE InternationalElectron Devices Meeting, 2005. IEDM Technical Digest.*, 2005, vol. 00, no. 1, pp. 754–757.

[16] M. Prezioso, F. Merrikh-Bayat, B. D. Hoskins, G. C. Adam, K. K. Likharev, and D. B. Strukov, “Training and operation of an integrated neuromorphic network based on metal-oxide memristors,” *Nature*, vol. 521, no. 7550, pp. 61–64, May 2015.

[17] T. Werner, E. Vianello, O. Bichler, A. Grossi, E. Nowak, J.-F. Nodin, B. Yvert, B. DeSalvo, and L. Perniola, “Experimental demonstration of short and long term synaptic plasticity using OxRAM multi k-bit arrays for reliable detection in highly noisy input data,” in *2016 IEEE International Electron Devices Meeting (IEDM)*, 2016, p. 16.6.1-16.6.4.

[18] C. Sung, H. Hwang, and I. K. Yoo, “Perspective: A review on memristive hardware for neuromorphic computation,” *J. Appl. Phys.*, vol. 124, no. 15, p. 151903, Oct. 2018.

[19] R. Tsu and L. Esaki, “Tunneling in a finite superlattice,” *Appl. Phys. Lett.*, vol. 22, no. 11, pp. 562–564, Jun. 1973.

[20] L. L. Chang, L. Esaki, and R. Tsu, “Resonant tunneling in semiconductor double barriers,” *Appl. Phys. Lett.*, vol. 24, no. 12, pp. 593–595, Jun. 1974.

[21] M. A. Reed, J. W. Lee, and H.-L. Tsai, “Resonant tunneling through a double GaAs/AlAs superlattice barrier, single quantum well heterostructure,” *Appl. Phys. Lett.*, vol. 49, no. 3, pp. 158–160, Jul. 1986.

[22] Jian Ping Sun, G. I. Haddad, P. Mazumder, and J. N. Schulman, “Resonant tunneling diodes: models and properties,” *Proc. IEEE*, vol. 86, no. 4, pp. 641–660, Apr. 1998.

[23] H. Ikeda, M. Iwasaki, Y. Ishikawa, and M. Tabe, “Resonant tunneling characteristics in SiO_2/Si double-barrier structures in a wide range of applied voltage,” *Appl. Phys. Lett.*, vol. 83, no. 7, pp. 1456–1458, Aug. 2003.

[24] W. S. Choi, S. A. Lee, J. H. You, S. Lee, and H. N. Lee, “Resonant tunnelling in a quantum oxide superlattice,” *Nat. Commun.*, vol. 6, p. 7424, Jun. 2015.

[25] W. Guo, A. B. Posadas, and A. A. Demkov, “Deal-Grove-Like Thermal Oxidation of Si (001) Under an Ultrathin Layer of $SrTiO_3$,” vol. Under Review, 2019.

[26] H. Iwai, “Roadmap for 22nm and beyond (Invited Paper),” *Microelectron. Eng.*, vol. 86, no. 7–9, pp. 1520–1528, Jul. 2009.

[27] D. Zhang and J. J.-Q. Lu, “3D Integration Technologies: An Overview,” in *Materials for Advanced Packaging*, D. Lu and C. P. Wong, Eds. Cham: Springer International Publishing, 2017, pp. 1–26.

[28] A. B. Posadas, K. J. Kormondy, W. Guo, P. Ponath, J. Geler-Kremer, T. Hadamek, and A. A. Demkov, “Scavenging of oxygen from $SrTiO_3$ during oxide thin film deposition and the formation of interfacial 2DEGs,” *J. Appl. Phys.*, vol. 121, no. 10, p. 105302, Mar. 2017.

[29] Y. Li, C. Wang, Z. Yao, H.-K. Kim, and N.-Y. Kim, “Comparative analysis of barium titanate thin films dry etching using inductively coupled plasmas by different fluorine-based mixture gas,” *Nanoscale Res. Lett.*, vol. 9, no. 1, p. 530, 2014.

[30] M. A. Bandres, Y. Lumer, H. H. Sheinfux, Y. Plotnik, and M. Segev, “Dynamic Waveguiding,” in *Conference on Lasers and Electro-Optics*, 2016, no. c, p. FF1A.2.

Bibliography

Abel, S. et al. “Controlling Tetragonality and Crystalline Orientation in $BaTiO_3$ Nano-Layers Grown on Si.” *Nanotechnology* 24.28 (2013): 285701. Web.

Abel, Stefan, Thilo Stoferle, et al. “A Hybrid Barium Titanate–Silicon Photonics Platform for Ultraefficient Electro-Optic Tuning.” *Journal of Lightwave Technology* 34.8 (2016): 1688–1693. Web. 5 Apr. 2017.

Abel, Stefan, Thilo Stöferle, et al. “A Strong Electro-Optically Active Lead-Free Ferroelectric Integrated on Silicon.” *Nature Communications* 4.1 (2013): 1671. Web.

Abel, Stefan, Felix Eltes, et al. “Large Pockels Effect in Micro- and Nanostructured Barium Titanate Integrated on Silicon.” *Nature Materials* 18.1 (2019): 42–47. Web.

Abel, Stefan, David J. Stark, et al. “Multi-Level Optical Weights in Integrated Circuits.” *2017 IEEE International Conference on Rebooting Computing (ICRC)*. Vol. 2017–Janua. IEEE, 2017. 1–3. Web.

Abel, Stefan, and Jean Fompeyrine. “Electro-Optically Active Oxides on Silicon for Photonics.” *Thin Films on Silicon*. Ed. Vijay Narayanan, Martin M Frank, and Alexander A Demkov. Vol. 8. World Scientific, 2016. 455–501. Web.

Ahn, D., and S. L. Chuang. “Exact Calculations of Quasibound States of an Isolated Quantum Well with Uniform Electric Field: Quantum-Well Stark Resonance.” *Physical Review B* 34.12 (1986): 9034–9037. Web.

Ahn, D., and S. L. Chuang. “Intersubband Optical Absorption in a Quantum Well with an Applied Electric Field.” *Physical Review B* 35.8 (1987): 4149–4151. Web.

Alexander, Koen, John Puthenparampil George, et al. “Broadband Electro-Optic Modulation Using Low-Loss PZT- on-Silicon Nitride Integrated Waveguides.” *CLEO 2017* (2017): JTh5C.7. Print.

Alexander, Koen, John P George, et al. “Nanophotonic Pockels Modulators on a Silicon Nitride Platform.” *Nature Communications* 9.1 (2018): 3444. Web. 28 May 2018.

Ando, Masanori et al. “Large Third-Order Optical Nonlinearities in Transition-Metal Oxides.” *Nature* 374.6523 (1995): 625–627. Web.

Arbabi, Amir, and Lynford L. Goddard. “Measurements of the Refractive Indices and Thermo-Optic Coefficients of S_3N_4 and SiO_x Using Microring Resonances.” *Optics Letters* 38.19 (2013): 3878. Web.

Atabaki, Amir H et al. “Sub-100-Nanosecond Thermal Reconfiguration of Silicon Photonic Devices.” *Optics Express* 21.13 (2013): 15706. Web. 13 Apr. 2018.

Baehr-Jones, Tom et al. “Ultralow Drive Voltage Silicon Traveling-Wave Modulator.” *Optics Express* 20.11 (2012): 12014. Web.

Baek, Seung-Hyub, and Chang-Beom Eom. “Epitaxial Integration of Perovskite-Based Multifunctional Oxides on Silicon.” *Acta Materialia* 61.8 (2013): 2734–2750. Web. 28 Aug. 2017.

Bandres, Miguel A. et al. “Dynamic Waveguiding.” *Conference on Lasers and Electro-Optics*. Washington, D.C.: OSA, 2016. FF1A.2. Web.

Bastard, G. et al. “Variational Calculations on a Quantum Well in an Electric Field.” *Physical Review B* 28.6 (1983): 3241–3245. Web.

Bastard, G. *Wave Mechanics Applied to Semiconductor Heterostructures*. United States: John Wiley and Sons Inc, 1990. Web.

Bernasconi, Pietro et al. “Temperature Dependence and Dispersion of Electro-optic and Elasto-optic Effect in Perovskite Crystals.” *Journal of Applied Physics* 78.4 (1995): 2651–2658. Web.

Bert, Julie A et al. “Direct Imaging of the Coexistence of Ferromagnetism and Superconductivity at the $LaAlO_3/SrTiO_3$ Interface.” *Nature Physics* 7.10 (2011): 767–771. Web.

Berthomieu, Catherine, and Rainer Hienerwadel. “Fourier Transform Infrared (FTIR) Spectroscopy.” *Photosynthesis Research* 101.2–3 (2009): 157–170. Web.

Betts, R.A., and C.W. Pitt. “Growth of Thin-Film Lithium Niobate by Molecular Beam Epitaxy.” *Electronics Letters* 21.21 (1985): 960. Web.

Bhattacharya, A. et al. “Signatures of Enhanced Ordering Temperatures in Digital Superlattices of $(LaMnO_3)_m/(SrMnO_3)_{2m}$.” *Applied Physics Letters* 90.22 (2007): 222503. Web.

Bi, Feng et al. “Room-Temperature Electronically-Controlled Ferromagnetism at the $LaAlO_3/SrTiO_3$ Interface.” *Nature Communications* 5 (2014): 5019. Web. 7 Feb. 2017.

Biscaras, J. et al. “Two-Dimensional Superconductivity at a Mott Insulator/Band Insulator Interface $LaTiO_3/SrTiO_3$.” *Nature Communications* 1.7 (2010): 1–5. Web. 29 Jan. 2017.

Bjaalie, L et al. “Oxide Interfaces for Novel Electronic Applications.” *New Journal of Physics* 16.2 (2014): 025005. Web. 29 Jan. 2017.

Björck, Matts, and Gabriella Andersson. “GenX: An Extensible X-Ray Reflectivity Refinement Program Utilizing Differential Evolution.” *J. Appl. Cryst* 40 (2007): 1174–1178. Web. 22 Aug. 2017.

Blöchl, P. E. “Projector Augmented-Wave Method.” *Physical Review B* 50.24 (1994): 17953–17979. Web. 25 Feb. 2017.

Bogaerts, W. et al. “Silicon Microring Resonators.” *Laser & Photonics Reviews* 6.1 (2012): 47–73. Web.

Bogaerts, Wim, and Lukas Chrostowski. “Silicon Photonics Circuit Design: Methods, Tools and Challenges.” *Laser & Photonics Reviews* 12.4 (2018): 1700237. Web.

Bogorin, Daniela F. et al. “$LaAlO_3/SrTiO_3$-Based Device Concepts.” *Multifunctional Oxide Heterostructures*. Oxford University Press, 2010. 364–388. Web. 18 July 2017.

Bohr, Mark et al. “The High-*k* Solution.” *IEEE Spectrum* 44.10 (2007): 29–35. Web.

Borghi, Massimo et al. “Homodyne Detection of Free Carrier Induced Electro-Optic Modulation in Strained Silicon Resonators.” *Journal of Lightwave Technology* 34.24 (2016): 5657–5668. Web.

Bragg, W H., and W L Bragg. “The Reflection of X-Rays by Crystals.” *Proceedings of the Royal Society A: Mathematical, Physical and Engineering Sciences* 88.605 (1913): 428–438. Web.

Brinkman, A. et al. “Magnetic Effects at the Interface between Non-Magnetic Oxides.” *Nature Materials* 6.7 (2007): 493–496. Web. 5 Feb. 2017.

Bristowe, N C, Emilio Artacho, and P B Littlewood. “Oxide Superlattices with Alternating *p* and *n* Interfaces.” *Physical Review B* 80.4 (2009): 045425. Web. 17 Apr. 2018.

Brooks, C M et al. “Growth of Homoepitaxial $SrTiO_3$ Thin Films by Molecular-Beam Epitaxy.” *Applied Physics Letters* 94.16 (2009): 162905. Web.

Brosi, Jan-michael et al. “Modulator with a Polymer-Infiltrated Silicon Photonic Crystal Waveguide.” *Optics express* 16.6 (2008): 180–185. Print.

Castera, Pau, Ana M. Gutierrez, et al. “Electro-Optical Modulation Based on Pockels Effect in $BaTiO_3$ With a Multi-Domain Structure.” *IEEE Photonics Technology Letters* 28.9 (2016): 990–993. Web.

Castera, Pau, Domenico Tulli, et al. “Influence of $BaTiO_3$ Ferroelectric Orientation for Electro-Optic Modulation on Silicon.” *Optics Express* 23.12 (2015): 15332. Web. 26 Apr. 2018.

Cavalleri, A. et al. “Femtosecond Structural Dynamics in VO_2 during an Ultrafast Solid-Solid Phase Transition.” *Physical Review Letters* 87.23 (2001): 237401. Web.

Chakhalian, Jak et al. “Colloquium: Emergent Properties in Plane View: Strong Correlations at Oxide Interfaces.” *Reviews of Modern Physics* 86.4 (2014): 1189–1202. Web. 11 Feb. 2017.

Chambers, Scott A. “Epitaxial Growth and Properties of Thin Film Oxides.” *Surface Science Reports* 39.5–6 (2000): 105–180. Web.

Chand, Naresh. “MBE Growth of High-Quality GaAs.” *Journal of Crystal Growth* 97.2 (1989): 415–429. Web.

Chang, L. L., L. Esaki, and R. Tsu. “Resonant Tunneling in Semiconductor Double Barriers.” *Applied Physics Letters* 24.12 (1974): 593–595. Web.

Chemla, D. S. et al. “Electroabsorption by Stark Effect on Room-temperature Excitons in GaAs/GaAlAs Multiple Quantum Well Structures.” *Applied Physics Letters* 42.10 (1983): 864–866. Web.

Chen, J. Q. et al. “Defect Dynamics and Spectral Observation of Twinning in Single Crystalline $LaAlO_3$ under Subbandgap Excitation.” *Applied Physics Letters* 98.4 (2011): 041904. Web.

Chen, Li et al. “Hybrid Silicon and Lithium Niobate Electro-Optical Ring Modulator.” *Optica* 1.2 (2014): 112. Web.

Chen, Li, Michael G. Wood, and Ronald M. Reano. “12.5 Pm/V Hybrid Silicon and Lithium Niobate Optical Microring Resonator with Integrated Electrodes.” *Optics Express* 21.22 (2013): 27003. Web.

Cheong, Sang-Wook, and Maxim Mostovoy. “Multiferroics: A Magnetic Twist for Ferroelectricity.” *Nature Materials* 6.1 (2007): 13–20. Web.

Chiles, Jeff et al. “Design, Fabrication, and Metrology of 10 × 100 Multi-Planar Integrated Photonic Routing Manifolds for Neural Networks.” *APL Photonics* 3.10 (2018): 106101. Web.

Chmielak, Bartos et al. “Pockels Effect Based Fully Integrated, Strained Silicon Electro-Optic Modulator.” *Optics Express* 19.18 (2011): 17212. Web.

Cho, A.Y., and J.R. Arthur. “Molecular Beam Epitaxy.” *Progress in Solid State Chemistry* 10 (1975): 157–191. Web.

Choi, Miri, Chungwei Lin, et al. “Quantum Confinement in Transition Metal Oxide Quantum Wells.” *Applied Physics Letters* 106.19 (2015): 192902. Web.

Choi, Miri, Agham Posadas, et al. “Strain Relaxation in Single Crystal $SrTiO_3$ Grown on Si (001) by Molecular Beam Epitaxy.” *Journal of Applied Physics* 111.6 (2012): 064112. Web.

Choi, Miri, Agham B. Posadas, et al. “Structural, Optical, and Electrical Properties of Strained La-Doped $SrTiO_3$ Films.” *Journal of Applied Physics* 116.4 (2014): 043705. Web. 28 Nov. 2016.

Choi, Woo Seok et al. “Resonant Tunnelling in a Quantum Oxide Superlattice.” *Nature Communications* 6 (2015): 7424. Web. 15 Sept. 2017.

Cocorullo, G., F. G. Della Corte, and I. Rendina. “Temperature Dependence of the Thermo-Optic Coefficient in Crystalline Silicon between Room Temperature and 550 K at the Wavelength of 1523 Nm.” *Applied Physics Letters* 74.22 (1999): 3338–3340. Web.

Coon, D. D., and R. P. G. Karunasiri. “New Mode of IR Detection Using Quantum Wells.” *Applied Physics Letters* 45.6 (1984): 649–651. Web. 29 Jan. 2017.

Courtland, Rachel. “Transistors Could Stop Shrinking in 2021.” *IEEE Spectrum* 53.9 (2016): 9–11. Web.

Covi, Erika et al. “Analog Memristive Synapse in Spiking Networks Implementing Unsupervised Learning.” *Frontiers in Neuroscience* 10.OCT (2016): 1–13. Web.

Cuong, Do Duc et al. “Oxygen Vacancy Clustering and Electron Localization in Oxygen-Deficient $SrTiO_3$: LDA + *U* Study.” *Physical Review Letters* 98.11 (2007): 115503. Web.

Czornomaz, L et al. “Scalability of Ultra-Thin-Body and BOX InGaAs MOSFETs on Silicon.” *Proc. European Solid-State Device Research Conf, (ESSDERC),*. N.p., 2013. 143–146. Print.

Czornomaz, Lukas et al. “Wafer Bonding: An Integration Route for Hybrid III-V/SiGe CMOS on 300mm.” *ECS Transactions* 64.5 (2014): 199–209. Web.

De Souza, R. A. “Oxygen Diffusion in $SrTiO_3$ and Related Perovskite Oxides.” *Advanced Functional Materials* 25.40 (2015): 6326–6342. Web.

Deal, B. E., and A. S. Grove. “General Relationship for the Thermal Oxidation of Silicon.” *Journal of Applied Physics* 36.12 (1965): 3770–3778. Web.

Della Corte, Francesco G. et al. “Temperature Dependence Analysis of the Thermo-Optic Effect in Silicon by Single and Double Oscillator Models.” *Journal of Applied Physics* 88.12 (2000): 7115–7119. Web.

Demkov, A. A. et al. “Using Zintl-Klemm Intermetallics in Oxide-Semiconductor Heteroepitaxy.” *Applied Physics Letters* 100.7 (2012): 071602. Web.

DeRose, Christopher T. et al. “Thermal Crosstalk Limits for Silicon Photonic DWDM Interconnects.” *2014 Optical Interconnects Conference*. Vol. 5. IEEE, 2014. 125–126. Web.

Ding, Jianfeng et al. “Mach-Zehnder Silicon Optical Modulator.” 20.7 (2012): 59–63. Print.

Ding, Ran et al. “A Compact Low-Power 320-Gb/s WDM Transmitter Based on Silicon Microrings.” *IEEE Photonics Journal* 6.3 (2014): 1–8. Web.

Doennig, David, and Rossitza Pentcheva. “Control of Orbital Reconstruction in $(LaAlO_3)_M/(SrTiO_3)_N$ (001) Quantum Wells by Strain and Confinement.” *Scientific Reports* 5.1 (2015): 7909. Web. 5 Feb. 2017.

Domínguez Bucio, Thalía et al. “Material and Optical Properties of Low-Temperature NH_3-Free PECVD SiN_x Layers for Photonic Applications.” *Journal of Physics D: Applied Physics* 50.2 (2017): 025106. Web.

Dong, Po, Wei Qian, Hong Liang, Roshanak Shafiiha, Ning-Ning Feng, et al. “Low Power and Compact Reconfigurable Multiplexing Devices Based on Silicon Microring Resonators.” *Optics Express* 18.10 (2010): 9852. Web.

Dong, Po, Wei Qian, Hong Liang, Roshanak Shafiiha, Dazeng Feng, et al. "Thermally Tunable Silicon Racetrack Resonators with Ultralow Tuning Power." *Optics Express* 18.19 (2010): 20298. Web.

Doolittle, W. Alan, Alexander G. Carver, and Walter Henderson. "Molecular Beam Epitaxy of Complex Metal-Oxides: Where Have We Come, Where Are We Going, and How Are We Going to Get There?" *Journal of Vacuum Science & Technology B: Microelectronics and Nanometer Structures* 23.3 (2005): 1272. Web.

Doyeol Ahn, and Shun-lien Chuang. "Calculation of Linear and Nonlinear Intersubband Optical Absorptions in a Quantum Well Model with an Applied Electric Field." *IEEE Journal of Quantum Electronics* 23.12 (1987): 2196–2204. Web.

Dubourdieu, Catherine et al. "Switching of Ferroelectric Polarization in Epitaxial $BaTiO_3$ Films on Silicon without a Conducting Bottom Electrode." *Nature Nanotechnology* 8.10 (2013): 748–754. Web.

Dupont, E.B., Dominique Delacourt, and Michel Papuchon. "Mid-Infrared Phase Modulation via Stark Effect on Intersubband Transitions in GaAs/GaAlAs Quantum Wells." *IEEE Journal of Quantum Electronics* 29.8 (1993): 2313–2318. Web.

Dutt, Avik et al. "On-Chip Dual-Comb Source for Spectroscopy." *Science Advances* 4.3 (2018): e1701858. Web.

Dwivedi, Sarvagya, Herbert D'heer, and Wim Bogaerts. "Maximizing Fabrication and Thermal Tolerances of All-Silicon FIR Wavelength Filters." *IEEE Photonics Technology Letters* 27.8 (2015): 871–874. Web.

Egerton, R. F. "Electron Energy-Loss Spectroscopy in the TEM." *Reports on Progress in Physics* 72.1 (2009): 016502. Web.

Eltes, Felix, Christian Mai, et al. "A $BaTiO_3$-Based Electro-Optic Pockels Modulator Monolithically Integrated on an Advanced Silicon Photonics Platform." *Journal of Lightwave Technology* 37.5 (2019): 1456–1462. Web.

Eltes, Felix, Marcel Kroh, et al. "A Novel 25 Gbps Electro-Optic Pockels Modulator Integrated on an Advanced Si Photonic Platform." *2017 IEEE International Electron Devices Meeting (IEDM)*. IEEE, 2017. 24.5.1-24.5.4. Web.

Eltes, Felix, Daniele Caimi, et al. "Low-Loss $BaTiO_3$–Si Waveguides for Nonlinear Integrated Photonics." *ACS Photonics* 3.9 (2016): 1698–1703. Web.

Faist, Jerome et al. "Quantum Cascade Laser." *Science* 264.5158 (1994): 553–556. Web. 29 Jan. 2017.

Fewster, Paul F. "Reciprocal Space Mapping." *Critical Reviews in Solid State and Materials Sciences* 22.2 (1997): 69–110. Web.

Frederikse, H. P R, and W. R. Hosler. “Hall Mobility in $SrTiO_3$.” *Physical Review* 161.3 (1967): 822–827. Web.

Fredrickson, Kurt D., Hosung Seo, and Alexander A. Demkov. “Mechanism of Oxidation Protection of the Si(001) Surface by Sub-Monolayer Sr Template.” *Journal of Applied Physics* 120.6 (2016): 065301. Web.

Geller, S, and V B Bala. “Crystallographic Studies of Perovskite-like Compounds. II. Rare Earth Alluminates.” *Acta Crystallographica* 9.12 (1956): 1019–1025. Web. 15 Aug. 2017.

Georgas, Michael et al. “Addressing Link-Level Design Tradeoffs for Integrated Photonic Interconnects.” *2011 IEEE Custom Integrated Circuits Conference (CICC)*. IEEE, 2011. 1–8. Web.

Girouard, Peter et al. “$\chi^{(2)}$ Modulator With 40-GHz Modulation Utilizing $BaTiO_3$ Photonic Crystal Waveguides.” *IEEE Journal of Quantum Electronics* 53.4 (2017): 1–10. Web.

Gokmen, Tayfun, and Yurii Vlasov. “Acceleration of Deep Neural Network Training with Resistive Cross-Point Devices: Design Considerations.” *Frontiers in Neuroscience* 10.JUL (2016): 1–13. Web.

Goncharova, L. V. et al. “Interface Structure and Thermal Stability of Epitaxial $SrTiO_3$ Thin Films on Si (001).” *Journal of Applied Physics* 100.1 (2006): 014912. Web.

Goykhman, Ilya, Boris Desiatov, and Uriel Levy. “Ultrathin Silicon Nitride Microring Resonator for Biophotonic Applications at 970 Nm Wavelength.” *Applied Physics Letters* 97.8 (2010): 081108. Web.

Green, William M. et al. “Ultra-Compact, Low RF Power, 10 Gb/s Silicon Mach-Zehnder Modulator.” *Optics Express* 15.25 (2007): 17106. Web.

Guo, Rui et al. “Functional Ferroelectric Tunnel Junctions on Silicon.” *Scientific Reports* 5.1 (2015): 12576. Web.

Guo, Wei et al. “EuO Epitaxy by Oxygen Scavenging on $SrTiO_3$ (001): Effect of $SrTiO_3$ Thickness and Temperature.” *Journal of Applied Physics* 124.23 (2018): 235301. Web.

Guo, Wei, Agham B. Posadas, and Alexander A. Demkov. “Deal-Grove-Like Thermal Oxidation of Si (001) Under an Ultrathin Layer of $SrTiO_3$.” Unpublishe (2019): n. pag. Print.

Gusev, E.P., C Cabral, et al. “Ultrathin HfO_2 Films Grown on Silicon by Atomic Layer Deposition for Advanced Gate Dielectrics Applications.” *Microelectronic Engineering* 69.2–4 (2003): 145–151. Web.

Gusev, E.P., D.A. Buchanan, et al. “Ultrathin High-K Gate Stacks for Advanced CMOS Devices.” *International Electron Devices Meeting. Technical Digest (Cat. No.01CH37224)*. IEEE, 2001. 20.1.1-20.1.4. Web.

Haffner, C. et al. “All-Plasmonic Mach–Zehnder Modulator Enabling Optical High-Speed Communication at the Microscale.” *Nature Photonics* 9.8 (2015): 525–528. Web.

Hall, E. H. “On a New Action of the Magnet on Electric Currents.” *American Journal of Mathematics* 2.3 (1879): 287. Web.

Hamann, H.F. et al. “Spatially-Resolved Imaging of Microprocessor Power (SIMP): Hotspots in Microprocessors.” *Thermal and Thermomechanical Proceedings 10th Intersociety Conference on Phenomena in Electronics Systems, 2006. ITHERM 2006.* Vol. 2006. IEEE, 2006. 121–125. Web.

Hanzig, Florian et al. “Crystallization Dynamics and Interface Stability of Strontium Titanate Thin Films on Silicon.” *Journal of Applied Crystallography* 48.2 (2015): 393–400. Web.

Harris, Nicholas C et al. “Integrated Source of Spectrally Filtered Correlated Photons for Large-Scale Quantum Photonic Systems.” *Physical Review X* 4.4 (2014): 041047. Web. 9 Apr. 2018.

Harwit, Alex, and J. S. Harris. “Observation of Stark Shifts in Quantum Well Intersubband Transitions.” *Applied Physics Letters* 50.11 (1987): 685–687. Web.

Hattori, Takeo. “Chemical Structures of the SiO_2 Si Interface.” *Critical Reviews in Solid State and Materials Sciences* 20.4 (1995): 339–382. Web.

Heck, Martijn J.R. “Highly Integrated Optical Phased Arrays: Photonic Integrated Circuits for Optical Beam Shaping and Beam Steering.” *Nanophotonics* 6.1 (2017): 93–107. Web.

Helm, Manfred. “Chapter 1 The Basic Physics of Intersubband Transitions.” *Semiconductors and Semimetals*. Vol. 62. N.p., 1999. 1–99. Web. 7 Feb. 2017.

Heni, Wolfgang et al. “Silicon–Organic and Plasmonic–Organic Hybrid Photonics.” *ACS Photonics* 4.7 (2017): 1576–1590. Web.

Herranz, G et al. “High Mobility in $LaAlO_3/SrTiO_3$ Heterostructures: Origin, Dimensionality, and Perspectives.” *Physical Review Letters* 98.21 (2007): 216803. Web. 20 Feb. 2017.

Hochberg, Michael, and Tom Baehr-Jones. “Towards Fabless Silicon Photonics.” *Nature Photonics* 4.8 (2010): 492–494. Web.

Hoessbacher, C. et al. “Plasmonic Modulator with >170 GHz Bandwidth Demonstrated at 100 GBd NRZ.” *Optics Express* 25.3 (2017): 1762. Web.

Holm, D.A., and H.F. Taylor. “Infrared Phase Modulators with Multiple Quantum Wells.” *IEEE Journal of Quantum Electronics* 25.11 (1989): 2266–2271. Web.

Horio, Yoshimi, Yasuyuki Hashimoto, and Ayahiko Ichimiya. "A New Type of RHEED Apparatus Equipped with an Energy Filter." *Applied Surface Science* 100–101.1 (1996): 292–296. Web.

Horst, Folkert et al. "Cascaded Mach-Zehnder Wavelength Filters in Silicon Photonics for Low Loss and Flat Pass-Band WDM (de-)Multiplexing." *Optics Express* 21.10 (2013): 11652. Web. 12 Apr. 2018.

Hryniewicz, J.V. et al. "Higher Order Filter Response in Coupled Microring Resonators." *IEEE Photonics Technology Letters* 12.3 (2000): 320–322. Web.

Hu, Xuan et al. "Modeling the Anisotropic Electro-Optic Interaction in Hybrid Silicon-Ferroelectric Optical Modulator." *Optics Express* 23.2 (2015): 1699. Web.

Huijben, Mark, Guus Rijnders, et al. "Electronically Coupled Complementary Interfaces between Perovskite Band Insulators." *Nature Materials* 5.7 (2006): 556–560. Web.

Huijben, Mark, Alexander Brinkman, et al. "Structure-Property Relation of $SrTiO_3$/$LaAlO_3$ Interfaces." *Advanced Materials* 21.17 (2009): 1665–1677. Web.

Hwang, H. Y. et al. "Emergent Phenomena at Oxide Interfaces." *Nature Materials* 11.2 (2012): 103–113. Web. 5 Feb. 2017.

Ichimiya, Ayahiko, and Philip I. Cohen. *Reflection High-Energy Electron Diffraction*. Cambridge: Cambridge University Press, 2004. Web.

Ieda, Masayuki, Goro Sawa, and Sousuke Kato. "A Consideration of Poole-Frenkel Effect on Electric Conduction in Insulators." *Journal of Applied Physics* 42.10 (1971): 3737–3740. Web.

Ikeda, Hiroya et al. "Resonant Tunneling Characteristics in SiO_2/Si Double-Barrier Structures in a Wide Range of Applied Voltage." *Applied Physics Letters* 83.7 (2003): 1456–1458. Web.

Imada, Masatoshi, Atsushi Fujimori, and Yoshinori Tokura. "Metal-Insulator Transitions." *Reviews of Modern Physics* 70.4 (1998): 1039–1263. Web.

Inaba, Katsuhiko. "X-Ray Thin Film Measurement Techniques." *The Rigaku Journal* 24.1 (2008): 10–15. Web.

Iwai, H. "Roadmap for 22nm and beyond (Invited Paper)." *Microelectronic Engineering* 86.7–9 (2009): 1520–1528. Web.

Iwata, Nobuyuki et al. "Preparation and Magnetic Properties of EuO Thin Films Epitaxially Grown on MgO and $SrTiO_3$ Substrates." *Journal of the Physical Society of Japan* 69.1 (2000): 230–236. Web.

Jacob, Ajey P. et al. "Scaling Challenges for Advanced CMOS Devices." *International Journal of High Speed Electronics and Systems* 26.01n02 (2017): 1740001. Web.

Janner, Davide et al. "Micro-Structured Integrated Electro-Optic $LiNbO_3$ Modulators." *Laser & Photonics Review* 3.3 (2009): 301–313. Web.

Janotti, A., D. Steiauf, and C. G. Van de Walle. "Strain Effects on the Electronic Structure of $SrTiO_3$: Toward High Electron Mobilities." *Physical Review B* 84.20 (2011): 201304. Web.

Javerzac-Galy, C. et al. "On-Chip Microwave-to-Optical Quantum Coherent Converter Based on a Superconducting Resonator Coupled to an Electro-Optic Microresonator." *Physical Review A* 94.5 (2016): 053815. Web.

Jian Ping Sun et al. "Resonant Tunneling Diodes: Models and Properties." *Proceedings of the IEEE* 86.4 (1998): 641–660. Web.

Jiang, Nan. "Electron Beam Damage in Oxides: A Review." *Reports on Progress in Physics* 79.1 (2016): 016501. Web.

Jin, Tiening et al. "Monolithic Mid-Infrared Integrated Photonics Using Silicon-on-Epitaxial Barium Titanate Thin Films." *ACS Applied Materials & Interfaces* 9.26 (2017): 21848–21855. Web. 26 Apr. 2018.

Johnson, B. R., N. Anand, et al. "*In Situ* Formation of Superconducting $YBa_2Cu_3O_{7-x}$ Thin Films Using Pure Ozone Vapor Oxidation." *Applied Physics Letters* 53.20 (2002): 1973–1975. Web.

Johnson, B. R., K. M. Beauchamp, et al. "*In Situ* Growth of $DyBa_2Cu_3O_{7-x}$ Thin Films by Molecular Beam Epitaxy." *Applied Physics Letters* 56.19 (1990): 1911–1913. Web.

Johs, Blaine et al. "Real-Time Monitoring and Control during MOVPE Growth of CdTe Using Multiwavelength Ellipsometry." *Thin Solid Films* 233.1–2 (1993): 293–296. Web.

Kabelac, J. et al. "Rf Oxygen Plasma Assisted Molecular Beam Epitaxy Growth of $BiFeO_3$ Thin Films on $SrTiO_3$ (001)." *Journal of Vacuum Science & Technology B: Microelectronics and Nanometer Structures* 25.3 (2007): 1049. Web.

Kalisky, Beena et al. "Critical Thickness for Ferromagnetism in $LaAlO_3/SrTiO_3$ Heterostructures." *Nature Communications* 3 (2012): 922. Web. 4 Feb. 2017.

Kamihara, Yoichi et al. "Iron-Based Layered Superconductor: LaOFeP." *Journal of the American Chemical Society* 128.31 (2006): 10012–10013. Web.

Kane, E. O. "Basic Concepts of Tunneling." *Tunneling Phenomena in Solids*. Boston, MA: Springer US, 1969. 1–11. Web.

Khatib, D, B Jannot, and P Jullien. "Theory of Electro-Optic Effect in the Tetragonal Phase of $BaTiO_3$." *Ferroelectrics Letters Section* 15.1 (1993): 1–7. Web.

Kiessig, Heinz. "Untersuchungen Zur Totalreflexion von Röntgenstrahlen." *Annalen der Physik* 402.6 (1931): 715–768. Web.

Kildemo, M., and B. Drévillon. "Real Time Monitoring of the Growth of Transparent Thin Films by Spectroscopic Ellipsometry." *Review of Scientific Instruments* 67.5 (1996): 1956–1960. Web.

Kim, C.M., and R.V. Ramaswamy. “Overlap Integral Factors in Integrated Optic Modulators and Switches.” *Journal of Lightwave Technology* 7.7 (1989): 1063–1070. Web.

Kita, Derek M et al. “High-Performance and Scalable on-Chip Digital Fourier Transform Spectroscopy.” *Nature Communications* 9.1 (2018): 4405. Web.

Komma, J. et al. “Thermo-Optic Coefficient of Silicon at 1550 Nm and Cryogenic Temperatures.” *Applied Physics Letters* 101.4 (2012): 041905. Web.

Kormondy, Kristy J. et al. “Large Positive Linear Magnetoresistance in the Two-Dimensional t_{2g} Electron Gas at the EuO/$SrTiO_3$ Interface.” *Scientific Reports* 8.1 (2018): 7721. Web.

Kormondy, Kristy J et al. “Microstructure and Ferroelectricity of $BaTiO_3$ Thin Films on Si for Integrated Photonics.” *Nanotechnology* 28.7 (2017): 075706. Web.

Kowarik, S., A. Gerlach, W. Leitenberger, et al. “Energy-Dispersive X-Ray Reflectivity and GID for Real-Time Growth Studies of Pentacene Thin Films.” *Thin Solid Films* 515.14 (2007): 5606–5610. Web.

Kowarik, S., A. Gerlach, M. W A Skoda, et al. “Real-Time Studies of Thin Film Growth: Measurement and Analysis of X-Ray Growth Oscillations beyond the Anti-Bragg Point.” *The European Physical Journal Special Topics* 167.1 (2009): 11–18. Web.

Krames, Michael R. et al. “Status and Future of High-Power Light-Emitting Diodes for Solid-State Lighting.” *Journal of Display Technology* 3.2 (2007): 160–175. Web. 29 Jan. 2017.

Kresse, G., and J. Furthmüller. “Efficient Iterative Schemes for *Ab Initio* Total-Energy Calculations Using a Plane-Wave Basis Set.” *Physical Review B* 54.16 (1996): 11169–11186. Web. 25 Feb. 2017.

Kund, M. et al. “Conductive Bridging RAM (CBRAM): An Emerging Non-Volatile Memory Technology Scalable to Sub 20nm.” *IEEE InternationalElectron Devices Meeting, 2005. IEDM Technical Digest.* Vol. 00. IEEE, 2005. 754–757. Web.

Kwo, J. et al. “*In Situ* Epitaxial Growth of $Y_1Ba_2Cu_3O_{7-x}$ Films by Molecular Beam Epitaxy with an Activated Oxygen Source.” *Applied Physics Letters* 53.26 (1988): 2683–2685. Web.

Lam, Cedric et al. “Fiber Optic Communication Technologies: What’s Needed for Datacenter Network Operations.” *IEEE Communications Magazine* 48.7 (2010): 32–39. Web.

Lee, Ho Nyung et al. “Strong Polarization Enhancement in Asymmetric Three-Component Ferroelectric Superlattices.” *Nature* 433.7024 (2005): 395–399. Web.

Lee, J.-S. et al. “Titanium d_{XY} Ferromagnetism at the $LaAlO_3$/$SrTiO_3$ Interface.” *Nature Materials* 12.8 (2013): 703–706. Web. 29 Jan. 2017.

Lee, Jaekwang, and Alexander A. Demkov. "Charge Origin and Localization at the *n*-Type $SrTiO_3/LaAlO_3$ Interface." *Physical Review B* 78.19 (2008): 193104. Web.

Leinders, S.M. et al. "A Sensitive Optical Micro-Machined Ultrasound Sensor (OMUS) Based on a Silicon Photonic Ring Resonator on an Acoustical Membrane." *Scientific Reports* 5.1 (2015): 14328. Web. 9 Apr. 2018.

Leuthold, J, C Koos, and W Freude. "Nonlinear Silicon Photonics." *Nature Photonics* 4.8 (2010): 535–544. Web. 9 Apr. 2018.

Leuthold, Juerg et al. "Silicon-Organic Hybrid Electro-Optical Devices." *IEEE Journal of Selected Topics in Quantum Electronics* 19.6 (2013): 114–126. Web.

Levine, B. F. "Quantum-Well Infrared Photodetectors." *Journal of Applied Physics* 74.8 (1993): R1. Web. 29 Jan. 2017.

Li, Guoliang et al. "25 Gb/s 1V-Driving CMOS Ring Modulator with Integrated Thermal Tuning." *Optics Express* 19.21 (2011): 20435. Web.

Li, Lu et al. "Coexistence of Magnetic Order and Two-Dimensional Superconductivity at $LaAlO_3/SrTiO_3$ Interfaces." *Nature Physics* 7.10 (2011): 762–766. Web. 5 Feb. 2017.

Li, Yang et al. "Comparative Analysis of Barium Titanate Thin Films Dry Etching Using Inductively Coupled Plasmas by Different Fluorine-Based Mixture Gas." *Nanoscale Research Letters* 9.1 (2014): 530. Web.

Liao, Ling et al. "High Speed Silicon Mach-Zehnder Modulator." *Optics Express* 13.8 (2005): 3129. Web.

Lim, Seung-Gu et al. "Dielectric Functions and Optical Bandgaps of High-*K* Dielectrics for Metal-Oxide-Semiconductor Field-Effect Transistors by Far Ultraviolet Spectroscopic Ellipsometry." *Journal of Applied Physics* 91.7 (2002): 4500–4505. Web.

Lin, Chungwei et al. "Optical Properties of Transition Metal Oxide Quantum Wells." *Journal of Applied Physics* 117.3 (2015): 034304. Web. 29 Jan. 2017.

Lin, Y.-S., R. Puthenkovilakam, and J. P. Chang. "Dielectric Property and Thermal Stability of HfO_2 on Silicon." *Applied Physics Letters* 81.11 (2002): 2041–2043. Web.

Lin, Y et al. "Epitaxial Growth of Dielectric $CaCu_3Ti_4O_{12}$ Thin Films on (001) $LaAlO_3$ by Pulsed Laser Deposition." *Applied Physics Letters* 81.4 (2002): 631–633. Web.

Liu, H C, M. Buchanan, and Z R Wasilewski. "How Good Is the Polarization Selection Rule for Intersubband Transitions?" *Applied Physics Letters* 72.14 (1998): 1682–1684. Web. 7 Feb. 2017.

Luo, Mengxi, and Degui Sun. "Ultra-Efficient Modulation of $BaTiO_3$ Crystal Thin Film Waveguide with a Two-Dimensional Optic-Electric Field Matching Scheme." *Journal of Applied Physics* 123.3 (2018): 034503. Web.

Mahan, John E et al. "A Review of the Geometrical Fundamentals of Reflection High-energy Electron Diffraction with Application to Silicon Surfaces." *Journal of Vacuum Science & Technology A: Vacuum, Surfaces, and Films* 8.5 (1990): 3692–3700. Web.

Manganelli, Costanza Lucia, Paolo Pintus, and Claudio Bonati. "Modeling of Strain-Induced Pockels Effect in Silicon." *Optics Express* 23.22 (2015): 28649. Web.

Mannhart, J et al. "Two-Dimensional Electron Gases at Oxide Interfaces." *MRS Bulletin* 33.11 (2008): 1027–1034. Web.

Marcus, Robert B. (Ed). *Measurement of High-Speed Signals in Solid State Devices*. Vol. 28. Academic Press, Inc, 1990. Web.

McCollam, A. et al. "Quantum Oscillations and Subband Properties of the Two-Dimensional Electron Gas at the $LaAlO_3/SrTiO_3$ Interface." *APL Materials* 2.2 (2014): 022102. Web.

McKee, R. A., F. J. Walker, E. D. Specht, et al. "Interface Stability and the Growth of Optical Quality Perovskites on MgO." *Physical Review Letters* 72.17 (1994): 2741–2744. Web.

McKee, R. A., F. J. Walker, J. R. Conner, et al. "Molecular Beam Epitaxy Growth of Epitaxial Barium Silicide, Barium Oxide, and Barium Titanate on Silicon." *Applied Physics Letters* 59.7 (1991): 782–784. Web. 9 Aug. 2016.

McKee, R. A., F. J. Walker, and M. F. Chisholm. "Crystalline Oxides on Silicon: The First Five Monolayers." *Physical Review Letters* 81.14 (1998): 3014–3017. Web.

Meier, A.R., F Niu, and B.W. Wessels. "Integration of $BaTiO_3$ on Si (001) Using MgO/STO Buffer Layers by Molecular Beam Epitaxy." *Journal of Crystal Growth* 294.2 (2006): 401–406. Web. 25 May 2017.

Messner, Andreas et al. "Integrated Ferroelectric $BaTiO_3$/Si Plasmonic Modulator for 100 Gbit/s and Beyond." *Optical Fiber Communication Conference*. Part F84-O. Washington, D.C., D.C.: OSA, 2018. M2I.6. Web.

Messner, Andreas et al. "Integrated Ferroelectric Plasmonic Optical Modulator." *Optical Fiber Communication Conference Postdeadline Papers*. Washington, D.C.: OSA, 2017. Th5C.7. Web.

Meyer, J R et al. "Infrared Electro-optical Modulators Based on Field-induced Γ- L Intervalley Transfer." *Applied Physics Letters* 67.19 (1995): 2756–2758. Web. 16 Nov. 2017.

Miller, D. A B et al. “Band-Edge Electroabsorption in Quantum Well Structures: The Quantum-Confined Stark Effect.” *Physical Review Letters* 53.22 (1984): 2173–2176. Web.

Miller, David A. B. “Energy Consumption in Optical Modulators for Interconnects.” *Optics Express* 20.S2 (2012): A293. Web.

Mistry, K. et al. “A 45nm Logic Technology with High-K+Metal Gate Transistors, Strained Silicon, 9 Cu Interconnect Layers, 193nm Dry Patterning, and 100% Pb-Free Packaging.” *2007 IEEE International Electron Devices Meeting*. IEEE, 2007. 247–250. Web.

Momma, Koichi, and Fujio Izumi. “VESTA 3 for Three-Dimensional Visualization of Crystal, Volumetric and Morphology Data.” *Journal of Applied Crystallography* 44.6 (2011): 1272–1276. Web.

Monkman, Eric J. et al. “Quantum Many-Body Interactions in Digital Oxide Superlattices.” *Nature Materials* 11.10 (2012): 855–859. Web.

Moore, Gordon E. “Cramming More Components onto Integrated Circuits.” *Electronics* 38.8 (1975): n. pag. Print.

Moss, David J. et al. “New CMOS-Compatible Platforms Based on Silicon Nitride and Hydex for Nonlinear Optics.” *Nature Photonics* 7.8 (2013): 597–607. Web.

Mostovoy, Maxim. “Multiferroics Go High-T_C.” *Nature Materials* 7.4 (2008): 269–270. Web.

Muller, David A et al. “Atomic-Scale Imaging of Nanoengineered Oxygen Vacancy Profiles in $SrTiO_3$.” *Nature* 430.7000 (2004): 657–661. Web.

Müller, J. et al. “Optical Peaking Enhancement in High-Speed Ring Modulators.” *Scientific Reports* 4 (2014): 6310. Web.

Müller, T. et al. “A Quantum Light-Emitting Diode for the Standard Telecom Window around 1,550 Nm.” *Nature Communications* 9.1 (2018): 862. Web.

Mundy, Julia A. et al. “Atomically Engineered Ferroic Layers Yield a Room-Temperature Magnetoelectric Multiferroic.” *Nature* 537.7621 (2016): 523–527. Web. 9 Feb. 2017.

Muñoz, Pascual et al. “Silicon Nitride Photonic Integration Platforms for Visible, Near-Infrared and Mid-Infrared Applications.” *Sensors* 17.9 (2017): 2088. Web.

Nakagawa, Naoyuki, Harold Y Hwang, and David A Muller. “Why Some Interfaces Cannot Be Sharp.” *Nature Materials* 5.3 (2006): 204–209. Web.

Ng, Wai Lek et al. “An Efficient Room-Temperature Silicon-Based Light-Emitting Diode.” *Nature* 410.6825 (2001): 192–194. Web.

Nikolova, Dessislava et al. “Scaling Silicon Photonic Switch Fabrics for Data Center Interconnection Networks.” *Optics Express* 23.2 (2015): 1159. Web.

Niu, G. et al. “Molecular Beam Epitaxy Growth of $BaTiO_3$ Thin Films and Crucial Impact of Oxygen Content Conditions on the Electrical Characteristics.” *Thin Solid Films* 520.14 (2012): 4595–4599. Web.

O’Brien, Jeremy L., Akira Furusawa, and Jelena Vučković. “Photonic Quantum Technologies.” *Nature Photonics* 3.12 (2009): 687–695. Web.

Ogawa, Y et al. “Nonlinear Magneto-Optical Kerr Rotation of an Oxide Superlattice with Artificially Broken Symmetry.” *Physical Review Letters* 90.21 (2003): 217403. Web.

Ohnishi, T et al. “Improved Stoichiometry and Misfit Control in Perovskite Thin Film Formation at a Critical Fluence by Pulsed Laser Deposition.” *Applied Physics Letters* 87.24 (2005): 241919. Web.

Ohnishi, Tsuyoshi et al. “Defects and Transport in Complex Oxide Thin Films.” *Journal of Applied Physics* 103.10 (2008): 103703. Web.

Ohtomo, A., and H. Y. Hwang. “A High-Mobility Electron Gas at the $LaAlO_3/SrTiO_3$ Heterointerface.” *Nature* 427.6973 (2004): 423–426. Web. 29 Jan. 2017.

Ortmann, J. Elliott, Sunah Kwon, et al. “Monolithic Integration of Transition Metal Oxide Multiple Quantum Wells on Silicon (001).” *Journal of Applied Physics* 125.15 (2019): 155302. Web.

Ortmann, J. Elliott, Nishant Nookala, et al. “Quantum Confinement in Oxide Heterostructures: Room-Temperature Intersubband Absorption in $SrTiO_3/LaAlO_3$ Multiple Quantum Wells.” *ACS Nano* 12.8 (2018): 7682–7689. Web.

Ortmann, J. Elliott, Felix Eltes, et al. “Ultra-Low Power Tuning in Hybrid Barium Titanate-Silicon Nitride Electro-Optic Devices on Silicon.” Under Revi (2019): n. pag. Print.

Ortmann, J. Elliott, Agham B Posadas, and Alexander A Demkov. “The MBE Growth of Arbitrarily Thick $SrTiO_3/LaAlO_3$ Quantum Well Heterostructures for Use in next-Generation Optoelectronic Devices.” *Journal of Applied Physics* 124.1 (2018): 015301. Web.

Ortmann, J Elliott et al. “Electric Field Tuning of $BaTiO_3$-on-Silicon Multi-Ring Resonators via the Pockels Effect.” *2018 IEEE 15th International Conference on Group IV Photonics (GFP)*. IEEE, 2018. 1–2. Web.

Park, J. W. et al. “Quasi-Single-Crystal (001) $SrTiO_3$ Templates on Si.” *Applied Physics Letters* 95.6 (2009): 061902. Web.

Park, Min Sik, S. H. Rhim, and Arthur J. Freeman. “Charge Compensation and Mixed Valency in $LaAlO_3/SrTiO_3$ Heterointerfaces Studied by the FLAPW Method.” *Physical Review B* 74.20 (2006): 205416. Web. 17 Apr. 2018.

Parratt, L. G. “Surface Studies of Solids by Total Reflection of X-Rays.” *Physical Review* 95.2 (1954): 359–369. Web.

Patel, David et al. “Design, Analysis, and Transmission System Performance of a 41 GHz Silicon Photonic Modulator.” *Optics Express* 23.11 (2015): 14263. Web.

Pathak, Shibnath, Dries Van Thourhout, and Wim Bogaerts. “Design Trade-Offs for Silicon-on-Insulator-Based AWGs for (de)Multiplexer Applications.” *Optics Letters* 38.16 (2013): 2961. Web.

Peng, Luke S.-J. et al. “Strain Relaxation during in Situ Growth of $SrTiO_3$ Thin Films.” *Applied Physics Letters* 83.22 (2003): 4592. Web. 29 Jan. 2017.

Perdew, J. P., and Alex Zunger. “Self-Interaction Correction to Density-Functional Approximations for Many-Electron Systems.” *Physical Review B* 23.10 (1981): 5048–5079. Web. 25 Feb. 2017.

Pernice, Wolfram H P et al. “Design of a Silicon Integrated Electro-Optic Modulator Using Ferroelectric $BaTiO_3$ Films.” *IEEE Photonics Technology Letters* 26.13 (2014): 1344–1347. Web.

Petousi, Despoina et al. “Analysis of Optical and Electrical Tradeoffs of Traveling-Wave Depletion-Type Si Mach–Zehnder Modulators for High-Speed Operation.” *IEEE Journal of Selected Topics in Quantum Electronics* 21.4 (2015): 199–206. Web.

Petraru, A et al. “Integrated Optical Mach-Zehnder Modulator Based on Polycrystalline $BaTiO_3$.” *Optics letters* 28.24 (2003): 2527–9. Web.

Politi, A. et al. “Integrated Quantum Photonics.” *IEEE Journal of Selected Topics in Quantum Electronics* 15.6 (2009): 1673–1684. Web.

Poon, Joyce K. et al. “Transmission and Group Delay of Microring Coupled-Resonator Optical Waveguides.” *Optics Letters* 31.4 (2006): 456. Web.

Posadas, Agham B. et al. “Scavenging of Oxygen from $SrTiO_3$ during Oxide Thin Film Deposition and the Formation of Interfacial 2DEGs.” *Journal of Applied Physics* 121.10 (2017): 105302. Web.

Poulton, Christopher V. et al. “Coherent Solid-State LIDAR with Silicon Photonic Optical Phased Arrays.” *Optics Letters* 42.20 (2017): 4091. Web.

Preskill, John. “Quantum Computing in the NISQ Era and Beyond.” *Quantum* 2.July (2018): 79. Web.

Prezioso, M. et al. “Training and Operation of an Integrated Neuromorphic Network Based on Metal-Oxide Memristors.” *Nature* 521.7550 (2015): 61–64. Web.

Prinzen, Andreas, Michael Waldow, and Heinrich Kurz. “Fabrication Tolerances of SOI Based Directional Couplers and Ring Resonators.” *Optics Express* 21.14 (2013): 17212. Web.

Qiang, Xiaogang et al. “Large-Scale Silicon Quantum Photonics Implementing Arbitrary Two-Qubit Processing.” *Nature Photonics* 12.9 (2018): 534–539. Web.

Qiao, L. et al. “Epitaxial Growth, Structure, and Intermixing at the $LaAlO_3/SrTiO_3$ Interface as the Film Stoichiometry Is Varied.” *Physical Review B* 83.8 (2011): 085408. Web.

Qiao, L et al. “Thermodynamic Instability at the Stoichiometric $LaAlO_3/SrTiO_3$ (001) Interface.” *Journal of Physics: Condensed Matter* 22.31 (2010): 312201. Web.

Rabe, Karin M., Charles H. Ahn, and Jean-Marc (eds) Triscone. *Physics of Ferroelectrics*. Vol. 105. Springer, 2007. Web.

Rabiei, Payam et al. “Heterogeneous Lithium Niobate Photonics on Silicon Substrates.” *Optics Express* 21.21 (2013): 25573. Web.

Ramesh, Ramamoorthy, and Darrell G Schlom. “Whither Oxide Electronics?” *MRS Bulletin* 33.11 (2008): 1006–1014. Web.

Rao, C N R. “Transition Metal Oxides.” *Annual Review of Physical Chemistry* 40.1 (1989): 291–326. Web.

Ravichandran, J. et al. “Tuning the Electronic Effective Mass in Double-Doped $SrTiO_3$.” *Physical Review B* 83.3 (2011): 035101. Web.

Ravichandran, Jayakanth et al. “An Epitaxial Transparent Conducting Perovskite Oxide: Double-Doped $SrTiO_3$.” *Chemistry of Materials* 22.13 (2010): 3983–3987. Web.

Reed, G. T. et al. “Silicon Optical Modulators.” *Nature Photonics* 4.8 (2010): 518–526. Web.

Reed, Graham T. et al. “Recent Breakthroughs in Carrier Depletion Based Silicon Optical Modulators.” *Nanophotonics* 3.4–5 (2014): 229–245. Web.

Reed, M A, J W Lee, and H-L Tsai. “Resonant Tunneling through a Double GaAs/AlAs Superlattice Barrier, Single Quantum Well Heterostructure.” *Applied Physics Letters* 49.3 (1986): 158–160. Web. 30 May 2017.

Reiner, J. W. et al. “Electrical Properties and Interfacial Structure of Epitaxial $LaAlO_3$ on Si (001).” *Journal of Applied Physics* 105.12 (2009): 124501. Web.

Reyren, N. et al. “Superconducting Interfaces Between Insulating Oxides.” *Science* 317.5842 (2007): n. pag. Print.

Ribes, G. et al. “Review on High-*k* Dielectrics Reliability Issues.” *IEEE Transactions on Device and Materials Reliability* 5.1 (2005): 5–19. Web.

Riley, James R. et al. “Three-Dimensional Mapping of Quantum Wells in a GaN/InGaN Core–Shell Nanowire Light-Emitting Diode Array.” *Nano Letters* 13.9 (2013): 4317–4325. Web. 29 Jan. 2017.

Ríos, Carlos et al. “Integrated All-Photonic Non-Volatile Multi-Level Memory.” *Nature Photonics* 9.September (2015): 725–732. Web.

Robertson, John. “Band Offsets of Wide-Band-Gap Oxides and Implications for Future Electronic Devices.” *Journal of Vacuum Science & Technology B: Microelectronics and Nanometer Structures* 18.3 (2000): 1785–1791. Web. 11 Aug. 2016.

Robertson, John. “High Dielectric Constant Gate Oxides for Metal Oxide Si Transistors.” *Reports on Progress in Physics* 69.2 (2006): 327–396. Web.

Robertson, John, and Robert M. Wallace. “High-K Materials and Metal Gates for CMOS Applications.” *Materials Science and Engineering: R: Reports* 88 (2015): 1–41. Web.

Rouvalis, Efthymios. “Indium Phosphide Based IQ-Modulators for Coherent Pluggable Optical Transceivers.” *2015 IEEE Compound Semiconductor Integrated Circuit Symposium, CSICS 2015*. New Orleans, LA: N.p., 2015. 1–4. Web.

Sai, Na, B. Meyer, and David Vanderbilt. “Compositional Inversion Symmetry Breaking in Ferroelectric Perovskites.” *Physical Review Letters* 84.24 (2000): 5636–5639. Web.

Sakudo, T. “Oxide Superconductors.” *Ferroelectrics* 95.1 (1989): 37–41. Web.

Saleh, Bahaa E A, and Malvin Carl Teich. *Fundamentals of Photonics*. New York, USA: John Wiley & Sons, Inc., 1991. Web. Wiley Series in Pure and Applied Optics.

Santander-Syro, A. F. et al. “Two-Dimensional Electron Gas with Universal Subbands at the Surface of $SrTiO_3$.” *Nature* 469.7329 (2011): 189–193. Web. 28 Aug. 2017.

Schlom, D. G. et al. “Molecular Beam Epitaxy of Layered Dy-Ba-Cu-O Compounds.” *Applied Physics Letters* 53.17 (1988): 1660–1662. Web.

Schlom, Darrell G. “Perspective: Oxide Molecular-Beam Epitaxy Rocks!” *APL Materials* 3.6 (2015): 062403. Web.

Schlom, Darrell G et al. “A Thin Film Approach to Engineering Functionality into Oxides.” *Journal of the American Ceramic Society* 91.8 (2008): 2429–2454. Web. 28 Aug. 2017.

Schubert, E Fred. “Light-Emitting Diodes.” *Wiley Encyclopedia of Electrical and Electronics Engineering*. Hoboken, NJ, USA: John Wiley & Sons, Inc., 2014. 1–10. Web. Major Reference Works.

Shen, Yichen et al. “Deep Learning with Coherent Nanophotonic Circuits.” *Nature Photonics* 11.7 (2017): 441–446. Web. 9 Apr. 2018.

Shi, Yongqiang, Lianshan Yan, and Alan Eli Willner. “High-Speed Electrooptic Modulator Characterization Using Optical Spectrum Analysis.” *Journal of Lightwave Technology* 21.10 (2003): 2358. Web.

Shieh, Tung-Ho, and Si-Chen Lee. “Transport Mechanism of X Band Electrons in AlAs Electrode through GaAs/AlAs/GaAs Structure by Varying GaAs Well Thickness.” *Applied Physics Letters* 63.24 (1993): 3350. Web.

Siemons, Wolter et al. “Origin of Charge Density at $LaAlO_3$ on $SrTiO_3$ Heterointerfaces: Possibility of Intrinsic Doping.” *Physical Review Letters* 98.19 (2007): 196802. Web. 14 Aug. 2017.

Sinha, S K et al. “X-Ray and Neutron Scattering from Rough Surfaces.” *Physical Review B* 38.4 (1988): 2297–2311. Web.

Sirenko, A. A. et al. “Soft-Mode Hardening in $SrTiO_3$ Thin Films.” *Nature* 404.6776 (2000): 373–376. Web. 7 Feb. 2017.

Sollner, T. C. L. G. et al. “Resonant Tunneling through Quantum Wells at Frequencies up to 2.5 THz.” *Applied Physics Letters* 43.6 (1983): 588–590. Web. 20 June 2017.

Soref, R., and B. Bennett. “Electrooptical Effects in Silicon.” *IEEE Journal of Quantum Electronics* 23.1 (1987): 123–129. Web.

Spah, R. J. et al. “Parameters for *in Situ* Growth of High T_c Superconducting Thin Films Using an Oxygen Plasma Source.” *Applied Physics Letters* 53.5 (1988): 441–443. Web.

Stan, Nikola et al. “Non-Perturbing Voltage Measurement in a Coaxial Cable with Slab-Coupled Optical Sensors.” *Applied Optics* 56.24 (2017): 6814–6821. Web.

Steane, Andrew. “Quantum Computing.” *Reports on Progress in Physics* 61.2 (1998): 117–173. Web.

Stutius, W., and W. Streifer. “Silicon Nitride Films on Silicon for Optical Waveguides.” *Applied Optics* 16.12 (1977): 3218. Web.

Sung, Changhyuck, Hyunsang Hwang, and In Kyeong Yoo. “Perspective: A Review on Memristive Hardware for Neuromorphic Computation.” *Journal of Applied Physics* 124.15 (2018): 151903. Web.

Suryanarayana, C., and M. Grant Norton. *X-Ray Diffraction*. Boston, MA: Springer US, 1998. Web.

Takada, Kazunori et al. “Superconductivity in Two-Dimensional CoO_2 Layers.” *Nature* 422.6927 (2003): 53–55. Web.

Takenaka, Mitsuru et al. “III–V/Si Hybrid MOS Optical Phase Shifter for Si Photonic Integrated Circuits.” *Journal of Lightwave Technology* 37.5 (2019): 1474–1483. Web.

Tan, I-H. et al. “A Self-consistent Solution of Schrödinger–Poisson Equations Using a Nonuniform Mesh.” *Journal of Applied Physics* 68.8 (1990): 4071–4076. Web.

Tarsa, E. J. et al. “Growth-Related Stress and Surface Morphology in Homoepitaxial $SrTiO_3$ Films.” *Applied Physics Letters* 68.4 (1996): 490. Web.

Thiel, S. “Tunable Quasi-Two-Dimensional Electron Gases in Oxide Heterostructures.” *Science* 313.5795 (2006): 1942–1945. Web.

Thomson, David et al. “Roadmap on Silicon Photonics.” *Journal of Optics* 18.7 (2016): 073003. Web.

Tian, W. et al. “Structural Evidence for Enhanced Polarization in a Commensurate Short-Period $BaTiO_3/SrTiO_3$ Superlattice.” *Applied Physics Letters* 89.9 (2006): 092905. Web.

Timurdogan, Erman et al. “An Ultralow Power Athermal Silicon Modulator.” *Nature Communications* 5.1 (2014): 4008. Web.

Tokuda, Y. et al. “Strontium Vacancy Clustering in Ti-Excess $SrTiO_3$ Thin Film.” *Applied Physics Letters* 99.3 (2011): 033110. Web.

Tokura, Y. “Orbital Physics in Transition-Metal Oxides.” *Science* 288.5465 (2000): 462–468. Web.

Tsu, R, and L Esaki. “Tunneling in a Finite Superlattice.” *Applied Physics Letters* 22.11 (1973): 562–564. Web. 20 June 2017.

Uecker, Reinhard et al. “Large-Lattice-Parameter Perovskite Single-Crystal Substrates.” *Journal of Crystal Growth* 457 (2017): 137–142. Web.

Van Den Broeck, D. M. et al. “Strain-Balanced InGaN/GaN Multiple Quantum Wells.” *Applied Physics Letters* 105.3 (2014): 031107. Web. 29 Jan. 2017.

Vandoorne, Kristof et al. “Experimental Demonstration of Reservoir Computing on a Silicon Photonics Chip.” *Nature Communications* 5 (2014): 3541. Web. 9 Apr. 2018.

Vila-Fungueiriño, José Manuel et al. “Epitaxial $La_{0.7}Sr_{0.3}MnO_3$ Thin Films on Silicon with Excellent Magnetic and Electric Properties by Combining Physical and Chemical Methods.” *Science and Technology of Advanced Materials* 19.1 (2018): 702–710. Web.

Wakelin, Suzanne, and Andrew C. Walker. “Digital Optical Computing.” *Physics Education* 29.3 (1994): 155–159. Web.

Wakita, K. et al. “Long-Wavelength Waveguide Multiple-Quantum-Well (MQW) Optical Modulator with 30:1 on/off Ratio.” *Electronics Letters* 22.17 (1986): 907. Web.

Waldrop, M. Mitchell. “The Chips Are down for Moore’s Law.” *Nature* 530.7589 (2016): 144–147. Web.

Wang, Shipeng et al. “On-Chip Reconfigurable Optical Add-Drop Multiplexer for Hybrid Wavelength/Mode-Division-Multiplexing Systems.” *Optics Letters* 42.14 (2017): 2802. Web.

Warusawithana, Maitri P. et al. “Artificial Dielectric Superlattices with Broken Inversion Symmetry.” *Physical Review Letters* 90.3 (2003): 036802. Web.

Wei, Yi et al. “Mechanism of Cleaning Si(100) Surface Using Sr or SrO for the Growth of Crystalline $SrTiO_3$ Films.” *Journal of Vacuum Science & Technology B: Microelectronics and Nanometer Structures* 20.4 (2002): 1402. Web.

Werner, T. et al. “Experimental Demonstration of Short and Long Term Synaptic Plasticity Using OxRAM Multi K-Bit Arrays for Reliable Detection in Highly Noisy Input Data.” *2016 IEEE International Electron Devices Meeting (IEDM)*. IEEE, 2016. 16.6.1-16.6.4. Web.

Wilk, G. D., R. M. Wallace, and J. M. Anthony. “High-κ Gate Dielectrics: Current Status and Materials Properties Considerations.” *Journal of Applied Physics* 89.10 (2001): 5243–5275. Web.

Willett-Gies, Travis, Eric DeLong, and Stefan Zollner. “Vibrational Properties of Bulk $LaAlO_3$ from Fourier-Transform Infrared Ellipsometry.” *Thin Solid Films* 571 (2014): 620–624. Web. 7 Feb. 2017.

Williams, David B., and C. Barry Carter. *Transmission Electron Microscopy*. Boston, MA: Springer US, 2009. Web.

Willmott, P. R. et al. “Structural Basis for the Conducting Interface between $LaAlO_3$ and $SrTiO_3$.” *Physical Review Letters* 99.15 (2007): 155502. Web.

Wooten, E.L. et al. “A Review of Lithium Niobate Modulators for Fiber-Optic Communications Systems.” *IEEE Journal of Selected Topics in Quantum Electronics* 6.1 (2000): 69–82. Web.

Wu, Q., T. D. Hewitt, and X.-C. Zhang. “Two-dimensional Electro-optic Imaging of THz Beams.” *Applied Physics Letters* 69.8 (1996): 1026–1028. Web.

Wu, Rui et al. “Pairing of Microring-Based Silicon Photonic Transceivers for Tuning Power Optimization.” *2018 23rd Asia and South Pacific Design Automation Conference (ASP-DAC)*. Vol. 2018–Janua. IEEE, 2018. 135–140. Web.

Wunderlich, Wilfried, Hiromichi Ohta, and Kunihito Koumoto. “Enhanced Effective Mass in Doped $SrTiO_3$ and Related Perovskites.” *Physica B: Condensed Matter* 404.16 (2009): 2202–2212. Web.

Xia, Fengnian et al. “Ultra-Compact High Order Ring Resonator Filters Using Submicron Silicon Photonic Wires for on-Chip Optical Interconnects.” *Optics Express* 15.19 (2007): 11934. Web. 12 Apr. 2018.

Xia, Fengnian, Lidija Sekaric, and Yurii Vlasov. “Ultracompact Optical Buffers on a Silicon Chip.” *Nature Photonics* 1.1 (2007): 65–71. Web.

Xiong, Chi et al. “Active Silicon Integrated Nanophotonics: Ferroelectric $BaTiO_3$ Devices.” *Nano Letters* 14.3 (2014): 1419–1425. Web. 5 Apr. 2017.

Xu, Ke et al. “Compatibility of Silicon Mach-Zehnder Modulators for Advanced Modulation Formats.” *Journal of Lightwave Technology* 31.15 (2013): 2550–2554. Web.

Xu, Qianfan et al. “Micrometre-Scale Silicon Electro-Optic Modulator.” *Nature* 435.7040 (2005): 325–327. Web. 9 Apr. 2018.

Yamada, Hiroyuki et al. “Perovskite Oxide Tricolor Superlattices with Artificially Broken Inversion Symmetry by Interface Effects.” *Applied Physics Letters* 81.25 (2002): 4793–4795. Web.

Yamada, Koji, Tai Tsuchizawa, et al. “High-Performance Silicon Photonics Technology for Telecommunications Applications.” *Science and Technology of Advanced Materials* 15.2 (2014): 024603. Web. 9 Apr. 2018.

Yamada, Koji, Yutaka Urino, et al. “Integrated Silicon-Based Optical Interconnect for Fast, Compact, Energy-Efficient Electronic Circuit Systems.” *NTT Technical Review* 11.2 (2010): n. pag. Print.

Yamamoto, Ryosuke et al. “Structural Comparison of *n*-Type and *p*-Type $LaAlO_3/SrTiO_3$ Interfaces.” *Physical Review Letters* 107.3 (2011): 036104. Web.

Yang, He et al. “Nanowire Network–based Multifunctional All-Optical Logic Gates.” *Science Advances* 4.7 (2018): eaar7954. Web.

Yariv, A., and P. Yeh. *Optical Waves in Crystals*. John Wiley & Sons, Inc., 1984. Print.

Yasaka, M. “X-Ray Thin-Film Measurement Techniques V. X-Ray Reflectivity Measurement.” *The Rigaku Journal* 26 (2010): 1–9. Print.

Yong, G. J. et al. “Thermal Stability of $SrTiO_3/SiO_2/Si$ Interfaces at Intermediate Oxygen Pressures.” *Journal of Applied Physics* 108.3 (2010): 033502. Web.

Zgonik, M. et al. “Dielectric, Elastic, Piezoelectric, Electro-Optic, and Elasto-Optic Tensors of $BaTiO_3$ Crystals.” *Physical Review B* 50.9 (1994): 5941–5949. Web.

Zhalehpour, Sasan, Jiachuan Lin, and Leslie Rusch. “SiP IQ Modulator Linearization by Memory Polynomial Pre-Distortion Model.” *International Photonics Conference of the IEEE*. Orlando, USA: N.p., 2017. TuH2.3. Print.

Zhang, Dingyou, and James J.-Q. Lu. “3D Integration Technologies: An Overview.” *Materials for Advanced Packaging*. Ed. Daniel Lu and C P Wong. Cham: Springer International Publishing, 2017. 1–26. Web.

Zhang, Yu, Rui Han, and Tiantang Xiang. “Application of Non-Contact Optic Voltage Sensor Based on Pockels Effect in ±800 KV Convertor Station.” *2016 IEEE International Conference on High Voltage Engineering and Application (ICHVE),*. N.p., 2016. Print.

Zhao, Kuaile et al. “Mid-Infrared Intersubband Absorptions in ZnO/ZnMgO Multiple Quantum Wells.” *Applied Physics Letters* 104.21 (2014): 212104. Web.

Zheng, Shuang et al. “Compact Tunable Photonic Comb Filter on a Silicon Platform.” *Optics Letters* 42.14 (2017): 2762. Web.

Zhong, Zhicheng, P. X. Xu, and Paul J. Kelly. “Polarity-Induced Oxygen Vacancies at $LaAlO_3$⁄$SrTiO_3$ Interfaces.” *Physical Review B* 82.16 (2010): 165127. Web.

Zhou, Qifa et al. “Piezoelectric Films for High Frequency Ultrasonic Transducers in Biomedical Applications.” *Progress in Materials Science* 56.2 (2011): 139–174. Web.

Zhou, Zhiping, Ruixuan Chen, et al. “Development Trends in Silicon Photonics for Data Centers.” *Optical Fiber Technology* 44.March (2018): 13–23. Web.

Zhou, Zhiping, Xingjun Wang, et al. “Silicon Photonics for Advanced Optical Communication Systems.” *Optical Engineering* 52.4 (2013): 045007. Web.

Zhuravel, A. P. et al. “Influence of $LaAlO_3$ Surface Topography on Rf Current Distribution in Superconducting Microwave Devices.” *Applied Physics Letters* 81.26 (2002): 4979–4981. Web.

Zubko, P et al. “Electrostatic Coupling and Local Structural Distortions at Interfaces in Ferroelectric/Paraelectric Superlattices.” *Nano Letters* 12.6 (2012): 2846–2851. Web. 25 Aug. 2017.